

Tord Engelhardt Andersen

# **Petrogenesis of Fe-Ti-P rich rock in the Siljan- Hvarnes Intrusion, S.E. Norway**

Immiscibility as a rock forming process in shallowly emplaced alcalic metaluminous granitoids

Master's thesis in Bedrock and Resource Geology

Supervisor: Suzanne McEnroe

Co-supervisor: Nolwenn Coint

June 2021



Tord Engelhardt Andersen

# **Petrogenesis of Fe-Ti-P rich rock in the Siljan- Hvarnes Intrusion, S.E. Norway**

Immiscibility as a rock forming process in shallowly  
emplaced alcalic metaluminous granitoids

Master's thesis in Bedrock and Resource Geology  
Supervisor: Suzanne McEnroe  
Co-supervisor: Nolwenn Coint  
June 2021

Norwegian University of Science and Technology  
Faculty of Engineering  
Department of Geoscience and Petroleum



Norwegian University of  
Science and Technology



# Abstract

The Siljan -Hvarnes Intrusion located in the Vestfold Graben, S.E. Norway, formed 277 Ma. during the most active volcanic period of the rifting of Oslo Graben. The intrusion consists of several nested rings developing westwards over a span of ~20 km. Little academic work has been conducted on this intrusion previously, and this study aims to increase the general petrogenesis of the pluton and investigate associated occurrences of Fe-Ti-P rich rock. Some of the larger mineralizations of Fe-Ti-P rich rock have previously been mined for iron ore, such as Eirik's Gruve, Jernskottet and the mine pits at Kåsemyrene. Today, apatite from the ore might represent an economical interest due to high phosphorus content and enrichment of REE (Rare Earth Elements).

Bulk rock analysis of both plutonic rocks and ore have been conducted with XRF and LA-ICP-MS. Mineral geochemical analysis was obtained with microprobe, and LA-ICP-MS. Additional geomagnetic analyses were conducted to evaluate if magnetic anomalies from larger Fe-Ti-P occurrences could be identified in open-source geomagnetic maps.

Results implied the pluton is shallowly emplaced and consists of ferroan alkalic metaluminous granitoids, which form a geochemical trend from monzonites to syenites. The granitoid rocks were later impregnated of monzodioritic dikes and quartz syenitic veins. Feldspar phenocryst analysis suggests the granitoids stem from various more deeply situated magma sources which today can be observed as areas with extensive magma mingling. Bulk analyses reveal all rocks in the pluton are enriched in REEs and especially LREE. The Fe-Ti-P rich rock have TREE (Total Rare Earth Element) content from 1500 ppm to 4000 ppm. Mineral analysis suggest apatite is the main carrier for REEs with REE content ranging from 1 wt.% - 3 wt.% at Kåsemyrene, and up to 7 wt.% in apatite from Eirik's Gruve. P<sub>2</sub>O<sub>5</sub> content of homogeneous Fe-Ti-P rich rock ranges from 4,4 wt.% - 5,4 wt.%. Chemical and textural analysis suggest the Fe-Ti-P rich rock formed by crystallization of a Fe-rich liquid separated during silicate liquid immiscibility. Larger Fe-Ti-P occurrences are interpreted to stem from sinking Fe-rich liquid which pooled along internal solid contacts in the magma chamber. The geomagnetic study revealed existing open-source geomagnetic maps have too coarse resolution to depict anomalies from known Fe-Ti-P rich ores. However, all Fe-Ti-P mineralizations tend to accumulate along overlapping magnetic and radiometric boundaries interpreted to represent lithological contacts.

# Sammendrag

Siljan -Hvarnes-intrusjonen ligger i Vestfold Graben, i S.E. Norge. Intrusjonen ble formet for 277 M. år siden under den mest aktive vulkanske perioden i dannelsen av Oslo Graben. Intrusjonen består av flere sammenflettede plutoniske ringstrukturer som ble dannet av sekvensielle intrusjoner som utviklet seg fra øst mot vest. Den totale lengden av intrusjonen er ca. 20 km. Det har blitt utført lite akademisk arbeid på denne intrusjonen tidligere, og denne studien tar sikte på å øke den generelle forståelsen av bergartsdannelsen i plutonen og de assosierte forekomstene av Fe-Ti-P-rik bergart. Noen av de større mineraliseringene av Fe-Ti-P-rik bergart i feltområdet har tidligere blitt utvunnet for jernmalm, slik som Eiriks Gruve, Jernskottet og dagbruddene ved Kåsemyrene. I dag kan apatitt fra malmen utgjøre en økonomisk interesse på grunn av høyt fosforinnhold og høy berikelse av sjeldne jordarter.

Bulk-analyse av Fe-Ti-P malm og plutoniske bergarter er utført med XRF og LA-ICP-MS. Geokjemisk mineralanalyse ble utført med mikroprobe og LA-ICP-MS. Ytterligere geomagnetiske analyser ble utført for å evaluere om magnetiske anomalier fra større Fe-Ti-P-forekomster kunne identifiseres i geomagnetiske kart med åpen kildekode fra NGU.

Resultatene antyder at plutonen intruderte i den øvre del av skorpen, og består av ferroiske alkaliske metalluminøse granitoider som danner en geokjemisk trend fra monzonittisk til syenittisk komposisjon. Granitoidbergartene ble senere impregneret av monzodiorittiske ganger og kvarts-syenittiske årer. Analyse av feltspat-fenokrystaller antyder at granitoidene stammer fra forskjellige dyptliggende magmakilder. Dette kan i dag observeres som områder assosiert med to eller flere magmatyper som opptrer sammen. Bulkanalyser avslører at generelt alle bergarter i plutonen er beriket på sjeldne jordarter, og spesielt på de lette jordartene. Fe-Ti-P-rik bergart har et totalinnhold på sjeldne jordarter på 1500 ppm til 4000 ppm. Mineralanalyse antyder at apatitt er hovedbæreren for sjeldne jordarter med et innhold som spenner fra 1 vekt% til 3 vekt% i prøvene fra Kåsemyrene, og opptil 7 vekt% i apatitt fra Eiriks Gruve.  $P_2O_5$ -innholdet i homogent Fe-Ti-P-rikt fjell varierer fra 4,4 vekt% - 5,4 vekt%. Kjemisk- og teksturanalyse antyder at den Fe-Ti-P-rike bergarten er dannet ved krystallisering av en jernrik væskefase. Denne ble mest sannsynlig dannet ved at en homogen magma skilte seg til to ikke-blandbare væsker, en silikat-rik væske og en jern-rik væske. Alle større Fe-Ti-P-forekomster tolkes til at de ble dannet av synkende Fe-rik væske som samlet seg langs solide grenser i magmakammeret. Den geomagnetiske studien avdekket at eksisterende og tilgjengelige geomagnetiske kart har for grov oppløsning til å vise magnetiske anomalier fra større kjente Fe-Ti-P-rike malmer. Imidlertid har alle Fe-Ti-P mineraliseringer en tendens til å opptre langs overlappende magnetiske og radiometriske grenser tolket for å representere litologiske kontakter.

# Acknowledgements

*I want to praise Nolwenn Coint for all the time and consideration you have spent on my field work and writing during the last two years. Without you, this thesis would not be possible. I would further like to use this opportunity to thank supervisor Suzanne McEnroe in guiding me through the unintuitive and theoretically heavy study of geomagnetism. Never had I thought I would have to refer to "quantum theory" in my work. I would further send a special thanks to Torill Sørløkk, Nathan Church and Graham Hagen-Peter for trusting me in using their expensive lab-equipment. I would like to thank Alf Olav Larsen for joining us in the field and showing us the mine pits at Kåsemyrene. Your work on the mining history in the Vestfold area has helped me put a historical context to the areas I have visited. Lastly, I would thank my girlfriend Hanne Petlund, your patience with me in a period of thesis writing and lockdowns have been extraordinary.*

# Contents

Abstract .....	V
Sammendrag .....	VI
Acknowledgements .....	VII
List of Figures .....	XI
List of Tables .....	XV
Abbreviations.....	XVI
1 Introduction.....	1
1.1 Aim of Thesis .....	2
1.2 Geological Background .....	2
1.2.1 Regional Geology .....	2
1.2.2 Larvik Plutonic Complex (LPC) .....	5
1.2.3 Siljan -Hvarnes intrusion.....	6
1.3 Local historical aspects of the Fe- Ti – P- rich rock.....	8
2 Theory .....	9
2.1 Geomagnetic theory .....	9
2.1.1 Magnetic response and total magnetization .....	12
<b>2.1.2</b> Königsberger ratio.....	13
2.1.3 Density calculation .....	13
2.2 Rock classification and distribution of elements .....	15
2.2.1 Substitution of trace elements .....	16
2.2.2 Rare Earth Elements.....	16
2.2.3 Partition of trace elements into minerals .....	17
2.2.4 Partitioning of trace elements into apatite .....	18
2.2.5 HFSE and LILE classification .....	18
2.2.6 Partitioning of LILE and HFSE in minerals: .....	19
2.2.7 Transition metals classification.....	19
2.2.8 Partitioning of transition metals into minerals .....	20
2.3 Classification diagrams.....	21
2.3.1 TAS- classification .....	21
2.3.2 Basalt classification .....	22
2.3.3 Granitoid classification .....	23
2.4 Differentiation processes .....	26
2.4.1 Fractional crystallization.....	26



2.4.2	Immiscibility .....	27
2.4.3	Magma mixing .....	28
2.4.4	Assimilation .....	29
2.4.5	Miarolitic pods and cavities .....	29
3	Methodology .....	30
3.1	Field work and sampling .....	30
3.2	Optical microscopy .....	30
3.3	Thin section scanning .....	30
3.4	XRF .....	30
3.4.1	XRF Trace element .....	31
3.4.2	XRF Major elements .....	31
3.5	EPMA .....	31
3.6	LA-ICP-MS analysis of apatite trace elements .....	32
3.7	Geophysical methodology .....	32
3.7.1	Preparation of samples .....	32
3.7.2	Density measurements .....	33
3.7.3	Susceptibility measurements .....	33
3.7.4	NRM measurements .....	33
4	Results .....	34
4.1	Rock Descriptions .....	34
4.1.1	Rhomb porphyry .....	36
4.1.2	Medium to coarse-grained syenite .....	37
4.1.3	Very coarse-grained syenite .....	39
4.1.4	Porphyritic and trachytic syenite .....	42
4.1.5	Monzodioritic dikes .....	44
4.1.6	Quartz syenitic dike .....	45
4.1.7	Fe- Ti-P rich rock .....	46
4.2	Key locations .....	49
4.2.1	Location 520: .....	49
4.2.2	Kåsemyrene .....	51
4.2.3	Søllandliene .....	56
4.3	Geochemical Analyses .....	62
4.3.1	Whole Rock Analyses .....	62
4.3.2	Mineral analysis .....	73
4.4	Results Geomagnetic study .....	96

4.4.1	Königsberger -Plot.....	96
4.4.2	Remanent magnetization assessment .....	97
5	Discussion .....	101
5.1	Overall assessment: The Siljan- Hvarnes intrusion .....	101
5.1.1	Emplacement depth.....	101
5.1.2	Rhomb porphyry .....	102
5.1.3	Medium to coarse grained syenite .....	103
5.1.4	Very coarse-grained syenite .....	105
5.1.5	Porphyritic-trachytic quartz monzonite .....	106
5.1.6	Monzodioritic dike .....	108
5.1.7	Porphyritic and trachytic syenite .....	109
5.1.8	Fe- Ti- P rich rock.....	112
5.2	Geomagnetic Study .....	124
6	Conclusion.....	127
	Recommendations for Future Work .....	127
7	References .....	128
	Appendix .....	i
	APPENDIX A: Geomagnetism .....	ii
	APPENDIX B: EPMA Analysis .....	i
	APPENDIX C: XRF Analysis.....	i
	APPENDIX D: Bulk Rock Trace Element Analysis .....	i
	APPENDIX E: Apatite LA-ICP-MS Analysis .....	i

# List of Figures

Figure 1-1: Modified geological map of the Larvik ring complex. Figure from (Andersen et al., 2014) with ages from (Sundvoll et al., 1990).....	5
Figure 2: Bedrock map of the Siljan-Hvarnes Intrusion.....	7
Figure 2-1: HFSE, LILE and MRFE groupings. See link <a href="https://bit.ly/2Ua0MQM">https://bit.ly/2Ua0MQM</a> , based on Railsback (2003), An Earth Scientists Periodic table and Best (2003). ....	19
Figure 2-2: Modified TAS diagram (Total Alkalis vs Silica) (Middlemost, 1994). ....	21
Figure 2-3: Basalt classification diagram (Yoder, H.S.; Tilley, 1962) .....	22
Figure 2-4: Granitoid classification based on quartz-, alkali-, plagioclase-, and nepheline normative composition (Streckeisen, 1974). ....	23
Figure 2-5: Diagram (A – C) suggested by Frost et al (2001) to discriminate between granitoids. ....	25
Figure 2-6: Liquid- liquid partition coefficient D plotted against ionic potential Z/r by Veksler and Charlier (2015). ....	28
Figure 4-1: Sampling location presented with sample number and symbols representing rock class. ....	35
Figure 4-2: Field photograph of syenitic intrusion in rhomb porphyry sequence. ....	36
Figure 4-3: Sketch of trachytic syenite (red) intruded in rhomb porphyry (grey). Fe-Ti-P rich bleb and magma mingling in lower right corner of the picture. ....	37
Figure 4-4: Fresh cut of blue- grey medium to coarse grained syenite (Sample 531). ...	38
Figure 4-5: Slab photo of the sharp contact in sample 536 .....	38
Figure 4-6: Slab photographs of the very coarse grained syenites. ....	39
Figure 4-7: Field photograph of the very coarse- grained syenite (511).....	40
Figure 4-8: Photomicrograph (PPL, 5x magnification) of an interstitial mafic pocket in sample 519.....	41
Figure 4-9: Photomicrograph of symplectitic teture of quartz and biotite (519).....	41
Figure 4-10: Slab photograph of porphyritic syenite with rounded phenocrysts in a fine-grained ground mass (sample 539).....	42
Figure 4-11: Slab photograph of pale grey feldspars with trachytic texture (sample 535). ....	43
Figure 4-12: Field photo of megacrysts in porphyritic syenite, close to sampling location for 538: .....	43
Figure 4-13: Field photo of location/ sample 509, monzodioritic dike cutting through coarse-grained syenite. ....	44
Figure 4-14: Sketch of location/ sample 509, outlined monzodioritic dike cutting through coarse grained syenite. ....	45
Figure 4-15: This sample (403) from Kåsemyrene displays the relationship between massive Fe-Ti-P ore and pale feldspar phenocrysts. ....	46

Figure 4-16: Thin section photomicrograph of sample 759 from Eastern mine pit, Kåsemyrene. Texture of medium grained Fe-Ti-P rich rock. ....	47
Figure 4-17: Intergrowth textures between biotite and feldspar, porphyritic Fe-Ti-P rich rock from Eiriks Gruve. 5x magnified, scanned XPL image of thin section 517. ....	48
Figure 4-18: Key location 520, 50m west of Rødstjønn revealing accumulation of Fe-Ti-P mineralization associated with local flow textures of feldspar phenocrysts.....	49
Figure 4-19: Enhanced colouring of Fe-Ti-P rich rock in coarse grained syenitic host rock, Key-Location 520. ....	50
Figure 4-20: Map over the described locations related to Kåsemyrene.....	51
Figure 4-21: Field photo of outcrop "Kåsemyrene Parking".....	52
Figure 4-22: PPL scan of thin section 763A with 5x magnification. ....	53
Figure 4-23: Field photographs from Key- location "Kåsemyrene Cliff". ....	54
Figure 4-24: Close up field photo of contact between fine-grained syenite and porphyritic Fe-Ti-P rich rock.....	54
Figure 4-25: Field photograph of the western mine-pit at Kåsemyrene. ....	55
Figure 4-26: Field photo of the eastern mine-pit at Kåsemyrene.....	55
Figure 4-27: (map Søllandliene): Søllandliene are represented with samples 510, 511, 512 and 513. ....	56
Figure 4-28: Field photo and sketch of the outcrop at Key-location Søllandliene. ....	57
Figure 4-29: Slab photo of trachytic to porphyritic monzonite (512 B).....	58
Figure 4-30: Field photo of lithological contact between very coarse-grained syenite and fine-grained trachyte. ....	58
Figure 4-31: (backside) Field photo of the opposite side of the outcrop at Søllandliene..	59
Figure 4-32: Schematic illustration of the lithologies based on Figure 4-31. ....	60
Figure 4-33: Accumulation of mafic minerals in a mingling melt consisting of ~20% rhombohedral phenocrysts.....	61
Figure 4-34: (Vein) Fe-Ti-P rich vein on contact between coarse grained rock and fine-grained trachytic quartz-monzonite.....	61
Figure 4-35: Modified TAS diagram (Middlemost, 1994). ....	63
Figure 4-36: Granitoid classification (Frost et al., 2001) ....	64
Figure 4-37: Harker plot depicting bulk analysis of major oxides of all samples. ....	66
Figure 4-38: Harker plot depicting bulk analysis of major oxides within the silica range 49 wt.% – 71 wt.%. ....	67
Figure 4-39: Whole rock analysis with transition metals plotted against TREE. ....	68
Figure 4-40: Bulk analyses Harker plot of HFSE (Nb, Zr, Hf, U and Th), Y and Sc. ....	69
Figure 4-41: Whole rock analysis plotting LILE and Eu* against TREE. ....	70
Figure 4-42: Average whole-rock REE values based on rock classifications.....	71

Figure 4-43: REE spider diagrams normalized to chondrite (Sun and McDonough, 1989) for whole-rock analyses. ....	72
Figure 4-44: (A) PPL, 5x magnification thin section scan of the porphyritic Fe-Ti-P rich rock (403B). ....	73
Figure 4-45: Ternary feldspar classification diagram (Parsons, 2010). ....	75
Figure 4-46: Photomicrograph and BSE image of feldspar analysed with microprobe (sample 536) ....	76
Figure 4-47: Subdivision of the EPMA analysis of 403B feldspars. ....	76
Figure 4-48: Binary diagrams of compositional variations observed in feldspar (microprobe data). ....	77
Figure 4-49: Biotite – Phlogopite classification diagram from Li et al. 2020 ....	78
Figure 4-50: Ternary diagram plotting anion occupancy of OH <sup>-</sup> , F <sup>-</sup> and O <sup>2-</sup> in the W-site in phlogopite. The values are based on calculations after Li et al. (2020). ....	79
Figure 4-51: XY diagrams from microprobe analysis of phlogopite in the Fe-Ti-P rich samples 403B, 503 and 761, and the syenitic sample 536. Legend given in Figure 4-50. ....	80
Figure 4-52: Pyroxene classification diagram with the three endmembers enstatite, wollastonite and ferrosilite (Morimoto 1988). ....	81
Figure 4-53: Harker diagrams of augite analysed in microprobe. ....	82
Figure 4-54: The calculated distribution of OH, Cl and F in apatite X site (Pasero et al. 2010). ....	84
Figure 4-55: Measurements obtained with microprobe plotting binary diagrams of FeO and TiO <sub>2</sub> against P <sub>2</sub> O <sub>5</sub> content in apatite. ....	84
Figure 4-56: Binary diagrams plotting results from apatite microprobe analysis. ....	85
Figure 4-57: Results from LA-ICP-MS analyses of apatite presented as binary diagrams. ....	87
Figure 4-58: Ratio diagrams depicting Sr/Y and Eu-anomaly in apatite obtained with LA-ICP-MS. ....	88
Figure 4-59: Average chondrite normalized REE values for apatite. ....	89
Figure 4-60: Spider diagrams depicting results from apatite LA-ICP-MS analysis sorted after thin section ....	90
Figure 4-61: Plane polarized 5x magnified photomicrograph of thin section 536 ....	91
Figure 4-62: Plane polarized, 5x magnified photomicrograph of fine to medium grained Fe-Ti-P rich rock (503). ....	92
Figure 4-63: The division of amphiboles from “supergroup” to “rootname” (Hawthorne et al., 2012) ....	93
Figure 4-64: Amphibole classification based on subgroup- and rootname composition (Hawthorne et al., 2012). ....	94
Figure 4-65: Binary diagrams plotting amphibole content of Al <sub>2</sub> O <sub>3</sub> , MnO, TiO <sub>2</sub> , and Na <sub>2</sub> O against SiO <sub>2</sub> content ....	95

Figure 4-66: Q plot based on lithologies. ....	96
Figure 4-67: Stereo nets of (A) Rhomb porphyry, (B) Fe-Ti-P rich rock, (C) all syenites and (D) all syenites with highlighting of the samples with the highest deviation from the mean vector. ....	98
Figure 4-68: Average magnetic NRM vector of syenites and rhomb porphyry (RP) plotted with the present-day field. ....	99
Figure 4-69: Geomagnetic anomaly map of the westernmost pluton in the Siljan-Hvarnes Intrusion. ....	100
Figure 5-1: Skriua as seen from Kåsemyrene. ....	103
Figure 5-2: Cut slab of very coarse- grained syenite from Kåsemyrene, sample 764. ..	106
Figure 5-3: (A) Remains of a mafic dike cutting through porphyritic syenite, Sjøllandliene. (B) Elongated mafic enclave in medium to coarse grained porphyritic syenite. ....	108
Figure 5-4: (A) rhombohedral feldspar phenocryst in sample 534. Ruler for scale. (B) Scan of thin section sample 538. Zoned feldspar phenocrysts in fine- grained matrix.....	110
Figure 5-5: Highlighted area of the remains of a phenocryst almost completely resorbed along internal fractures (sample 535). ....	110
Figure 5-6: Bulk analysis of TREE (Total Rare Earth Elements) vs. P <sub>2</sub> O <sub>5</sub> content. ....	113
Figure 5-7: Alkali- FeO <sub>TOT</sub> -MgO variations of the Siljan- Hvarnes Intrusion (SHI) – and Larvik Ring Complex (LRC)- and Fe-Ti-P rich rocks. ....	114
Figure 5-8: XY diagrams highlighting compositional differences between fine-grained Fe-Ti-P rich rocks and silicic rocks (Adapted from Charlier and Grove, 2012). ....	117
Figure 5-9: Ternary diagrams highlighting the potential one and two liquid stability fields (Adapted from (Charlier and Grove, 2012)). ....	118
Figure 5-10: Photomicrograph of oligoclase phenocryst with anorthoclase rim in sample 403B and SrO vs Al <sub>2</sub> O <sub>3</sub> plot depicting the chemical change between the two phases....	120
Figure 5-11: (A) Samples from this study with an interpreted two- liquid field and line of descent for the Siljan- Hvarnes Intrusion (SHI) – and Larvik Ring Complex (LRC) (Neumann, 1980). (B) Tholeiitic line of descent entering the two-liquid field (Charlier and Grove, 2012). ....	121
Figure 5-12: Vein of Fe-Ti-P rich rock associated with syenite intruded in the rhomb porphyry sequence. ....	122
Figure 5-13: Photomicrograph of rhomb porphyry ground mass (524). Note elongated feldspar (transparent) and Fe-Ti- oxides (opaque) show moderate orientation. ....	125
Figure 5-14: Magnetic domain based on particle size, shape, and interparticle spacing (Figure 8 in Harrison and Feinberg (2009)). ....	125
Figure 5-15: Geomagnetic map imposed on top of DTM 10 hill shade. ....	126
Figure 0-1: Experimental map of K – Th&U ratio layered on top of the geomagnetic map ii	

# List of Tables

Table 1: Local rock names established by (Brøgger, 1890) with their modern classification (Neumann, 1980; Larsen et al., 2008; Borg, 2011). .....	3
Table 2: Categories of magnetism. Modified table from Ånestad (2020), based on Clark (1997), Dekkers (1988), Harrison and Finberg (2009), McEnroe et al. (2009), Potter et al. (2011) and Reynolds (2011). (Dekkers, 1988; Clark, 1997; Potter et al., 2011; Ånestad, 2020) .....	10
Table 3: Sample classification based on geochemistry and texture.....	34
Table 4: Legend for EPMA analyses.....	74
Table 5: Biotite sites and common occupying ions (Li et al., 2020). .....	78
Table 6: The elemental distribution between crystallographic positions in pyroxene (Morimoto, 1988). .....	81
Table 7: Apatite site and common ion occupancy (Pasero et al., 2010).....	83
Table 8: Legend for LA-ICP-MS analyses of apatite grains.....	86
Table 9: Amphibole sites and common occupying elements (Hawthorne et al., 2012)....	92
Table 10: Results from EPMA analysis of amphiboles (Locock, 2014).....	93
Table 11: Species and end-member formula of amphiboles (Hawthorne et al., 2012)....	94
Table 12: Mean vector trend and plunge for syenites and rhomb porphyries. ....	97

## Abbreviations

Ppm	=	Parts per million
Wt.%	=	Wight percent
LRC	=	Larvik Ring Complex
SHI	=	Siljan- Hvarnes Intrusion
$fO_2$	=	Oxygen fugacity
REE	=	Rare earth elements
LREE	=	Light earth elements
MREE	=	Medium rare earth elements
HREE	=	Heavy rare earth elements
TREO	=	Total rare earth oxides
TREM	=	Total rare earth metals
LILE	=	Large ion lithophile elements
HFSE	=	High field strength elements
EPMA	=	Electron Probe Micro Analyser
LA-ICP-MS	=	Laser Ablation Inductively Coupled Plasma Mass Spectrometry
XRF	=	X-ray fluorescence
PPL	=	Plane Polarized Light
XPL	=	Cross Polarized Light
TMI	=	Total Magnetic Field Intensity
SD	=	Single Domain
PSD	=	Pseudo Single Domain
MD	=	Multi Domain
NGU	=	Norwegian Geological Survey
NTNU	=	Norwegian University of Science and Technology



Amp	=	Amphibole
Ap	=	Apatite
Bt	=	Biotite
Cpx	=	Clinopyroxene
Opx	=	Orthopyroxene
Fsp	=	Feldspar
Ol	=	Olivine
Zrn	=	Zircon
Ox	=	Oxide
Ilm	=	Ilmenite
Mt	=	Magnetite
Spn	=	Sphene

# 1 Introduction

This study was initiated as a side project to NGUs assessment of larger apatite resources in Norway. Apatite [ $\text{Ca}_5(\text{PO}_4)_3(\text{OH}, \text{F}, \text{Cl})$ ] is the most common phosphate mineral on Earth, and form stable crystals over a variety of condition, from the lithospheric mantle to the Earth's surface (Harlov and Rakovan, 2015). Even though apatite usually forms as a minor phase in rocks, it can become an important rock forming mineral in sedimentary and igneous rock (ibid). The largest apatite deposits are mostly of sedimentary origin and form in offshore marine conditions on continental shelves (van Kauwenbergh, 2010). The largest volumes of mined apatite stem from sedimentary rocks, which generally consists of higher natural grade, but contain more contaminations of unwanted Cd, As, U, Th, Mg, and Al ((Ihlen et al., 2014)). Only 10 – 15% of the phosphorus mined today stem from igneous rocks, which consists of a lower grade and are in many cases naturally purer (ibid). The advantage with the purer composition of the igneous apatite is that it can be processed to a higher grade separate compared to the sedimentary apatite (van Kauwenbergh, 2010).

Phosphorus rock serves as the global source for phosphate, which are mainly used in fertilizer production (75% – 80%) while the remaining part is used other industries (Ihlen et al., 2014). As phosphate rock is a limited source, there have been some questions for how long the present consumption is sustainable. Some sources claim most reserves are going to be exhausted during the next hundred years (van Kauwenbergh, 2010). IFDC (International Fertilizer Development Center) concluded there are indications for at least 300 – 400 more years of production (van Kauwenbergh, 2010). However, the grade of phosphorous in rock decline with 0,45 wt.%  $\text{P}_2\text{O}_5$  every decade, and the present economical grade for igneous apatite lays within 4 – 5 wt.%  $\text{P}_2\text{O}_5$  (Ihlen et al., 2014).

Igneous apatite has been encountered on several locations within the Larvik plutonic ring complex (Ihlen et al., 2014). The apatite is associated with a mafic rock consisting mainly of Fe- Ti oxides, pyroxene, and olivine (often referred to as "jacupirangite" in literature, which is defined as an ultramafic nepheline- bearing clinopyroxenite (Howell, 1957). This is not consistent with the observations from Siljan, and the rock is therefore referred to as Fe-Ti-P rich rock). Some of the larger deposits in the Larvik ring complex have been examined by Norsk Hydro, where only the Kodal deposit have been classified as highly economical potential (Ihlen et al., 2014).

According to (Ihlen et al., 2014), are all Fe-Ti-P rich rock hosted within the nepheline-normative monzonites and syeno- monzonites in the Larvik RC. This makes the Fe-Ti-P rich rock located in the Siljan-Hvarnes intrusion interesting as it occurs in a more evolved environment consisting of quartz- normative syenite. Additionally, chemical analyses of these rocks reveal high concentrations of REEs (Rare Earth Elements) and HFSE (High Field Strength Elements) which might represent an economical potential. REEs are a group of 16 elements which are crucial in the production of EI- engines, wind turbines, catalysts, screen technology and LED-lights (NGU kommunikasjon & samfunn, 2019). Further, magmatic apatite [ $\text{Ca}_5(\text{PO}_4)_3(\text{F})$ ] is known to incorporate REEs in the crystal lattice [(Ca, LREE) $_5(\text{PO}_4, \text{SiO}_4)_3(\text{F})$ ] (Belousova et al., 2002; Ihlen et al., 2014; Harlov and Rakovan, 2015).

## 1.1 Aim of Thesis

The primary objective of this master thesis is to explore the petrogenesis and properties of the Fe-Ti-P rich rocks occurring in the westernmost part of the Siljan- Hvarnes intrusion. The study is mainly based on sample geochemistry by XRF (X-Ray Fluorescence) and LA-ICP-MS (Laser Ablation Inductively Coupled Plasma Mass Spectrometry) analysis of whole rock samples, and EPMA (Electron microprobe Micro Analyser) and LA-ICP-MS analysis of minerals. Field relations and thin sections were studied to better understand the Fe-Ti-P rich rocks relation to the hosting syenites.

A secondary objective was to assess the geomagnetic properties of the Fe-Ti-P rich rocks, as magnetite is a major rock forming phase which inhibit a naturally strong magnetic field. Oriented samples were collected in the field and prepared and analyzed at NTNU.

Any modeling of ore size and estimation of economic potential is beyond the scope of this thesis.

## 1.2 Geological Background

### 1.2.1 Regional Geology

The Oslo graben is a failed prolonged rift which was active in the Late Carboniferous- and Early Permian period (Neumann et al., 2004). It is related to the larger extensional magmatic regime which took place in an area stretching from southern Scandinavia to norther Germany (ibid). The magmatic system intruded into the crust of the Baltic shield, which consisted of Precambrian basement rocks and overlying sedimentary rocks dated from late Precambrian to Silurian period. The basement rocks were metamorphosed during the Sveconorvegian orogeny 1200 – 900 Ma ago and show no deformation from the Caledonian Orogeny (Pedersen et al., 1995).

Oslo graben forms a north – south trending wedge which is smallest at its northernmost extent at lake Mjøsa, and widest in south at the Sorgenfrei- Tornquist Zone (Neumann et al. 2004). This translates into an approximately 200 km long and 35 – 65 km wide zone consisting primary of magmatic intrusive and extrusive rocks with minor pockets of sedimentary rocks. The later stages of the rifting included emplacement of large, shallow batholiths which locally intruded the overlying extrusive rocks (Neumann, 1980).

The present erosion level is equivalent to a depth of 2 – 3 km below the original surface level (Sundvoll et al., 1990). This allows for both intrusive and extrusive rocks to be studied, offering the possibility of examining both temporal and geochemical relation between magmatic bodies. Volumetric calculations have been conducted on the surface rocks, and rocks of monzonitic composition (Iarvikites, Kjelsåsites and rhomb porphyries (Table 1)) make up 40% of the exposed- and subsurface rocks (Ramberg, 1974; Neumann, 1980). Gravity studies of the Oslo region have revealed the presence of a high-density body situated deep under the present surface (ibid). This is interpreted to be mafic to ultramafic bodies, which accumulated at the mantle- crust boundary. Volumetric calculations of these bodies reveal that they make up an estimated 90% of all magmatic rocks in the Oslo Graben area. This supports the theory of the shallow situated rocks being derivations from partial melting or fractionation of a basaltic parent (ibid).

*Table 1: Local rock names established by (Brøgger, 1890) with their modern classification (Neumann, 1980; Larsen et al., 2008; Borg, 2011).*

<b>Setting</b>	<b>Local Name</b>	<b>Rock name</b>
Intrusive	Larvikite	= Monzonite
	Ekerite	= Peralkaline – alkali feldspar granite
	Kjelsåsite	= Plagioclase rich larvikite
	Nordmarkite	= Quartz- bearing alkali- feldspar syenite
	Akerite	= Quartz- monzonite
	Tønsbergite	= Red quartz-bearing larvikite
	Hedrumite	= Porphyritic, alcaic syenite with more than 10% feldspathoids
	Foyaite	= Nepheline syenite
Extrusive	Rhomb Porphyry	= Porphyritic latite- trachyte

The tectono- magmatic history of the graben has been divided into six stages (Larsen et al., 2008). The stages represent the tectonic regimes and evolution of the petrology of the rocks. The temporal extent of the period is debated. Pedersen et al. (1995), argues the magmatic period lasted 50 Ma. while Olaussen and Dahlgren (2007), argued for 70 Ma.

#### *1.2.1.1 Stages I*

Stage 1 occurred in Late Carboniferous and lasted from 310 to 296 Ma.(Olaussen and Dahlgren, 2007). This stage is recognized by pre-stage rifting of the Baltic shield (ibid). The processes involved includes forming of a microsyenitic sill complex and camptonites in the overlying sediments (ibid).

#### *1.2.1.2 Stage II*

Stage 2 occurred in the transition between Carboniferous- and Permian period (Olaussen and Dahlgren, 2007). This is when the first basaltic fissure eruptions began, forming plateau lavas (Corfu and Dahlgren, 2008). Dating reveals the first eruptions happened in the Vestfold Graben Segment about 195 Ma ago and extended towards north and into the Akershus Graben Segment a few Ma. Later (Olaussen and Dahlgren, 2007). The thickest known sequence of basaltic lava is in Brunlanes and measures 800 m (Larsen et al., 2008). The basalt flows consist of silica undersaturated melilitites and nephelinites (ibid).

#### *1.2.1.3 Stage III*

According to Olaussen and Dahlgren (2007), took stage 3 place in Early Permian dated to 292 to 275 Ma. Large north – south trending faults formed, facilitating for further growth of fissure volcanos(ibid). The plain basalt was followed by extensive latitic- trachytic lava flows containing feldspar phenocrysts, the rhomb porphyry lavas. The rhomb porphyry formed lava plateaus which are believed to be the thickest in south around Larvik and thinning laterally and northwards (ibid). The Vestfold Lava Plateau is estimated to have consisted of about 50 lava streams, cumulating to a thickness of 3000 m (ibid). The end of this period is recognized with the formation of the first large monzonitic batholiths

(Larvikite) (Larsen et al., 2008). Both the larvikite and rhomb porphyry has an intermediate composition, ranging from quartz under-, to weakly over saturated (Neumann, 1980).

#### *1.2.1.4 Stage IV*

Stage 4 lasted from Early to Middle Permian period, dated to 284 – 265 Ma (Olaussen and Dahlgren, 2007). This period is mainly recognized by the evolution of central volcanos. New large batholiths form towards north, and the magmatic composition evolves from intermediate to felsic (ibid). Among these are the Drammen Granites and Finnemarka Granite, both situated around Drammen (ibid). The first calderas do also form in this period, some of the largest are the Ramnes- Nittedal- and Drammen calderas (Larsen et al., 2008).

#### *1.2.1.5 Stage V*

Olaussen and Dahlgren (2007), states stage 5 took place from 270 to 250 Ma. in the Mid to Late Permian Period. During this time span the batholiths of granitic and syenitic composition formed, such as the Ekerites and Nordmarkites (ibid). This represents the most evolved plutonic rocks of the Oslo Graben (Barth, 1945).

#### *1.2.1.6 Stage IV*

Stage 6 took place 250 – 245 Ma. in the Early Triassic period (Torsvik et al., 1998; Heeremans et al., 2000 in Larsen et al., 2008). This is when the last small granites were formed (Larsen et al., 2008).

## 1.2.2 Larvik Plutonic Complex (LPC)

The Larvik- Ring complex (Figure 1-1) is the largest body of monzonitic rocks in the Oslo Region and are situated in the Vestfold Graben (Neumann, 1980). The pluton consists of 10 defined intrusions (ibid). These can be observed as semi-circular sections with chilled cross cutting contacts into each other. These structures imply a progressive evolution towards west (Petersen, 1978). The oldest, easternmost ring sections consists of quartz bearing larvikite and tønbergite (Neumann, 1980). Westward the larvikites change gradually to become silica undersaturated. The innermost ring sections, 9 and 10 consists of lardalite and foyaite/ hedrumite, which are nepheline normative syenites (ibid). The ring complex is cut by numerous pegmatitic dikes. Nepheline syenite pegmatites occur in the western section (Brøgger, 1890) while quartz syenite pegmatites occur in the eastern part (G. Raade, pers. Comm., 1978 in Neumann 1980). Trace element analysis reveals unique evolutionary trends for each of the ring structures, leading to the conclusion that the batholiths cannot stem from one single parent magma (Neumann, 1980).

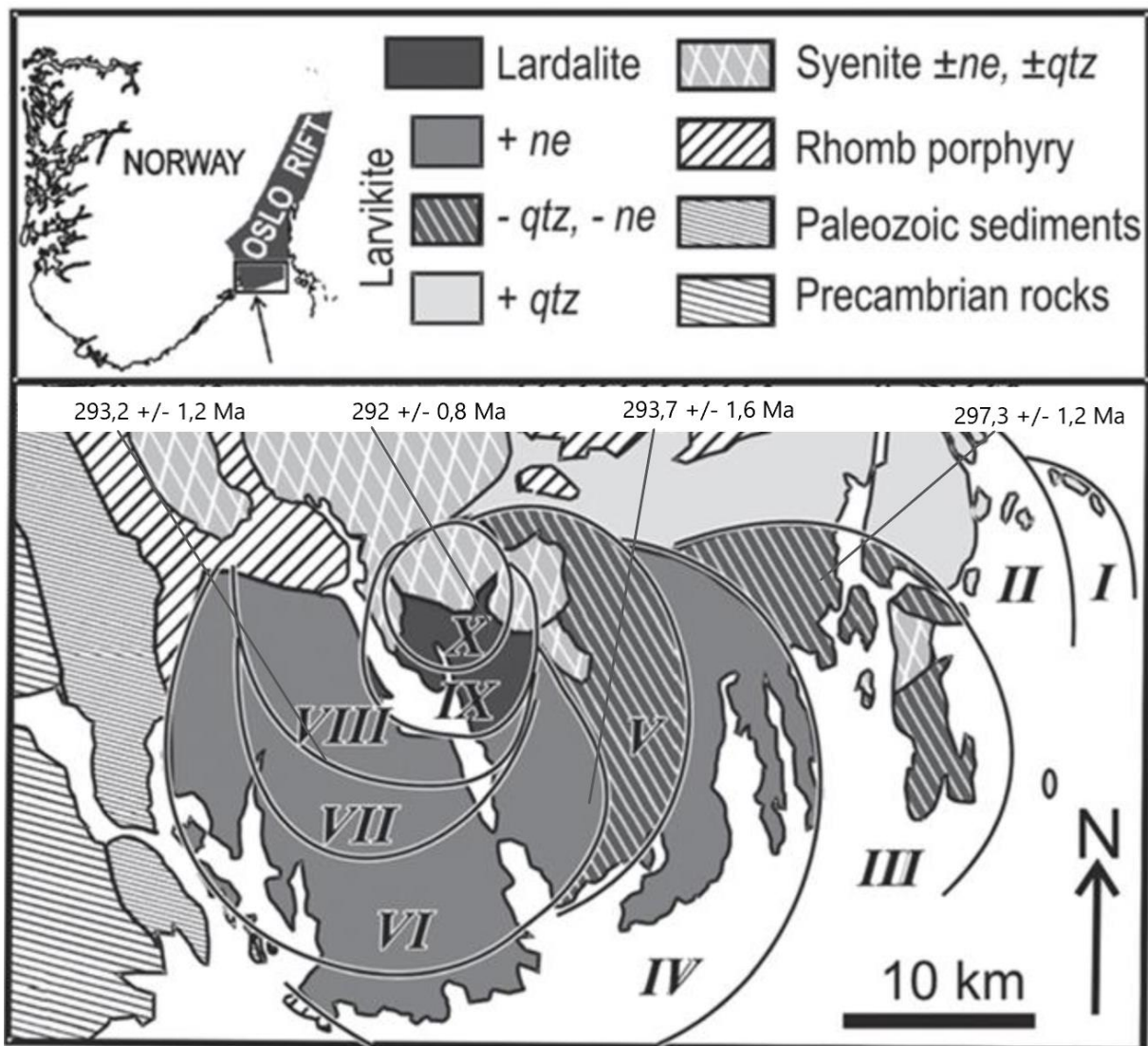


Figure 1-1: Modified geological map of the Larvik ring complex. Figure from (Andersen et al., 2014) with ages from (Sundvoll et al., 1990)

Neumann (1980; 1986) and Rasmussen et al. (1988), argues that the intermediate rocks have its origin from a deeply situated mantle- derived parent magma. During periods of low tectonic extensional stress, mantle originated basaltic melt were trapped on the mantle – crust boundary, unable to penetrate through the light crust. The basaltic melt did not evolve towards an alkaline or tholeiitic trend as no thermal barrier exists at this depth and pressure (~35 km or 10 kb). While the basalt was trapped it started to crystallize ultramafic minerals, where the olivine – pyroxene liquidus boundary laid within, or close to, the field of silica saturation (Neumann, 1980).

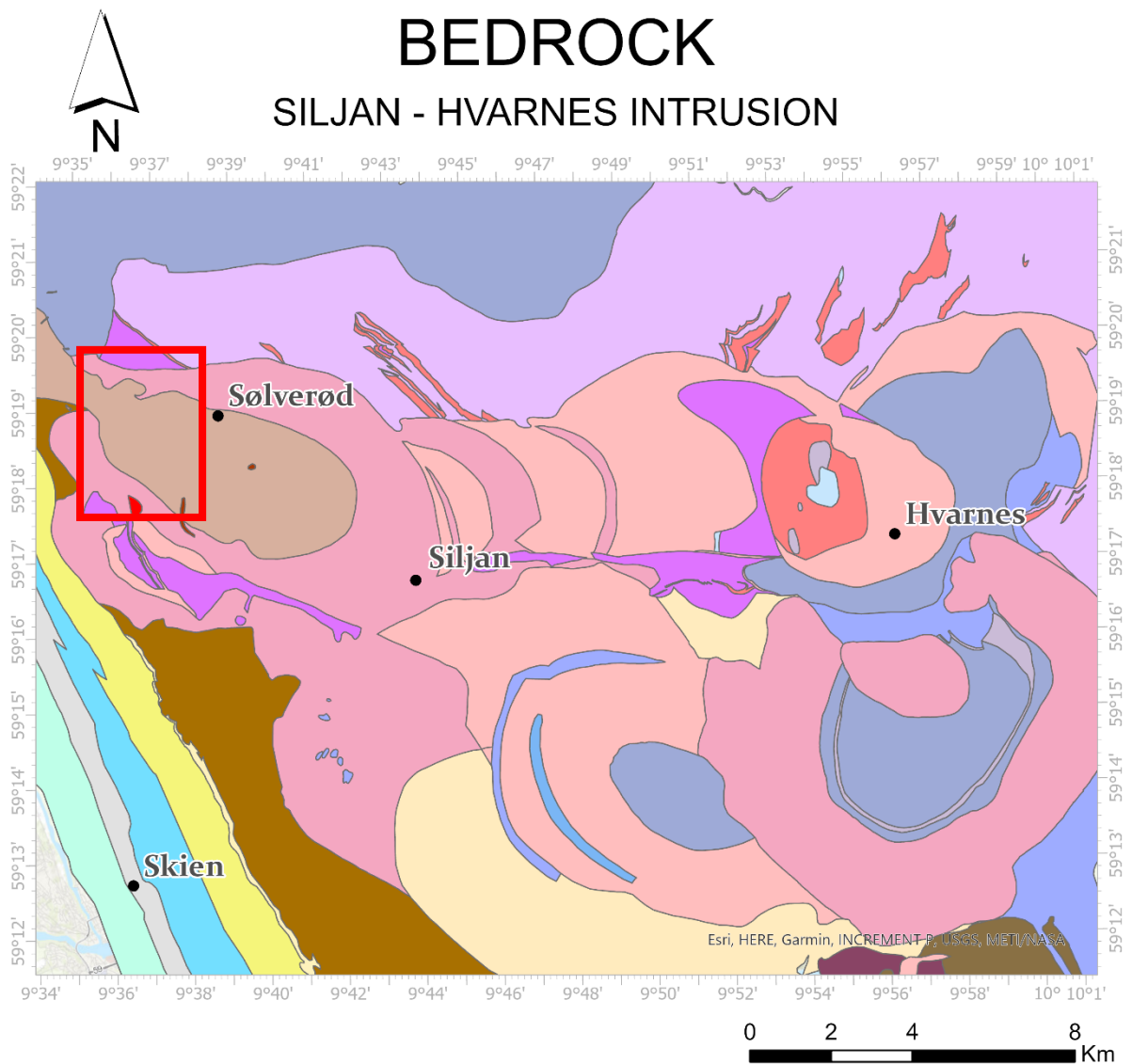
Further crystal fractionation of magmas ranging from alkaline to transitional basalts under 7 – 10 kb pressure resulted in an approximately silica saturated, intermediate residual melt generally enriched in REE's. The fractionation ensued until the residual melt had enough buoyancy to force itself to the upper crust or surface due to density filtering, while large masses of dense cumulates were left in the lower crust (Neumann, 1980).

Neumann (1980), further argues that during the ascent of the intermediate melt, gradual lowering of the pressure led to the establishment of a thermal divide between diopside-forsterite- anorthite join which pushed the forsterite – orthopyroxene liquidus boundary into the silica – oversaturation field. Subsequent fractionation under low pressure determined whether the melt would be strongly over- or under saturated as a function of silica activity during the period of ascension. In other words, the determining factor for a melt to become silica over- or under saturated was the depth of crystallization of the melt in the lower crust.


























To summarize, the geochemistry of the different ring sections in the LPC can be attributed to forming of several unrelated magmas at the MOHO (Neumann, 1980). However, the textural and chemical similarities can be accredited to a fairly uniform degree of fractional crystallization in an environment with relatively similar physiochemical parameters (ibid). Further, the accumulation of mafic melts close to the mantle- crust boundary is believed to have substantially increased the geothermal gradient in the upper lithosphere, which might have led to some partial melting of the crust. However, Neumann (1980) states that this have not been successfully proved.

### 1.2.3 Siljan -Hvarnes intrusion

While the ring structures in Larvik has been the subject for research and debate since Brøgger published his works about the Oslo magmatic complex in 1890, little scientific work have been done regarding the Siljan – Hvarnes intrusion. The Intrusion is situated in the Vestfold Graben segment, more precisely northwest of the Larvik ring complex and south of the Skrim – Mykle magmatic complex (Pedersen et al., 1995). The complex consists of an approximately 20 km long and 3 – 5 km wide series of monzonitic to syenitic intrusions nested into each other. The structural relationships reveal that the intrusions began in east, close to present Hvarnes, and developed towards Siljan in west (ibid). The northern Skrim- Mykle complex consists of two larger intrusive composite bodies. Respectively the Skrim Larvikite and the Mykle Ekerite (ibid). Pedersen et al (1995), conducted U-Pb-dating in zircon and baddeleyite crystals from plutonic rocks in both complexes. The Skrim – Mykle complex is dated to be 281 – 279 Ma., while Siljan- Hvarnes complex is about 277 Ma. Figure 2 depicts the Siljan-Hvarnes intrusion bedrock map.



### LEGEND

 Alkali feltspar syenite	 Larvikite, well oriented fld
 Basalt	 Larvikitt, opx carrying (Hedde type)
 Diabas	 Larvikite, porphyritic
 Explosive Breccia	 Latite (rhomb porphyry)
 Gabbro	 Claystone, Marl
 Granite	 Nepheline syenite
 Limestone (knollekalk) and Shale	 Rhomb Porphyry lava
 Pure Limestone and Knollekalk	 Sandstone and Conglomerate
 Quartz Syenite	 Sandstone and Conglomerate, local tuff
 Lardalite, porphyritic	 Syenite
 Lardalite	 Syenite-Larvikite Hybrid
 Larvikite, fine-grained, porphyritic	 Trachyte/Rhyolite
 Larvikite, massif	

Spatial Reference  
 PCS: ETRS 1989 UTM Zone 32N  
 GCS: GCS ETRS 1989  
 By: Tord Andersen

Figure 2: Bedrock map of the Siljan-Hvarnes Intrusion. Red rectangle represents the field area.



### 1.3 Local historical aspects of the Fe- Ti – P- rich rock

The mining pits explored in the field area (Key location Kåsemyrene, Jernskottet and Eiriks Gruve) were mined for iron most likely during the 16<sup>th</sup> century, and out of the size of the mining pits, it is evident that the ores were not large and/or rich enough to represent a truly economical prospect. The largest of the two pits along Kåsemyrene is about 3 x3 m and 2 m deep where the pit- walls consist of Fe-Ti-P rich rock, witnessing of an end of mining before the ore was entirely extracted. Even though they were of low economic interest then, they might represent some historical interest today:

The Vestfold area represent an interesting part of the Norwegian mining history. Large magnetite rich ores hosted in quartz veins in the Precambrian granites were found north of Skien city in 1538 by Hans Glaser (Larsen, 1993). Bergmeister Glaser was sent by the Danish Norwegian king, Christian the 3<sup>rd</sup>, to prospect for metals in Norway. Upon hearing the news of the discoveries, the king demanded the establishment of Fossum Ironworks located in Skien, and thus were the first ironwork in Norway established in 1543 (ibid).

Larsen (1993), further states the initial mining was done on the ores situated just north of Skien. Over time, the mining operation expanded, and more ore were found in the nearby Fossum forests. The newly established iron works impeded large changes in the local infrastructure and economy; local farmers had to provide charcoal to the iron works, which were produced by burning large masses of wood under an oxygen restricted environment (Bøen, Gunvor; Bøen, n.d.; Skiensatlas, n.d.).

However, the first 80 years of the operation is described as difficult as the deposits were usually small, of low gehalt and scattered over a wide area (Larsen, 1993). This led to several small parallel mining operations which were costly and ineffective. The everlasting search for metals continued, and in 1655 a large iron deposit was found in Fen (ibid). This led to a more stable supply, and a new initiative to continue the ironworks ensued. With increased prospecting and developing infrastructure, ore was transported from mines in Arendal and Kragerø to Skien. The mining operation ended in 1867, as Fossum Ironworks were unable to adapt to the European market where rock coal became the major heat source rather than charcoal (ibid). The entire iron works industry lasted a total of 324 years. Two decades later (1886) were the woods with around Siljan bought from Fossum by Treschow- Fritzøe which is the major owners of the area today (ibid).

The mine pits in the field area are likely to stem from this period. However, no good sources were found which could truly place the date of the local mining operations. Eiriks Gruve and the mine pits at Kåsemyrene is suggested to be from the 16<sup>th</sup> century (Skilbred, 2016; Vaagland, 2016), while no estimations were found for Jernskottet.

## 2 Theory


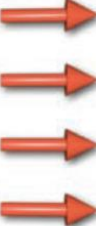
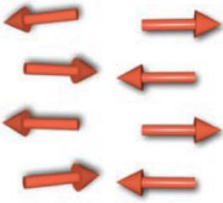
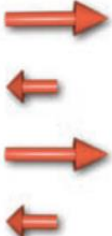
The theory section is presented in two parts. The first section introduces some of the geomagnetic principles, while the second part present geochemical principles and ways to classify rock types.

### 2.1 Geomagnetic theory

According to Reynolds (2011) can the Earth's magnetic field be compared to the magnetic properties of a dipolar rod. Each end of the rod represents either a positive or a negative magnetic pole, in which magnetic flux converges from the north to the south pole. This magnetic force generates a magnetic field,  $H$ , which is measurable for both strength and direction (Reynolds, 2011). Due to the convergent shape of the magnetic field the measured magnetic field are stronger at Earth's magnetic poles  $\sim 60$  nT compared to the equator  $\sim 30$  nT. This is due to the magnetic flux converging radially out or inwards from the poles, and equator being in the middle, becomes a magnetic low (McEnroe et al., 2009). The Earth's magnetic field is situated with the magnetic north towards the geographic south pole, and have an inclination of  $11,5^\circ$  away from Earths rotational axis (Reynolds, 2011). According to Merrill et al. (1996) has the Earth's magnetic poles switched numerous times at irregular intervals

All materials we surround ourselves with has a definable magnetic property. In everyday life it is most common to think of magnets and the metallic surfaces it can attach to as having magnetic properties. However, the magnetic properties of all elements and objects can be described with quantum theory. According to Harrison and Feinberg (2009), provides quantum theory an explanation to the magnetic properties of all materials, as magnetic moment is determined by the configuration of the electrons orbiting the atom. The configuration of electrons includes electron spin, the number of electrons in orbit, and the orbital configuration, and all contribute to the magnetic property the material obtains (ibid). Based on the behavioural patterns of a material, it is possible to distinguish five categories of magnetism, presented in Table 2:

Table 2: Categories of magnetism. Modified table from Ånestad (2020), based on Clarck (1997), Dekkers (1988), Harrison and Finberg (2009), McEnroe et al. (2009), Potter et al. (2011) and Reynolds (2011)

Type of magnetism	Atom configuration	Magnetic properties	Common minerals
Diamagnetic	Complete electron shells. The orbital motions align to oppose the external field.	No remanent magnetization. Weak, negative susceptibility under applied field.	(All materials) Calcite, feldspar, halite, magnesite and quartz.
Paramagnetic 	Unpaired electron pairs. These single electrons tend to align in the direction of the applied field.	No remanent magnetization. Weak, positive susceptibility under applied field.	Ilmenite, Olivine (fayalite), pyroxene, garnets, serpentine.
Ferromagnetic 	Unpaired electrons which favour parallel alignment even under no applied field.	High remanent magnetisation. High susceptibility. Has a Curie Temperature.	Cobalt, iron, nickel and some REE-alloys
Canted- and antiferromagnetic (shown respectively) 	Canted: Oppositely, canted magnetic sublattices.  Antiferro: Oppositely, parallelly aligned magnetic sublattices.	Canted: Weak net magnetic moment, weak positive susceptibility.  Antiferro: No net magnetic moment. Weak positive susceptibility.	Canted: Hematite  Antiferro: Goethite and hexagonal pyrrhotite.
Ferrimagnetic 	Electron spin pairs are in opposite directions, but the magnetic momentum is stronger in one sublattice.	Net magnetic moment. High susceptibility.	Magnetite, Trevorite and monoclinic pyrrhotite.

According to Harrison and Feinberg (2009) are the dominant magnetic phases on Earth iron oxides and iron – titanium oxides. Iron is a metal which can occur ferric ( $\text{Fe}^{3+}$ ) or ferrous ( $\text{Fe}^{2+}$ ) ions. This gives the ions a partly filled 3d electron shell, which is the cause for their permanent magnetic moment (ibid). The 3d shell can incorporate 10 electrons, in 5 spaces, where each space is filled with an electron with positive spin, and one with negative spin, both creating a magnetic moment (ibid). As  $\text{Fe}^{3+}$  has 5 unpaired electrons, the magnetic moment is ( $5 \times 1/2 = 5/2$ ), or  $5 \mu_B$ .  $\text{Fe}^{2+}$  has 6 electrons in the 3d shell, where two share the same space and the spins nullify each other, resulting in 4 unpaired electrons (ibid). Thus, the magnetic moment is ( $4/2 = 2$ ), or  $4 \mu_B$ . An additional magnetic contribution is the angular momentum (ibid).  $\text{Fe}^{3+}$  has 5 unpaired electrons will be balanced, while  $\text{Fe}^{2+}$  has an angular momentum (L) of 2. However, the angular momentum of ferrous iron is almost completely blocked due to the electrostatic interaction with the neighbouring oxygen ligands. This leaves spin as the dominant contributor to magnetic moment (ibid).

(From Harrison and Feinberg, 2009): In most minerals which incorporates iron, the angular momentum from juxtaposed ions will not interact strongly with each other. For these minerals, the thermal energy will be higher than the magnetic moment, and ions will constantly change orientation. Thus, these minerals will never be spontaneously magnetic, and are called paramagnetic minerals. In magnetic minerals, however, the magnetic moment is higher than the thermal energy, and the ions will align either parallelly or anti-parallelly dependent on the lattice configuration. If the mineral is substantially heated, the thermal energy will be the dominant force and the once magnetic mineral will become paramagnetic. This temperature- boundary is called the "Curie" or "Néel" temperature. During cooling past the Curie temperature, the minerals will again become magnetic by re-alignment of the ions.

In the absence of a magnetic field, the magnetic moment will align after the low-energy axis of the crystal structure (Harrison and Feinberg, 2009). All structures have two or more "easy axis", dependent on the electron configuration, and in between the "easy axis" are the energy unfavourable high energy axis. This property is called "magneto-crystalline anisotropy" and is an important concept within mineral magnetism. When a magnetic mineral cool will the magnetic moment of ions align after the external magnetic field, and when the mineral cools below the Curie temperature, the magnetic moment will be blocked within in the grain (ibid). In this manner, are the magnetic remanence going to be preserved in a grain, and under correct circumstances last for millions, possibly billions of years (ibid).

Harrison and Feinberg (2009), states magnetite is a common source for paleomagnetic analysis, even though magnetite alone does not have a strong enough magneto-crystalline anisotropy to preserve the paleo-remanence. However, the magnetite's suitability for paleo-remanent studies are a result of the contributory factors of grain shape and size. In needly magnetite grains each end will serve as a magnetic pole, as this is energetically beneficial (ibid). The size of the grain, however, will determine if the grain fall inn under one of three categories: For an equidimensional magnetite grain under 65 nm are the magnetic moment going to be determined by the easy axis of the grain. This results in two surface poles, and the grain is said to be single domain (SD) (ibid). For a very large grain will this configuration no longer be energetically beneficial, and the grain will consist of smaller uniform magnetic domains separated by multidomain walls. This configuration is called multidomain (MD) grains (ibid). The transitional size range between SD- and MD grains are called pseudo single domain (PSD). According to Harrison and Feinberg (2009), is the SD configuration in this state no longer energetically favourable, and the magnetic

surface poles are exchanged in favour of a magnetic vortex. Here, the magnetization will be curled around a central magnetic core. Thus, the paleoremanent magnetization are mainly going to be controlled by the highly magnetically stable SD grains (ibid). PSD and MD grains, however, are much more prone to alterations of the magnetic moment when exposed to changes from an external field (ibid).

### 2.1.1 Magnetic response and total magnetization

Reynolds (2011), states that magnetic response in a mineral is described by two independent parameters, natural remanent magnetization ( $J_r$ ) and induced magnetization ( $J_i$ ). When the **total magnetization** of a rock is measured in-situ ( $J$ ), the measurement is the vector sum of these two components (ibid):

$$J = J_i + J_r \quad (I)$$

Induced magnetization describes a materials ability to produce a magnetic field when it is exposed to an external magnetic field (Reynolds, 2011). **Susceptibility** ( $\kappa$ ) is a dimensionless, quantitative measurement of a materials ability to magnetize ( $M$ ) in the presence of an external field ( $H$ ) (ibid). Reynolds (2011) further categorizes materials as either paramagnetic if the susceptibility is positive, or diamagnetic if it is negative. For all isotropic and linear minerals, the magnetization of the material is proportional to the external field with the factor  $\kappa$  (ibid):

$$\vec{M} = \kappa \vec{H} \quad (II)$$

Natural remanent magnetization is a vectorial parameter found in ferro-, canted antiferro- and ferrimagnetic materials (Reynolds, 2011).

This magnetization is usually composed of more than one component. Primary NRM is acquired during rock formation, and for igneous rocks this would typically be thermoremanent magnetization where NRM is acquired by cooling and crystallizing minerals below the curie temperature in the presence of an external field (Butler and Butler, 1992). However, this primary magnetization can be altered subsequently, which adds a secondary vectorially component. Total NRM will in these cases be:

$$total\ NRM = primary\ NRM + secondary\ NRM \quad (III)$$

### 2.1.2 Königsberger ratio

The Königsberger ratio, or Q- value, is a dimensionless parameter which describes the relation between induced and remanent magnetization (Clark, 1997).

$$Q = \frac{J_r}{J_i} \quad (IV)$$

Thus, the total magnetization of a rock with  $Q > 1$  is dominated by the remanent magnetization. Q- value analysis is necessary for interpreting the source of magnetic anomalies, and ferrimagnetic minerals such as magnetite and monoclinic pyrrhotite is typically associated with high remanent magnetization (Airo, 2015). The Q value for intrusive and extrusive rocks are often in the range 1- 10, while ore- deposits of ferrimagnetic minerals often exceed 100. Faulting zones and hydrothermally altered zones will often show reduced remanence (ibid).

### 2.1.3 Density calculation

The density of an object relates the mass of the object to its volume. Rock density is therefore dependent on mineralogy, pore fill and fracture content (Dentith and Mudge, 2014). Archimedes principle states that the buoyancy of an object submerged in a fluid equals the weight of the displaced fluid. By using this principle, the density of the sample ( $\rho_s$ ) can be calculated from knowing the weight of the sample in air ( $W_s$ ) and immersed in fluid ( $W_f$ ). First, the weight of the displaced fluid ( $W_{df}$ ) must be calculated as the difference between the sample weight in air and immersed in water (snl):

$$W_{df} = W_s - W_f \quad (V)$$

The weight ( $W$ ) is by definition the product of the sample mass ( $m_s$ ) and gravitational acceleration ( $g$ ). The mass of an object is defined as the objects density ( $\rho$ ) multiplied by its volume ( $V$ ):

$$W = m * g \quad (VI)$$

Where,

$$m = \rho * V \quad (VII)$$

and

$$W = \rho * V * g \quad (VIII)$$

Since the samples are entirely submerged, the volume of the sample ( $V_s$ ) and the volume of the displaced fluid ( $V_{df}$ ) is equal. Therefore, the following equation can be stated:

$$\frac{W_s}{W_{df}} = \frac{\rho_s * V_s * g}{\rho_f * V_s * g} \quad (IX)$$

By canceling the sample volume and gravitational force, the equation can be rearranged with respect to the sample density. As the density of water at 18 °C is approximately 1 g/cm<sup>3</sup>, it is now possible to calculate the sample densities:

$$\rho_s = \frac{W_s * \rho_f}{W_{df}} \quad (X)$$

To calculate the volume of the sample, it is simply to rearrange the relation between mass, density and volume as stated in equation VII:

$$V_s = \frac{m_s}{\rho_s} \quad (XI)$$

## 2.2 Rock classification and distribution of elements

Geochemical analysis of a rock's constituent elements serves as an important tool for understanding its origin and evolution. A common classification of a rock's constituents is based on elements abundances. The three groups are major-, minor- and trace elements, with abundances of more than 1 wt.% (weight percent), 1 – 0,1 wt.% and less than 0.1 wt.% respectively (Winter, 2001). **Major elements** control the mineralogy and evolution of the cooling magma. They are therefore suitable to use for rock classification, interpret chemical and physical parameters and interpret magma evolution (ibid). **Minor elements** will mainly occur as substitutions of major elements in principal minerals. However, if they are concentrated in sufficient amounts, they can form their own mineral phase called accessory minerals (ibid). **Trace elements** occur in so small concentrations that they will only occur as substitutions (ibid). This group have proven to be especially useful to track magma evolution study by being the best group for determining magmatic differential processes (Neumann, 1980; Winter, 2001; Robb, 2015).



### 2.2.1 Substitution of trace elements

Trace elements analysis is an ideal tool for interpretation of magma evolution, as the properties of the trace element dictates which magmatic phase it will partition into (Winter, 2001; Robb, 2015). One of the most famous studies of behavioural trends in substitutions were conducted by Goldschmidt in 1937. He presented the following three rules which predict the behaviour of the substituting elements based on the ionic radius and valence:

1. Two ions with the same radius and valence should enter into solid solution in amounts proportional to their concentration.
2. If two ions have the same valence and similar ionic radius, the smaller ion is preferred into the solid while the larger remains in the liquid/ melt.
3. If two ions have an approximately equal radius, but different valence, the higher charged ion is preferentially incorporated into the solid.

Secondly, it's important to be able to describe an elements affinity to either partition into the liquid- or the solid phase. This is given by the partition coefficient ( $Kd$ ), which is an equilibrium constant where  $I$  is the given element (Winter, 2001):

$$Kd_i = \frac{C_i^{mineral}}{C_i^{melt}} \quad (XII)$$

$C^{melt}$  is the concentration of the element in the liquid phase, and  $C^{mineral}$  is the elements concentration in the solid phase. The partition coefficient reflects whether an element is compatible and partitions into the solid ( $Kd > 1$ ), or incompatible and remains in the liquid ( $Kd < 1$ ) (ibid). This behavior is not absolute for an element, but will be affected by the mineralogy, temperature, and oxygen fugacity (ibid). To describe partitioning of trace elements in a whole rock, the distribution coefficient ( $D$ ) is used.

$$\bar{D}_i = \sum W_A D_i^A \quad (XIII)$$

Here is  $W_A$  the weight fraction of the mineral  $A$  in a rock, while  $D_i^A$  is the distribution coefficient for the element  $I$  in mineral  $A$  (Robb, 2015).

### 2.2.2 Rare Earth Elements

The rare earth elements (REEs) comprise the lanthanides ((La, Ce, Pr, Nd, Pm, Sm, Eu, Gd, Tb, Dy, Ho, Er, Tm, Yb and Lu) and additionally Y and Sc (Winter, 2001). This is a group of elements which occur as trace elements and have relatively similar chemical and physical attributes. These common physical attributes lead to a coherent decrease of ionic radii of the REEs as the atom number increases (ibid). The REEs are split into the groups HREE (heavy rare earth elements), MREE (medium rare earth elements) and LREE (light rare earth elements) (ibid). The HREE characterized with low ionic radii have a higher compatibility than the LREE and will therefore be favoured in the solid phase (Jennings et al., 2011). REEs occurring in rock plot with a phenomenon called the Oddo- Harkin's effect, where every even atom-numbered REE has a significant higher natural concentration compared to the odd numbered REEs (Winter, 2001). To avoid sawtooth- pattern graphs, the REEs are commonly normalized chondrite, which produce smooth graphs which depict enrichment or depletion of REEs compared to the chondrite (Sun and McDonough, 1989). Other rock types have also been used for normalization, however, in this thesis the denoted  $N$  refers to the elements being normalized to chondrite.

All REEs have a stable 3+ valence, except for Ce and Eu which also can occur as 4+ and 2+, respectively (Hoskin and Ireland, 2000; Belousova et al., 2002). The reduced divalent cation ( $\text{Eu}^{2+}$ ) can substitute for  $\text{Ca}^{2+}$  due to their similar size and charge configuration (Figure 2-1).  $\text{Eu}^{3+}$ , however, is an incompatible element and will therefore partition more strongly into the melt (Winter, 2001). The primary controlling factor for Eu incorporation into Ca- minerals is therefore the oxygen fugacity (ibid). The relative enrichment of Eu can be calculated by the following formula:

$$\frac{\text{Eu}}{\text{Eu}^*} = \frac{\text{Eu}_N}{\sqrt{\text{Sm}_N \times \text{Gd}_N}} \quad (\text{XIV})$$

$\text{Eu}/\text{Eu}^*$  is a ratio where values above 1 is regarded a positive anomaly which implies that the rock has crystallized Ca- minerals in a reduced environment (ibid). As an example, if a magma crystallizes plagioclase, a higher portion of the  $\text{Eu}^{2+}$  will go into the crystal phase compared to the other  $\text{REE}^{3+}$ . Negative anomaly (below 1) implies that the system already has experienced removal of Eu, which can be due to fractionation of among other minerals plagioclase, apatite, or ca-pyroxenes (ibid).

### 2.2.3 Partition of trace elements into minerals

The partitioning of Eu stands out as a special case among the REE due to its selective behaviour due to  $f\text{O}_2$  and crystallization of Ca rich minerals such as apatite, plagioclase, and Ca-pyroxene (Winter, 2001). The selective behaviour of the  $\text{REE}^{3+}$ , however, is dependent on the ionic potential ( $Z/r$ ). As mentioned in the previous section is HREE lithophile compared to the LREE, thus HREE partition into early forming minerals. Zircon and garnets are known to accommodate HREE; in zircon HREE have a smaller ionic radii which makes them more suitable for substitution with  $\text{Zr}^{4+}$  (Hoskin and Ireland, 2000), and garnet substitute HREE by coupled substitution into dodecahedral sites (Winter, 2001). MREEs are often partitioned into titanite and amphibole, while apatite and plagioclase often are enriched in LREE.

## 2.2.4 Partitioning of trace elements into apatite

Apatites is a common accessory mineral, but can be a dominant phase in some igneous rocks (e.g. Nelsonites) (Harlov and Rakovan, 2015). The apatite crystal lattice forms a rigid structure which is stable under a wide range of pressure and temperature ranges. It can accommodate a wide range of trace elements (Belousova et al., 2002) which make apatite a prime tool for petrogenetic analyses:

Especially the REEs are well suited for analyses. They are incorporated into (or removed from) the structure by the following coupled substitutions (Harlov and Rakovan, 2015):



The incorporation of trace elements is strongly related to the degree of fractionation and oxidation state of the host magma and will therefore reflect upon their petrogenetic environment. The amount of REE's may also be affected by post solidus metasomatic processes (Harlov and Rakovan, 2015). The halogen content of the X site may also offer some insight to the origin of the mineral: Volcanic – plutonic apatites are often dominated by F<sup>-</sup> and OH<sup>-</sup>, while mafic systems, such as layered intrusions are Cl<sup>-</sup> dominated. Metasomatic processes can also be proven through changes of halogen composition and zonation within a grain (Webster and Piccoli, 2015).

## 2.2.5 HFSE and LILE classification

Winter (2001) presents the classification of HFS/ HFSE (High Field Strength Elements) and LIL/ LILE (Large Ion Lithophile Elements) as an additional useful system of grouping trace elements. This classification is based on the ratio between valence ( $z$ ) and ionic radius  $I$ , and the boundary between the groups are set at  $z/r = 2$  (Figure 2-1):

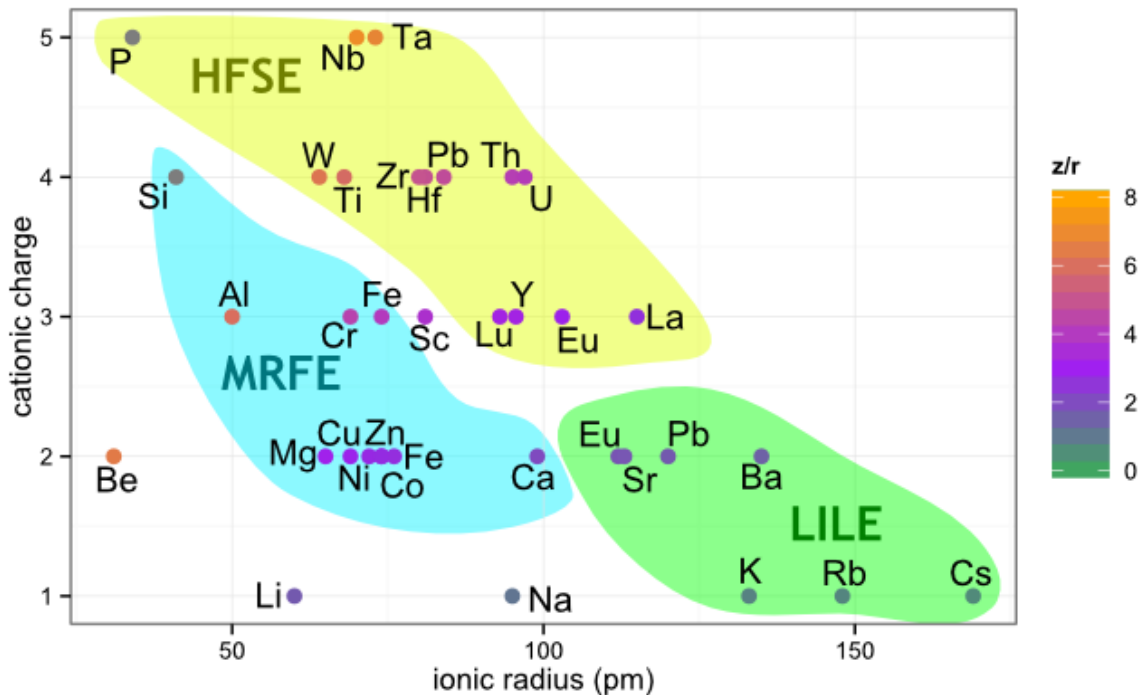


Figure 2-1: HFSE, LILE and MRFE groupings. See link <https://bit.ly/2Ua0MQM>, based on Railsback (2003), *An Earth Scientists Periodic table* and Best (2003).

The LIL elements comprise of (K, Rb, Cs, Ba, Sr, Pb<sup>2+</sup> and Eu<sup>2+</sup>) and are characterized by being highly soluble and incompatible. Thus, LILE will partition into the fluid phase and behave mobile during processes such as fluid alteration (Winter, 2001).

### 2.2.6 Partitioning of LILE and HFSE in minerals:

Figure (HFSE-LILE) highlight how Sr shares characteristics with Eu<sup>2+</sup> and will therefore typically substitute for Ca<sup>2+</sup> in plagioclase. Rb and Cs will substitute for K in late forming minerals such as K-mica and K-feldspar (Winter, 2001). HFSE comprises of the REEs in addition to Th, U, Pb<sup>4+</sup>, Zr, Hf, Ti, Nb, Ta, Y and Sc (ibid). These elements are characterized by high ionic charge and low ionic radius, which makes these elements act immobile and stable in the solid phase (ibid). This trait causes the HFSE concentration to mainly be controlled by magmatic processes, and concentrations will be little affected by subsequent metamorphism and alteration processes (ibid).

### 2.2.7 Transition metals classification

The last division of trace element groups are the transition metals. These include Fe, Mn, Sc, Ti, V, Cr, Co, Ni, Cu and Zn (Best, 2003). Most of these elements occur in the MRFE (mantle rock forming elements) field in Figure 2-1. This group consists of, or are associated with, the elements that build up the mantle rock forming minerals such as olivine, garnet and pyroxene (ibid). Thus, Fe and Mn will be major elements while rest of the transitional metals usually occur as minor- or trace elements (ibid).

### 2.2.8 Partitioning of transition metals into minerals

Winter (2001) states there is no coherent geochemical behaviour linked to the transition metals as a group, but studies have proved these general trends: Clinopyroxene can accommodate both  $\text{Fe}^{2+}$  and  $\text{Fe}^{3+}$  which makes it suitable to substitute for a wide range of transition metals (ibid). A diagnostic feature for clinopyroxene would be its ability to incorporate Sc for  $\text{Fe}^{3+}$ . Co and Ni are typically associated with olivine (ibid). Thus, the transition metals affinity to early forming minerals causes them to concentrate in mafic and ultramafic rocks, and they will be less prominent to non-existing in evolved systems (ibid). A primary magma, in equilibrium with a mantle source, is recognized with high concentrations of Cr (>1000 ppm), Ni (>400) and Mg (>0.66).

## 2.3 Classification diagrams

### 2.3.1 TAS- classification

Rock- classification diagrams are based on the rock's major element composition, and is an important tool in igneous geology, especially in cases where the crystals are too small to be observed. (BAS et al., 1986) published a classification of igneous rocks based on chemical composition. This consists of 15 classes based on comparing total alkalis ( $\text{Na}_2\text{O} + \text{K}_2\text{O}$ ) against silica ( $\text{SiO}_2$ ). The original diagram was developed for extrusive rocks; however, this diagram is modified according to intrusive rocks (Middlemost, 1994).

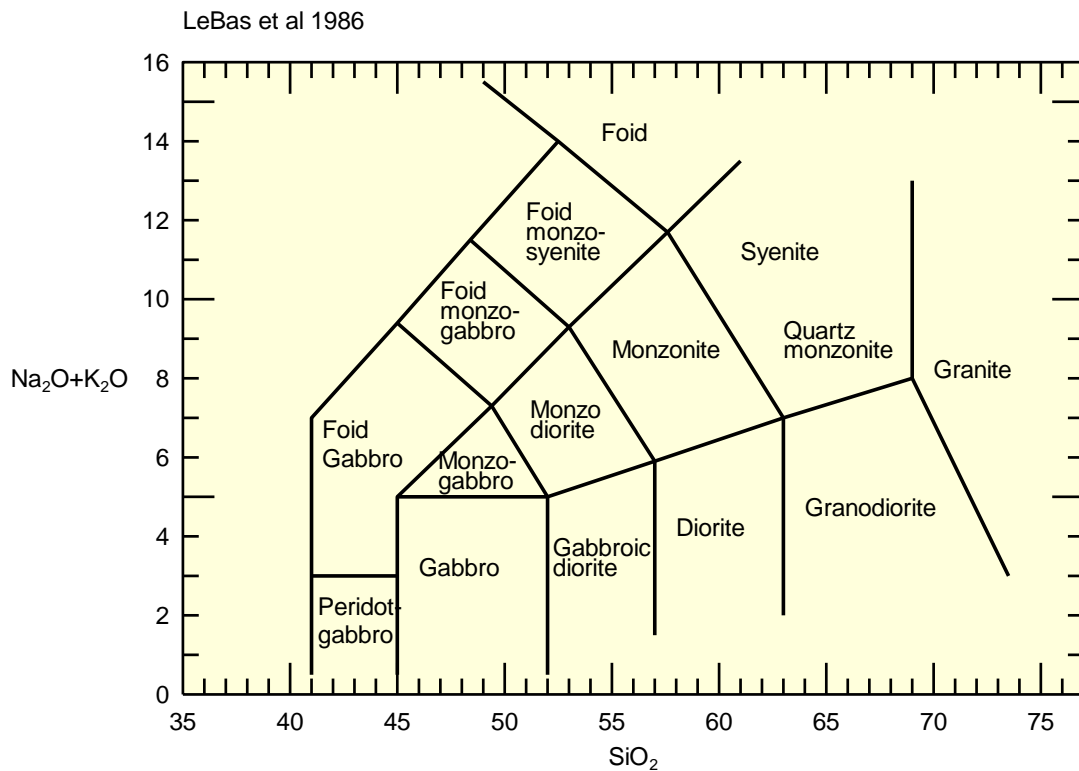


Figure 2-2: Modified TAS diagram (Total Alkalis vs Silica) (Middlemost, 1994).

### 2.3.2 Basalt classification

The basalt tetrahedron developed by Yoder and Tilley (1962), (Figure 2-3) is used to classify basalts based on the normative mineral composition of *ne* (nepheline), *di* (diopside), *q* (quartz) and *ol* (olivine). The shaded *di-hy-ab* plane is the field between silica saturated and undersaturated rocks, where basalts plotting on the right side will contain a stable phase of a silica polymorph and basalts plotting on the left side will crystallize a stable phase with olivine. Thus, the names of the rocks are quartz tholeiite and olivine tholeiite, respectively. The *di-ol-ab* plane is a thermal divide which exists in low pressure environments, which will hinder a cooling melt of crossing the field from alkaline basalt to olivine tholeiite. The thermal divide is called the critical plane of silica undersaturation, and basalts plotting left of this will form nepheline, a mineral which cannot co-exist with quartz.

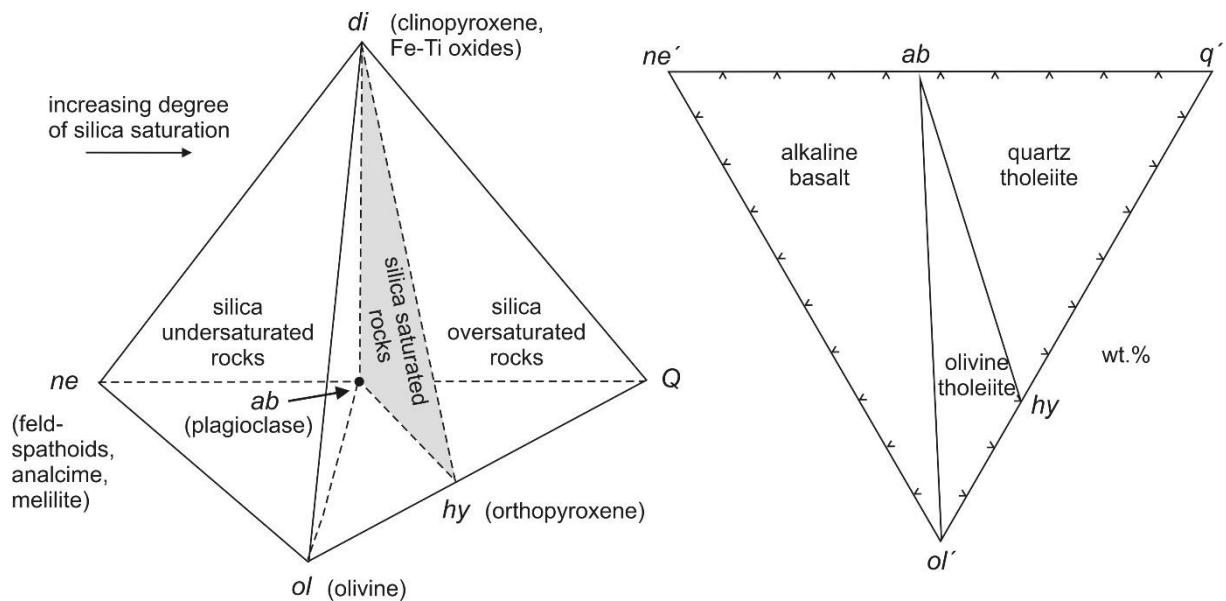


Figure 2-3: Basalt classification diagram (Yoder, H.S.; Tilley, 1962) based on silica saturation grade. Normative minerals are displayed in italics. Left: Basalt tetrahedron. Right The base of the tetrahedron seen from *di* (clinopyroxene).

### 2.3.3 Granitoid classification

Granitoid is a class of rocks which comprises of a collection of coarse-grained igneous rocks mainly composed of quartz, plagioclase, and feldspar. This group is the most prevalent in the crust (Winter, 2001). Granitoids does not usually stem from one source but are rather a product of mixing between mantle-derived mafic magma and crustal-derived magmas (Streckeisen, 1974; Frost et al., 2001). Despite being so common, there is no single, internationally agreed upon scheme of classification. There are about 20 different schemes in use today, which are based in different selection criteria such as geochemistry, mineral modality, and tectonic origin (Frost et al., 2001). One of the most commonly applied schemes is Streckeisen's ternary diagram from 1967, now applied by the IUGS (Figure 2-4). It is based on two ternary diagrams, the QAP (Quartz, alkali- feldspar, plagioclase) – and FAP (Foid/ Nepheline, alkali- feldspar, plagioclase). The advantage with this diagram is that it can be applied in the field, as it is based on mineral modality and does not require time consuming or expensive analysis. The major back- draw is that it does not take compositional variations in account, such as minor phases which might carry great significant petrologic implications (Frost et al., 2001).

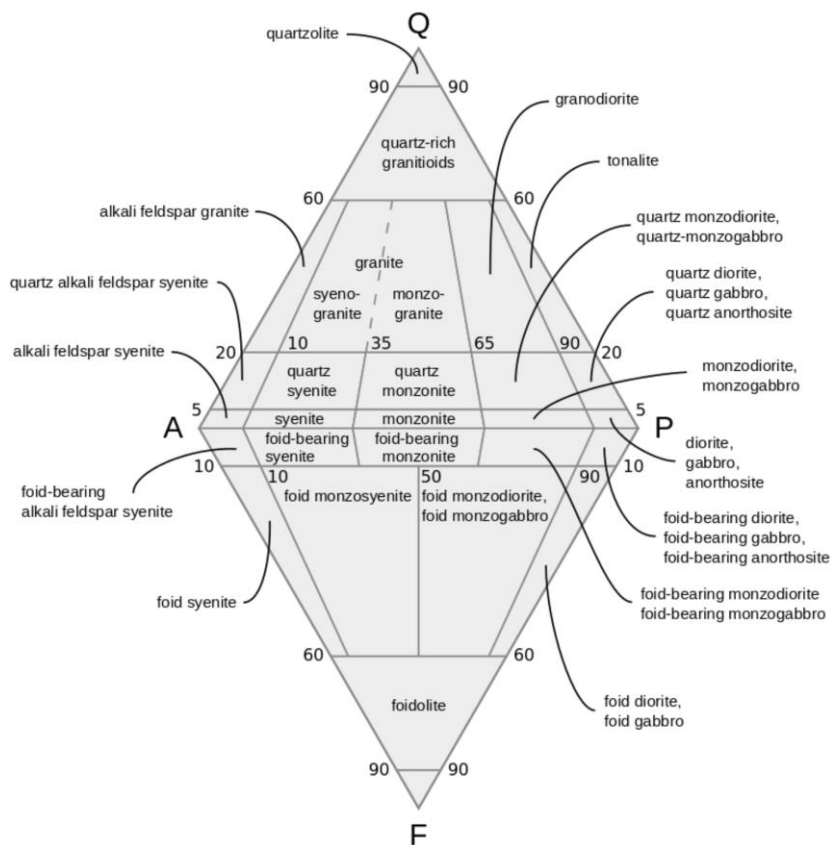


Figure 2-4: Granitoid classification based on quartz-, alkali-, plagioclase-, and nepheline normative composition (Streckeisen, 1974).

Frost et al. 2001 suggested a granitoid classification scheme founded on three geochemical parameters. This is the Fe- number/ Fe\*, modified alkali- lime index (MALI) and aluminum saturation index (ASI), which results in a subdivision of 16 granitoid classes.



The first variable is to establish whether a granitoid is ferroic or magnesian (Figure 2-5 A). This can be calculated by using the formula  $Fe\text{-}number = FeO/(FeO+MgO)$  where the concentration of ferrous iron ( $Fe^{2+}$ ) is known (Frost et al., 2001). For analytical methods which does not discriminate between ferrous and ferric ( $Fe^{3+}$ ) iron the formula  $Fe^* = FeO^{tot}/(FeO^{tot} + MgO)$  is applied (ibid). In both cases Fe- concentration is plotted against  $SiO_2$  concentrations. Frost et al. 2001 states that the  $Fe\text{-}nr.$  formula is preferential over the  $Fe^*$  where  $Fe^{3+}/Fe^{2+}$  concentrations are known. This is based on analysis of a-type and Cordilleran granitoids, which are respectively the archetypical ferroic and magnesian granitoids. The study revealed that Fe-nr. calculations gave more precise segregation of the two classes compared to  $Fe^*$  calculations. The exception is when the  $Fe^{3+}/Fe^{2+}$  ratio varies a lot for a rock due to late sub- solidus oxidation. In these cases,  $Fe^*$  would be preferential.

Iron number conveys information about the differential history of the granitoid rock. A-type granitoids have a characteristically higher iron content than granitoids associated with subduction type regimes (Petro et al., 1979; Anderson, 1983; Maniar & Piccoli, 1989, Frost & Frost, 1997; in Frost et al., 2001).

Winter et al. (2001), uses the MALI (modified alkali- lime index) to further discriminate the granitoids (Figure 2-5 B). In this calculation  $(Na_2O + K_2O - CaO)$  is plotted against  $SiO_2$ . There are four subcategories divided by curves fitted to well-studied plutonic evolutionary trends. These sub-groups are alkali, alkali- calcic, calc- alkali, and calcic. Trends are positively correlated with silica content. However, they carry no statistical significance. The MALI parameter describes the composition and abundance of feldspars in the rock, which again can be related to the magmatic source.

The last level of categorizing Winter et al. (2001) suggests is the ASI (aluminum saturation index) =  $[Al / (Ca - 1,67P + Na + K)]$  (Figure 2-5 C). This formula is based on a molecular ratio which is used to subdivide granitoids into three groups based on the level of Al saturation (Shand, 1943; Winter, 2001). The formula also takes height for the presence of apatite and is referred to as the modified ASI. Rocks fulfilling the following criteria:  $Al_2O_3 > (CaO + Na_2O + K_2O)$  are peraluminous (ibid). These rocks have a higher Al concentration than that which can be accommodated for in feldspars and must therefore have another Al- phase present (Figure 2-5 D). In modelling, this is accounted for with normative cordierite, but can in nature occur as Al- rich biotite for marginally peraluminous rocks or muscovite, garnet or other  $Al_2SiO_5$  polymorphs for highly peraluminous rocks.

If  $[Al_2O_3 < (CaO + Na_2O + K_2O)]$ , but  $[Al_2O_3 > (Na_2O + K_2O)]$ , the rock falls into the category **metaluminous** (Winter, 2001). This category is recognized with an abundance of Ca after the Al phase have been accommodated into feldspars. The excess Ca is usually accommodated into pyroxenes, hornblende, and biotite (Figure 2-5 D).

The last subdivision is **peralkaline** rocks where  $[Al_2O_3 < (Na_2O + K_2O)]$  (Shand, 1944; Winter, 2001). In this case there is an excess of alkalis after Al has been accommodated into feldspars. The diagnostic trait for this group is that Na is accommodated into ferromagnesian silicates such as Na- amphiboles and pyroxenes (Figure 2-5 D).

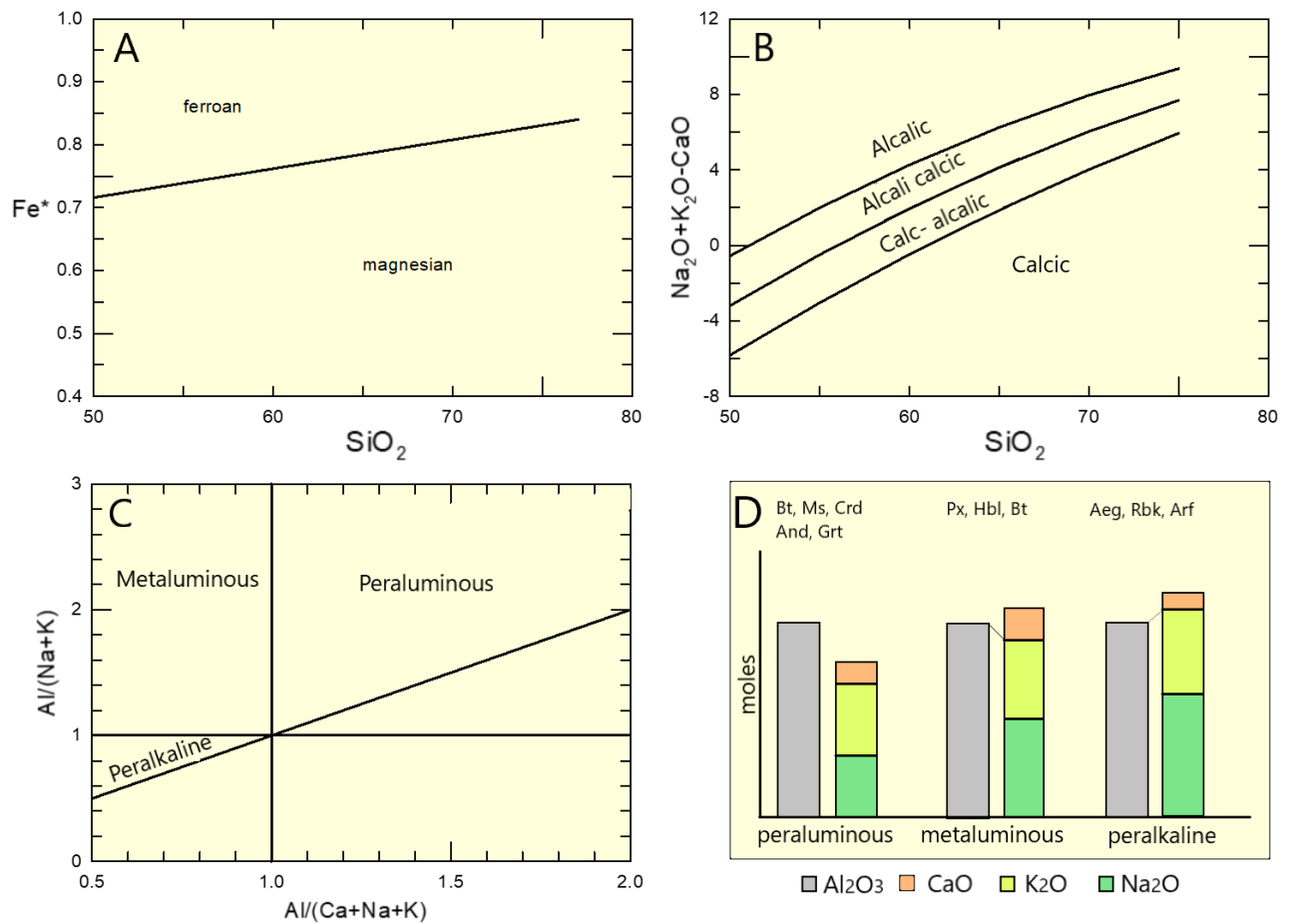


Figure 2-5: Diagram (A – C) suggested by Frost et al (2001) to discriminate between granitoids. (A)  $Fe^*$  diagram, (B) Modified Alkali Lime Index (MALI), and (C) Aluminium Saturation Index (ASI). (D) illustrates how aluminium saturation affects which mineral phases crystallizes

## 2.4 Differentiation processes

Differential processes is a term for the variety of processes which causes magmatic evolution. The study of these processes is crucial to understand the evolution of magma from the creation of primary melts in the mantle and until felsic volcanoes erupt on the surface.

### 2.4.1 Fractional crystallization

Fractional crystallization is the differential process where the chemical composition of the melt evolves as a result of mineral crystallization and accumulation due to cooling magma temperature (Winter, 2001; Best, 2003). The chemical evolution of the residual melt composition will depend on the nature and proportions of which mineral phases crystallizes. There are several processes which leads to minerals segregation from the melt. It may be due to gravitational settling of mafic minerals and upward extraction of the residual melt if the two phases have a high-density contrast, or an external force pushing the residual melt out of the crystal mush (Winter, 2001; Neumann, 1980). When the crystals are separated from the melt, it will no longer be possible to maintain chemical equilibrium between the two phases (ibid). Due to the different solidus temperatures and chemical compositions of minerals, the chemical composition of the residual melt will be diagnostically modified as a function of the latest removed crystal phase (Winter, 2001). This is visible in major-, minor-, and trace element diagrams, and Harker diagrams are frequently applied to graphically show these evolutions.

In addition to chemical analysis, interpretations of magmatic textures can be used to determine if fractional crystallization have taken place in a magmatic system. Cumulate textures are recognized as accumulated phenocrysts sharing boundaries with each other with one or several crystal phases filling the interstitial spaces (Winter, 2001).

Multiple factors will influence the crystallization process of the minerals. The major determining factors are cooling temperatures, pressure, chemical composition and viscosity of the melt (Winter, 2001; Tegner et al., 2006; Best, 2013). Changes in one or all of these parameters will have important effects on the magma evolution. Addition or subtraction of volatiles such as H<sub>2</sub>O, CO<sub>2</sub> and O<sub>2</sub> will also change the evolution (Winter, 2001). H<sub>2</sub>O is a carrier for hydrophile elements and will additionally lower the solidus temperature of the melt. The concentration of free O<sub>2</sub> (oxygen fugacity) determines the ionic charge of several multivalent elements, e.g., if iron will occur as Fe<sup>2+</sup> or Fe<sup>3+</sup> and crystallize as either hematite or magnetite (Winter, 2001; Reynolds, 2011). The viscosity of the melt will determine how easily a melt is extracted. In the Oslo rift, volatiles and viscosity played a major role in the deposition of extrusive melts; the evolutionary stage of rhomb porphyry corresponds to a relatively high viscosity which would lead to a restricted flow (Larsen et al., 2008). However, this is not the case as multiple flows have been identified covering vast areas. It is therefore suggested that fluorine volatiles lowered the viscosity of the melt (ibid).

## 2.4.2 Immiscibility

Liquid immiscibility is the phenomenon of two or more liquid phases in equilibrium not able to mix. A common example of this is oil and water, where the less dense oil forms as a layer on top of the water. Immiscibility have been observed for magmatic systems under a small range of conditions (Winter, 2001). The thermodynamical explanation for immiscibility is that the initial magma will be stable as one homogeneous phase at high temperatures, due to high vibrational energy of the constituent atoms and molecules (Honour et al., 2019). Through changes in temperature, pressure, or composition the homogeneous phase can develop towards an immiscibility field (Freestone, 1990). The transition between these two fields in a silicate melt is called binodal, binodal- curve or binodal surface (Charlier and Grove, 2012). Within this immiscible field will the sum of free energy be lower for two separate liquids compared to that of one homogeneous (Freestone, 1990).

The onset of immiscibility between silica- and iron-rich liquids in tholeiitic systems have long been a topic for debate. It has been recreated multiple times through experiments, but with poor understanding of the constraints on the liquid immiscibility field. Fairly recent studies (Charlier & Grove, 2012; Jackobsen et al., 2005) have established a better understanding of the immiscibility field along the tholeiitic line of descent. The immiscibility occurs at relatively low pressures,  $\sim 1000 - 1040$  °C, under anhydrous conditions in late stage of the crystallization sequence (Charlier & Grove, 2012; Jackobsen et al., 2005). The melt does not need to be extremely enriched in iron to reach immiscibility. Elevation of alkali, phosphorous and titanium contents promote unmixing at lower iron content. High pressure and water, however, will drive the liquid line of descent away from the immiscibility field as it promotes early depletion of iron.

However, encountering rocks of contrasting composition in the field does not immediately imply differentiation by liquid immiscibility. Such rocks can be formed by several processes, and there are three tests which can be applied to determine whether the rock was formed by immiscible processes or not (Winter, 2001).

The first evidence of an immiscible process is that it can be reproduced experimentally, or that they plot on the boundaries of already established immiscibility gaps (Winter, 2001).

Second, at the onset of immiscibility, the conjugate melts must be in chemical equilibrium. (Charlier and Grove, 2012).

Last, the segregation process from one to two liquids leads to a distinctive partitioning of minor- and trace elements (Jakobsen et al., 2005; Veksler and Charlier, 2015). Hence, trace element patterns can be used to evaluate if the liquids originate from immiscibility. Experiments conducted by Veksler and Chalier (2015), have shown that some incompatible elements are preferentially incorporated in the Fe- rich melt. The most distinct enrichments are Fe, Ti, P, REE's and transition metals (Figure 2-6). This trait can be used to distinguish Fe-rich immiscible melt from cumulates originating from crystal fractionation, as the former would be significantly enriched in various incompatible trace elements compared to the latter.

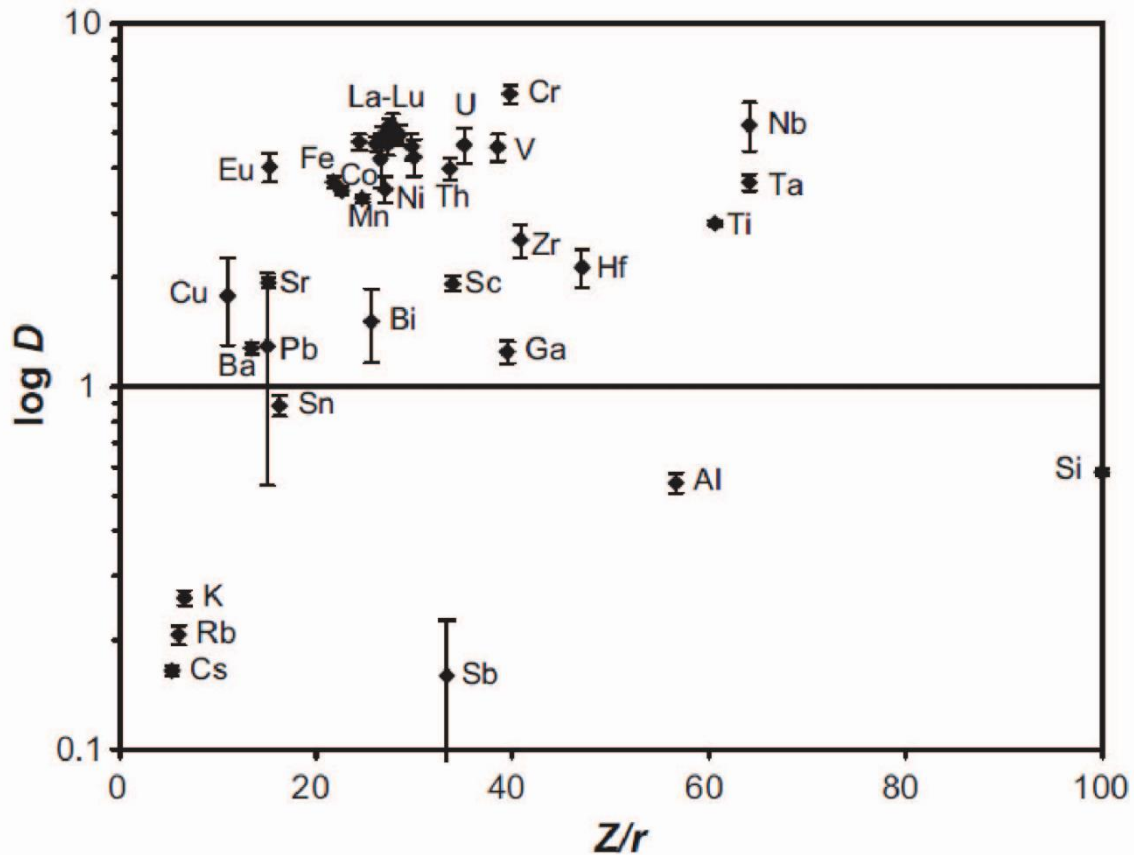


Figure 2-6: Liquid- liquid partition coefficient  $D$  plotted against ionic potential  $Z/r$  by Veksler and Charlier (2015). Vertical bars represent standard deviation.

### 2.4.3 Magma mixing

Magma mixing is the process where two or more magmas meet and mix (Winter, 2001). This is a common process within magma chambers, as most magmatic systems result from multiple magma injections (Farina et al., 2012; Sommer and Kröner, 2019). The extent of mixing is controlled by the contrasting magma properties, such as temperature, density, viscosity, composition, volatiles, and turbulence. If the property contrast is large between the magmas, mixing will result in two juxtaposed, visibly distinguishable phases (Winter, 2001). Such rocks are referred to as comingling or mingling. Comingling magmas and immiscible magmas can be difficult to distinguish in the field (Winter, 2001).

One possible way to determine which process occurred is to study trace element composition in zonation in minerals. Compositional changes in the magma can be recorded by further crystallization of mineral phases (Winter, 2001). Mineral geochemistry might also be used to identify crystal populations which implies different crystallization environment. Bulk rock analyses can also be applied to determine magma mixing (ibid). If two magmas mix to a homogeneous melt, the resulting magma composition will plot somewhere in between the two end- members (ibid). This trend will only be evident in mixing between two strongly contrasting magmas (e.g., between granitic and mafic composition).

#### 2.4.4 Assimilation

Assimilation is the process where fragments of the host rock are incorporated into the magmatic system (Winter, 2001). The degree of assimilation is mainly controlled by the contrasting melting temperatures of the intrusive- and host rock (ibid). The temperature of the intrusive rock must at least be able to heat the host rock to melting temperature and keep heating until partial melt is produced and assimilated (ibid). Internal convection in the magma chamber is important to keep a steady heating rate of the wall- and roof rock of the magma chamber, without, the bordering intrusive rocks will cool and become stagnant, hindering any further assimilation processes (ibid). Lastly, the degree of stoping will further influence the degree of assimilation: Winter (2001), describe stoping as the phenomenon where roof or wall pendants break off and fall into the magma chamber. This process will increase surface area exposed to the melt and enable a higher degree of assimilation. Major element composition will be relatively unaltered by low degrees of assimilation. However, the intrusive melt can be highly enriched in trace elements and certain isotopes due to partial melting of the host rock (ibid).

There are several approaches to determine whether an intrusive rock have undergone assimilation. One of the most diagnostic evidence would be to study the isotopic ratios of the Sm/Nd system. Another approach, which does not include isotopic analyses, is to study relationships between compatible and incompatible elements. A melt which has undergone crustal assimilation is expected to be enriched in incompatible elements like Nb, Ta, Rb, Th, U and K relative to the more compatible elements Ti, Tb, Y, Tm and Yb (DePaolo, 1981; Winter, 2001). Field observations which can further imply assimilation is the occurrence of partly resorbed xenoliths. However, observations of xenoliths are not by itself a definite evidence for assimilation, as it might be caused by magma mingling as well.

#### 2.4.5 Mirolitic pods and cavities

Miarolitic pods and cavities were created when fluids segregated from the melt and were trapped in the pluton. Being lighter than the surrounding melt, fluid bubbles tend to ascend and create a concentration of miarolitic cavities towards the roof of the magma chamber (Lindqvist and Suominen, 2017). The separation and migration of H<sub>2</sub>O from the magma affects the systems melting temperature; as the crystallization temperature will increase as H<sub>2</sub>O is removed. Sudden separation of fluids will rapidly increase the solidus, which subsequently causes an increased crystallization rate. This have been suggested to be a common way of forming porphyritic texture in silicic plutons (Jahns and Burnham, 1969; Winter, 2001)

## 3 Methodology

### 3.1 Field work and sampling

A total of 12 field days were spent for this study, distributed over 4 periods in 2019 – 2020. The first visit to the field area lasted 2 days in August 2019 and I was assisted by Nolvann Coint and Peter Graham Hagen. The second assisted period lasted 5 days in June 2020 where I was joined by Nolvann Coint. 2 other solo visits were conducted, 2 days during Easter of 2020 and 3 days in June 2020. The field area for this study is restricted to the westernmost and youngest intrusion of the Siljan – Hvarnes complex. Samples were collected along a north-south trending profile crossing a valley which also extends over the centre of the pluton. The exposure of outcrops varies from the hillsides to the bottom of the valley, where the hillside often has exposed cliff sides, while the valley floor is covered with sediments and vegetation. The area was generally covered with either dense forests or farmland. Old outcrops had moss cover on rocks, limiting the rock exposure. Field equipment included a pad with ArcGIS software and GPS module, and a Silva geological compass. A total of 58 samples were collected where the priority was to acquire samples which were oriented for geomagnetic analyses and large enough for representative whole rock analysis. The samples are presented in the respective Appendixes.

### 3.2 Optical microscopy

All thin sections were studied with a petrographic Nikon polarizing microscope. Both transmitted and reflected light were crucial to identify minerals and determine mineral assemblages and relations. (Bard, 1986a), was used as a guide for textures, (Pracejus, 2015) as a guide to opaque mineral microscopy and (Deer et al., 1975) a guide to transparent mineral microscopy.

### 3.3 Thin section scanning

The thin sections were scanned with an Olympus BX51 petrographic microscope modified with an Olympus UC90 microscope camera and Marzhauser Wetzlar motorized microscope stage. 5x magnification XPL, PPL and RFL scans were acquired from each thin section.

### 3.4 XRF

27 samples were prepared and analysed for trace and major elements during January and February 2020 at NTNU. The initial preparations included sledging of large samples to pieces which would fit the jaw-crusher. Samples which consisted of two lithologies were cut with rock saw and split into two samples. Pieces including both rock types were deemed unfit for XRF-analysis. Samples were further crushed with a wolfram-carbide jaw crusher. The sample sizes were reduced by using riffle splitters multiple times until the sample-sizes reached ~40 mL. These were milled with a Retsch Vibratory Disk Mill RS 2000 in a 50 mL wolfram-carbide chamber. To avoid contamination the jaw crusher and disc mill were cleaned with ethanol between each sample, and Fe- Ti- P trace element rich samples were crushed last as an extra step of precaution to avoid contamination of REE-s. The element analysis was conducted in the 4 kW, minerals edition Zetium spectrometer.

### 3.4.1 XRF Trace element

Pressed pellets were produced by mixing 9,6 g sample and 2,4 g LICO- wax. The two components were mixed for 2 minutes with a Fluxana Fine Vortex. The pellets were created in a Herzog TP 60 manual pellet press under a pressure of 200 kN.

### 3.4.2 XRF Major elements

2.5 g sample powder were heated to 1000 °C for 1 hour and reweighted to calculate loss on ignition (LOI). 0.500 +/-  $2 \cdot 10^{-3}$  g sample were mixed with 5 g flux and 60 mL LiI before being melted to glass pellets in a Claisse Theox Advanced oven using the "General Oxide melting setting". Samples 502, 508, 510 and 512 A fractured under the cooling procedure, and were therefore added additional 60 mL LiI and remelted. Sample SILJ111509 had a LOI of 3,07% where most samples were in the range of +/- 1%. A new batch were heated and LOI were measured to 3,10% and therefore deemed to be in orders. All negative LOI values (increase of weight) were measured on apatite and magnetite rich samples. The weight gain is most likely accredited to oxidation of magnetite to hematite.

## 3.5 EPMA

Four thin sections (761, 403B, 503 and 536) were analysed at NTNU using the JEOL JFX-8530F PLUS Electron Probe Micro-Analyzer (EPMA). Beam acceleration was set to 15 kV for all sample points, while the probe-diameter was adjusted depending on mineral type. The apparatus was calibrated for four mineral classes, apatite, pyroxene, biotite and amphibole, and feldspar. Probing configuration were set to circle 5 µm for apatite, circle 3 µm for pyroxene and amphiboles, while square 3 µm, length 6 with 10 counts per seconds were set for feldspar. Scans with larger surface were selected for apatite and feldspars to avoid migration of alkali ions. Sample 536 had to be re-analysed due to poor overall analyses quality. An additional layer of 2 µm carbon coating was added.



### 3.6 LA-ICP-MS analysis of apatite trace elements

145-point analysis for trace elements were conducted on 115 apatite crystals distributed over 10 thin sections (511, 512, 514, 517, 520, 524, 759, 760, 761 and 764) with LA-ICP-MS (Laser- Ablation Inductively Coupled Plasma Mass Spectrometer). The isotopes which were analysed were:  $^{29}\text{Si}$ ,  $^{31}\text{P}$ ,  $^{35}\text{Cl}$ ,  $^{43}\text{Ca}$ ,  $^{44}\text{Ca}$ ,  $^{47}\text{Ti}$ ,  $^{49}\text{Ti}$ ,  $^{51}\text{V}$ ,  $^{55}\text{Mn}$ ,  $^{75}\text{As}$ ,  $^{88}\text{Sr}$ ,  $^{89}\text{Y}$ ,  $^{90}\text{Zr}$ ,  $^{111}\text{Cd}$ ,  $^{137}\text{Ba}$ ,  $^{139}\text{La}$ ,  $^{140}\text{Ce}$ ,  $^{141}\text{Pr}$ ,  $^{146}\text{Nd}$ ,  $^{147}\text{Sm}$ ,  $^{153}\text{Eu}$ ,  $^{157}\text{Gd}$ ,  $^{159}\text{Tb}$ ,  $^{163}\text{Dy}$ ,  $^{165}\text{Ho}$ ,  $^{166}\text{Er}$ ,  $^{169}\text{Tm}$ ,  $^{172}\text{Yb}$ ,  $^{175}\text{Lu}$ ,  $^{206}\text{Pb}$ ,  $^{207}\text{Pb}$ ,  $^{208}\text{Pb}$ ,  $^{232}\text{Th}$ ,  $^{238}\text{U}$  and  $^{248}(\text{ThO})$ .

Primary preparations included selection and collecting photographs of interesting zones using a Nikon petrographic microscope with attached camera. The analysis was conducted at the Geological Survey of Norway using a Photon Machines 193 nm excimer laser coupled to an Agilent 8900 QqQ-ICP-MS. Spot size was set to 25- $\mu\text{m}$ -diameter beam with a pulse rate of 6 Hz and laser energy of  $\sim 3.5 \text{ J/cm}^2$ . The ablated material is transported with He-carrier gas and mixed with Ar gas before entering an Ar-plasma. Sampling time were set to 20 seconds "gas-blank" baselines, followed by 25 seconds of ablation, and finishing with a 5 second washout period. Dur- DonG and McClure Mountain were used as control samples, while NIST-612 was used to reduce the data (Pettke et al., 2012; Chew et al., 2016). The former as glass standard and the two latter as apatite references. The "Trace Element" scheme on Iolite4 software were used to conduct data reduction. Calcium 43 were used as an internal standard. All ablation periods were trimmed with start and end crop set to 1,5 and 1 second, respectively. Samples where the laser shot through to the glass or unwanted inclusions were adequately shortened or discarded.

### 3.7 Geophysical methodology

#### 3.7.1 Preparation of samples

Samples collected in the field intended for magnetic analysis were measured with dip direction and dip, and marked with a waterproof marker, pointing an arrow down the dip direction. The samples were selected on the basis of representing different lithologies along the sampling profile through the latest intrusion. 13 samples were selected for geophysical analyses, and preparations of the samples consisted of drilling cores with a diameter of 21 mm and cut at a length of  $\sim 22 \text{ mm}$ . This resulted in 86 sample- cylinders. The cylinders were labeled with sample name, number to reference drill hole and letter to reference the cuts from the same core. ("Sample number"\_"core number""cut letter"). E.g., two cores were drilled from 510, and each core were long enough to be cut into two samples, resulting in 510\_1A and B and 510\_2A and B.

Cores were collected from samples: 501, 502, 504, 510, 512, 514, 515, 5-9 - 522, 524 - 533, and 535 - 539. The natural remanent magnetization (NRM) and susceptibility of the samples were then measured to determine the Q- values.

### 3.7.2 Density measurements

The cylindrical samples were immersed in distilled water for 24 hours prior to the measuring of the samples. This was conducted to achieve approximately full saturation of pore- spaces and cracks with the intent of reducing buoyancy accredited to trapped gasses. The samples were measured with a Mettler Toledo ML104 scale with an accuracy down to  $10^{-4}$  grams. The samples were first measured immersed in water, then dried over a half-day period before being measured in air. By using Archimedes principle, volume and density of the samples was calculated. (See Theory, Geophysical section).

### 3.7.3 Susceptibility measurements

The susceptibility was measured with a Agico MFK1-A Multi-Function Kappabridge using Safyr6 software. The volume of the samples was set to  $1 \text{ cm}^3$  for later to be corrected by volume acquired from the volume – density calculations:

$$\text{Instrument reading } (\kappa_{re}) = \frac{\text{Raw susceptibility reading}}{\text{Assumed sample volume}} \quad (\text{XVII})$$

To correct for the assumed volume, the following calculation was performed:

$$\text{True susc.} = \text{instrument reading} * \frac{\text{Assumed volume}}{\text{Measured volume}} \quad (\text{XVIII})$$

### 3.7.4 NRM measurements

The NRM were measured with the Agico JR-6A Dual Speed Spinner Magnetometer with Rema6W software. The NRM is localized inside a Faraday cage to nullify external magnetic fields. The orientational settings for the magnetometer were set to 6, 0, 6, 0 in compliance with the samples being oriented with dip direction and dip. Volume of the samples were set to a default of  $11,15 \text{ cm}^3$ . The results yielded measurements of the NRM vector represented with declination, inclination, and modulus (magnetic field strength in A/m). The modulus was later corrected with respect to the actual volume of the samples.

## 4 Results

The results are divided into four parts. The first section contains descriptions of each defined lithology with a generalized thin section description and field relations. The second part called key locations describe important outcrops where Fe-Ti-P rich rock is visible. Third part consist of geochemical analyses including whole rock XRF of major and trace oxides, EPMA mineral analysis and LA-ICP-MS results of apatite analysis. The fourth and last section contains results from the geomagnetic study.

### 4.1 Rock Descriptions

The lithologies have been classified based on geochemical composition (TAS) and textures. These are presented in Table 3 and sample locations depicted in Figure 4-1.

Table 3: Sample classification based on geochemistry and texture.

TAS class	RP	Syenite			
Texttrue	Porphyritic	fine	med - coarse	V. coarse	porphyritic/ trachytic
Samples	521	510	502	511	508
	523	520	516	519	
	524	533	531	764	515
	525		536		522
	537		765		532
			766		534
			767		535
					539
					538

Monzodiorite	Qtz Monzonite	Monzonite	Fe-Ti-P	
Aphanitic	Porphyritic	Porphyritic	Porphyritic	Fine - med grained
509	512A	512B	507	503
		513	514	505
			516B	526
			517	759
			518	760
			761	762
			403A	402A
			403B	
			403C	

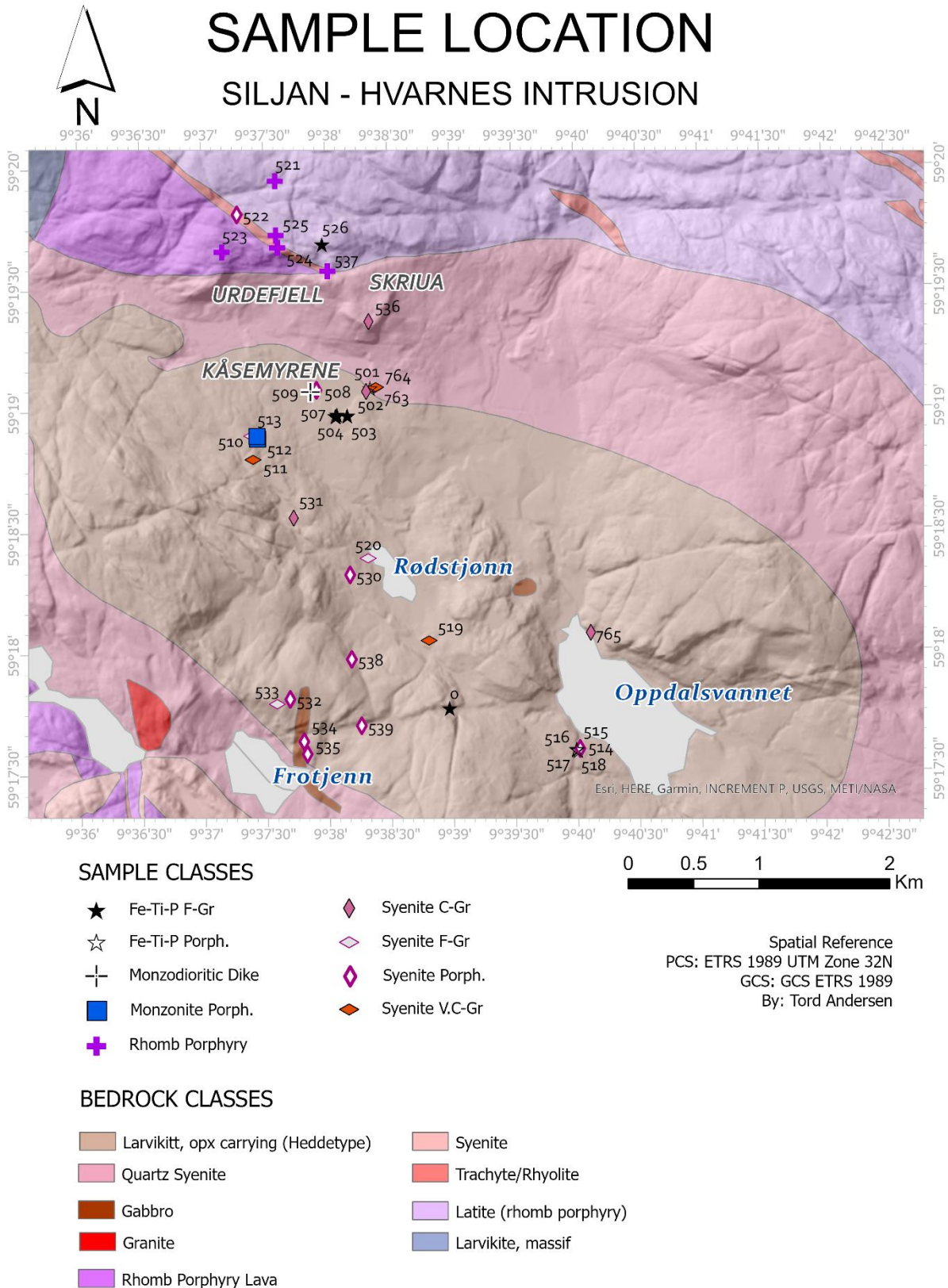


Figure 4-1: Sampling location presented with sample number and symbols representing rock class.

### 4.1.1 Rhomb porphyry

The Rhomb Porphyries studied in this thesis are found in the northern part of the field area. They are located north of Skriua and Urdefjell, topographically above the other observed rock types. The rhomb porphyry consists of a dark grey aphanitic matrix which contain feldspar phenocrysts usually between 1 and 2.5 cm. The rhomb porphyry consists of multiple approximately horizontally deposited lava flows showing both inter- and intra-textural variations. The phenocryst size and habit range from common 1- 2.5 cm rhomb-shaped to 7 cm blocky feldspars (Sample 525). In some outcrops feldspar are oriented and define a lineation of magmatic origin and the general phenocryst modality vary from 10% to 50%.

Thin sections of sample 111524 and 111525 show an aphanitic matrix with microlithic flow textures containing 40 – 50 modal % 1-2 cm large, rounded feldspar phenocrysts. The rounded phenocrysts show  $\mu\text{m}$ - scale embayment typical for resorption, dusty appearance and ubiquitous  $\mu\text{m}$  scale inclusions of biotite and opaque minerals. The matrix consists of < 50  $\mu\text{m}$  large prismatic minerals distributed as 20-30 modal% prismatic feldspar, 10 modal% biotite, 10 modal% dendritic titanomagnetite, 5 modal% pyroxene minerals, and < 1 modal% anhedral  $\sim$  100  $\mu\text{m}$  large apatite crystals. Dendritic triangular and cubic titanomagnetite in the size range 0,1 – 0,3 mm occurs sporadically in the matrix, often associated with mafic blebs of biotite and apatite.

The topographically lower sections of the rhomb porphyry series are intruded by fine – grained, red trachyte. The boundary of the intrusive syenite varies between angular and sharp to irregular and lobate (Figure 4-2 and Figure 4-3). Locally, 1-5 cm-wide irregular concentrations of Fe-Ti-P-rich minerals occur at the contact. The intrusion contains a 20 cm large rhomb porphyry xenolith showing internal network of red trachyte.



Figure 4-2: Field photograph of syenitic intrusion in rhomb porphyry sequence.



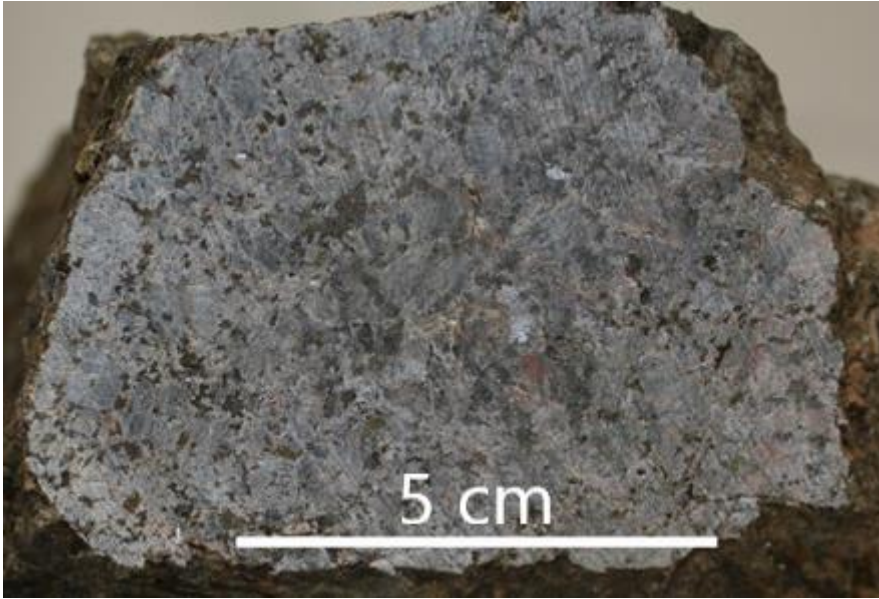
Figure 4-3: Sketch of trachytic syenite (red) intruded in rhomb porphyry (grey). Fe-Ti-P rich bleb and magma mingling in lower right corner of the picture.

#### 4.1.2 Medium to coarse-grained syenite

Medium to coarse-grained syenite (502, 516 A, 531 (Figure 4-4), 536, 765, 766 and 767) is found topographically below the rhomb porphyry in the northern part of the field area. It is also the most common rock type in the valley below Skriua and Urdefjell. The southern contact towards the superpositioned porphyritic syenites is located just south of Rødstjønn. The outcrops show varying degrees of weathering, from dominantly weathered pale feldspars with ghost enclaves of mafic minerals to fresh surfaces of reddish to grey feldspars. Veins in cm scale of fine-grained granite (Figure 4-5) and cm-scale miarolitic cavities are common in this lithology.

This rock is composed of 90 modal% ~ 1 cm long, subhedral feldspars of both orthoclase and anorthoclase, where anorthoclase is dominant. Antiperthitic textures are common in alkali feldspars, and the feldspars typically shares undulating intergrown boundaries. Interstitial pockets are filled with (1) quartz (1 to 10 modal%) occurs as anhedral crystals often filling angular spaces between feldspars, eventually forming oikocrysts when the modal percent of quartz reach more than 5%. (2) Mafic minerals consist mostly of brown to blue amphibole (~5 modal%), minor to accessory amounts of biotite, euhedral to rounded subhedral 1 mm large equant titanomagnetites. and 0,5 – 1 mm subhedral prismatic apatite. Euhedral 0,5 – 1 mm large zircons are found as a common accessory mineral in both interstitial phases. Amphiboles or occasionally biotite form oikocrysts in the interstitial mafic pockets, and usually show varying degrees of alteration.

The largest occurrences of Fe- Ti- P rich rocks are associated this rock-type. This is further discussed in the section "Key locations".



*Figure 4-4: Fresh cut of blue- grey medium to coarse grained syenite (Sample 531).*



*Figure 4-5: Slab photo of the sharp contact in sample 536 between orange medium grained syenite and fine-grained granitic/ quartz syenitic dike.*

### 4.1.3 Very coarse-grained syenite

Very coarse-grained syenite is observed at three different locations, at Søllandiene (511), along the road 50 m east of Kåsemyrene, and 500 m south, southeast of Rødstjønn (519). Figure 4-6 is provided to show textural variances in slabs, and Figure 4-7 depict a field photo of the 511 outcrop.

The very coarse-grained syenite consists of ~ 90 modal% subhedral feldspar in the size range 2 – 4 cm. The phenocrysts show varying degree of zonation with grey cores contains frequent inclusions, feldspar lamellae and a dusty appearance while the rims are red to pale grey between 1 to 3 mm wide. The highest degree of alteration is associated with neighbouring interstitial mafic minerals, while the least altered phenocrysts reveal iridescent shimmer. Locally, rims towards mafic minerals differs from the cores by lacking inclusions, appearing fresh and displaying albite twinning. Common inclusions in the phenocrysts are ~ 0,1- 0,3 mm large acicular apatite, ~0,25 mm wide rounded pyroxene, 0,1 mm large titanomagnetites and euhedral zircon. Interstitial pockets are dominantly filled with mafic minerals, however quartz is locally found as an accessory mineral. The mafic pockets contain various proportions of mafic minerals. Amphibole, biotite, ilmenite and titanomagnetites are most abundant, while apatite, olivine, augite, titanite and zircon are accessory minerals.

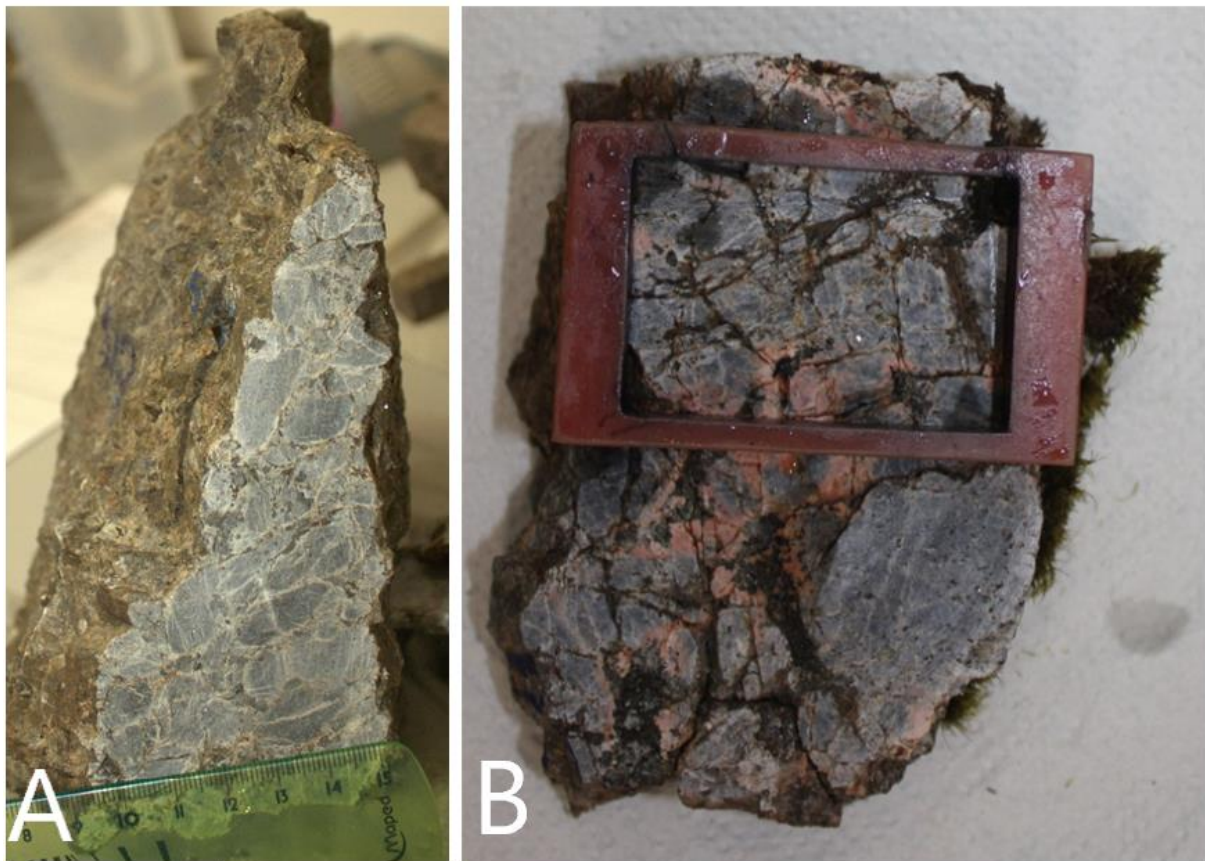


Figure 4-6: Slab photographs of the very coarse grained syenites. (A) The phenocrysts show pale, 1 mm thick rims (519). Ruler for scale. (B) Very coarse grained syenite with alteration of grey to red feldspar along boundaries to Fe-Ti-P rich interstitial blebs (511). Thin section outliner for scale.





*Figure 4-7: Field photograph of the very coarse- grained syenite (511). This outcrop is further described in Key locations – Søllandliene.*

Symplectites of biotite and quartz have formed in local mafic pockets associated with augite in sample 519. The latter appears dusty with partly resorbed edges and gradual transition to blue- green amphibole. Subhedral 0,1 – 0,2 mm apatite is found as inclusions in all mineral phases. Amphibole and biotite form oikocrysts and are the dominant mineral phases in the pockets. The contact between amphibole and biotite varies from gradual to sharp (Figure 4-8 and Figure 4-9).

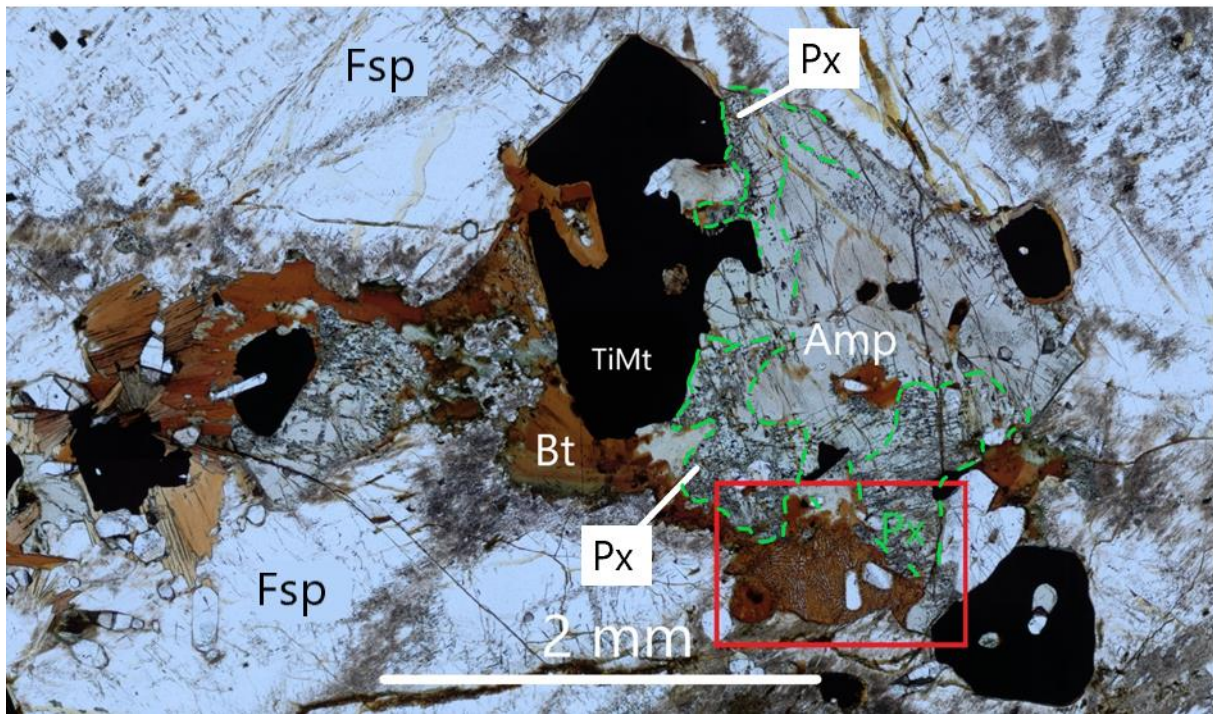


Figure 4-8: Photomicrograph (PPL, 5x magnification) of an interstitial mafic pocket in sample 519. The large mineral marked as amp (amphibole) contains local areas outlined with green dotted line. These patches contain heavily altered pyroxene with 90° cleavage and high relief.

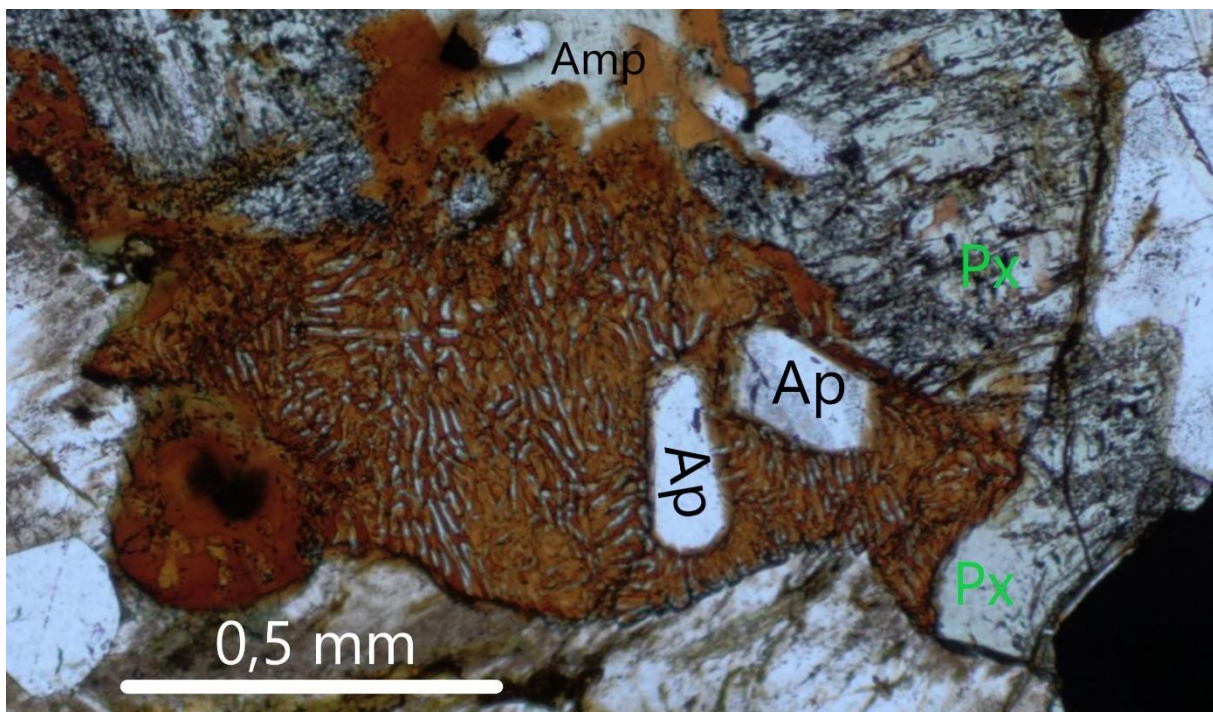
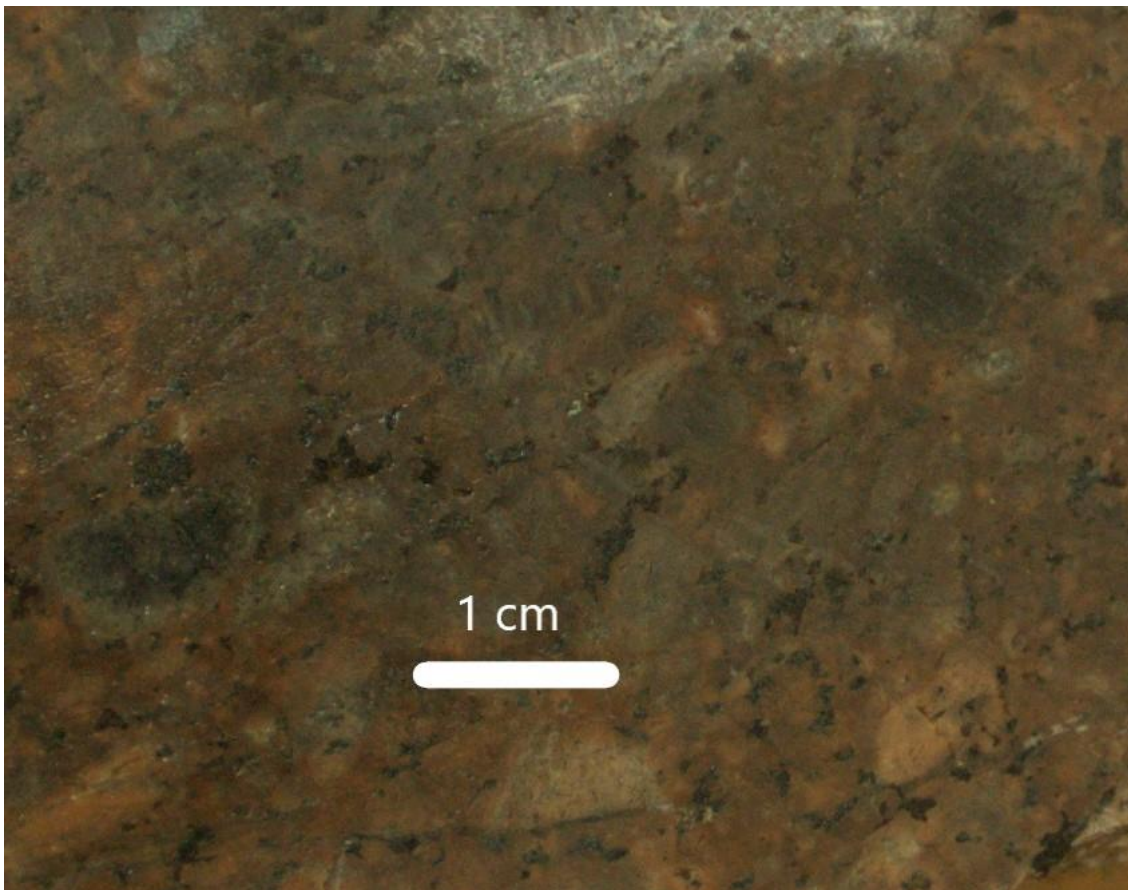


Figure 4-9: Photomicrograph of symplectitic texture of quartz and biotite (519).

#### 4.1.4 Porphyritic and trachytic syenite

Porphyritic syenite are located south of, and topographically higher than the coarse-grained syenite. It is characterized by 1- 3 cm-large blocky and rhombohedral feldspar phenocrysts, varying from 10-50 modal percent, and sparse megacrysts (>5 cm-large feldspars). Zoning in megacrysts is often visible in hand specimens. The porphyritic syenites show local variation of phenocryst size, and alignment, while the groundmass varies from fine- to medium-grained, and equant to trachytic. Elongated feldspars in the ground mass are also locally aligned with the phenocrysts. The ground mass consists of red, commonly 0,1-0,5 mm elongated feldspars surrounded by interstitial 0,1 mm-wide mafic mineral clusters containing apatite, amphibole, biotite and titanomagnetites. Quartz, the only Fe and Mg-free mineral that occurs in mafic mineral clusters, makes up 2 to 10% of the mode. Vesicles ~0,1 mm wide is also ubiquitous in the trachytic groundmass. This rock class have large variations in textures, which is illustrated in Figure 4-10, Figure 4-11, and Figure 4-12.



*Figure 4-10: Slab photograph of porphyritic syenite with rounded phenocrysts in a fine-grained ground mass (sample 539). The phenocrysts show different degree of alteration and zonation.*

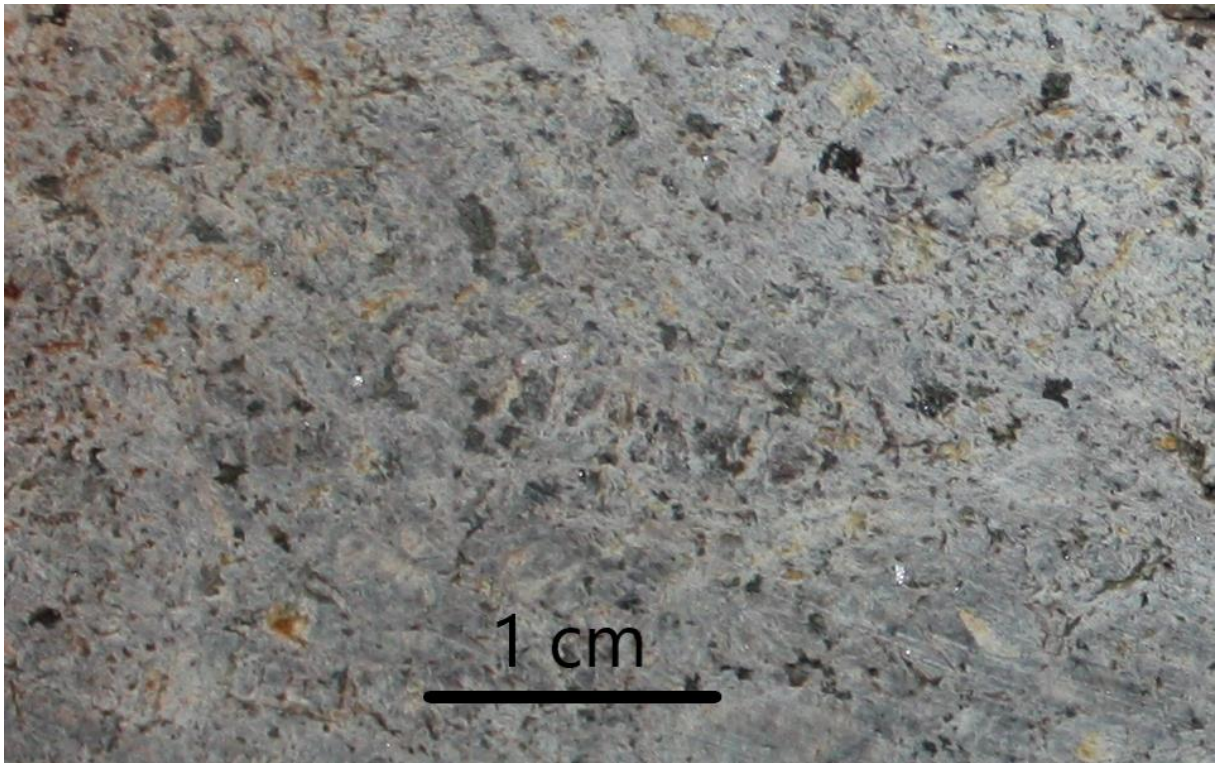


Figure 4-11: Slab photograph of pale grey feldspars with trachytic texture (sample 535).



Figure 4-12: Field photo of megacrysts in porphyritic syenite, close to sampling location for 538: blocky, zoned megacrysts up to 5 cm long in a red fine-grained groundmass. Note that the area on the left side of the pen has a higher modal% of phenocrysts compared to the right. Locally, in the same outcrop, feldspar phenocrysts are oriented (not on picture).

#### 4.1.5 Monzodioritic dikes

Several monzodioritic dikes cut through the coarse-grained syenite in the area west of Kåsemyrene mines (location for sample 509), and towards Sjøllandliene.

Sample 509 is from a 20 cm-wide aphanitic, mesocratic, monzodioritic dike cutting through a leucocratic coarse-grained syenite (Figure 4-13). Microphenocrysts occur as tabular 0,2 mm long chlorite pseudomorph (20 modal%) and elongated, dendritic pyrite with coating of hematite (1 modal%). The matrix is composed of 50 modal% of 0.002 mm-large, altered feldspar, 20 % 0,1 – 0,2 mm-large subhedral equant mafic crystals, and 10% titanomagnetite.

All monzodioritic dikes have sharp contacts with the host rock and consists of aphanitic homogeneous rock. The location of 509 display a 40 cm long lateral displacement of the dike. The displacement, illustrated in the photo below (Figure 4-14), shows a clean cut with brittle fracturing in the most adjacent parts of the dike. The host rock, however, show little to nonbrittle fracturing, with a band of leucocratic melt in between the cut dike.



*Figure 4-13: Field photo of location/ sample 509, monzodioritic dike cutting through coarse-grained syenite. The dike shows a lateral displacement and brittle fracturing, while the hosting syenite only shows minor signs of deformation through shear forces. Camera lens cap for scale.*



Figure 4-14: Sketch of location/ sample 509, outlined monzodioritic dike cutting through coarse grained syenite. Also outlined are patches of leucocratic rock between the split dike.

#### 4.1.6 Quartz syenitic dike

Syenitic dikes are encountered in the entire field area (Bright pink rock in Figure 4-18). The width of the dikes varies from dm to m scale showing relatively sharp contacts to the host rock (Figure 4-5). Local areas contain mm and cm scale networks where the syenite have penetrated deeper into the host rock. The rock forming minerals are commonly 1 - 2 cm large subhedral feldspar phenocrysts in an equigranular, fine- to medium-grained ground mass. Sample 520 (50 m west of Rødstjønn, see "Key Location 520") represents the remains of a fine-grained syenitic intrusion with a dip- direction/ dip of 065/58:

The groundmass consists of 70 – 80 modal% 0,3-0,5 mm dusty equigranular subhedral feldspars. Alkali feldspars show microcline twinning and perthitic textures while oligoclase show Carlsbad- and Albite twinning. Intergrowth textures in feldspar – feldspar boundaries are common. Quartz modal% ranges from 10 – 20% and form anhedral crystals filling angular spaces between feldspars. Seemingly disconnected crystals sharing same extinction angles reveal quartz occurs as 0,5 mm large oikocrysts. Mafic minerals occur in 0,5 mm clusters. Biotite (1 to 2 % of the rock), form anhedral to interstitial crystals between 0,2 – 0,5 mm, and more rarely oikocrysts up to 1,5 mm. A majority of the biotite grains show local alterations towards green biotite. Ilmenite and titanomagnetite occur as 0,05 – 0,5 subhedral crystals and constitute 1 to 2 % of the rock.. Apatite, titanite, pyrite and zircon occur as accessory minerals, where apatite and zircon form euhedral to subhedral 0,2 – 0,4 mm crystals, while titanite form up to 2 mm large, heavily altered crystals.

#### 4.1.7 Fe- Ti-P rich rock

Iron- Ti- P-rich rocks are melanocratic rocks that display equigranular fine- to medium-grained textures. They occur as cm-scale veins, cm to dm patches or m-scale massive concentrations. All are associated with a syenitic host rock. Centimetre-scale veins and clusters of Fe- Ti-P-rich rocks are ubiquitous throughout the coarse-grained syenite and in mingling zones further described below. Larger, m- scale deposits studied in this thesis have been partially or fully mined and is often overgrown by dense vegetation. Larger outcrops reveal a gradual transition from syenitic rock to the pure Fe-Ti-P ore (Figure 4-15 and Figure 4-19). This zone commonly consists of weakly oriented 0,5 – 2 cm large feldspar phenocrysts in a fine-grained Fe-Ti-P groundmass. The large occurrences are associated with magma mingling and mixing of coarse-grained syenite or porphyritic syenite, +/- fine-grained syenite, +/- rhomb porphyry, and +/- very coarse-grained syenite. (See section "Key Locations").

Fe-Ti-P ore consists of 20- 50 modal% anhedral, 0,5 – 2 mm embayed augite containing inclusions of ilmenite, titanomagnetites and apatite. Ilmenite and titanomagnetite represent 20-30 modal% and occupy interstitial positions. 0,5 – 2 mm subhedral to interstitial biotite make up 1-40 modal% and commonly contains inclusions of amphibole and Fe-Ti oxides. Pyroxene is an accessory mineral and occur as 0,5 mm rounded grains commonly with reaction rims. Homogeneous Fe-Ti-P rich rock is depicted in Figure 4-16. Grains with an orientation that show the basal cleavage often exposes hematite exsolution lamella. Samples containing small amount of biotite are often rich in pargasite (a Ti- Ca rich amphibole), which reach up to 30 modal%, instead. Pargasite form anhedral to interstitial grains containing frequent inclusions of apatite and oxides. Apatite represents 5 – 20 modal% and occur as 0,05 – 0,2 mm acicular inclusions mainly in pyroxene and feldspar, and as 0,1 – 1 mm subhedral to euhedral crystals or aggregates. Some grains are zoned and contain  $\mu\text{m}$ -scale inclusions of fluids and oxides. Allanite (?), monazite, pyrite, titanite and zircon occur as accessory minerals.



Figure 4-15: This sample (403) from Kåsemyrene displays the relationship between massive Fe-Ti-P ore and pale feldspar phenocrysts. Rectangles are outlines for thin sections. Thin section B (middle) is presented in result section "mineral analysis".

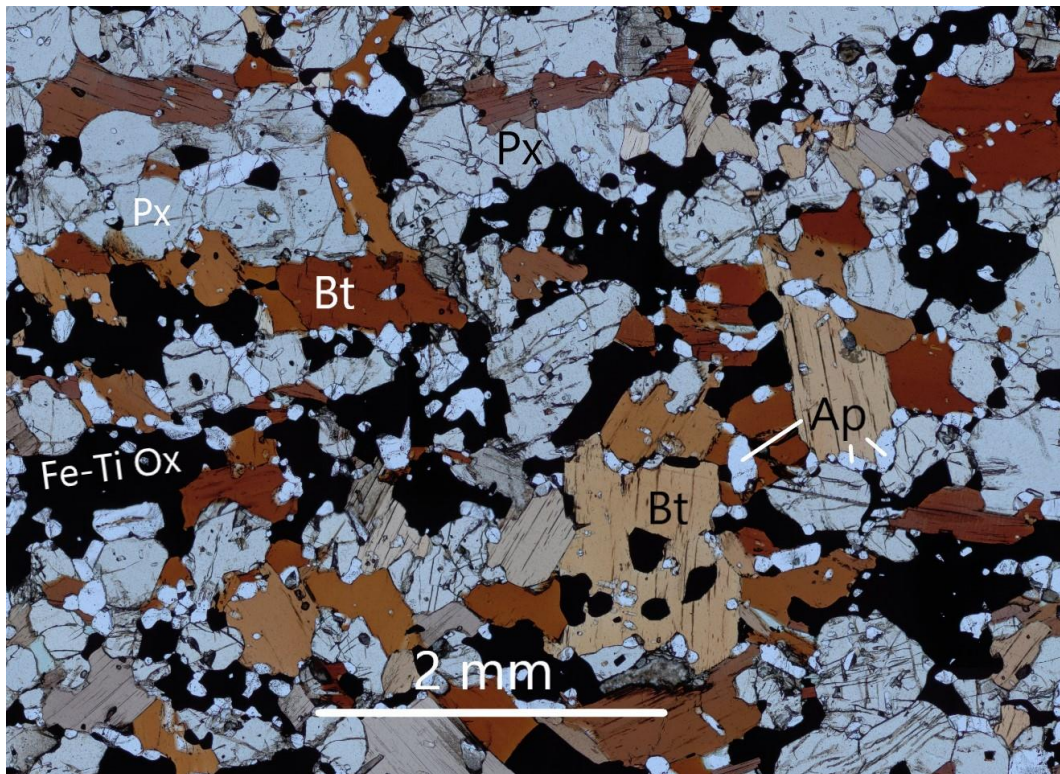


Figure 4-16: Thin section photomicrograph of sample 759 from Eastern mine pit, Kåsemyrene. Texture of medium grained Fe-Ti-P rich rock.

Feldspar occurs either as phenocrysts in the porphyritic Fe-Ti-P rich rock or more rarely as anhedral to interstitial 0,5 – 2 mm large grains associated with the porphyritic Fe-Ti-P rich rock. The phenocrysts are dominantly 0,5 – 2 cm alkali feldspars with exsolution lamellae and ubiquitous inclusions of 0,05 – 0,5 mm large apatite, biotite, pyroxene, and oxides. The grain boundaries to the mafic minerals are undulating with frequent embayment containing oxides and biotite. Some phenocrysts contain rounded cores with rims sharing the same attributes as the previously described phenocrysts (Figure 4-17 and Figure 4-44).



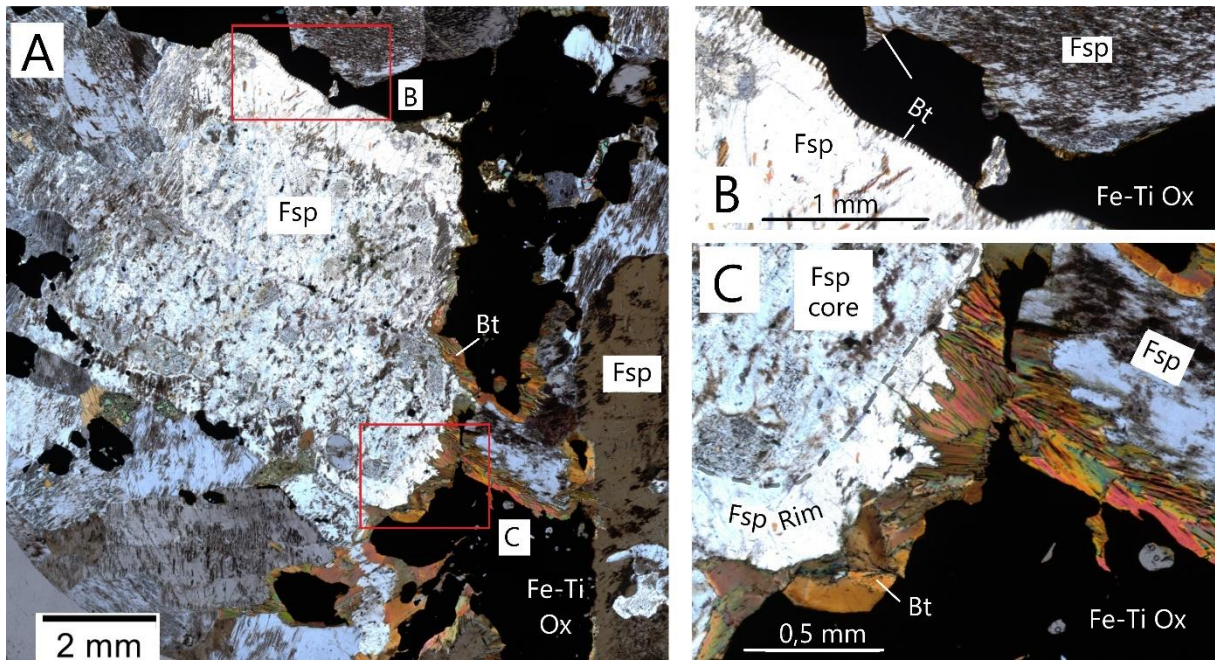


Figure 4-17: Intergrowth textures between biotite and feldspar, porphyritic Fe-Ti-P rich rock from Eiriks Gruve. 5x magnified, scanned XPL image of thin section 517.

Sample 517 from Eiriks gruve represent a transitional gradient of Fe-Ti-P rich rock into a coarse grained syenite. The alkali-feldspar in center of (A) have formed simple Carlsbad twins and the core is visibly "dusty". The core has a fresh rim with only minor amounts of inclusions of acicular biotite (B). The biotite is further observed growing radially from the Fe-Ti oxides and into the rim, creating 0,05 – 0,1 mm long needles. Figure (C) depict a 0,2-0,4 mm thick continuous rim of biotite between the felspar and Fe-Ti oxides. The growth pattern of the biotite occurs as both as penetrating into the feldspar rim, and as anhedral- interstitial.

## 4.2 Key locations

### 4.2.1 Location 520:

Location 520 is a 5 m wide, 2 m-high road cut along the road west of Rødstjønn, in the area of the expected contact between coarse grained syenite and porphyritic syenite (Figure 4-18 and Figure 4-19). Lower left close up in Figure 4-19 depict the sharp lower concave contact between Fe-Ti-P rich rock and coarse grained syenite, and the upwards transition from fine- grained Fe-Ti-P ore to a porphyritic rock with feldspar phenocrysts and fine-grained Fe-Ti-P groundmass. The fine-grained Fe-Ti-P-rich rock contains fine grained syenitic bands, ~1 cm thick which follows semi- parallel to the sharp lower contact. 20 – 40 cm above the contact (partly out of the picture) grey iridescent blocky feldspar phenocrysts to megacrysts (1- 5 cm) are weakly oriented. Figure 4-19 top right close up depicts the dipping contact where the fine-grained Fe-Ti-P rich-rock is reduced to a patchy 1 cm layer, and the phenocrysts making up 50 – 70 modal% are aligned with the dip-direction.



*Figure 4-18: Key location 520, 50m west of Rødstjønn revealing accumulation of Fe-Ti-P mineralization associated with local flow textures of feldspar phenocrysts.*

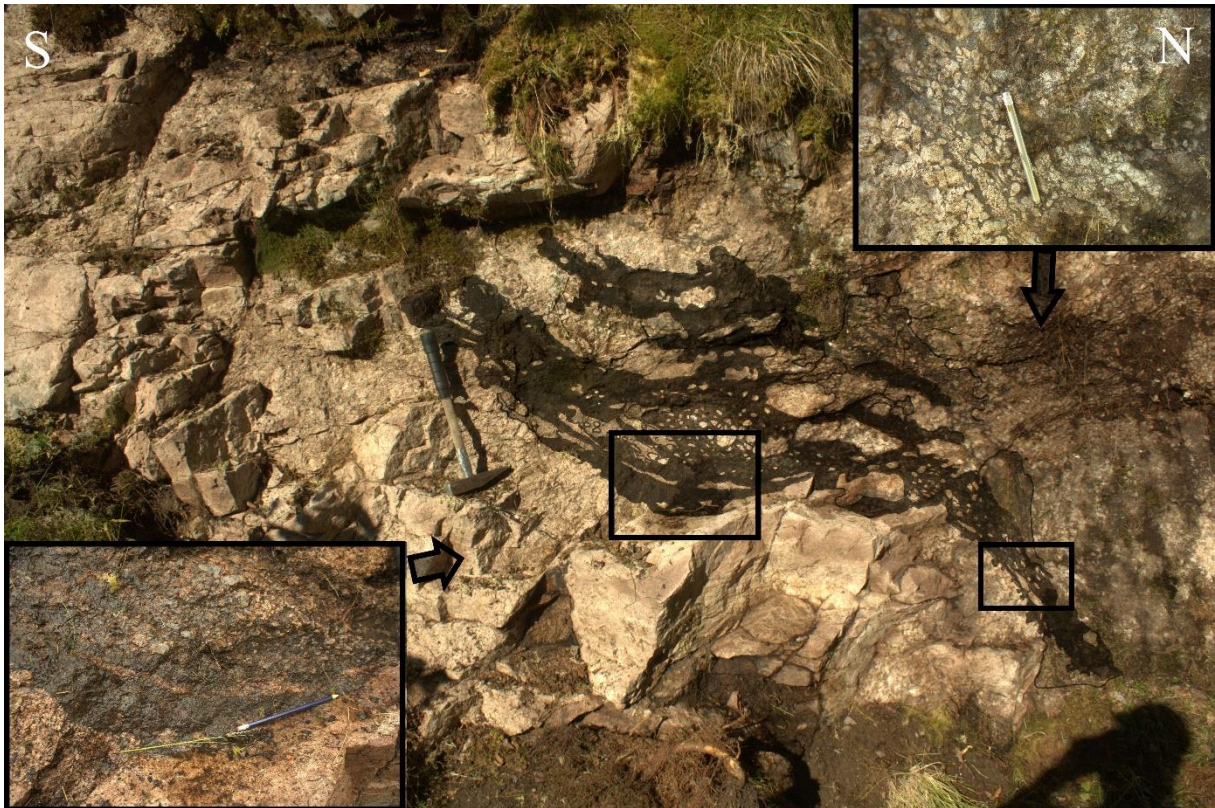


Figure 4-19: Enhanced colouring of Fe-Ti-P rich rock in coarse grained syenitic host rock, Key-Location 520. Left close- up picture emphasizes the sharp lower contact and gradual increase of feldspar phenocrysts upwards. Right close- up emphasizes the alignment of the phenocrysts. Note hammer for scale in large picture and pencil in close- up photos.

## 4.2.2 Kåsemyrene

The area around Kåsemyrene are heavily vegetated and good outcrops are far and few between. Three outcrops with mixing, mingling and Fe-Ti-P rich rocks have been located, namely the "parking location", a cliff and the two mine-pits (Figure 4-20: Map over the described locations related to Kåsemyrene .Figure 4-20).

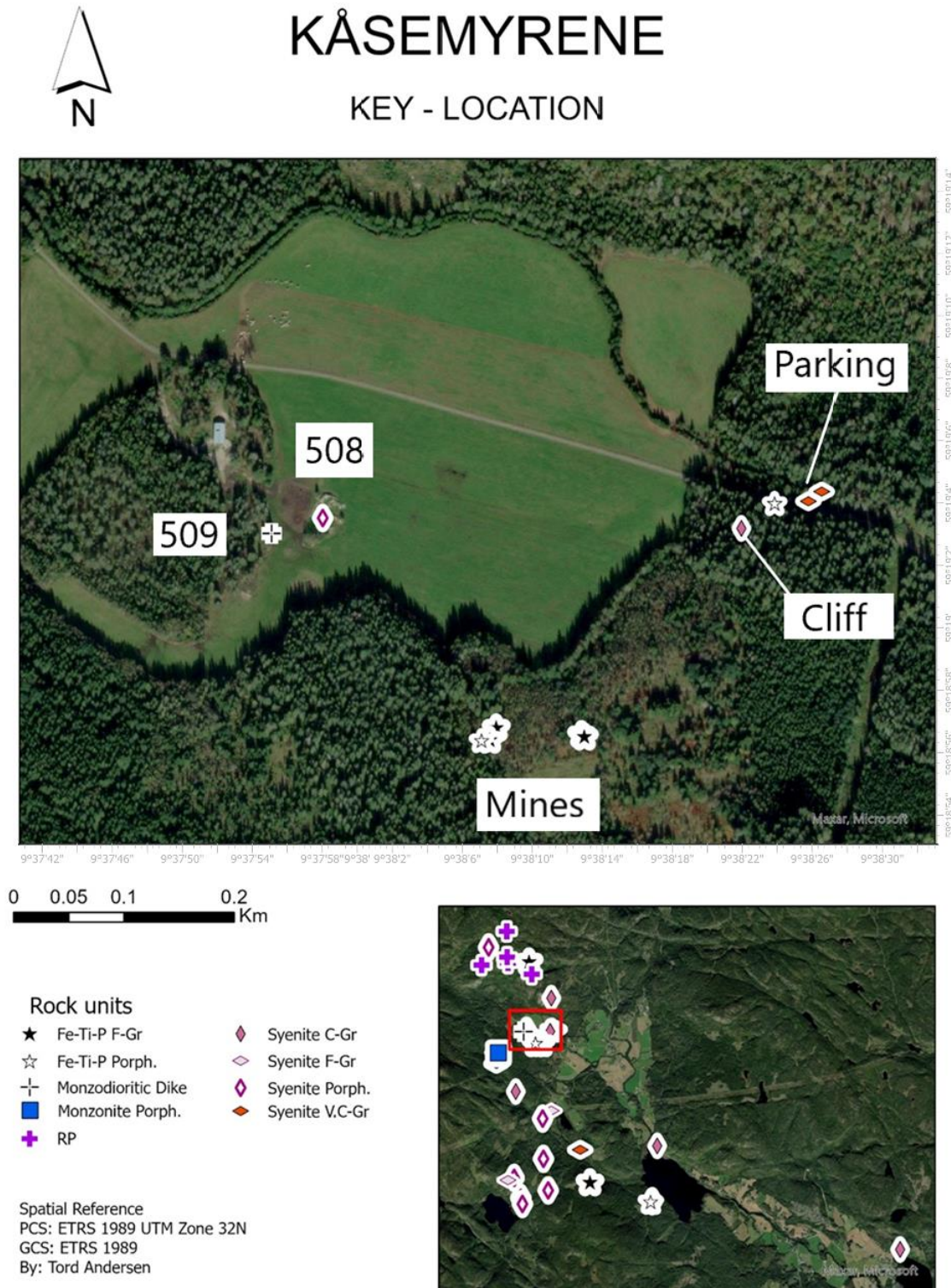


Figure 4-20: Map over the described locations related to Kåsemyrene .

#### 4.2.2.1 Kåsemyrene – Parking

The “parking location” consists of several m wide outcrops of the bed rock. Figure 4-21 (A) depicts mingling of at least three magmas; fine grained syenite, very-coarse grained syenite, very coarse grained syenite with up to 5 cm megacrysts, and mafic melt occurring as patches. The mafic melt has semi sharp contact to the fine grained syenite and a more transitional contact to the very coarse- grained syenite. Figure 4-21 (B) depicts an outcrop 5 m to the south consisting of a porphyritic syenite with a fine- grained matrix and 0,5 – 2 cm long weakly rounded phenocrysts.

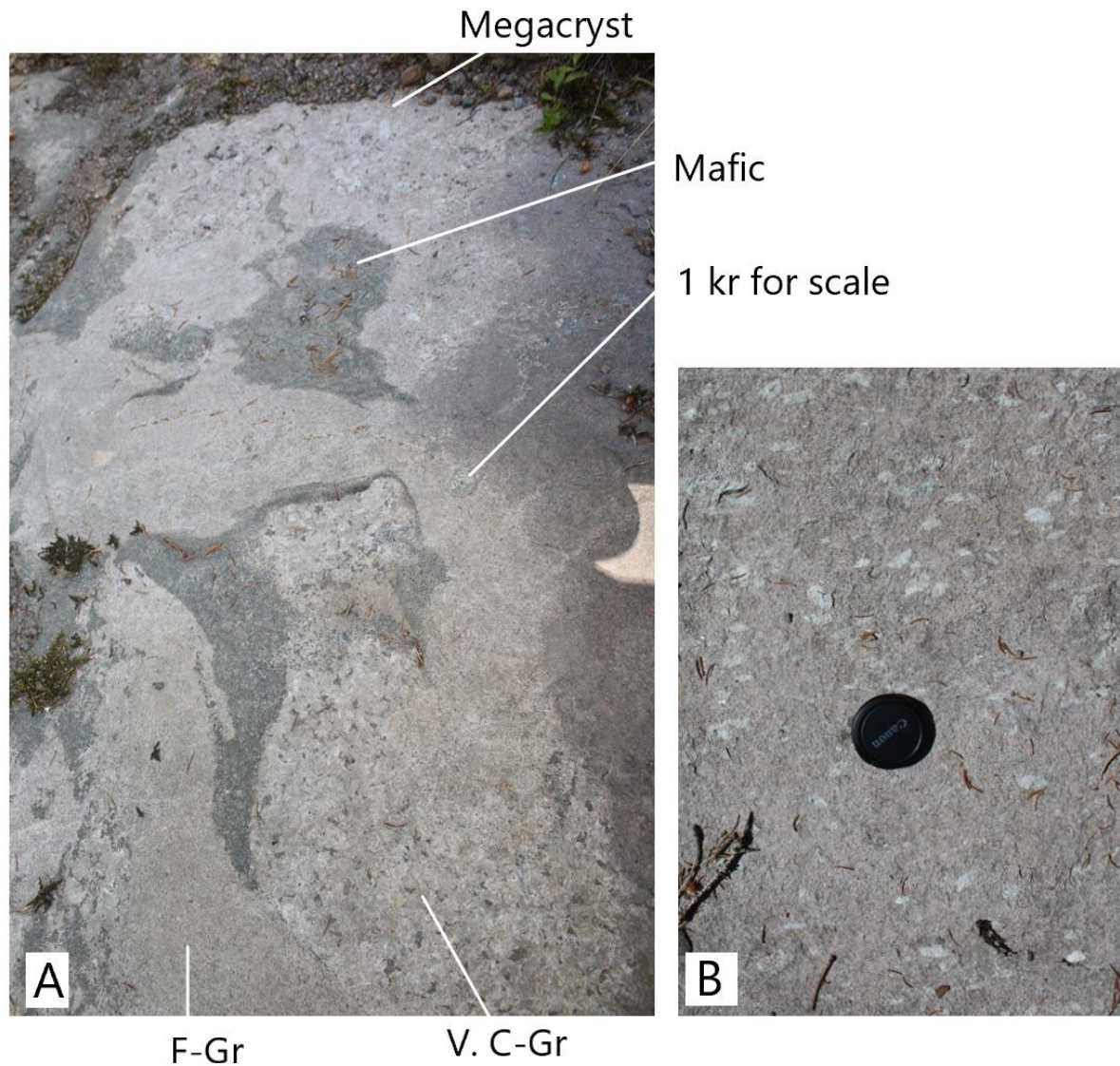


Figure 4-21: Field photo of outcrop "Kåsemyrene Parking". 1 Kr coin and camera lens cap for scale

Thin section 536 (Figure 4-22) is collected from an outcrop 15 m east for the parking, at the riverbank. The thin section shows a sharp contact between fine grained lower mafic section and the upper coarse grained syenite. The transparent vein cutting the syenite consists mainly of quartz but does also contain ~ 0,5 mm crystals of euhedral carbonatite. The following thin section description applies solely to the mafic section, and the occurrence of minerals are modal %. The mafic section contains 5% euhedral 0,5 – 1,5 mm long zircon crystals. Amphibole occurs as subhedral pale- brown to blue-green crystals (30%). Feldspar crystals are anhedral to interstitial (20%). Other interstitial phases are quartz (20%) and sphene (5%), which both locally form oikocrysts up to 2 mm long. 0,05 – 0,5 mm long subhedral apatite is found as a minor phase. 0,5 – 1 mm large sub- to euhedral oxides make up 20%.

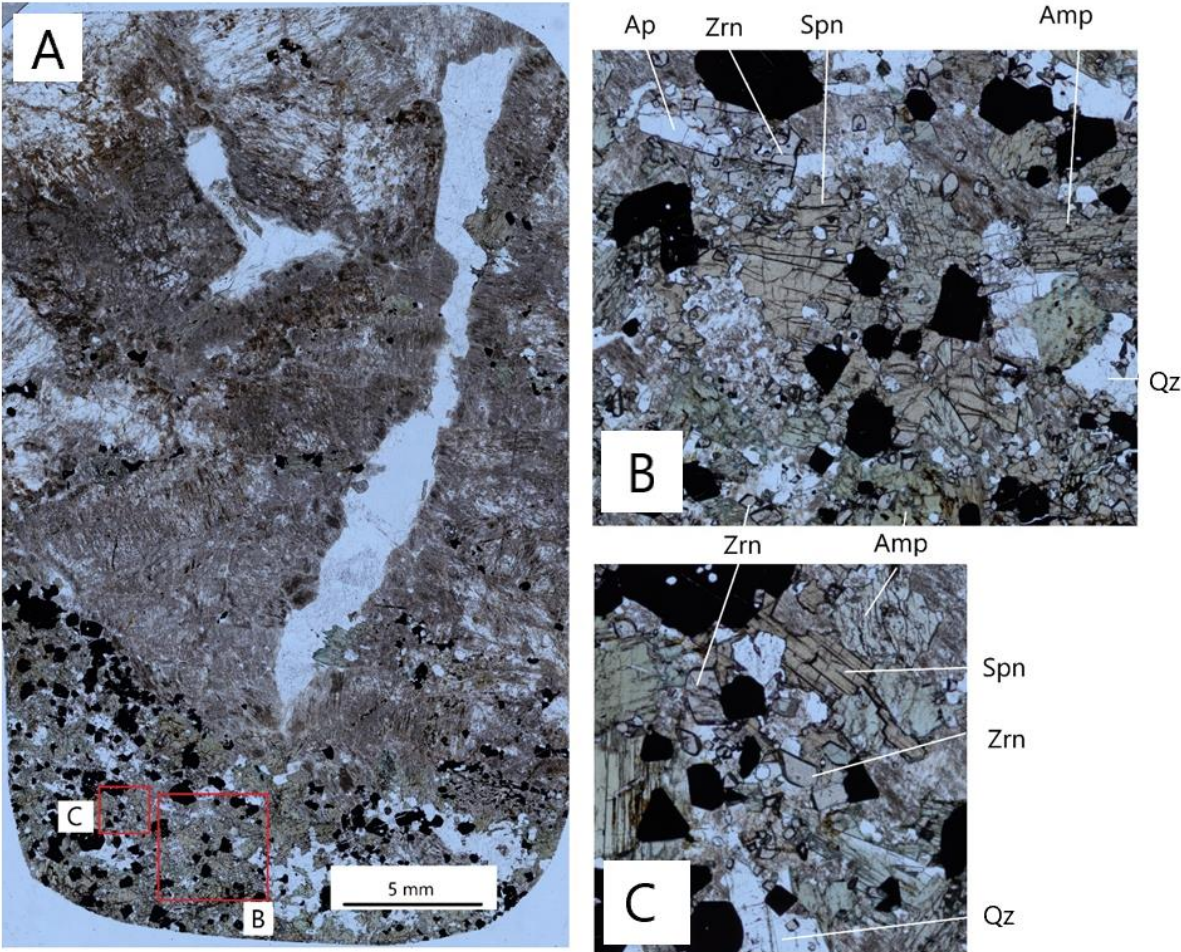


Figure 4-22: PPL scan of thin section 763A with 5x magnification.

#### 4.2.2.2 Kåsemyrene – Cliff

The “Kåsemyrene cliff” is a vertical 15 m long and up to 2 m high moderately overgrown outcrop oriented northeast- southwest. Several rocks occur with mingling and mixing textures, among them fine-grained syenite, coarse-grained syenite, porphyritic Fe-Ti-P rich rock (picture below), and a porphyritic rock consisting of up to 3 cm rhombohedral phenocrysts, some with swallow-tail twinning in a fine-grained groundmass (Appendix, figure swallowtail). All figures below depict porphyritic Fe-Ti-P rich rock with weak to moderate orientation of feldspar phenocrysts.

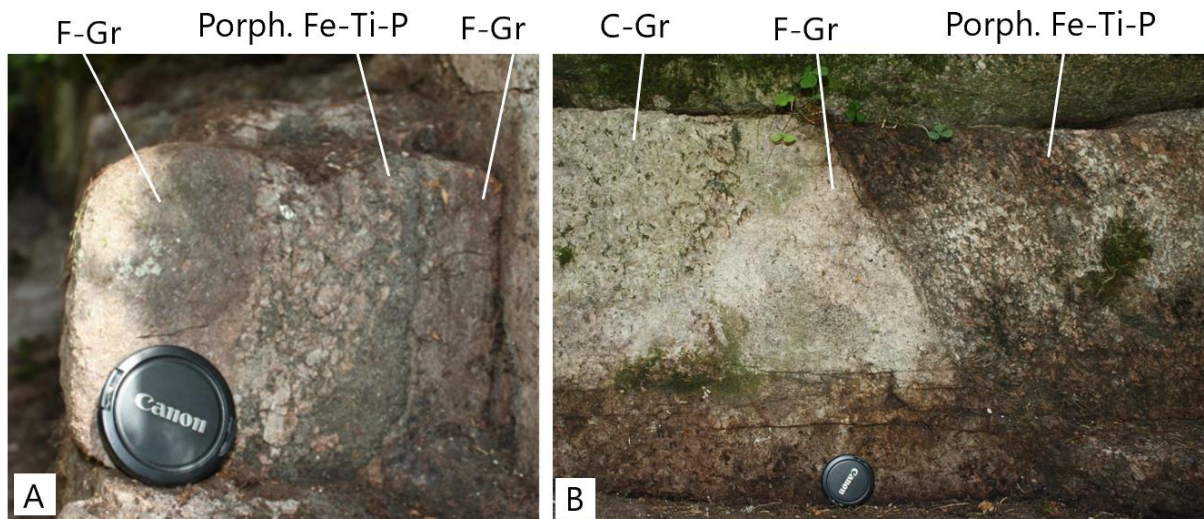


Figure 4-23: Field photographs from Key- location “Kåsemyrene Cliff”. (A) porphyritic Fe-Ti-P with sharp contact to fine grained syenite. (B) Fine- grained syenite separating coarse grained syenite and porphyritic Fe-Ti-P rich rock. Lens cap for scale.

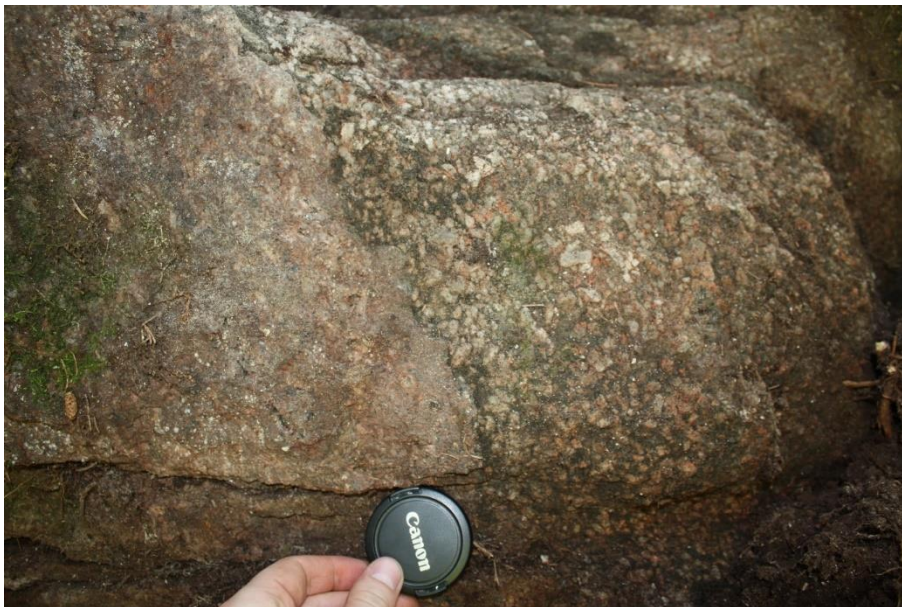


Figure 4-24: Close up field photo of contact between fine-grained syenite and porphyritic Fe-Ti-P rich rock. The contact irregular and sharp. Lens cap as scale.

#### 4.2.2.3 Kåsemyrene mines

The Kåsemyrene mines are heavily overgrown and filled with debris, illustrated with Figure 4-25 and Figure 4-26. The pits are approximately 80 m apart. The wall rocks of both mines consist mainly of fine-grained Fe-Ti-P rich rock with local porphyritic patches with 0,5 – 2 cm rounded feldspar phenocrysts.



Figure 4-25: Field photograph of the western mine-pit at Kåsemyrene. Depth in picture is deceiving, and the pit is 4 m long, 2 m wide and 1,5 m deep.



Figure 4-26: Field photo of the eastern mine-pit at Kåsemyrene. Depth in picture is deceiving, and the pit is 4 m long, 4 m wide and 2 m deep.



### 4.2.3 Søllandliene

The 4 m high overhang outcrop in Søllandliene (Map: Figure 4-27) depicts an enigmatic mixing and mingling pattern. Figure 4-31 and Figure 4-32 depict magma mixing, mingling and veins of Fe-Ti-P rich melt. Figure 4-28 represent a view towards northwest, and three lithologies stand out as layers (left to right): Very coarse-grained rock consisting of 2-4 cm grey megacrysts with developed red rims Figure 4-6 B. The coarse-grained rock shares an irregular contact with the second layer (Figure 4-30). The second layer appearing as a 20-40 cm wide fine-grained quartz monzonite consisting of ~20 modal% mafic minerals, and third, the trachytic to porphyritic monzonite with 20 -30 modal% 0,5-2 cm long, zoned, and rounded ternary feldspar phenocrysts in a fine-grained grey groundmass majorly consisting of feldspar and plagioclase. Apatite, biotite, brown amphiboles, and oxides occur as minor phases while zircon is an accessory mineral (Figure 4-29).

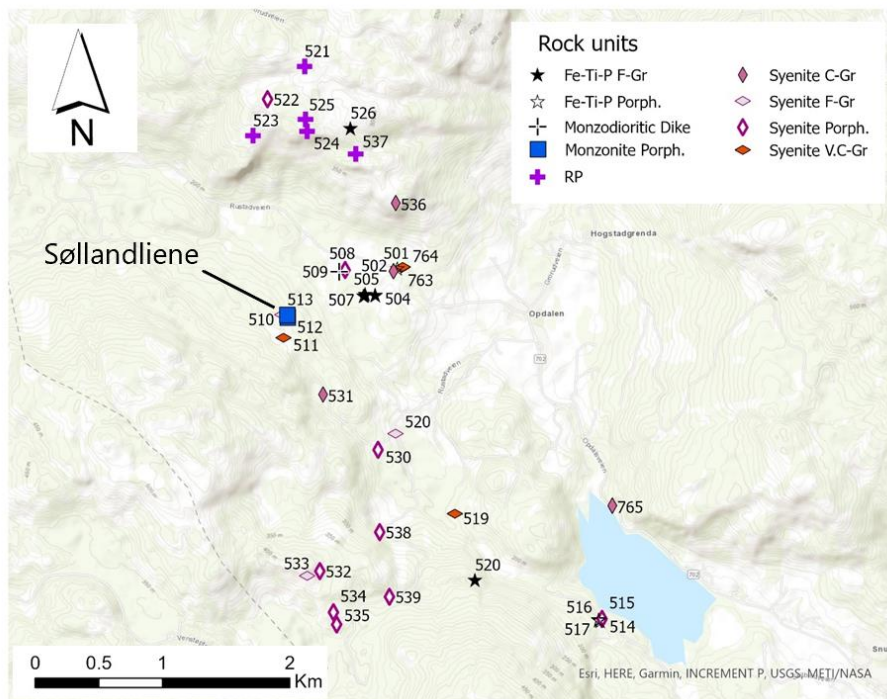


Figure 4-27: (map Søllandliene): Søllandliene are represented with samples 510, 511, 512 and 513.

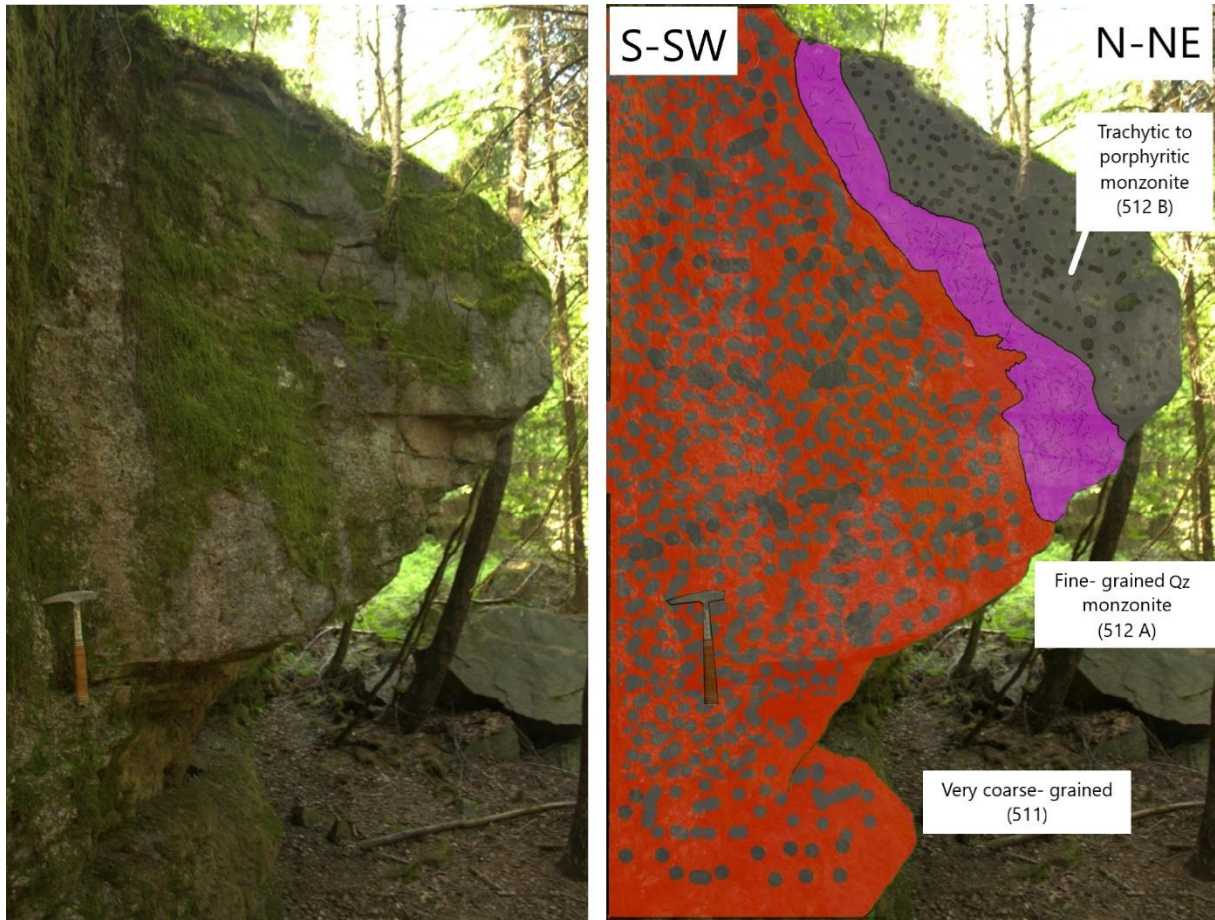


Figure 4-28: Field photo and sketch of the outcrop at Key-location Søllandliene. Sketch emphasises lithologies. Hammer for scale.



Figure 4-29: Slab photo of trachytic to porphyritic monzonite (512 B).



Figure 4-30: Field photo of lithological contact between very coarse-grained syenite and fine-grained trachyte.

The immediate back side of the outcrop does not show the same layering. Here, the very coarse-grained rock appears as a 1,5 m wide rectangular body situated in the grey trachytic to porphyritic monzonite. A cm scale layer of fine-grained quartz monzonite envelopes the coarse-grained body, which are seen radiate out in the lower left corner of the rectangular body and penetrates the porphyritic monzonite (Figure 4-31). The fine-grained quartz monzonite has an irregular contact with the coarse-grained rock and is observed creating a fine-grained network between the megacrysts.

A mingling magma with rhombohedral phenocrysts is recognized in the top of the picture. It shows an irregular contact with the trachytic monzonite. A 15 cm wide patch of the same lithology is observed (Figure 4-33) with a transitional increase in mafic composition (from 5 to 50 modal%). Additionally, a Fe-Ti-P rich vein is situated on the boundary between the lowermost layer of coarse-grained rock and the over-lying fine-grained quartz monzonite, depicted in Figure 4-34.



Figure 4-31: (backside) Field photo of the opposite side of the outcrop at Sjølandliene. Viewed from SW towards NE. Hammer for scale.

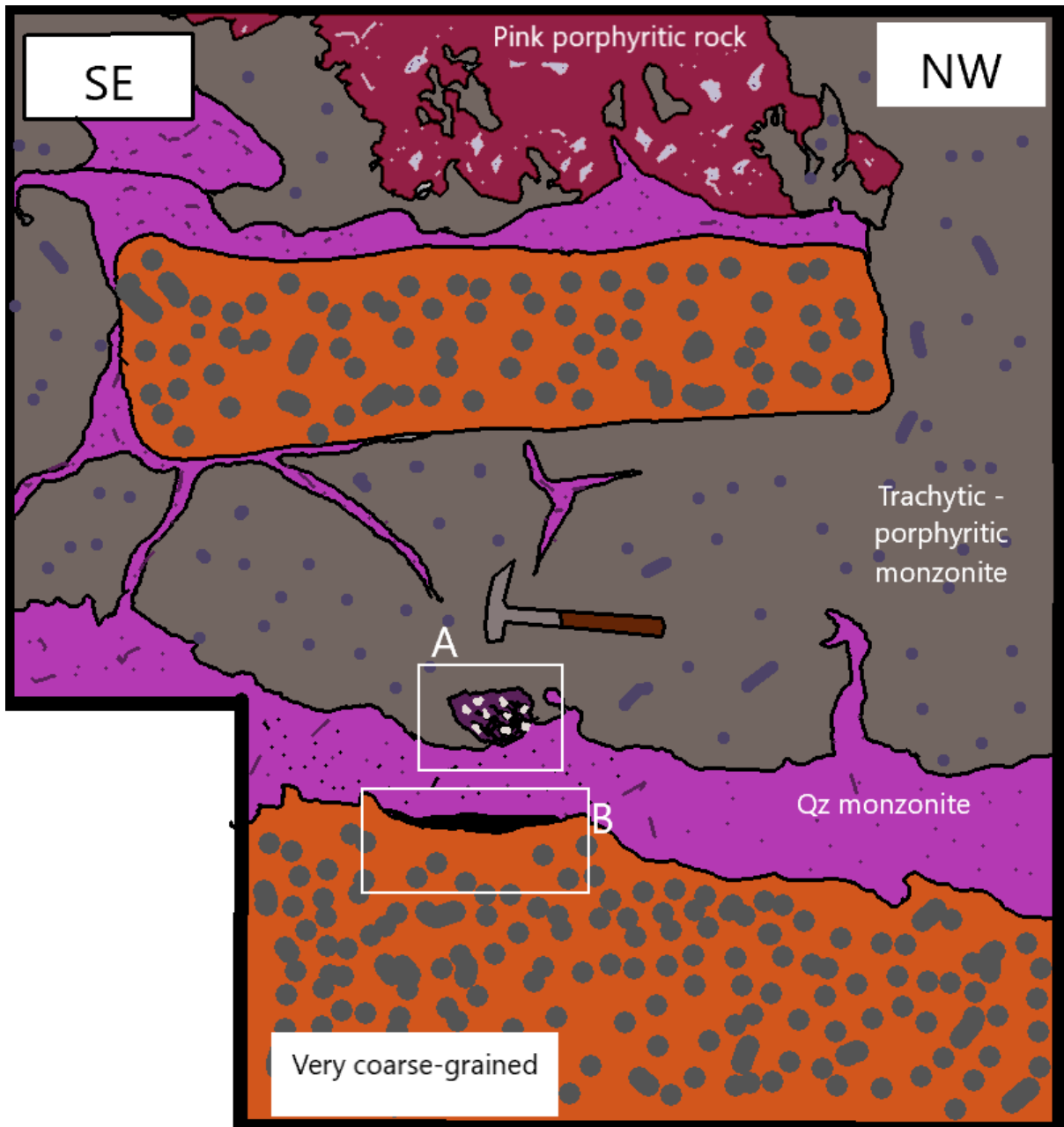


Figure 4-32: Schematic illustration of the lithologies based on Figure 4-31. Rectangle A is depicted in Figure 4-33, and rectangle B of Figure 4-34.



*Figure 4-33: Accumulation of mafic minerals in a mingling melt consisting of ~20% rhombohedral phenocrysts.*



*Figure 4-34: (Vein) Fe-Ti-P rich vein on contact between coarse grained rock and fine-grained trachytic quartz-monzonite.*

## 4.3 Geochemical Analyses

### 4.3.1 Whole Rock Analyses

Bulk rock chemistry analyses were conducted on the following samples: 759, 760, 761, 764, 765, 766 and 767 from the 2019 field season, and 501, 502, 503, 505, 507, 508, 509, 510, 512 A, 512 B, 513, 514, 515, 516 A, 516 B, 517, 518, 519, 520, 525, 526, 531, 534, 535, 536, 538, and 539 from the 2020 field season. The 2019 samples were analysed at NGU for major and trace elements, where major element analysis was conducted with XRF and trace element analysis XRF and LA-ICP-MS. The 2020 samples were analysed with XRF at NTNU for major and trace elements, and an additional trace element analysis were outsourced and conducted with ICP by ALS in Sweden.

Major oxide analysis comprises of Al<sub>2</sub>O<sub>3</sub>, BaO, CaO, Cr<sub>2</sub>O<sub>3</sub>, CuO, Fe<sub>2</sub>O<sub>3</sub>, FeO, HfO<sub>2</sub>, K<sub>2</sub>O, MgO, Mn<sub>3</sub>O<sub>4</sub>, Na<sub>2</sub>O, NiO, P<sub>2</sub>O<sub>5</sub>, PbO, SiO<sub>2</sub>, SO<sub>3</sub>, SrO, TiO<sub>2</sub>, V<sub>2</sub>O<sub>5</sub>, ZnO, and ZrO<sub>2</sub>, and are measured in wt.% (APPNDIX C). Samples of Fe-Ti-P rich rock have generally a negative LOI, attributed to oxidation of iron oxides. Sample 509 have a LOI of 3,071%, and an additional run were conducted to rule out user errors. The sum of major oxides is between 97,8 and 98,9 for sample 516 A, 535, 759, 760, 764, and 766. These samples are generally rich in trace elements and adding trace elements to the total sum raises all samples above 99,0. All other samples has an acceptable sum between 99,0% and 100,3.

The 2019 NGU LA-ICP-S bulk analysis consists of REEs, Be, Bi, Cs, Y, Zr, Nb, Ba, Hf, Ta, Th, U and W. Results are presented in Appendix D where red values represent analytes plotting outside the calibration range. These values are mainly REE concentrations in Fe-Ti-P rich rock higher than the calibration range. 2019 NGU XRF trace element analysis consisted of Ag, As\*, Ba\*, Cd, Ce\*, Co\*, Cr\*, Cu\*, Ga\*, La\*, Mo\*, Nb\*, Nd\*, Ni\*, Pb\*, Rb\*, Sb, Sc\*, Sn\*, Sr\*, Th\*, U\*, V\*, Y\*, Zn\*, Zr\*, Cl, F, S and Hf. Asterisk signify accredited parameters. Note all elements are measured in ppm except for C, F and S which is presented in wt.%. Note that Cerium content in sample 759 and 760 were higher than the calibration range.

Samples from 2020 were analysed at with ICP at ALS, Sweden for the elements Ba, Ce, Cr, Cs, Dy, Er, Eu, Ga, Gd, Hf, Ho, La, Lu, Nb, Nd, Pr, Rb, Sm, Sn, Sr, Ta, Tb, Th, Tm, U, V, W, Y, Yb, Zr. An additional XRF trace element analysis was conducted at NTNU where Sc, V, Cr, Mn, Co, Ni, Cu, Zn, Ga, Ge, As, Se, Br, Rb, Sr, Y, Zr, Nb, Mo, Ag, Cd, Sn, Sb, Te, I, Cs, Ba, La, Ce, Nd, Sm, Yb, Hf, Ta, W, Tl, Pb, Bi, Th, and U were measured. For those elements which overlap between the XRF and ICP analyses, ICP were preferred due to the higher accuracy in the measurements.

#### 4.3.1.1 TAS diagram

Figure 4-35 represent the first step of creating a chemically based classification, which is the modified total Alkali vs Silica (TAS) developed by (BAS et al., 1986) and modified by (Middlemost, 1994). Most of the samples from the Siljan pluton plots as syenites. The porphyritic monzonites and the syenites, form a positive semi-continuous trend from a SiO<sub>2</sub> content of 58 to 66 wt.% (except for the fine grained syenites and quartz monzonite). The fine-grained quartz syenites plot on the boundary to granite at ~ 69 wt.% SiO<sub>2</sub> and a relatively low alkali value of 10 wt.% compared to the most evolved coarse-grained syenite at ~12 wt.%. The rhomb porphyry plot on the silica undersaturated side as foid-monzosyenite, while the monzodiorite is barely silica-saturated. Note that the Porphyritic Fe-Ti-P plot as a foid-gabbro, but this is purposely not applied as a rock name (This is explained in section 5.1.8.1.2 Geochemical Indicators for Silicate Liquid Immiscibility, page 116). The homogeneous fine to medium- grained Fe-Ti-P rich rock has a SiO<sub>2</sub> content between 20 and 30 wt.%, and plots therefore outside the TAS and granitoid classification diagrams.

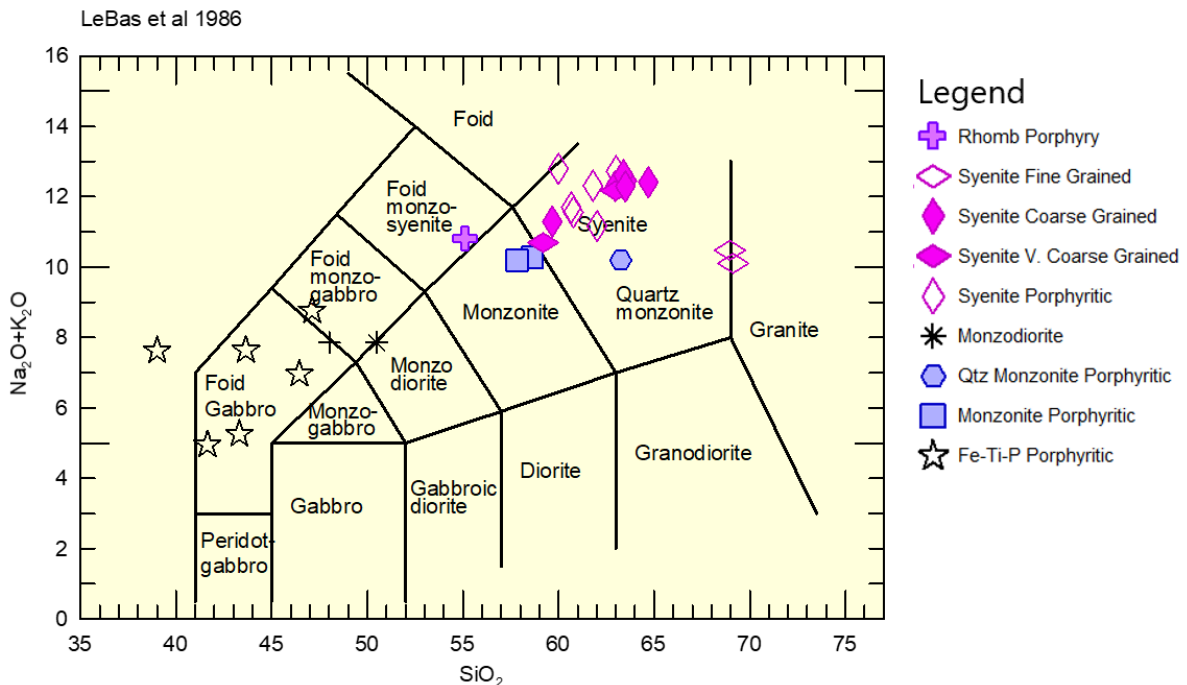


Figure 4-35: Modified TAS diagram (Middlemost, 1994).

#### 4.3.1.2 Granitoid classification diagrams

The classification of the granitoid rocks is based on the procedure suggested by Frost et al. (2001), which sub-divides the granitoid with the three variables Fe\* (= FeO<sub>T</sub>/(FeO<sub>T</sub> + MgO)), the modified alkali-lime index (MALI) and lastly the aluminium saturation index (ASI) (Figure 4-36 A – C, respectively).



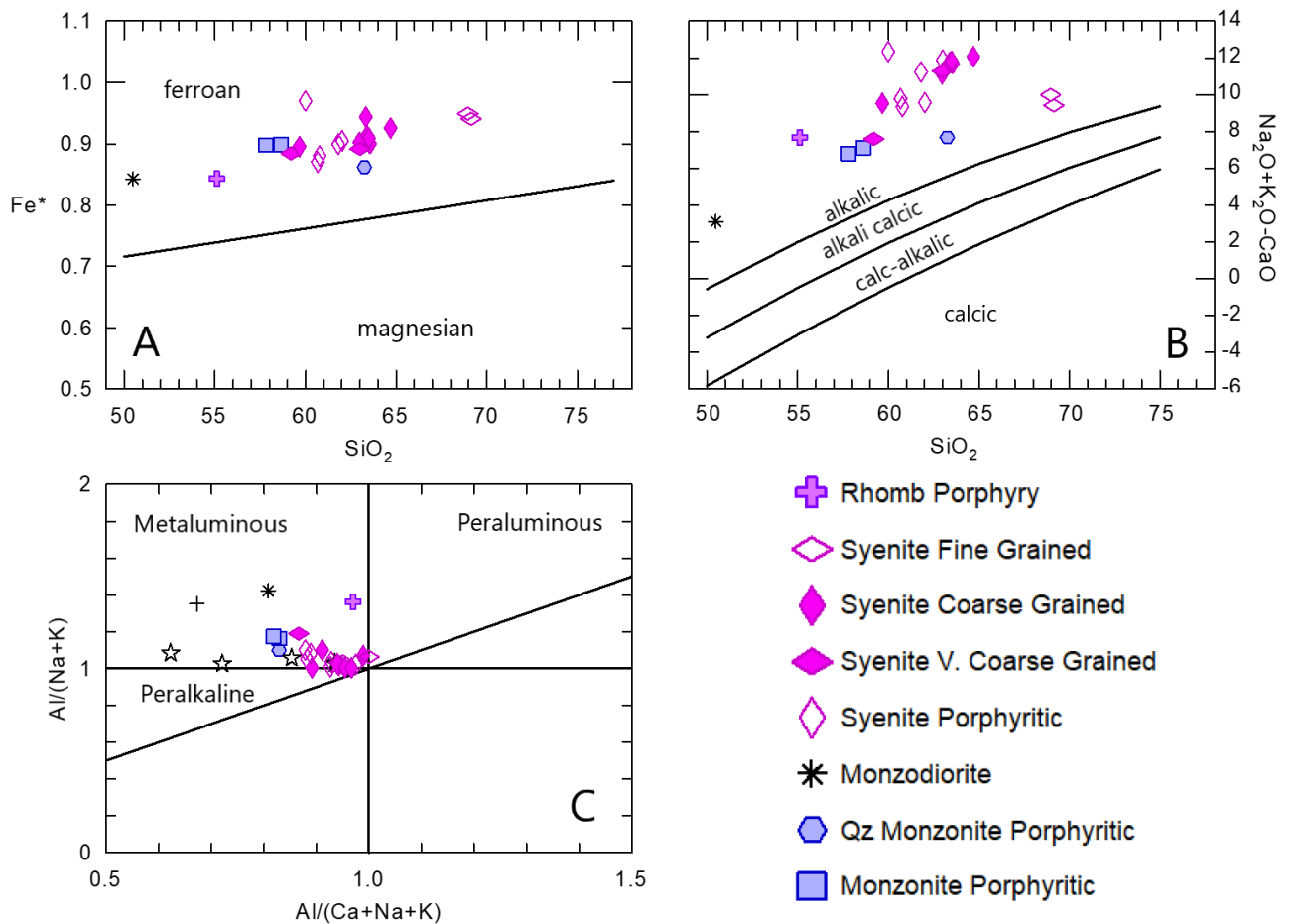


Figure 4-36: Granitoid classification (Frost et al., 2001) (A) Iron- magnesian index, (B) MALI, and (C) ASI.

All granitoids plot as *ferroan alkalic metaluminous granitoids*, which according to Frost et al. (2001) is typical for within plate plutons. The granitoid classification does also include the ferroan monzodiorite (sample 509). All samples have formed a semi- parallel trend to the ferroan – magnesian boundary (Figure A), with no truly large deviations in the Fe – Mg enrichment. In the MALI diagram (Figure B), increases the distance to the alkali-calcic boundary with increasing SiO<sub>2</sub> content for the general monzonite – syenite trend. The ASI plot (Figure C) has a weak negative correlation where the monzonite – syenite trend goes from metaluminous monzonite to almost peralkaline coarse-grained syenite and peraluminous fine-grained syenite.

#### *4.3.1.3 Bulk Rock Major Oxide Harker Diagrams*

The Harker plot (Figure 4-37) depicts all samples, while Figure 4-38 limits the x-axis from 49 wt.% -71wt.% SiO<sub>2</sub> to enhance the internal variations of the granitoids. Figure 4-37 show a consistent trend in all sub- diagrams from the Fe-Ti-P rich rocks to the syenites. The fine to medium- grained Fe-Ti-P rich samples have relatively homogeneous chemical composition, and are rich in Mg, Fe, Ti, Ca and P<sub>2</sub>O<sub>5</sub>. The porphyritic Fe-Ti-P-rich rocks show the over all- larges internal variations and largest deviations from the thought trend line, which are especially pronounced in the MgO-, CaO- and P<sub>2</sub>O<sub>5</sub> plots. The granitoids show little internal variations, and with opposite enrichment of the Fe-Ti-P rich rocks, plot with high contents of Al, Na and K.

The Harker plot with emphasis on the silica rich samples (Figure 4-38) show the general trend from monzonites – porphyritic syenites – coarse grained syenites is evident for all major elements. However, the very coarse-grained syenite at 59 wt.% SiO<sub>2</sub> (sample 519) plot similarly as the monzonites for MgO, CaO, K<sub>2</sub>O and P<sub>2</sub>O<sub>5</sub>. The other very coarse-grained syenite sample (764) plots similarly to the medium- to coarse-grained syenite at 64 wt.% SiO<sub>2</sub>. The porphyritic syenites plot between 61 and 64 wt.% SiO<sub>2</sub> and form the group with the largest lateral variations in all major oxide diagrams. The medium to coarse grained syenites form a relatively homogeneous group between 63 and 65 wt.% SiO<sub>2</sub>. The fine-grained syenites have the highest silica content at 69 wt.%. They plot as outliers, deviating from the monzonite- syenite trendline for all major oxides. Another outlier is the quartz monzonite which is relatively enriched in the mafic associated elements Mg, Fe, Ti, Ca and P, and depleted in Al, Na and K.

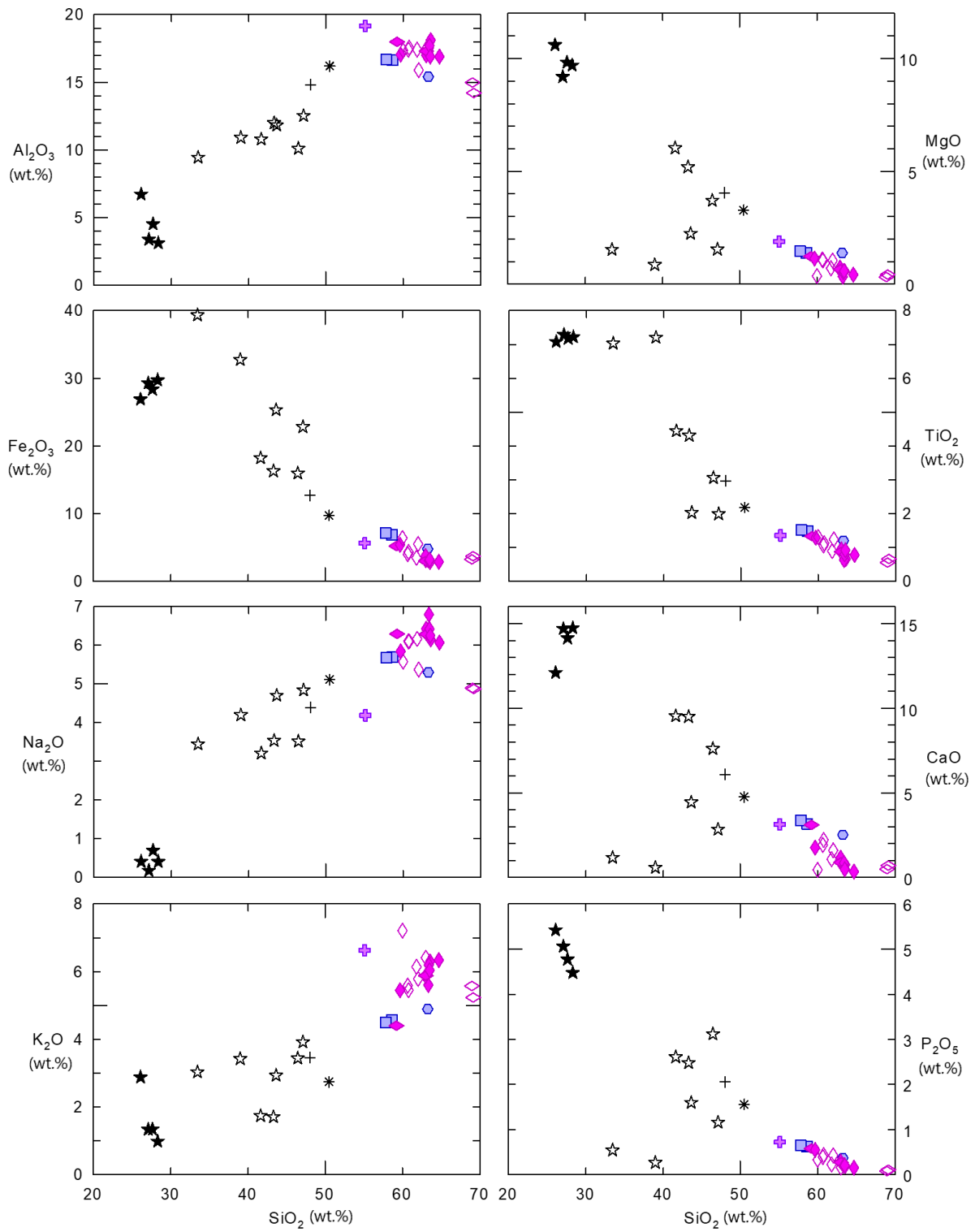


Figure 4-37: Harker plot depicting bulk analysis of major oxides of all samples.

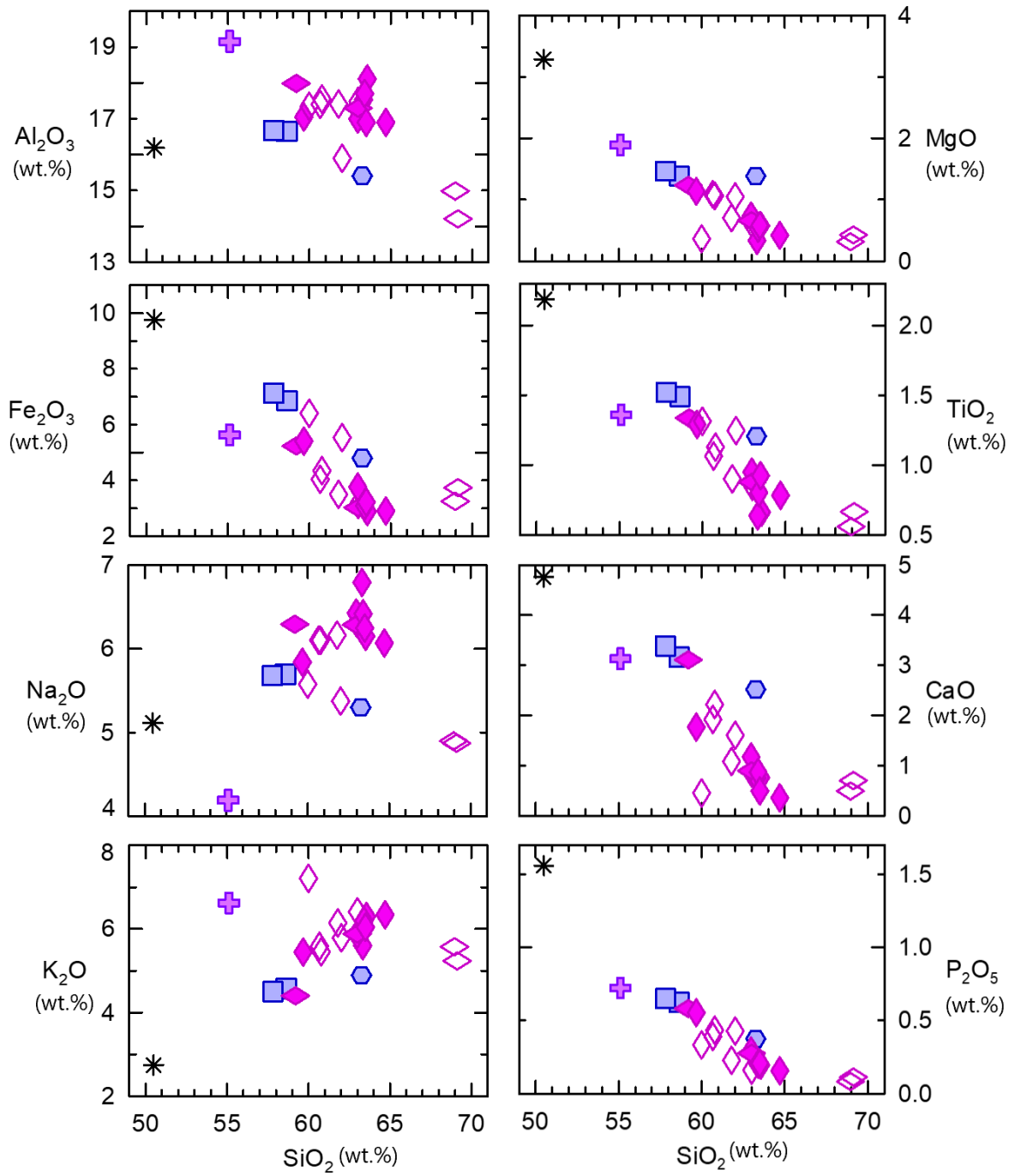


Figure 4-38: Harker plot depicting bulk analysis of major oxides within the silica range 49 wt.% – 71 wt.%.

#### 4.3.1.4 Bulk Rock Trace Element Harker Diagrams

The bulk rock trace element diagrams are subdivided into Figure 4-39, Figure 4-40, and Figure 4-41 which present transition metal-, HFSE-, and LILE content, respectively. Figure 4-41 does also include the chondrite normalized Eu-anomaly plot. All trace element contents are plotted against the Total Rare Earth Element content (TREE) in ppm.

The figures reveal Fe-Ti-P rich rocks are generally enriched in transition metals, Y and Sc, with all samples plotting with a negative Eu- anomaly. The granitoids have a generally low transition metal content, but are enriched in HFSE and LILE. Sample 502, 519, 509 and 508 are the only samples to plot with a positive Eu- anomaly. Additionally, note how two trends form in the HFSE – plot. The granitoids form a sharply increasing positive trend from syenites to monzonites, while the Fe-Ti-P rich rock form a separate weak positive correlation (Excluded Y and Sc as they are not HFSE, but added to the diagram for the convenience). Y and partly Sc show a strong correlation to the TREE content.

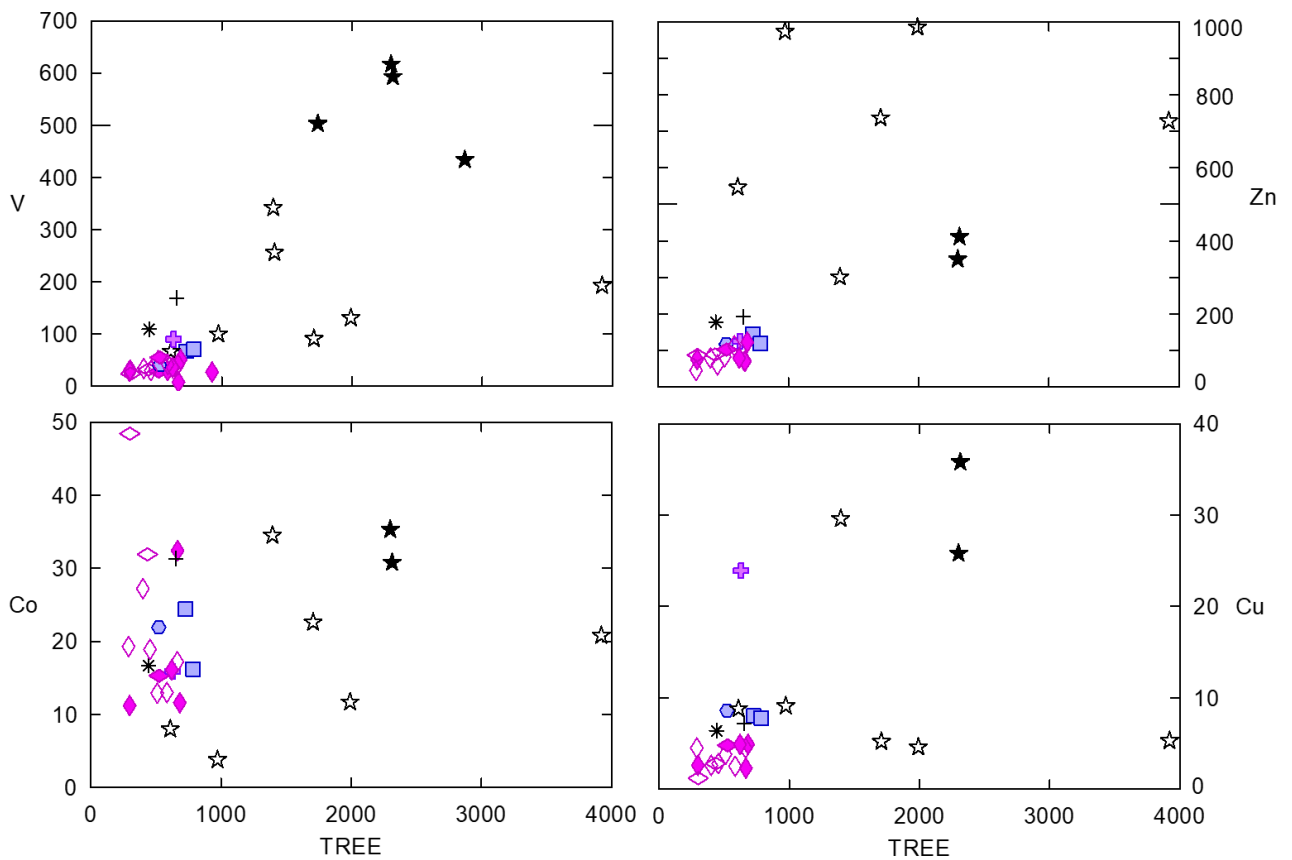


Figure 4-39: Whole rock analysis with transition metals plotted against TREE.

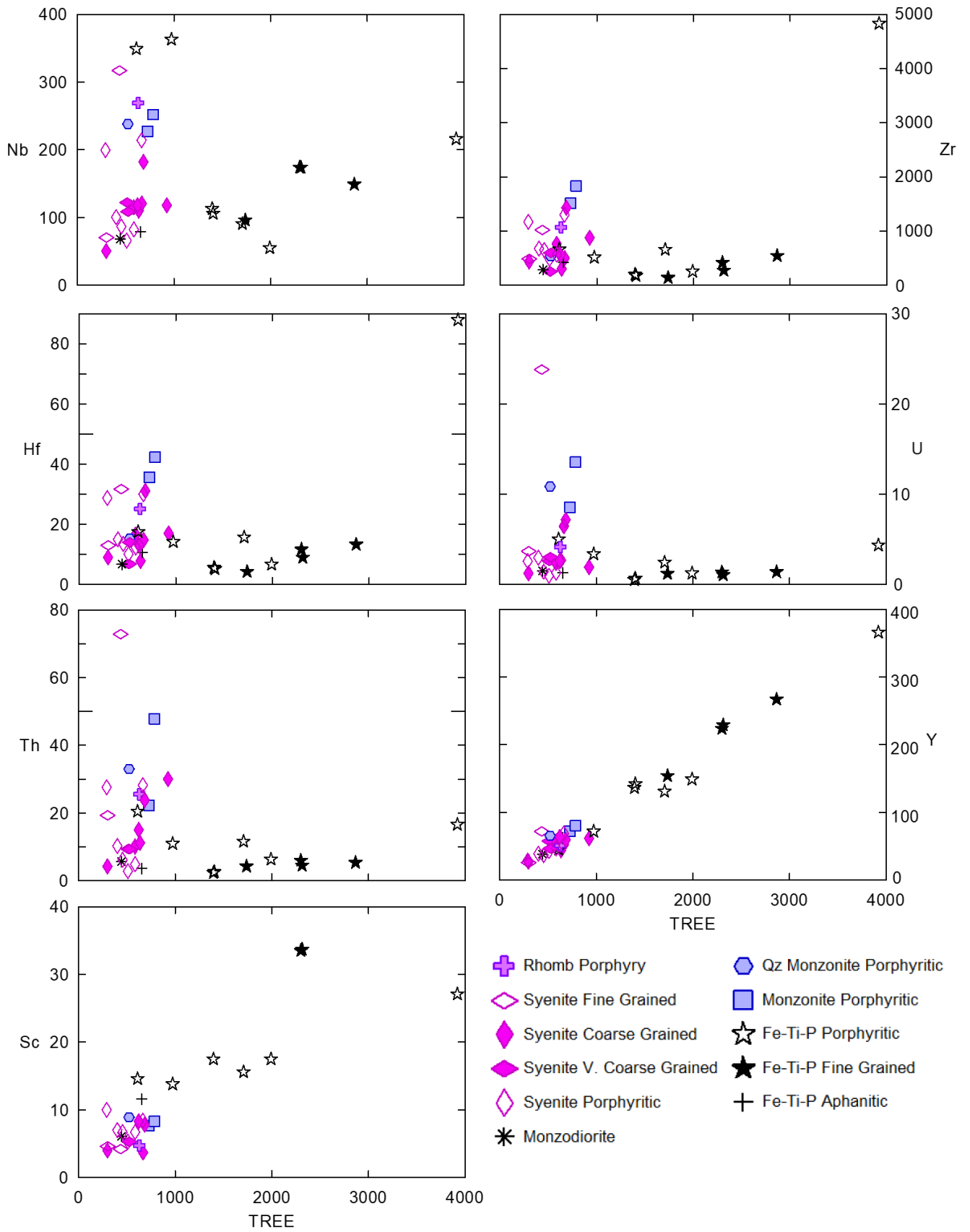


Figure 4-40: Bulk analyses Harker plot of HFSE (Nb, Zr, Hf, U and Th), Y and Sc.

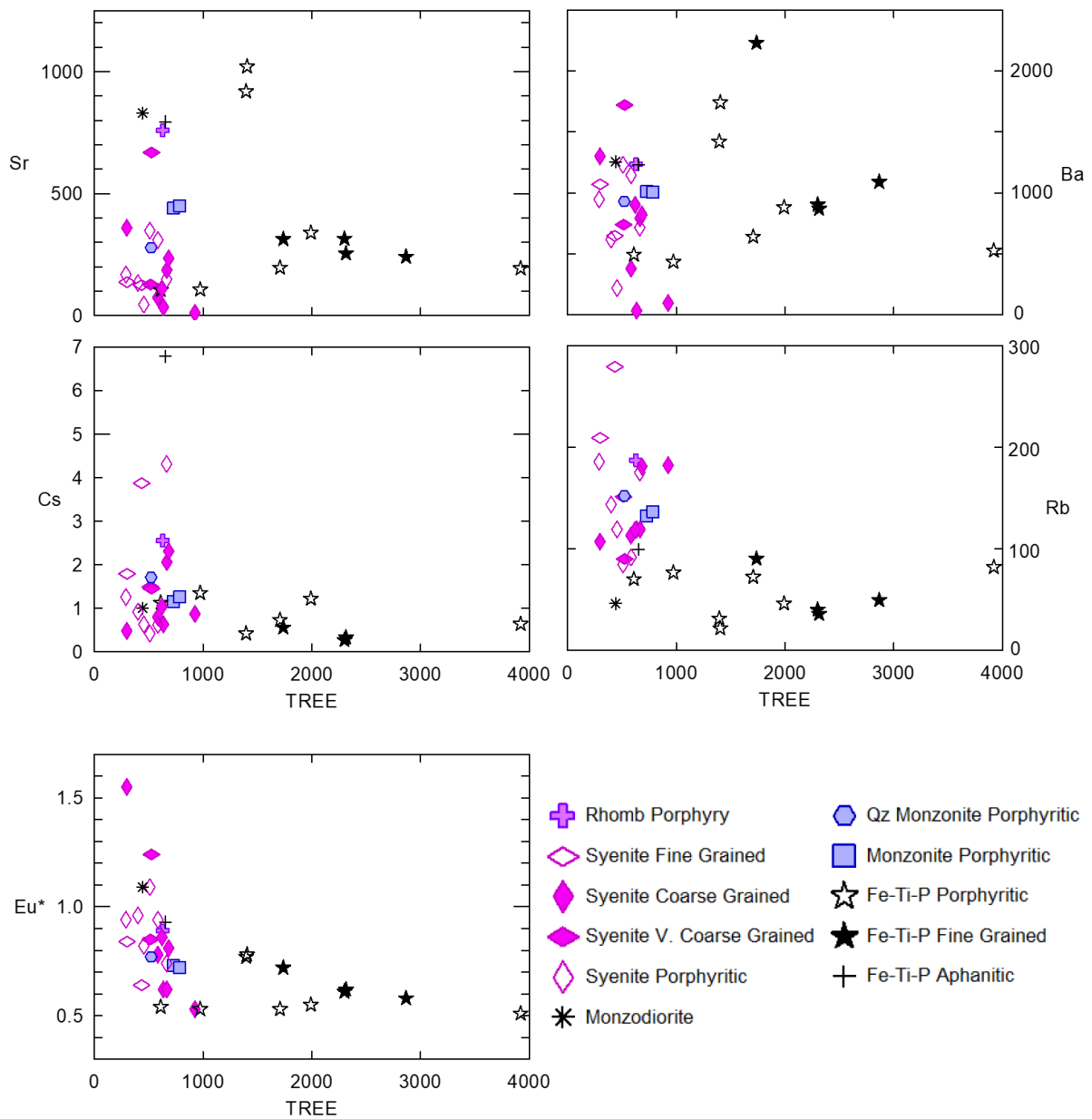


Figure 4-41: Whole rock analysis plotting LILE and Eu\* against TREE.

### 4.3.1.5 REE Spider Diagrams

The chondrite normalized spider diagrams comprises of Figure 4-42, which depicts average rock/chondrite values for the 11 rock classes, and Figure 4-43 which depict every sample within each class. The former diagram is added to give an approximate understanding of how the rock types plot in relation to each other.

All samples are enriched in REE, and strongly enriched in the LREE. The fine- to medium-grained Fe-Ti-P rich rocks have the highest average REE content, which is approximately 3x higher than the monzonites. The sample with the highest measured REE content is the porphyritic Fe-Ti-P rich rock 501 from Kåsemyrene. The monzonites with the quartz monzonite are the most enriched rocks among the granitoids, and form relatively homogeneous trend lines. The fine- grained syenites have the over- all lowest REE content, and form jagged, inconsistent trendlines.

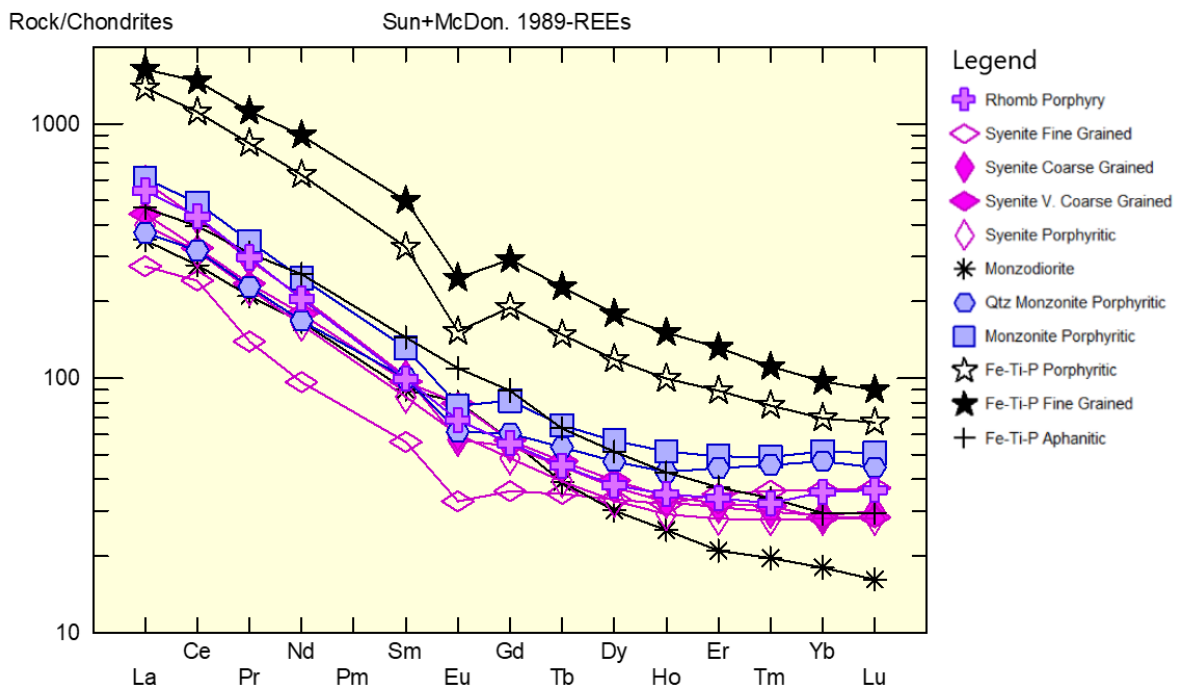


Figure 4-42: Average whole-rock REE values based on rock classifications. (Average values are based on 1, 2, 5, 2, 6, 1, 1, 2, 7, 4, and 1 numbers of analyses, respectively presented from rock classes in legend) (Sun and McDonough, 1989).



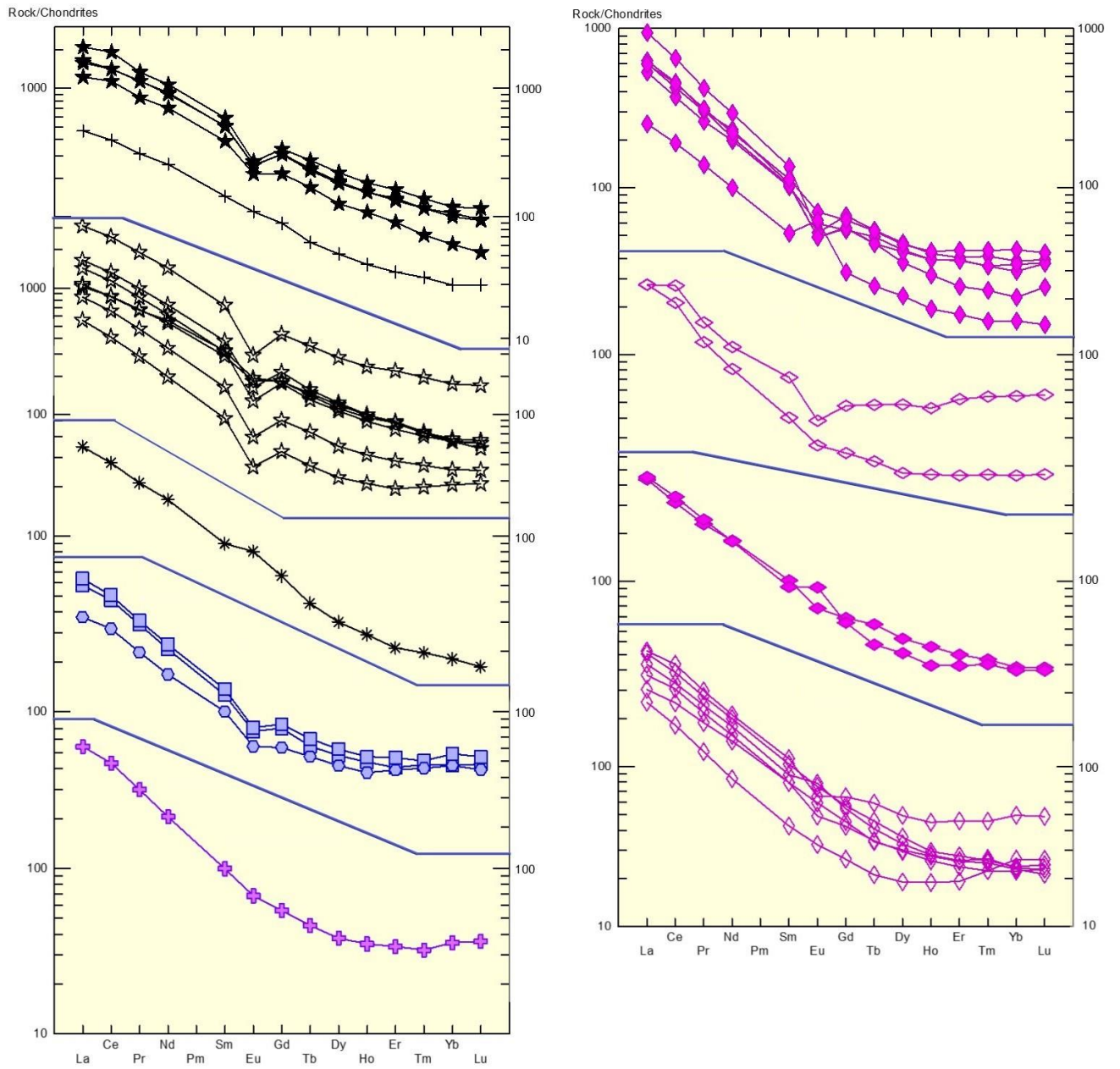


Figure 4-43: REE spider diagrams normalized to chondrite (Sun and McDonough, 1989) for whole-rock analyses.

### 4.3.2 Mineral analysis

Four thin sections were analysed with the microprobe, three representing Fe-Ti-P-rich rocks (403B, 503 and 761) and one from the host-syenite (536). Five mineral phases were analysed: amphibole, apatite, biotite, feldspar, and pyroxene. The legend of this section diverges from previous sections as the measured points are divided with respect to the mineral association and whether the analytes are inclusions or not. This is further explained with Figure 4-44 and Table 4.

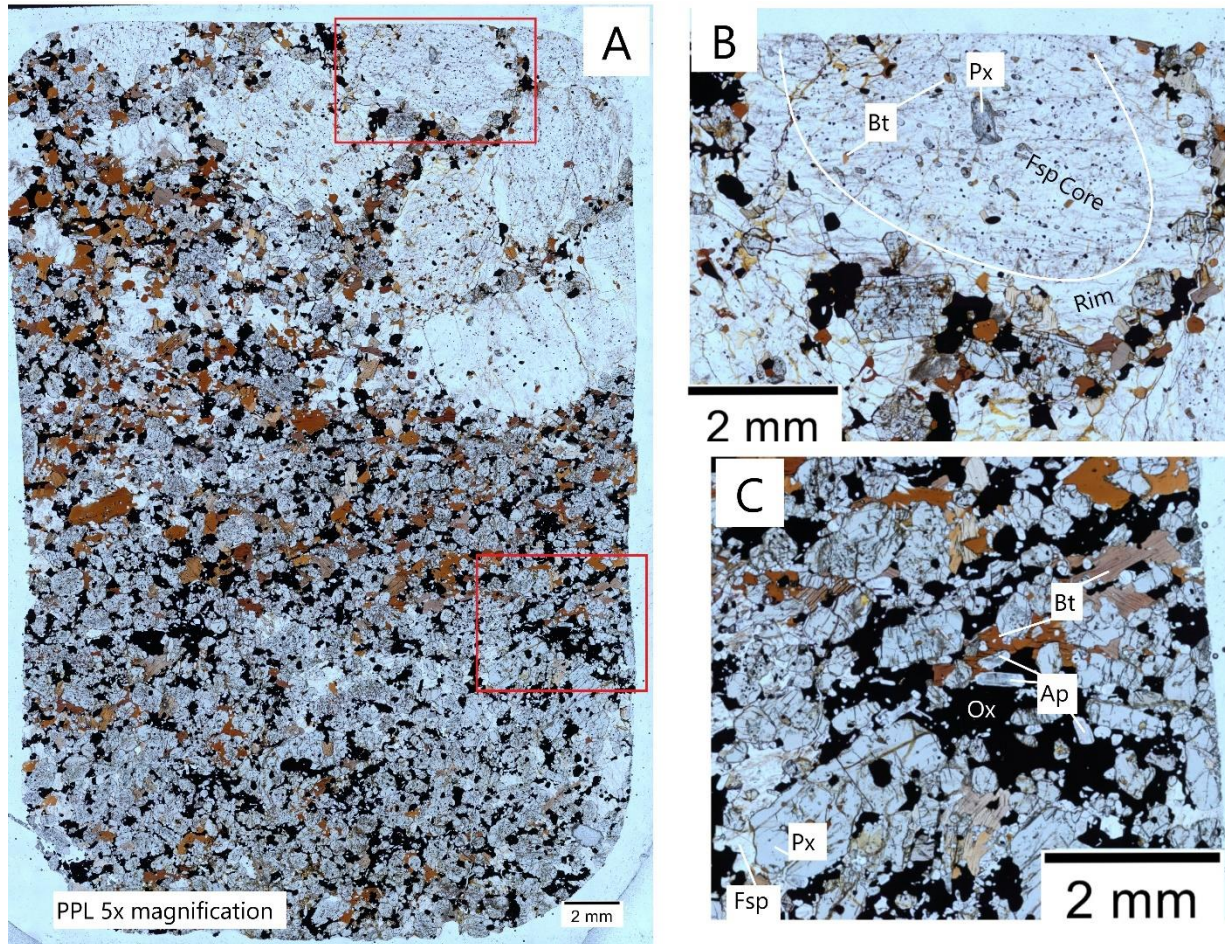












Figure 4-44: (A) PPL, 5x magnification thin section scan of the porphyritic Fe-Ti-P rich rock (403B). Top of the thin section contains zoned feldspar phenocrysts while the lower part is the Fe-Ti-P rich rock. Note that some of the phenocrysts contain dusty cores. (B) Close up of zoned feldspar phenocryst where the core contains inclusions of pyroxene, biotite, oxides, and apatite in the size range 0,05 – 0,5 mm contributing to the dusty appearance. In contrast, the rim contains fewer, but larger inclusions. (C) Close up of fine-grained mafic zone of the thin section comprising of subhedral pyroxene and apatite, and anhedral to interstitial oxides, biotite, and feldspar in the size range 0,5 – 2 mm. Feldspar in this zone share many visible similarities to the rim zone of the phenocrysts.

Table 4: Legend for EPMA analyses. Minerals symbols are based on sample and mineral association. Open symbols represent minerals associated with a silicic phase (most often feldspar), filled symbols represent minerals in mafic interstitial pockets or in Fe-Ti-P ground mass.

Symbol	Sample	Rock description	Specifications:
	536	Medium to coarse-grained syenite	The mineral occurs as inclusions in feldspars, or as a single grain interlocked between feldspar grains.
			The mineral occurs in mafic pockets between feldspar in a cumulate texture. (See fig. 536 TS A and B, amphibole subsection).
	503	Fine to medium-grained Fe-Ti-P rich rock	The entire sample consists of Fe-Ti-P groundmass, thus only one symbol is needed to describe the mineral association.
	761	Porphyritic Fe-Ti-P rich rock	The mineral occurs as inclusions in feldspar phenocrysts or is the phenocryst itself
			The mineral is associated with the Fe-Ti-P groundmass.
	403B	Porphyritic Fe-Ti-P rich rock	The mineral occurs as inclusions in feldspar phenocrysts. See fig. 403B_TS B.
			The mineral is associated with the Fe-Ti-P groundmass. See fig 403B_TS (B) mafic minerals between feldspar phenocrysts or (C) as fine- medium grained ore.
	403B	Porphyritic Fe-Ti-P rich rock	Applies only to feldspar analyses of 403B: Measurements from the center of the feldspar phenocryst cores. See fig 403TS_B (B).
			Applies only to feldspar analyses of 403B: Measurements from the middle zone of the feldspar phenocrysts.
			Applies only to feldspar analyses of 403B: Measurements from the phenocryst rim zone (Fig 403B (B)) and interstitial feldspar from the mafic zone (Fig. 403B (C)).

### 4.3.2.1 Feldspar Microprobe Analysis

Figure 4-45 depicts the feldspar classification diagram adapted from Parsons (2010). The Fe-Ti-P rich sample 761 plots mainly as oligoclase with two outliers plotting with a slightly higher Ca composition. The Fe-Ti-P rich sample 403B plots in two groups, oligoclase and anorthoclase. Both Fe-Ti-P rich samples (403B and 761) plot closer to the miscibility gap compared to the syenitic sample (536). The syenitic sample consists mainly of anorthoclase. However, the feldspar phenocryst shows a high degree of alteration along edges (Figure 4-46 A). The 536 K-feldspar and Na-feldspar stem from this heavy altered rim (Figure 4-46 B).

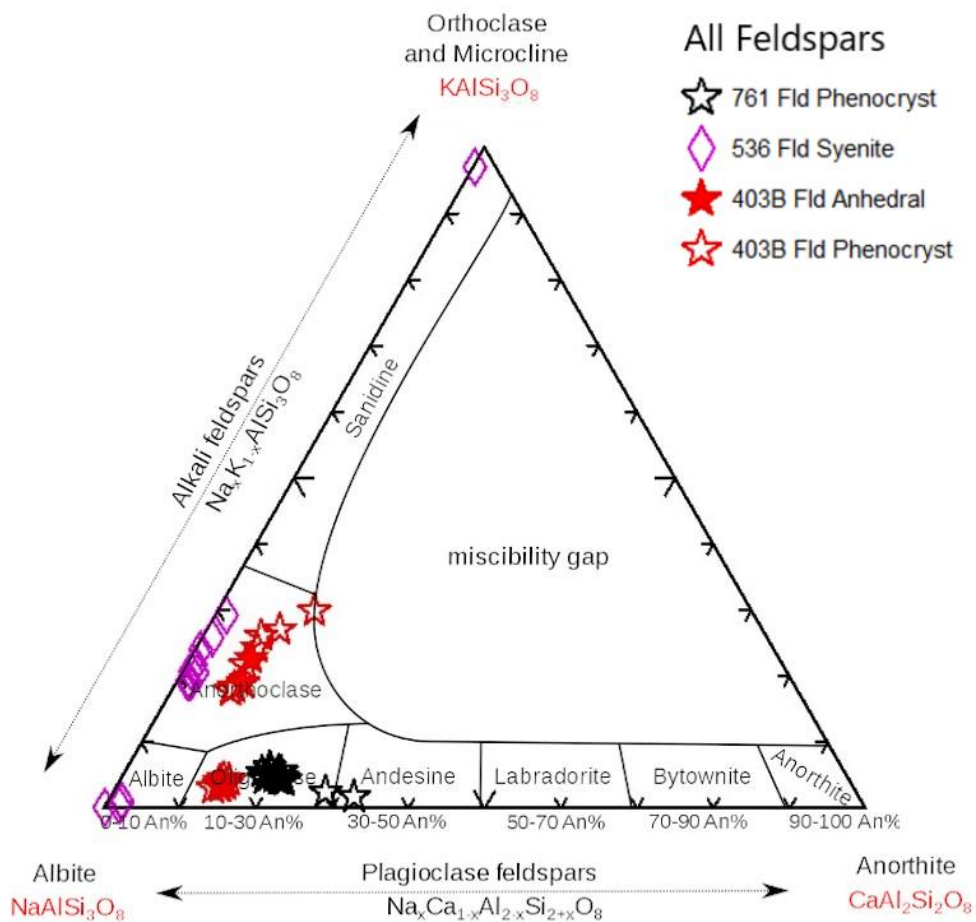


Figure 4-45: Ternary feldspar classification diagram (Parsons, 2010). The measurements are from the porphyritic Fe-Ti-P rich samples 403B and 761, and the medium to coarse-grained syenite sample 536.

A more detailed study of sample 403B was conducted as it contains an oligoclase phase like sample 761, and an anorthoclase phase comparable to syenitic sample 536. The measurements were conducted along a transect from the centre of the phenocryst (Figure 4-44 B) and out to the rim. Additional measurements were conducted on the interstitial feldspar in the Fe-Ti-P rich groundmass (Figure 4-44 C). Figure 4-47 depict how the core plots as homogeneous oligoclase, while the rim zone and interstitial feldspar plot over a wider compositional area as anorthoclase.

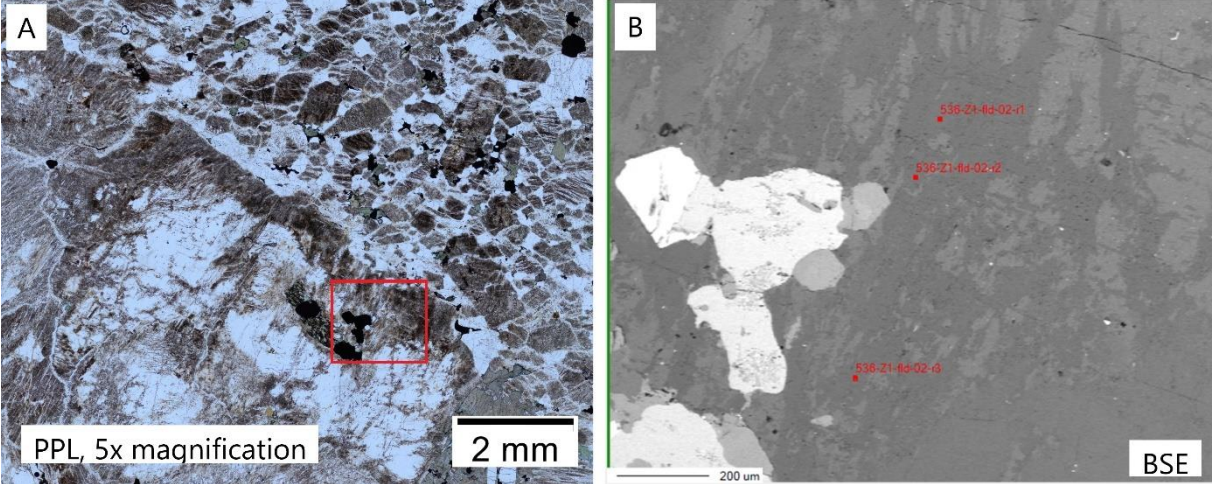


Figure 4-46: Photomicrograph and BSE image of feldspar analysed with microprobe (sample 536) (A) Photomicrograph of the contact between coarse-grained syenite and a fine-grained granitic dike. Feldspar phenocrysts show relatively clear cores and dusty 0.5 – 1 mm thick rims. The red square outlines the area for the BSE image. (B) BSE image of the altered zone showing feldspar lamellae where the dark grey is albite while the light grey is anorthoclase.

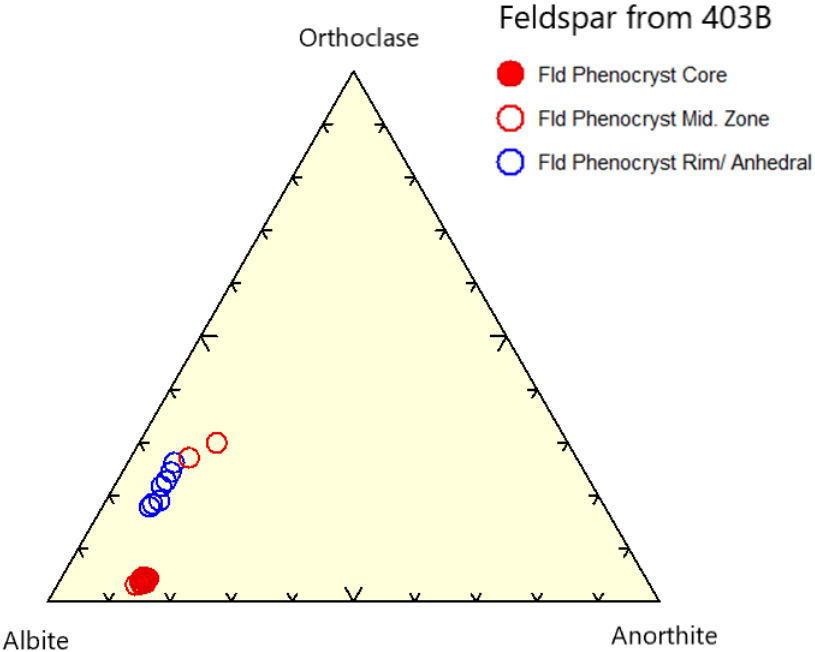


Figure 4-47: Subdivision of the EPMA analysis of 403B feldspars. Note the legend discriminates between feldspar cores, mid zones, and rim/ anhedral. Measurements stem from the phenocryst and interstitial feldspar depicted in Figure 4-44 B and C.

Figure 4-48 show binary diagrams plotting SrO and SrO/CaO content against Al<sub>2</sub>O<sub>3</sub> content for all samples (A and B) and 403B specifically (C and D). The SrO and Al<sub>2</sub>O<sub>3</sub> content is lowest for sample 536 and highest for 761. Sample 403B plot as two groups where the high Al content relates to oligoclase cores and low Al content relates to the rim zonation and interstitial anorthoclase. Note that only four 536 measured points plot on the figure as most SrO values are under the detection limit. The SrO/CaO ratio reveals the Fe-Ti-P sample 761 plot with a homogeneous, stable ratio, while the syenitic sample 536 have the largest internal variance. Sample 403B, however, plot with a homogeneous SrO/CaO ratio in the oligoclase core, while the anorthoclase rim and interstitial phase plot with a considerably higher and more variable ratio.

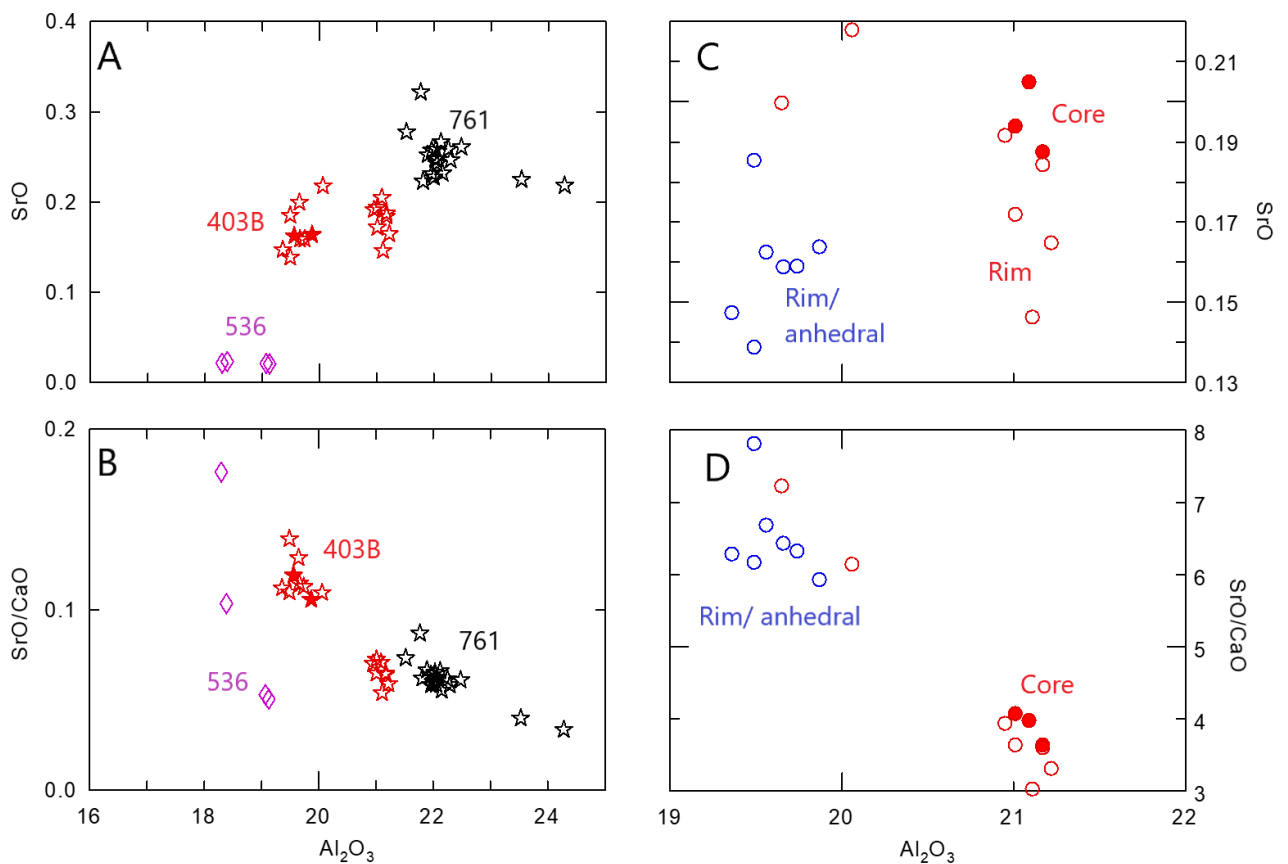


Figure 4-48: Binary diagrams of compositional variations observed in feldspar (microprobe data). Left side figures A and B show SrO and the ratio SrO/CaO plotted against Al<sub>2</sub>O<sub>3</sub> content in wt.% for all feldspar samples. The right-side figures (C and D) depict the subdivision of the 403B feldspars based on the same graphs.

### 4.3.2.2 Biotite Microprobe Analysis

The term biotite (sensu lato) comprises phlogopite and biotite (sensu stricto) where phlogopite form the Mg rich endmember of the biotite solid solution series (Li et al., 2020). Table 5 show common configuration of ions (ibid). The boundary for phlogopite is defined as  $Mg/(Fe_{tot} + Mg)$  over 0,70 (Figure 4-49) (Deer et al., 1975). Simplified formula of biotite (sensu lato) from Li et al. (2020):

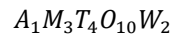


Table 5: Biotite sites and common occupying ions (Li et al., 2020).

Site	Site geometry	Cations/ anions
A	Interlayer site	K, Na, Ba, Ca
M	Octahedral	Mg, Fe <sup>2+</sup> , Fe <sup>3+</sup> , Al, Ti, Mn, Cr, Li
T	Tetrahedral	Si, Al, Fe <sup>3+</sup>
W	Anion site, O(4)	OH, <sup>W</sup> O <sup>2-</sup> , F, Cl

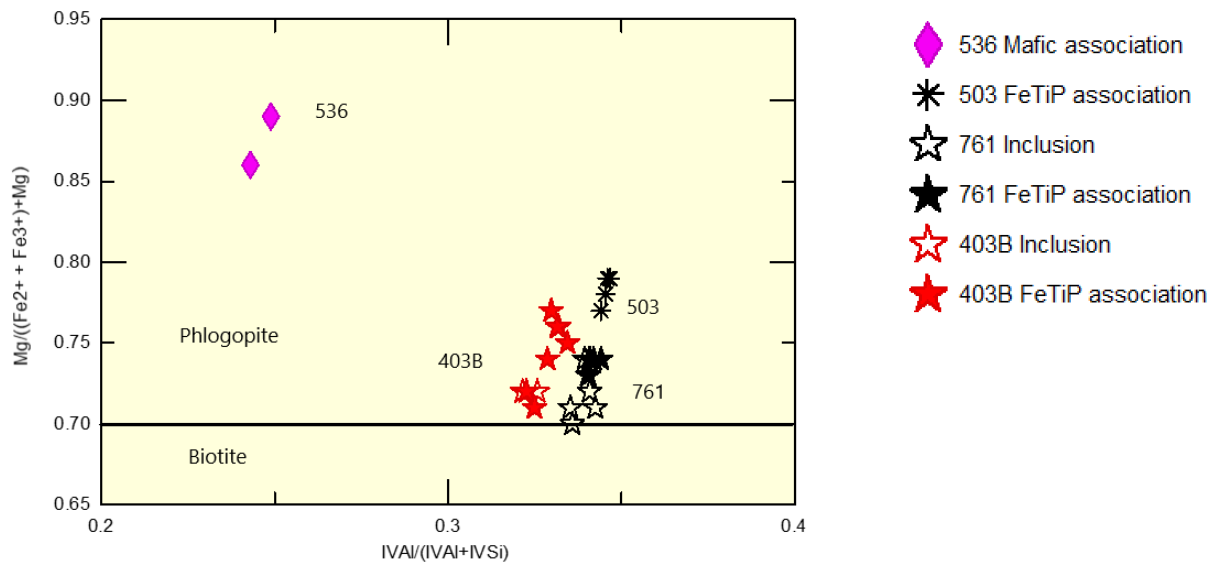


Figure 4-49: Biotite – Phlogopite classification diagram from Li et al. 2020 , plotting  $Mg/(Mg + Fe)$  against  $IVAl/(IVAl + IVSi)$ . The "inclusion" remark in the legend refers to phlogopite as inclusion in feldspar.

All measured biotite grains (*sensu lato*) plot as phlogopite. Figure 4-50 show phlogopite from Fe-Ti-P rich samples have an anion site (W) occupancy centred around an average of 9.6% F<sup>-</sup>, 43.0% OH<sup>-</sup> and 47.0% O<sup>2-</sup> with a standard deviation of 1.5, 3.4 and 4.0, respectively. Phlogopite in sample 536 however, has an average concentration of 32.0% F<sup>-</sup>, 44.3 OH<sup>-</sup> and 23.7% O<sup>2-</sup> with standard deviations of 0.7, 0.7 and 0.1, respectively.

Figure 4-51 A, B and D plot K<sub>2</sub>O, Na<sub>2</sub>O and FeO<sub>T</sub> against TiO<sub>2</sub>. The phlogopite from the syenitic sample 536 show low TiO<sub>2</sub> content, but comparable K<sub>2</sub>O and Na<sub>2</sub>O values to the phlogopite locked as inclusions in feldspar from sample 403B and 761. Sub-figure (D) has an apparent trend in the porphyritic Fe-Ti-P samples 403B and 761, where the FeO<sub>T</sub> content decreases relatively fast as the TiO<sub>2</sub> content simultaneously increases. Note that the phlogopite occurring as inclusions has the highest FeO<sub>T</sub> content, while the phlogopite in the Fe-Ti-P groundmass is richest in TiO<sub>2</sub>. The fine to medium- grained Fe-Ti-P rich sample (503), however, show a minimal decrease in TiO<sub>2</sub> and FeO<sub>T</sub> from core to rim within the same phlogopite grains. Subfigure (C) plot calculated wt.% of O<sup>2-</sup> against OH<sup>-</sup>. Both Fe-Ti-P rich samples (403B and 761) show a trend where the O<sup>2-</sup> content increases from phlogopite as inclusions in feldspar to phlogopite in the Fe-Ti-P groundmass.

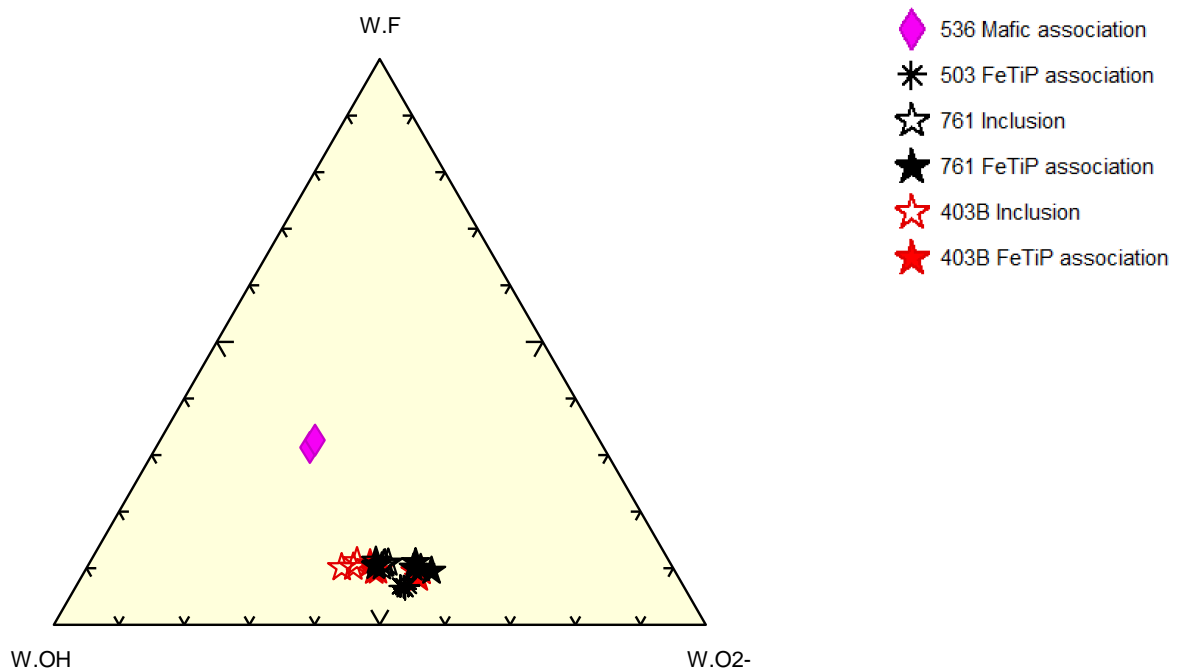


Figure 4-50: Ternary diagram plotting anion occupancy of OH<sup>-</sup>, F<sup>-</sup> and O<sup>2-</sup> in the W-site in phlogopite. The values are based on calculations after Li et al. (2020).



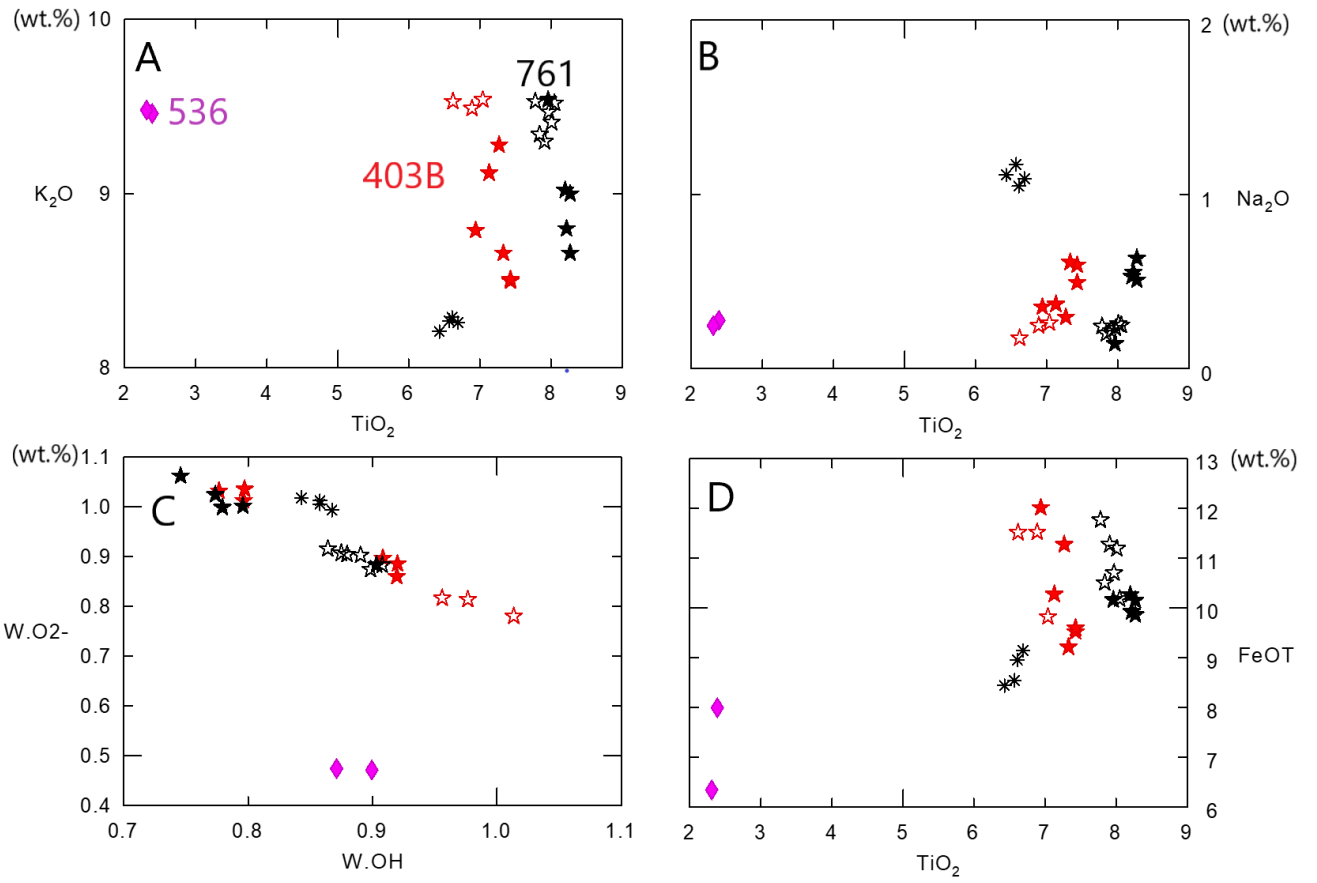


Figure 4-51: XY diagrams from microprobe analysis of phlogopite in the Fe-Ti-P rich samples 403B, 503 and 761, and the syenitic sample 536. Legend given in Figure 4-50.

### 4.3.2.3 Pyroxene classification

This dataset only comprises pyroxene analyses from the Fe-Ti-P-rich samples 403B, 503 and 764. Microprobe analyses from pyroxene in the syenite (536) yielded low total oxide sum (96-97 wt.%) and were removed from the dataset. Microprobe data for pyroxene were classified according to Morimoto and co-authors (1988). Table 6 categorizes the most common cation occupancies based on site, and the general chemical formula for pyroxene is as following (MORIMOTO, 1988):

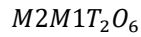


Table 6: The elemental distribution between crystallographic positions in pyroxene (Morimoto, 1988).

Site	Site geometry	Cations
M2	Octahedral	Mg <sup>2+</sup> , Fe <sup>2+</sup> , Mn <sup>2+</sup> , Li <sup>+</sup> , Ca <sup>2+</sup> , Na <sup>+</sup>
M1	Octahedral	Al <sup>3+</sup> , Fe <sup>3+</sup> , Ti <sup>4+</sup> , Cr <sup>3+</sup> , V <sup>3+</sup> , Ti <sup>3+</sup> , Zr <sup>4+</sup> , Sc <sup>3+</sup> , Zn <sup>2+</sup> , Mg <sup>2+</sup> , Fe <sup>2+</sup> , Mn <sup>2+</sup>
T	Tetrahedral	Si <sup>4+</sup> , Al <sup>3+</sup> , Fe <sup>3+</sup>

Pyroxene analyses plot in the field of Ca-Mg-Fe pyroxenes and are thus classified using the Enstatite (En) – Wollastonite (Wo) – Ferrosilite (Fs) ternary diagram, as recommended by Morimoto (1988). Pyroxenes from sample 403B, 503 and 761 have relatively uniform chemistry as all plot as augites close to the diopside boundary (Figure 4-52).

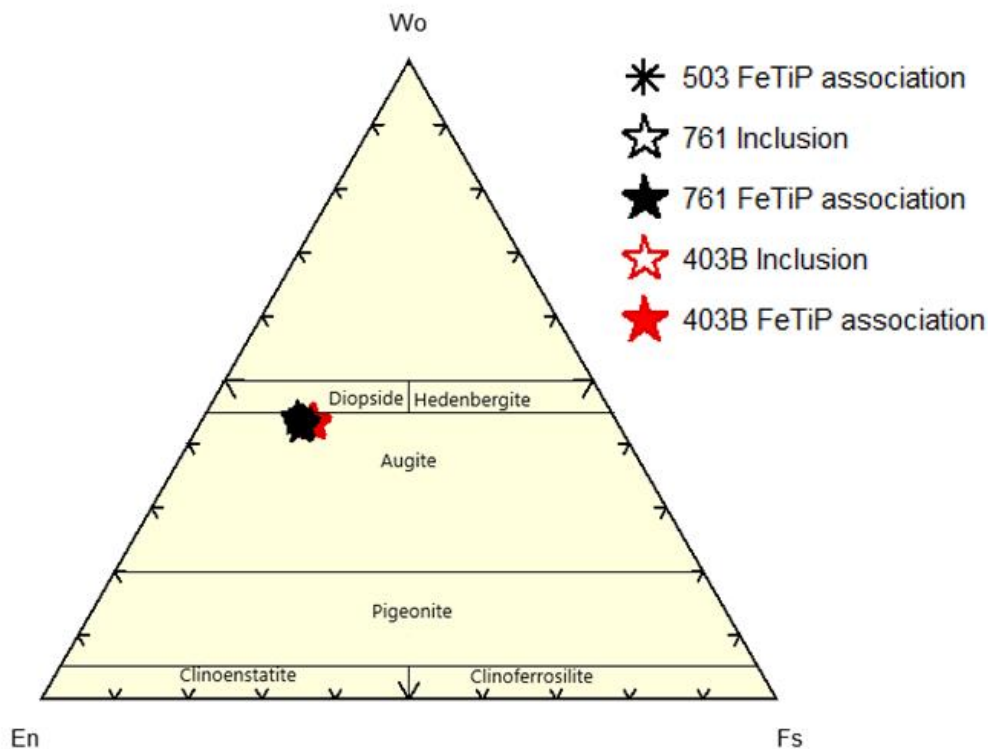


Figure 4-52: Pyroxene classification diagram with the three endmembers enstatite, wollastonite and ferrosilite (Morimoto 1988). EPMA results from sample 403B, 503 and 761 plotting as the monoclinic mineral augite. Despite being of relatively similar composition, some trends can be recognized in Figure 4-53. Sample 403B are generally richest in FeO<sub>T</sub>, MnO, and Na<sub>2</sub>O,

while sample 761 is the richest sample in  $\text{TiO}_2$ ,  $\text{MgO}$  and  $\text{Al}_2\text{O}_3$ . Sample 503, however, is richest in  $\text{SiO}_2$  and  $\text{CaO}$ . The oxides  $\text{FeO}_T$ ,  $\text{MnO}$ ,  $\text{Na}_2\text{O}$  and  $\text{MgO}$  appear to form sub-horizontal trends for sample 403B and 761, respectively. This contrasts with the weak negative trends in the  $\text{TiO}_2$  and  $\text{Al}_2\text{O}_3$  plots. Notably, are the augites occurring as inclusions in feldspar lowest in  $\text{SiO}_2$  and therefore also richest in  $\text{TiO}_2$  and  $\text{Al}_2\text{O}_3$ .

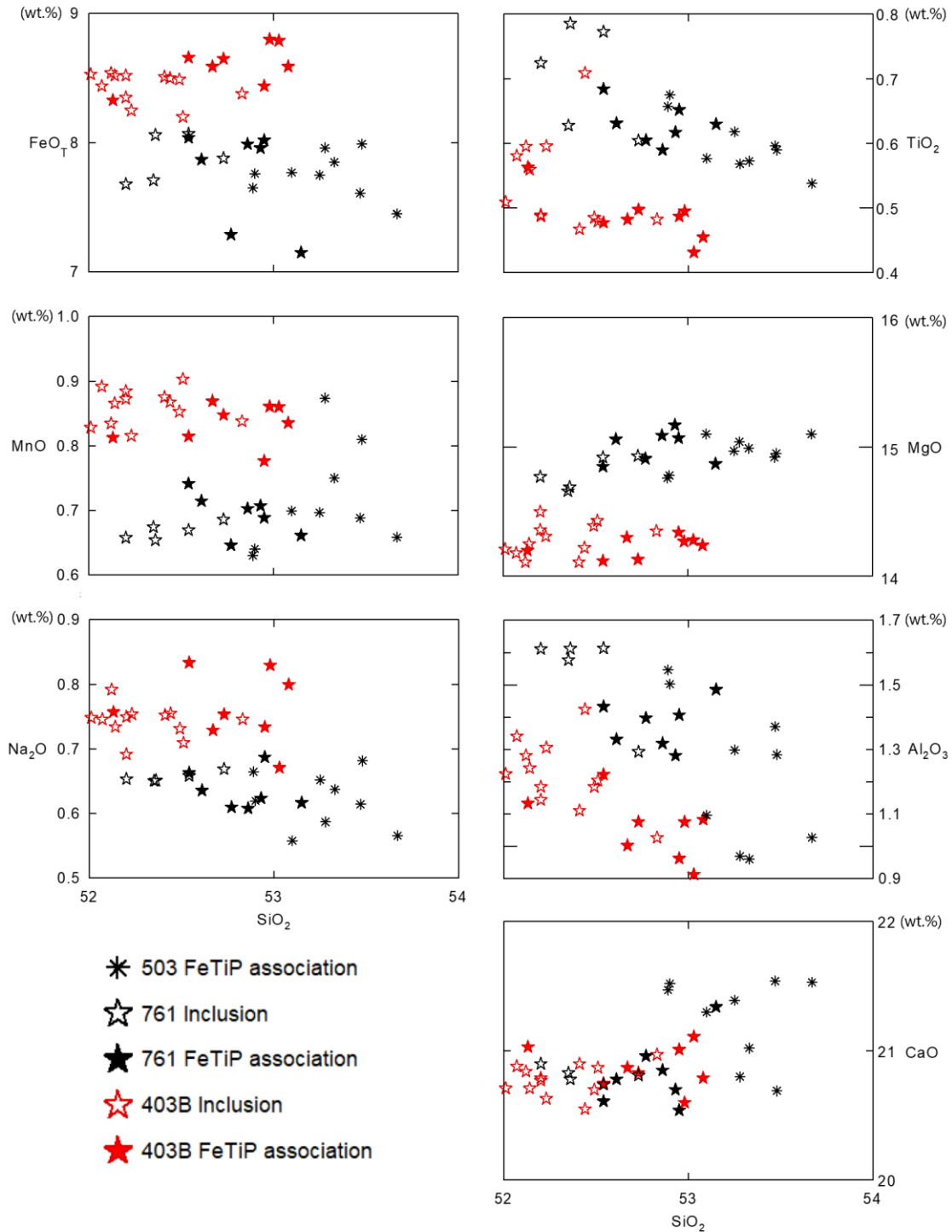


Figure 4-53: Harker diagrams of augite analysed in microprobe..

#### 4.3.2.4 Apatite Analysis

Apatite has remarkable properties regarding incorporation of trace elements which is an important tool in interpretation of magmatic history of the rock (e.g., (Belousova et al., 2002; Jennings et al., 2011; Bruand et al., 2016)). Therefore, apatite analysis was prioritized and conducted by both EPMA (NTNU) and LA-ICP-MS (NGU). Chlorine was disregarded from the LA-ICP-MS results as the DurDonG fraction apatite reference materials lack reference concentrations for the analyte. Arsenic and Cadmium were omitted due to inaccuracy in measured values compared to the standards (both ~45% higher with uncertainties of ~70% and ~60% 2 RSD, respectively). Potential interference in As is discussed in (Chew et al., 2016). Ti had to be disregarded as the masses 47 and 49 may interfere with  $^{31}\text{P}^{16}\text{O}$  and  $^{31}\text{P}^{18}\text{O}$  from the apatite. Further,  $^{31}\text{P}$  was below the limit of quantification in standard NIST 612. Lastly, lead is omitted due to measured large negative biases in the apatite standards DurDonG and McClure Mountain, here the standards are demonstrably heterogeneous in Pb concentration (Chew et al., 2016)

The apatite supergroup minerals are recognized with the generic chemical formula  $^{\text{IX}}\text{M}_1^{\text{VI}}\text{M}_2^{\text{IV}}\text{M}_3(\text{TO}_4)_3\text{X}$  ( $Z=2$ ) (Harlov and Rakovan, 2015). This supergroup contains over 40 known mineral species (ibid). The apatite supergroup is further divided into five groups based on content of Ca, Pb, Sr, Ba and Mn in the M site and P, V and As in the T site (ibid). These five groups are the apatite group, hedyphane group, belovite group, britholite group and ellestadite group. The apatite group contains 16 endmembers where the solid solution of fluorapatite, chlorapatite and hydroxylapatite are the most abundant subgroup in the crust (Harlov and Rakovan, 2015. p. 177). These minerals have the ideal chemical formula  $\text{Ca}_5(\text{PO}_4)_3\text{F}$ ,  $\text{Ca}_5(\text{PO}_4)_3\text{Cl}$  and  $\text{Ca}_5(\text{PO}_4)_3\text{OH}$ , respectively (Pasero et al., 2010), and it is these three minerals which will be referred to as "apatite" in this thesis.

Table 7: Apatite site and common ion occupancy (Pasero et al., 2010).

Site	Cations/ anions
M	$\text{Ca}^{2+}$ , $\text{Pb}^{2+}$ , $\text{Ba}^{2+}$ , $\text{Sr}^{2+}$ , $\text{Mn}^{2+}$ , $\text{Na}^+$ , $\text{Ce}^{3+}$ , $\text{La}^{3+}$ , $\text{Y}^{3+}$ , $\text{Bi}^{3+}$
T	$\text{P}^{5+}$ , $\text{As}^{5+}$ , $\text{V}^{5+}$ , $\text{Si}^{4+}$ , $\text{S}^{6+}$ , $\text{B}^{3+}$
X	F, Cl, $\text{OH}^-$

#### 4.3.2.4.1 Apatite Microprobe Analysis

Forty-two measurements on 26 apatite grains were performed with EMPA in four thin sections (403B, 503, 536 and 761). The OH, Cl, F ternary diagram (Figure 4-54) reveal all apatites measured in the microprobe are F- dominated, with negligible content of Cl. All mafic associated apatite measurements from the syenitic sample 536 plotted with over 100% F in X-site and were removed. Figure 4-56 has *measured* values of F plotted in binary diagram where the *calculated* limit for F-in X site is added. Figure 4-55 reveal low contents of FeO and TiO<sub>2</sub> in apatite. (Microprobe spots were aimed at areas without inclusions to avoid Fe-Ti contamination).

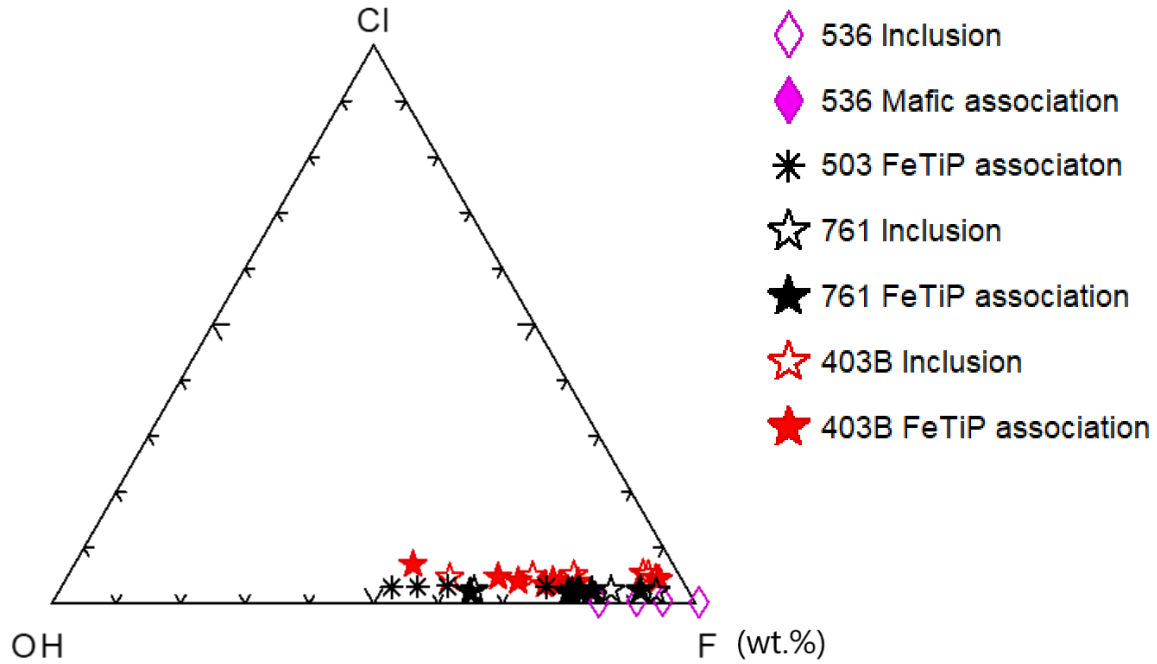


Figure 4-54: The calculated distribution of OH, Cl and F in apatite X site (Pasero et al. 2010).

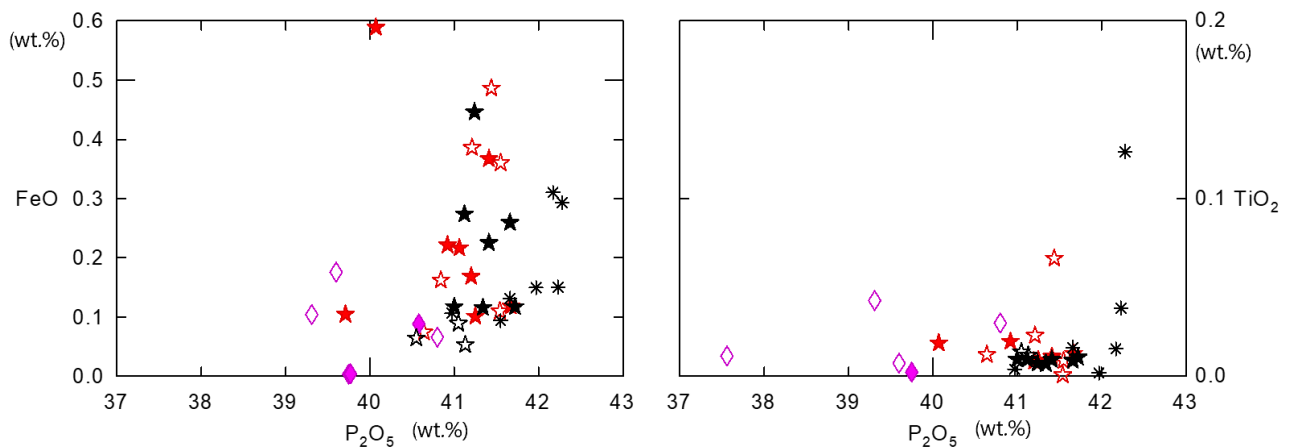


Figure 4-55: Measurements obtained with microprobe plotting binary diagrams of FeO and TiO<sub>2</sub> against P<sub>2</sub>O<sub>5</sub> content in apatite.

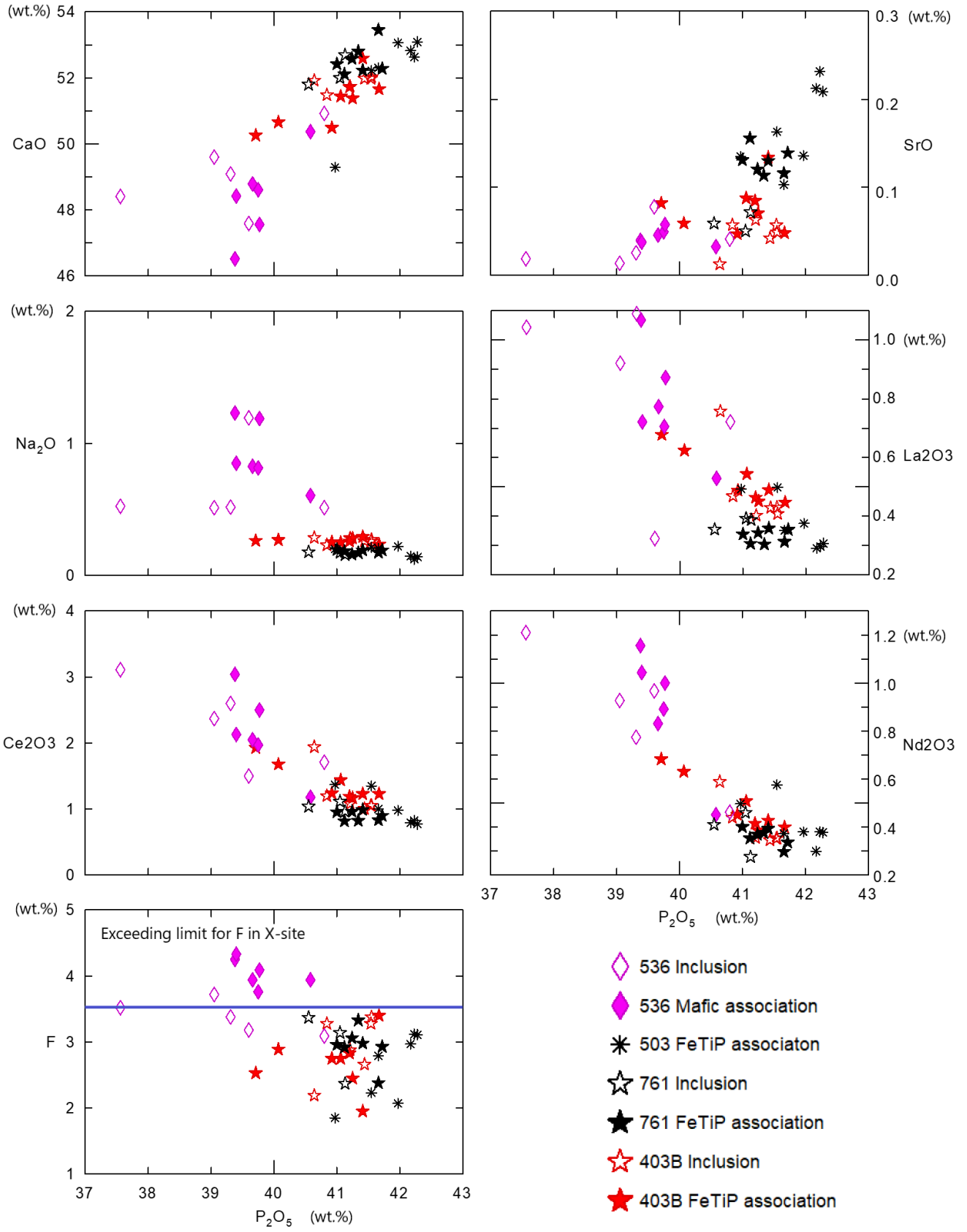








Figure 4-56: Binary diagrams plotting results from apatite microprobe analysis.

The syenitic sample (536) has the lowest P, Fe, Ti, Ca, and Sr content of all apatites measured in the microprobe. However, they are the enriched in Na, F and the three LRE elements La, Ce and Nd. The enrichment appears to be independent of whether the apatite occurs as inclusions in apatite or as sub- euhedral phases in interstitial mafic pockets. Apatites from Fe-Ti-P rich samples (403B, 503 and 761) are enriched in Fe, Ca, and Sr. It appears there is a distinction in Ca and Sr content between apatites occurring as inclusions and apatite in Fe-Ti-P rich groundmass, where the latter is slightly more enriched.

#### 4.3.2.4.2 Apatite LA ICP-MS Analysis

LA-ICP-MS analysis were conducted on 10 thin sections with focus on variation in trace elements between lithologies. Table 8 represent an explanation for the new legend applied to this analysis:

*Table 8: Legend for LA-ICP-MS analyses of apatite grains.*

<b>Symbol</b>	<b>Rock type</b>	<b>Sample</b>	<b>Location</b>
	Rhomb porphyry	524	RP sequence
	Syenite fine-grained	520	Key- Location Rødstjønn
	Syenite very coarse-grained	511	Søllandliene
		764	Kåsemyrene
	Quartz monzonite	512	Søllandliene
	Porphyritic Fe-Ti-P rich rock	761	Kåsemyrene
		514, 517	Eiriks gruve
	Fine to medium grained Fe-Ti-P rich rock	759, 760	Kåsemyrene

The apatites form well defined groupings for Sr (x-axis), where the granitoids are relatively depleted and the content gradually increases for the porphyritic Fe-Ti-P rich samples (514, 517 and 761) and are highest in the homogeneous Fe-Ti-P rich rock (760 and 759).

The rhomb porphyry (524) shows incomparably high values of V and high concentrations of Mn and Zr. The 4 highest values stem from a mafic blob enclosed in a feldspar phenocryst. These 4 analytes are also the only apatites measured with a positive Eu-anomaly (Figure 4-58 B). The other rhomb porphyry measurements stem from apatite associated with the aphanitic groundmass.

The Fe-Ti-P rich samples and granitoids generally form two separate trends. The granitoids have a high vertical variance where the very coarse grained syenite is the most enriched in Y, Th and U (511 is richest in U and Th, while 764 is Y -rich). The sample with the highest Zr values is the monzonite sample 512, which remarkably contains some of the lowest measurements of Zr as well (0,54 ppm).

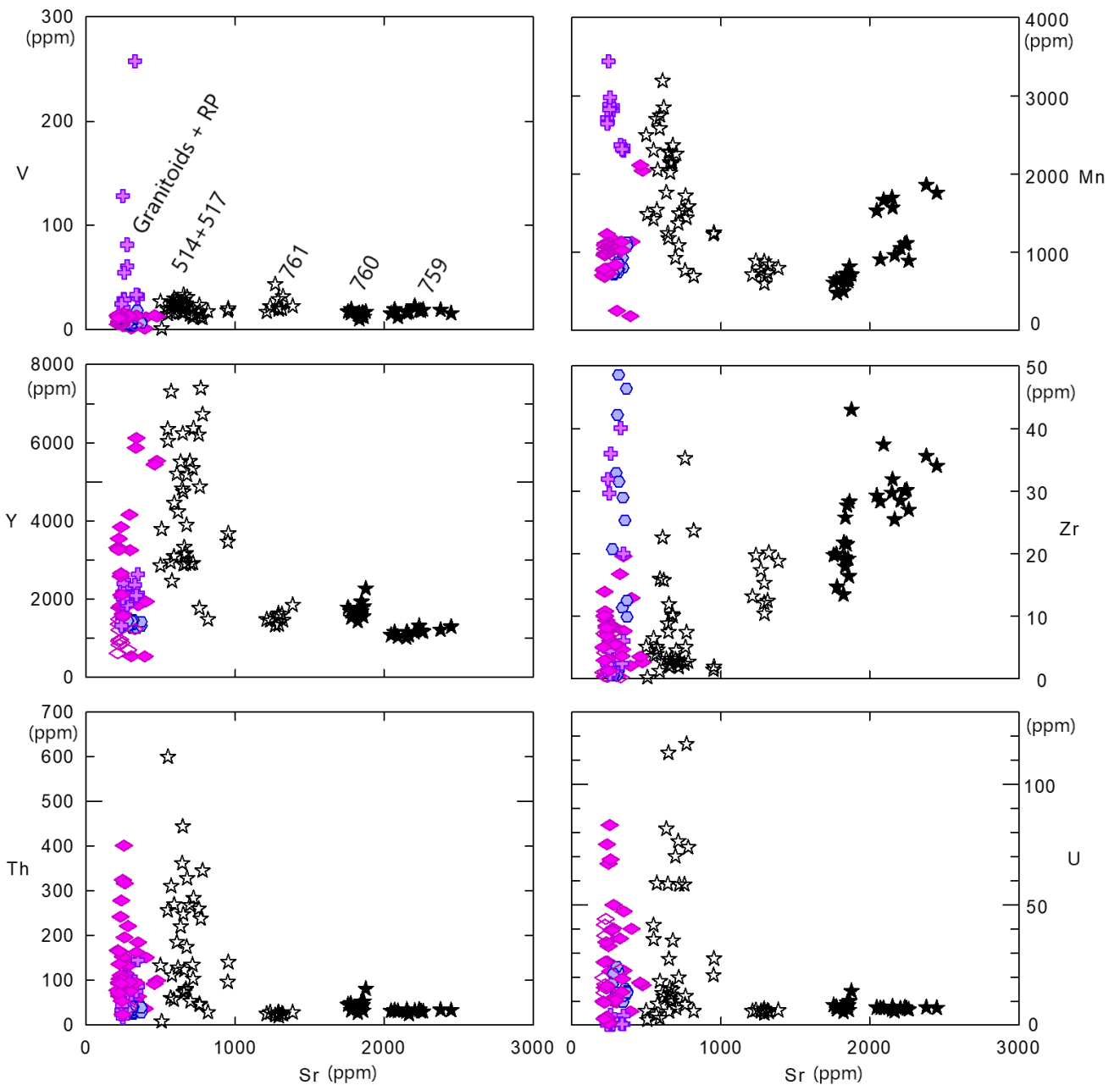


Figure 4-57: Results from LA-ICP-MS analyses of apatite presented as binary diagrams.

The Fe-Ti-P rich rocks appear to follow a common trend for V and Zr, as they are slightly enriched in V compared to the granitoids, and form a positive correlation regarding Zr. For the other graphs, the porphyritic Fe-Ti-P samples from Eiriks Gruve (514 and 517) plot with the highest variance and highest values of Mn, Y, Th and U. The Fe-Ti-P samples from Kåsemyrene (761, 760, and 759) form a weak positive correlation for Mn and are relatively depleted in Th and U.



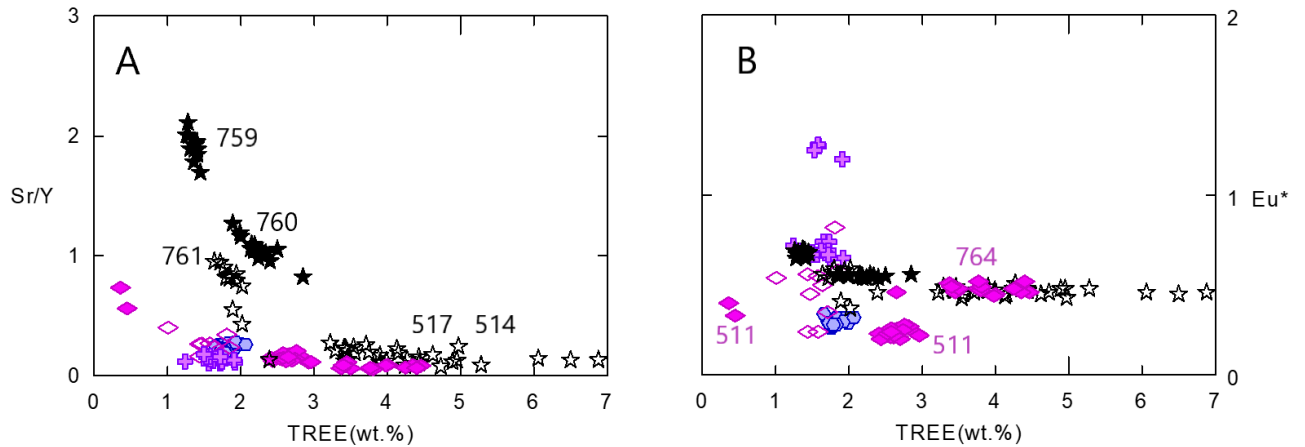


Figure 4-58: Ratio diagrams depicting Sr/Y and Eu-anomaly in apatite obtained with LA-ICP-MS.

Figure 4-58 plot the two ratios Sr/Y and Eu-anomaly against TREE (Total Rare Earth Elements), where both graphs are indicative of melt fractionation (Belousova et al., 2002; Jennings et al., 2011; Bruand et al., 2016). The granitoids and rhomb porphyry form a low sub- horizontal trendline in Figure (A), while the Fe-Ti-P rich samples follows a near inverse exponential trendline. The Eu- anomaly (Figure B) is negative for all analytes except for four measurements in the rhomb porphyry (524).

Figure 4-59 show the average trends for REE in apatite measured with LA-ICP-MS. All samples are enriched in REE, with an extreme enrichment of the LREE. The porphyritic Fe-Ti-P rich samples (514 and 517) together with the very coarse- grained syenite (764) are most enriched with the trend starting at chondrite levels equivalent to 2 – 3,5 wt.% La. The apatites from the fine-grained Fe-Ti-P rich rock plot relatively similarly as the quartz monzonite and rhomb porphyry. The fine grained- syenite (520) reveal the lowest overall concentrations of REEs. The averages are based on 511: n=18, 512: n= 17, 514: n= 17, 517: n= 16, 520: n=10, 524: n=14, 759: n=12, 760: n=14, 761: n=11, and 764: n= 15 counts.

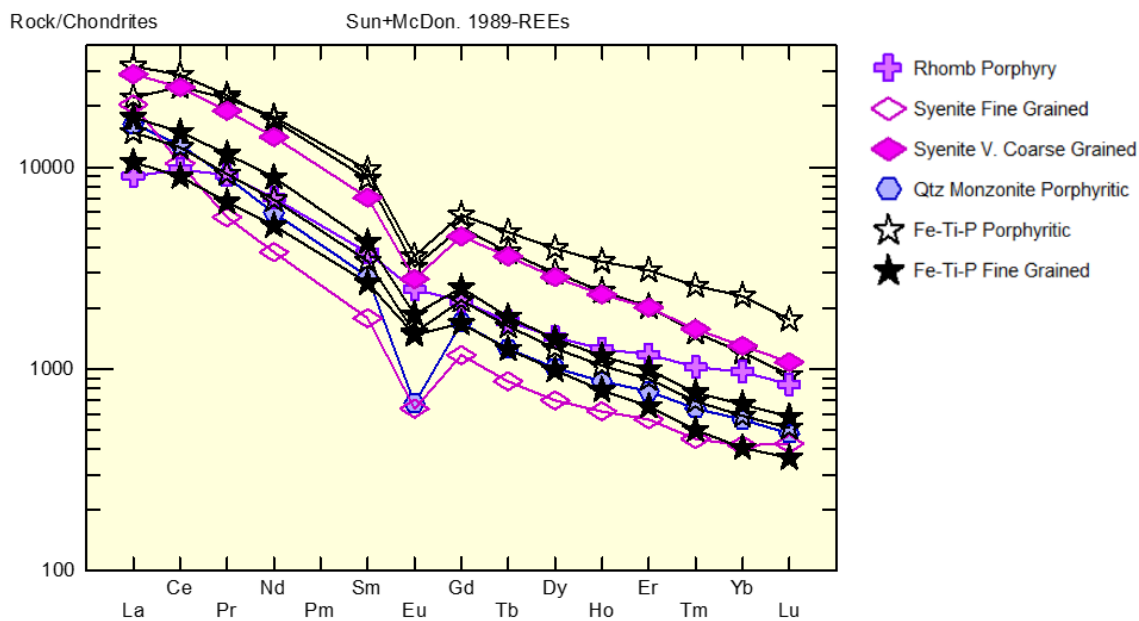


Figure 4-59: Average chondrite normalized REE values for apatite.

Rare Earth Element spider diagrams representing every apatite analyte is represented in Figure 4-60. The Fe-Ti-P rich samples from Kåsemyrene (759, 760 and 761) have relatively straight trendlines with moderate negative Eu-anomaly and show little internal variance. The Fe-Ti-P rich samples from Eiriks Gruve (514 and 517), however, show greater variance between the trend lines, where some samples reveal depletion of La and partly Ce. The apatites in the quartz monzonite are homogeneous, while the other granitoids comprises the group with most internal variations. The very coarse- grained syenite 764 plot with little variation among the LREEs, and a more significant variance among the HREEs.

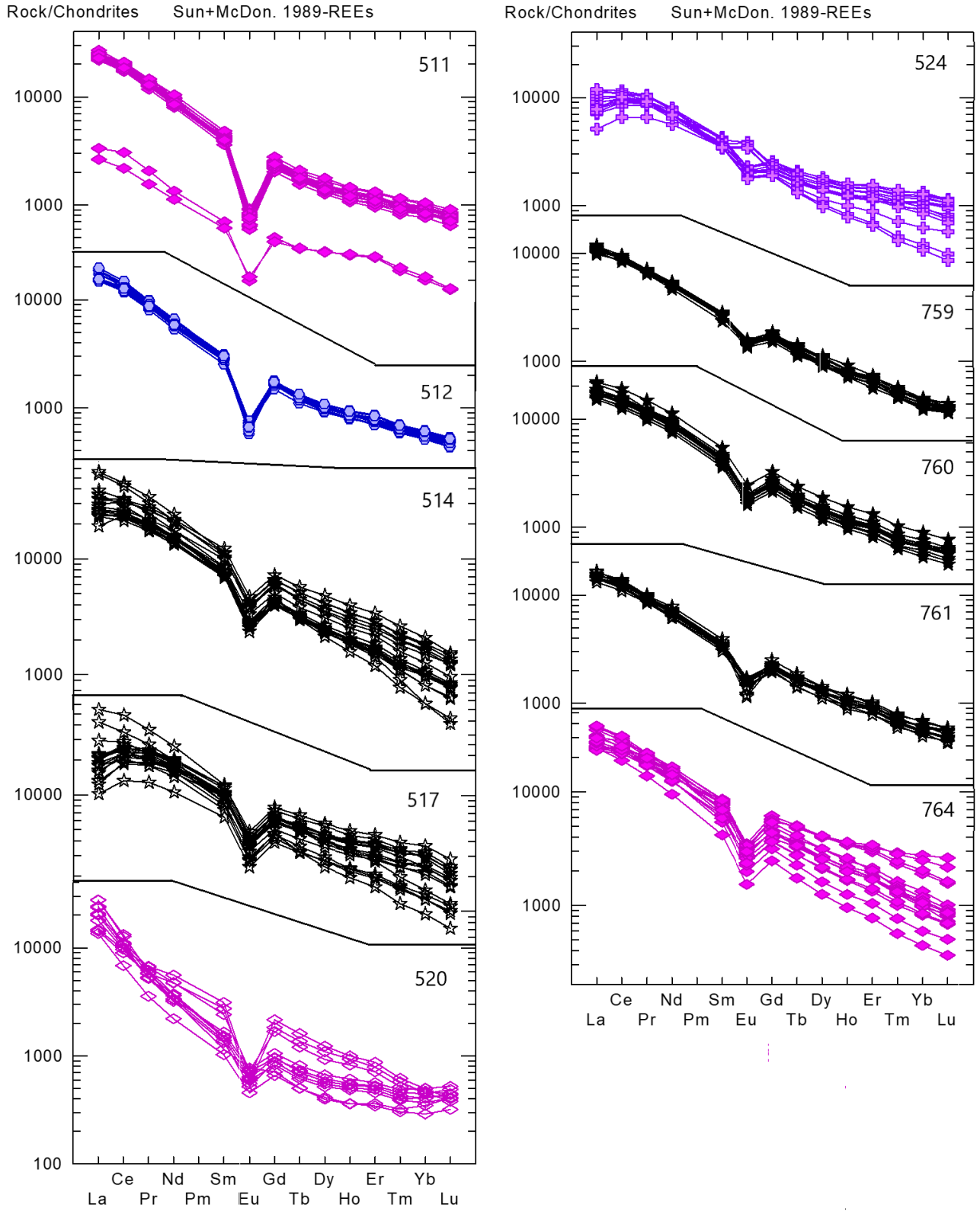


Figure 4-60: Spider diagrams depicting results from apatite LA-ICP-MS analysis sorted after thin section (nr. to the right).

#### 4.3.2.5 Amphibole Analysis

The microprobe amphibole analysis comprises of 8 measured points from the homogeneous Fe – Ti-P rich sample 503 and 11 measurements from the syenitic sample 536. The amphiboles in the Fe-Ti-P rich rock are recognized as brown, subhedral with well-developed cleavage (Figure 4-62). The amphiboles in the syenite show various degree of alteration, with a beige/ brown core with cleavage and alteration towards a blue- green (often fibrous) rim (Figure 4-61 B).

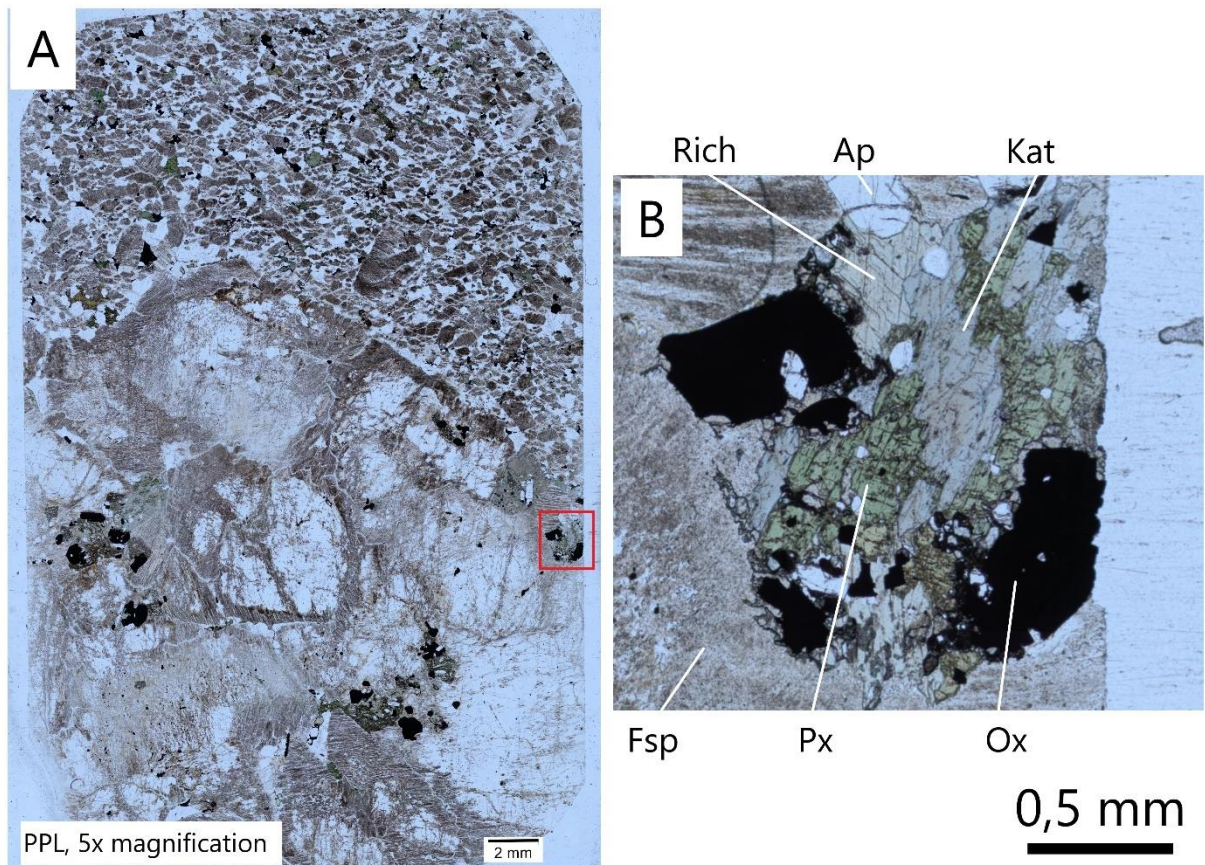


Figure 4-61: Plane polarized 5x magnified photomicrograph of thin section 536 (A), and (B) photomicrograph of ~1.5 mm wide mafic enclave consisting of altered pyroxene, richterite amphibole, katophorite amphibole, apatite, and oxides.

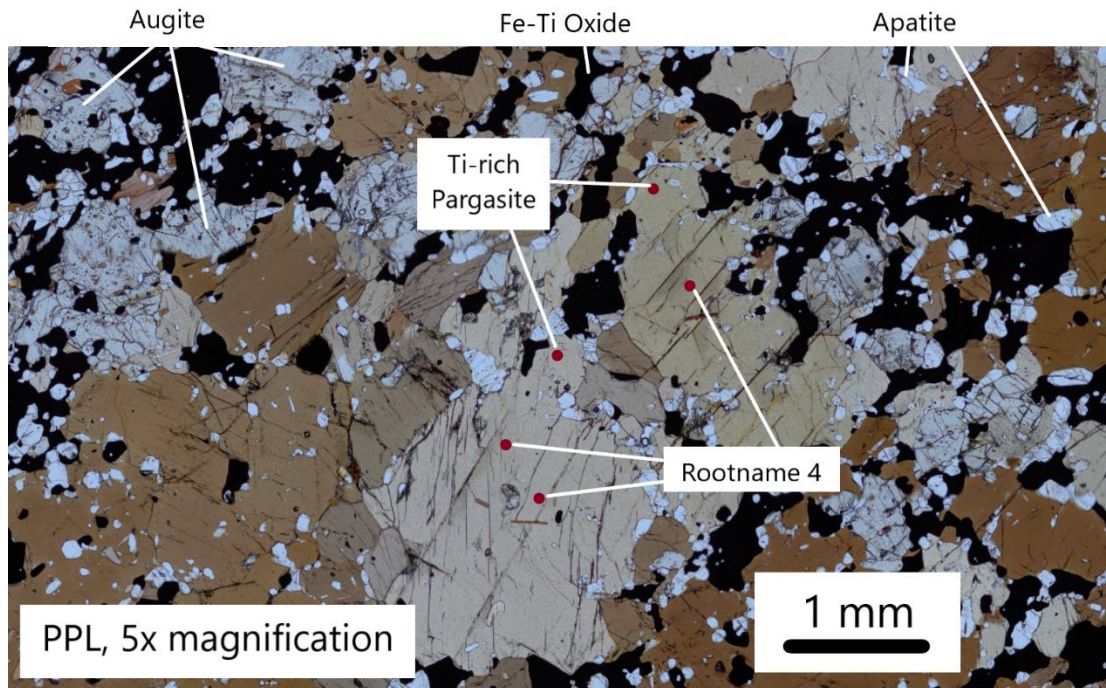


Figure 4-62: Plane polarized, 5x magnified photomicrograph of fine to medium grained Fe-Ti-P rich rock (503). EPMA spots (red dots) reveal how the two amphibole grains changes from "Rootname 4" amphibole in centre to Ti-rich pargasite close to the grain boundary.

The general formula for amphibole is  $AB_2C_5T_8O_{22}W_2$  and serves as the premise Hawthorne et al. (2012) founded the classification system for EMPA analyses. Locock (2014) developed open-source Excel spreadsheets for calculation of ion- site occupancy and rootname classification. The classification divides the amphibole supergroup into two groups based on the W- site occupancy of either  $^W(OH, F, Cl)$  dominance or  $^WO$  dominance. The  $^W(OH, F, Cl)$  dominant amphiboles are further divided into eight subgroups based on dominant charge- arrangements and type of B- site cations (Hawthorne et al., 2012). The A and C cations are used to assign names which specifies compositional variances within the subgroup (ibid). Table 9 show the common occupying ions and their site preferences, and Figure 4-63 depict the continuous discrimination from supergroup to rootname for the analytes in this study. Table 10 yield the result of the microprobe analysis, Table 11 provides the respective endmember formula and Figure 4-64 show how the analytes plot on classification diagrams.

Table 9: Amphibole sites and common occupying elements (Hawthorne et al., 2012).

Site	Cations/ anions
A	$\square$ , Na, K, Ca, Pb, Li
B	Na, Ca, $Mn^{2+}$ , $Fe^{2+}$ , Mg, Li
C	Mg, $Fe^{2+}$ , $Mn^{2+}$ , Al, $Fe^{3+}$ , $Mn^{3+}$ , $Cr^{3+}$ , $Ti^{4+}$ , Li
T	Si, Al, $Ti^{4+}$ , Be
W	(OH), F, Cl, $O^{2-}$

Table 10: Results from EPMA analysis of amphiboles (Locock, 2014).

Sample	Subgroup	Species
503-Z1-amp-1-c		Rootname 4
503-Z1-amp-1-m		Rootname 4
503-Z1-amp-1-r		Ti-rich pargasite
503-Z1-amp-2-c	Ca	Rootname 4
503-Z1-amp-2-r		Ti-rich pargasite
503-Z1-amp-3-c		Rootname 4
503-Z1-amp-3-m		Ferri- Rootname 4
503-Z1-amp-3-r		Ferri- Rootname 4
536-Z1-Amp-01-c1		Richterite
536-Z1-Amp-01-c2		Richterite
536-Z1-Amp-02-c1		Ferri-fluoro-katophorite
536-Z1-Amp-02-c2		Ferri-fluoro-katophorite
536-Z1-Amp-03-c1		Richterite
536-Z1-Amp-03-r1	Ca, Na	ferri-katophorite
536-Z1-Amp-04-c1		Richterite
536-Z1-Amp-05-c1		Richterite
536-Z1-Amp-05-m1		Richterite
536-Z1-Amp-05-r1		Fluoro-richterite
536-Z2-Amp-01-c1		Richterite

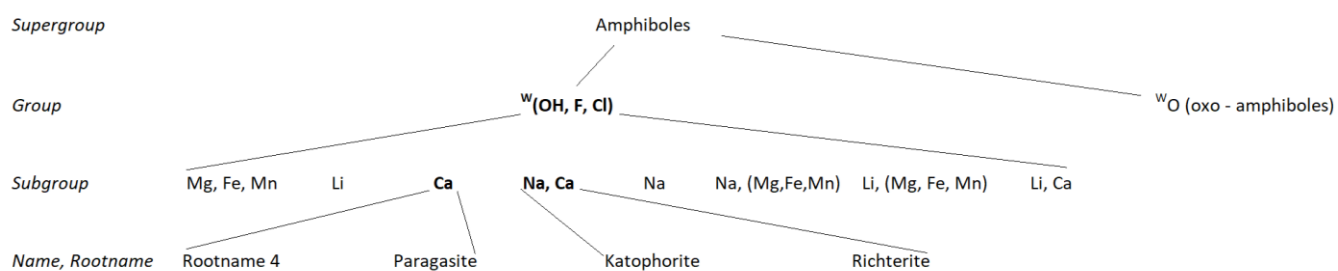


Figure 4-63: The division of amphiboles from "supergroup" to "rootname" (Hawthorne et al., 2012) with emphasis on the four amphibole species studied in this EPMA analysis.

Table 11: Species and end-member formula of amphiboles (Hawthorne et al., 2012).

Species	End-member formula
Rootname 4	$\text{NaCa}_2(\text{Mg}_4\text{Ti})(\text{Si}_5\text{Al}_3)\text{O}_{22}(\text{OH})_2$
Pargasite	$\text{NaCa}_2(\text{Mg}_4\text{Al})(\text{Si}_6\text{Al}_2)\text{O}_{22}(\text{OH})_2$
Katophorite	$\text{Na}(\text{NaCa})(\text{Mg}_4\text{Al})(\text{Si}_7\text{Al})\text{O}_{22}(\text{OH})_2$
Richterite	$\text{Na}(\text{NaCa})\text{Mg}_5\text{Si}_8\text{O}_{22}(\text{OH})_2$

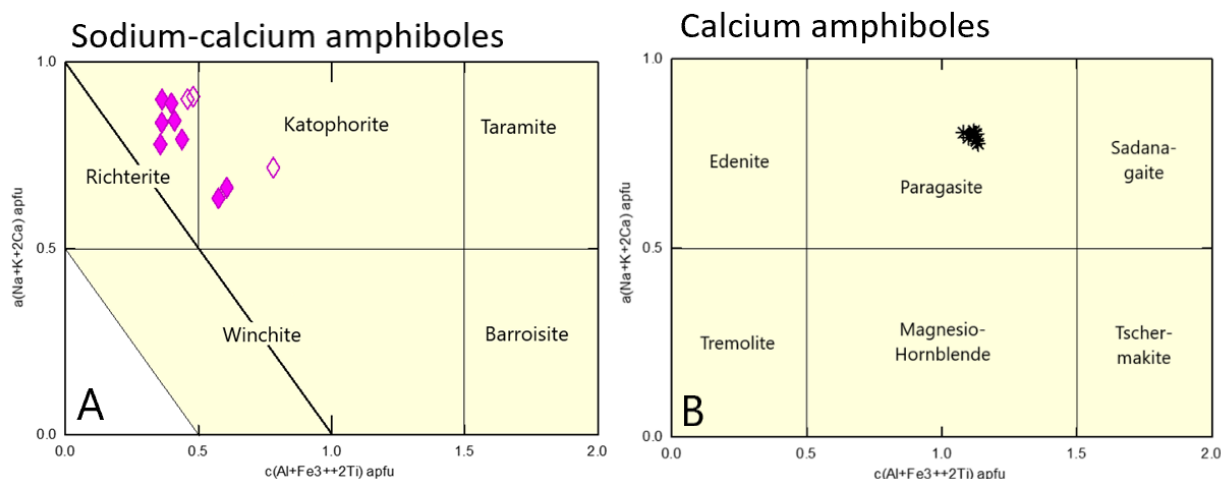


Figure 4-64: Amphibole classification based on subgroup- and rootname composition (Hawthorne et al., 2012). (A) Amphiboles from sample 536 plotted in the sodium- calcium scheme. (B) Amphiboles from sample 503 plotted in the calcium scheme, "rootname 4" does not plot in any diagram given by (Hawthorne et al., 2012) or (Locock, 2014).

Ti can be incorporated into amphibole by heterovalent cation substitution (Hawthorne et al., 2012). This type of substitution will lead to a new charge arrangement and hence a new root composition. Thus, C- site compositions with  $\text{Ti} > 0,5$  apfu involve new rootnames. A composition where  $0,50 > \text{Ti} > 0,30$  will be indicated as "Ti-rich". Ti rich pargasite and rootname 4 are relatively similar in composition, yet they are assigned different rootnames. (Figure 4-65) depicts how the Fe-Ti-P rich sample 503 with pargasite and rootname 4 amphiboles are high in  $\text{Al}_2\text{O}_3$  and  $\text{TiO}_2$  compared to the more  $\text{SiO}_2$ ,  $\text{MnO}$ , and  $\text{Na}_2\text{O}$  rich richterite and katophorite from 536. The Ca- rich amphiboles (503) show a tight grouping in all diagrams, while the Na-Ca amphiboles (536) have comparably large internal variations.

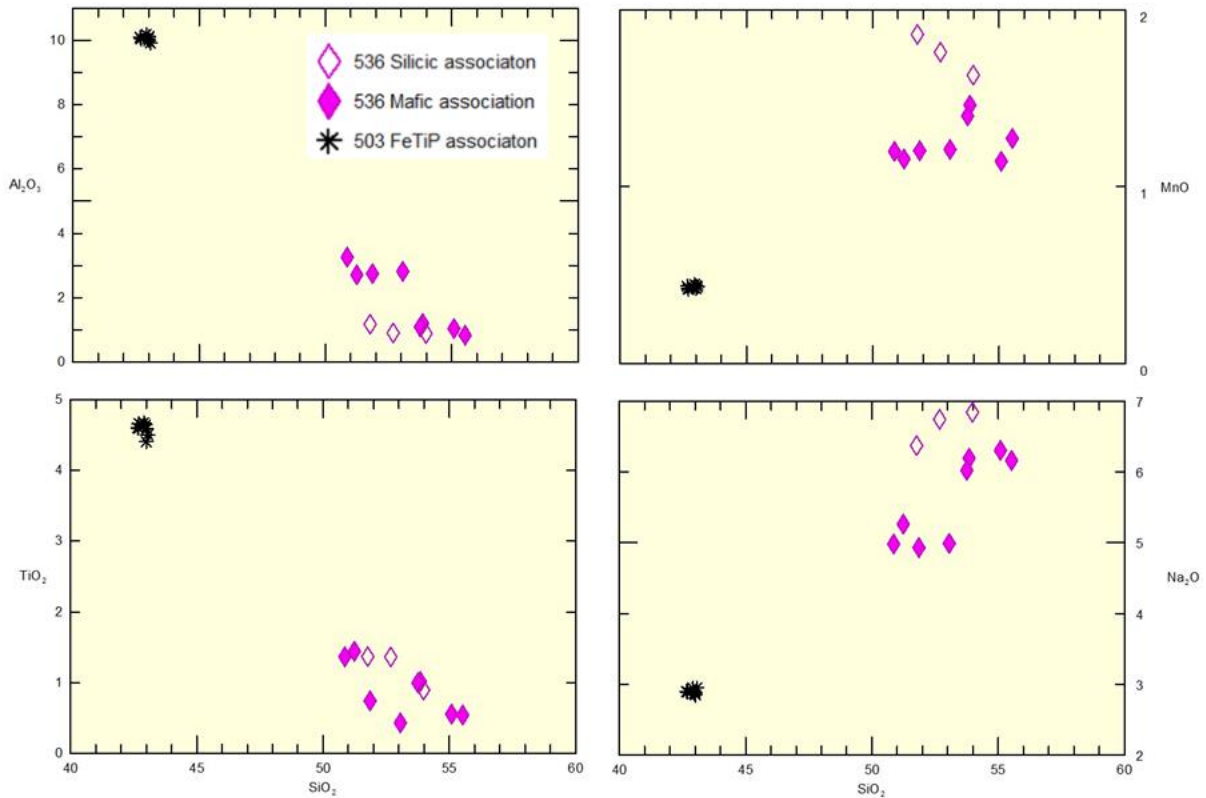


Figure 4-65: Binary diagrams plotting amphibole content of  $Al_2O_3$ , MnO,  $TiO_2$ , and  $Na_2O$  against  $SiO_2$  content (536 and 503). Concentrations in wt.%.

#### 4.3.2.6 Mineral Analyses Summary

Microprobe analysis of Fe-Ti-P rich samples reveal the felspar comprises of two phases, oligoclase and anorthoclase. Oligoclase occurs mainly as felspar phenocryst cores while the anorthoclase occurs as rim zonation and as interstitial crystals in the Fe-Ti-P rich groundmass. All measured biotite (sensu lato) plot as phlogopite, pyroxene as augite and amphibole as pargasite and "rootname 4". All mineral phases in the Fe-Ti-P rich samples are enriched in Fe, Ti, Ca, and Sr compared to the syenitic sample. The felspar in the syenitic sample comprises of anorthoclase cores with alteration rims of K- and Na felspar. The amphiboles plot as richterite and katophorite. All analysed mineral phases in the syenite are generally richer in Na and K, and minerals with analysed anion site composition (phlogopite, apatite) have incorporated a higher content of F.

Apatite analyses reveal the Fe-Ti-P associated apatites from Eiriks Gruve has the highest content of REEs. The REE content of the apatites from the Kåsemyrene Mines is comparable to the content of the apatites from the granitoids but has less internal compositional variation. The syenitic apatite REE spider diagrams show great internal variation. The apatite Harker plots reveal Fe-Ti-P associated-, and granitoid associated apatites commonly form two separate trend lines.



## 4.4 Results Geomagnetic study

Sampling for a geomagnetic study were conducted for mainly two purposes. First, to determine if any of the larger Fe-Ti-P rich ore bodies created magnetic anomalies on present geomagnetic maps available from NGU, and secondly to determine what might cause the extreme negative magnetic anomaly in the north of the field area (seen as the blue spot coinciding with the rhomb porphyry samples in Figure 4-69). The results yield a Königsberger Plot (Q-plot, Figure 4-66) and stereonet plotting NRM values (Figure 4-67 and Figure 4-68). The magnetic field for Siljan were obtained at (NCEI, 2020), and further results are presented in Appendix A.

### 4.4.1 Königsberger -Plot

The Q-plot (Figure 4-66) show three distinct groups based on lithology and Q-values. The rhomb porphyry cluster (521, 524, 525) is extremely NRM dominated, with a ratio ranging from 2365 to 5946. The rhomb porphyry outliers (plotting with the syenites) are sample 528 and 537. The syenitic cluster plot mainly with a Q-value between 1 and 10. The Fe-Ti-P rich rocks represent the last cluster, which form a vertical trend with stable induced magnetisation and increasing remanent magnetization. Only three samples plot with Q-values lower than  $Q = 1$ , namely the porphyritic Fe-Ti-P rock 514\_2A, the fine-grained syenite 520 and porphyritic syenite 535.

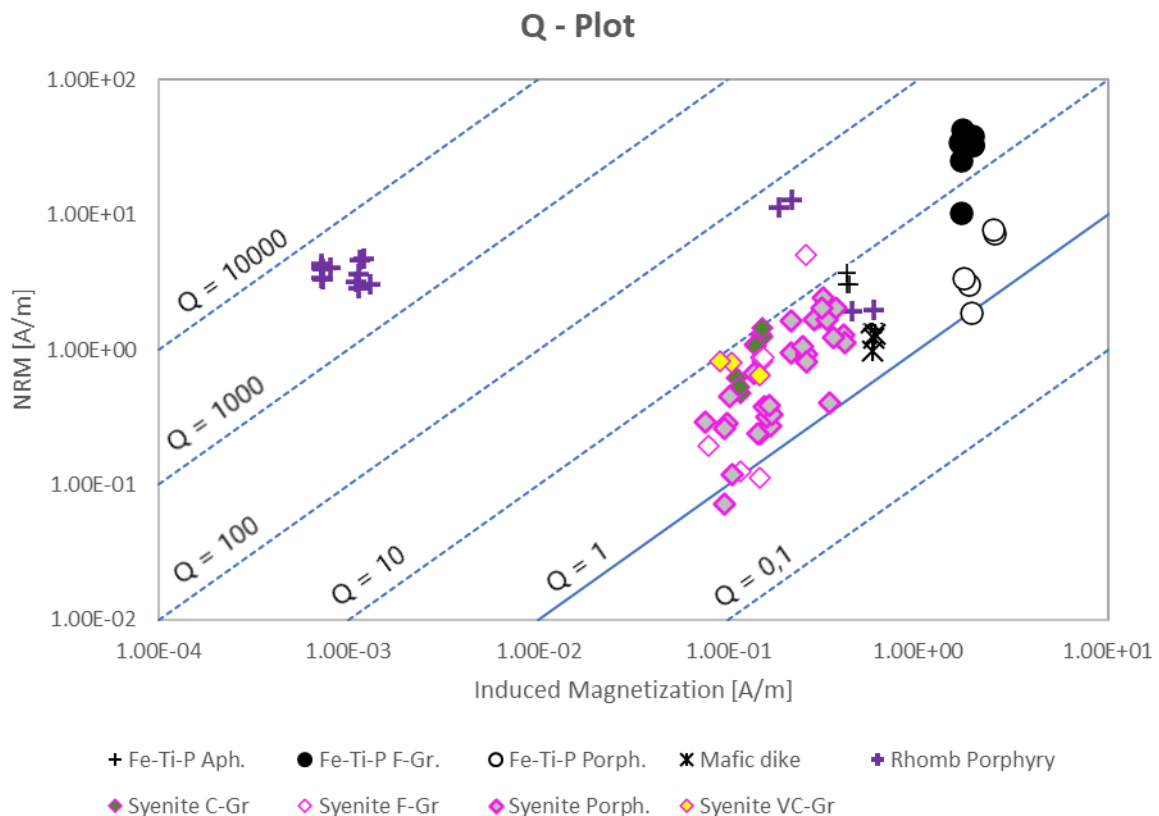


Figure 4-66: Q plot based on lithologies.

#### 4.4.2 Remanent magnetization assessment

The rhomb porphyries (524, 525 and 537) have natural remanent magnetic vectors pointing on the upper hemisphere with, where each sample show little internal variation (Figure 4-67 A). The remanent vector of sample 524 is approximately oppositely directed of the present-day field (003.4/72.4). Sample 521, 525 and 528 plot south- southeast where the two former plunge down between 4 and 21 degrees and 528 rises upwards 8 degrees. The average value for the rhomb porphyry samples is 149,8/-21,1 (trend/plunge).

Figure B shows the NRM vectors of the Fe-Ti-P rich rocks. There appear to be no common orientation for the samples. Additionally, are sample 504s two vectors divided by 91.1 (or 88.9) degrees. The same divide can be observed for sample 505, where two vectors point up and two vectors point down with 93,1/86,9 degrees between. Figure C and D reveal a high proportion of the syenitic samples plot close to the present-day field. Sample 531, however, form a grouping on the opposite side of the stereo net. Figure 4-68 show the average NRM vector for the syenite and rhomb porphyry samples plotted together with the present-day field. The shortest angle from the present-day field to the two average vectors is 15,9 and 54,7 degrees for the syenite and rhomb porphyry, respectively. Table 12 contain the statistics for the calculation of the syenite and rhomb porphyry averages.

*Table 12: Mean vector trend and plunge for syenites and rhomb porphyries. Upper hemisphere represented by "+", and lower hemisphere "-".*

<b>Syenites</b>							
	N	Trend	Plunge	a95	a99	kappa	mean length
all	48	309.3	72.3	--	--	1.5	0.3397
(+)	34	5.7	73.5	16.4	20.6	3.2	0.7001
(-)	14	231.5	-51.8	29.7	38.3	2.6	0.6635
<b>Rhomb Porphyries</b>							
all	16	149.8	-21.1	27	34.7	2.8	0.669
(+)	3	102.6	27.7	--	--	1	0.5375
(-)	13	156.4	-26.9	22.9	29.5	3.9	0.7828

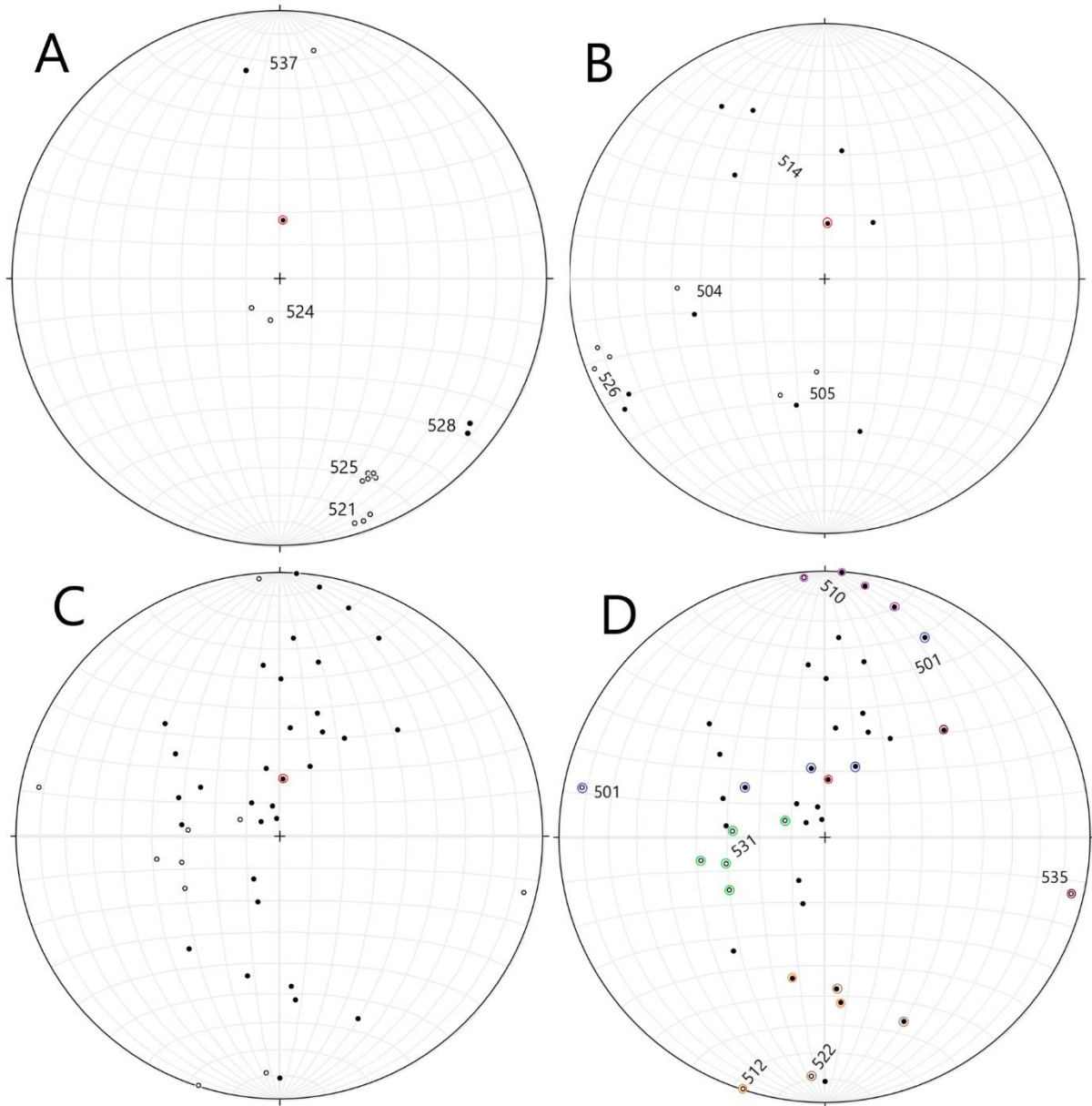
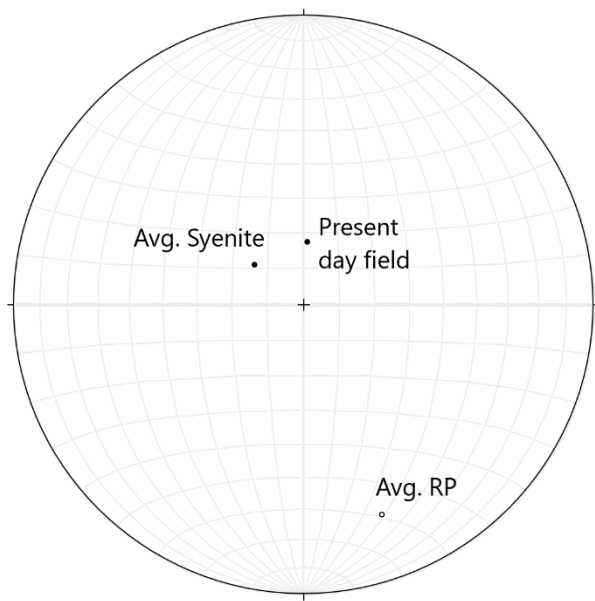


Figure 4-67: Stereo nets of (A) Rhomb porphyry, (B) Fe-Ti-P rich rock, (C) all syenites and (D) all syenites with highlighting of the samples with the highest deviation from the mean vector. The red dot in all stereo nets represent the present-day magnetic field at Siljan.

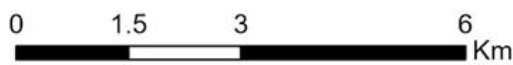
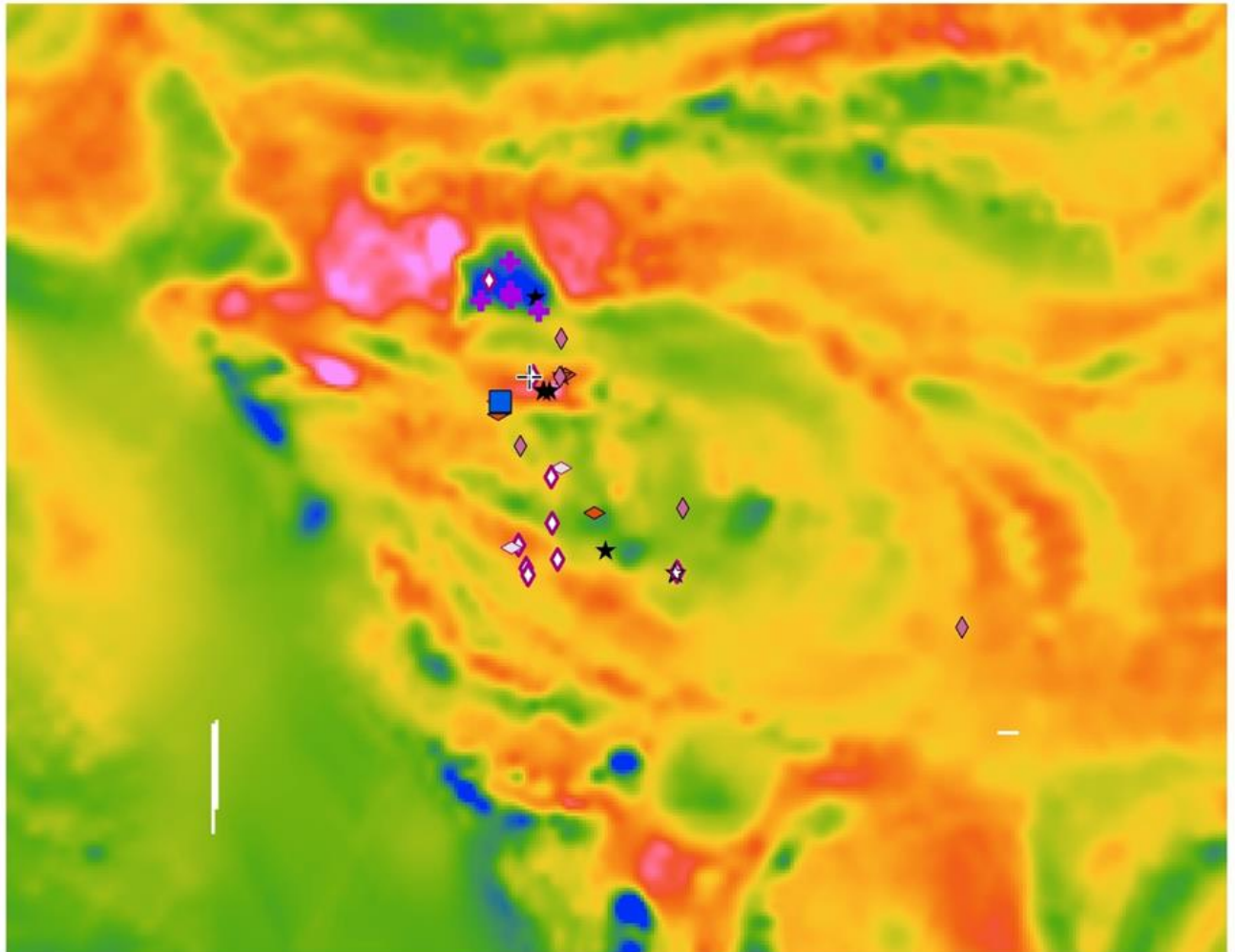


*Figure 4-68: Average magnetic NRM vector of syenites and rhomb porphyry (RP) plotted with the present-day field.*



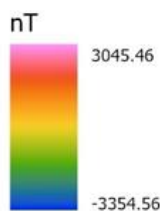
# GEOMAGNETIC MAP

## SILJAN - HVARNES INTRUSION



### Rock units

- |                      |                  |
|----------------------|------------------|
| ★ Fe-Ti-P F-Gr       | ◇ Syenite C-Gr   |
| ☆ Fe-Ti-P Porph.     | ◇ Syenite F-Gr   |
| ⊕ Monzodioritic Dike | ◇ Syenite Porph. |
| ■ Monzonite Porph.   | ◇ Syenite V.C-Gr |
| ⊕ RP                 |                  |



Spatial Reference  
PCS: ETRS 1989 UTM Zone 32N  
GCS: GCS ETRS 1989

By: Tord Andersen

Figure 4-69: Geomagnetic anomaly map of the westernmost pluton in the Siljan-Hvarnes Intrusion. Several ring structures form within the last pluton in the Siljan- Hvarnes intrusion. Most porphyritic syenites plot on the transition from medium (yellow) to high (red) magnetic anomaly. Rhomb porphyries plot on top of a large negative magnetic anomaly. Fe-Ti-P rich rocks plot on transition zones from either high to medium (Kåsemyrene) or medium to low (537 (northernmost), Jernskottet and Eiriks Gruve).

## 5 Discussion

### 5.1 Overall assessment: The Siljan- Hvarnes intrusion

#### 5.1.1 Emplacement depth

Pedersen et al. (2005) concluded the present-day surface level is equivalent to a depth of 2 – 3 km compared to when the volcanism was most active during the Permian period. Pedersen et al. 1995 dated the Siljan- Hvarnes complex to be 277 Ma. This is equivalent to late stage III in the geological development of the Oslo rift. This stage marks the transition from extrusive volcanism with rhomb porphyry and larvikite batholiths to the forming of more felsic central volcanoes and later caldera forming (Larsen et al., 2008). There has been no effort in calculating the pressure regime of the pluton. However, two field observations stand out as further supporting the current depth estimates of Siljan:

Firstly, miarolitic pods and cavities are common in all syenites. These were created when fluids segregated from the melt and were trapped in the pluton. These relics of trapped volatiles are usually found in shallow parts of the magma chamber where pressure was low enough to allow for fluid separation. The release and migration of H<sub>2</sub>O causes an increase in the solidus temperature of the main magma, which leads to rapid crystallization. This is a common way of forming porphyritic texture in silicic plutons (Winter, 2001; Jans and Burnham, 1969).

Secondly the lithological intrusive contact between the syenite and rhomb porphyry can be used to approximately estimate the depth. The Siljan intrusion is located in the Vestfold plateau which is estimated to have experienced more than 40 separate extrusive flows of rhomb porphyry, accumulating to an approximately three kilometres-thick sequence on top of the basalt sequences and Precambrian bedrock (Oftedahl, 1952, 1953, 1978a; Larsen, 1978) within Sundsvoll et al. 1990). As there have been no observations of basalt sequences in the field area, it is reasonable to assume that the pluton has intruded a significant distance up into the rhomb porphyry. Without knowing the extent of erosion of the Permian rocks, it is still possible to assume that the present-day surface-level cannot be more than ~3 km deep into the Permian crust.

### 5.1.2 Rhomb porphyry

The rhomb porphyry forms a massive sequence north in the field area (Sample map) and based on the variance in phenocryst size and shape, it is assumed the mapped area include several lava flows even though no contact were located. Rhomb porphyries in the Vestfold graben is Rb-Sr dated to be between 291 +/- 18 Ma and 294 +/- 6 Ma (Sundsvoll and Larsen, 1990). The lower sections of the RP sequence contain occasional basaltic flows, whereas the upper part contains trachytic and ignimbritic flows (Oftedal, 1953; Ramberg and Larsen, 1978; Larsen and Sundsvoll, 1983. Sources from Pedersen et al. 1995). The Siljan- Hvarnes intrusion is dated to 277.3 +/- 0,8 Ma, which separate the extrusive and intrusive events with approximately 14 Ma.

Rhomb porphyry sample 525 is silica undersaturated (Figure 4-35) and plots as one of the richest samples in  $Al_2O_3$ , MgO,  $Fe_2O_3$ , TiO, CaO,  $K_2O$  and  $P_2O_5$  in the Harker diagrams (Figure 4-38) It plots between the monzonitic and syenitic samples regarding average whole rock REE values (Figure 4-39 to Figure 4-41) and displays no consequent Eu anomaly (Figure 4-41). The LA-ICP-MS apatite analyses of rhomb porphyry sample 524 contains the only apatites which has positive Eu anomalies. The crystals with a positive anomaly occur as inclusions in a mafic enclave within a feldspar phenocryst and might represent apatites crystallized in a different magmatic environment compared to the apatites found in the ground mass (which display negative Eu anomalies) (Figure 4-58).

Figure 4-3 depicts a trachytic syenite intruding the rhomb porphyry sequence where the lithological contact changes from sharp to irregular over a span of one meter. The intrusive syenite contains a rhomb porphyry xenolith with locally rounded edges and internal cm scale blebs of red melt. The same red blebs can be observed under the sharp contact in the lower left part of the figure. The red blebs are interpreted to represent small, networked intrusions of syenite following fractures in the rhomb porphyry. The irregular contact between the rhomb porphyry and the syenite and the rounded shape of the xenolith does probably represent heating of rhomb porphyry to a ductile state. However, there are little evidence for pervasive assimilation of the rhomb porphyry side and wall rock in the syenitic intrusion.

Firstly, there are no evident observations for a metamorphic aureole around the pluton. A metamorphic aureole refers to the alteration in composition, structure, or texture of the host rock in contact with an igneous intrusion (Richards and Collins, 2002). Secondly, according to Tegner et al. (2006), is assimilation which largely alters chemical composition associated with deeply situated and large magma chambers emplaced into metasedimentary country rocks. Calculations suggest 75% of the heat energy in the magma chamber went to melting xenoliths which caused the assimilation (ibid). Thus, assimilation of rhomb porphyry consisting of an intermediate composition (estimated melting temperature of 1050-1100°C (Larsen, 1978)) in the syenitic magma is therefore regarded as highly unlikely. Further, Neumann (1980) and Neumann et al. (2004), suggest assimilation might have occurred between larvikite and country rock during the ascension to emplacement in magma chamber, but states there are no clear evidence. Neumann (1980) proposes that assimilation of nordmarkite and sedimentary rocks formed the rock type akerite found north of Oslo. Borg, (2011) does not find evidence for this and suggests akerite follow the evolutionary trend from larvikite towards more silica-rich nordmarkite. Hence, no literature suggest assimilation took place anywhere in the Oslo graben area.

To conclude, the rhomb porphyry flows formed approximately 14 Ma before the Siljan-Hvarnes intrusion formed. The syenitic pluton were partly (or entirely?) emplaced in the rhomb porphyry, and field observations indicate assimilation of wall- and roof rock were improbable in the shallowly placed magma chamber. Thus, in situ assimilation of rhomb porphyry and fractional crystallization (AFC) (Tegner et al., 2006) is most likely not a Fe-Ti-P rich rock forming process. However, assimilation of the magma at a deeper and earlier stage cannot be ruled out.

### 5.1.3 Medium to coarse grained syenite

The medium to coarse grained syenite occurs mainly in the center of the pluton and represent a common and relatively homogeneous lithology. E.g., the medium to coarse grained syenite in Figure 4-61 (536). Field observations suggest Skriua mountain (Figure 5-1) mainly consists of this lithology. In addition to being texturally homogeneous, are the samples also geochemically homogeneous. The TAS plot and Harker bulk rock figures (Figure 4-35 to Figure 4-41) show the medium to coarse grained syenites plot as the most evolved rocks in the monzonite- syenite trend with little variation between samples. However, sample 531 form a geochemical outlier in the medium to coarse grained syenite-group and are geochemically more like the trachytic to porphyritic syenites. This specimen is sampled from an area between Søllandliene and the area of trachytic and porphyritic syenites and it is likely sample 531 related to this group.

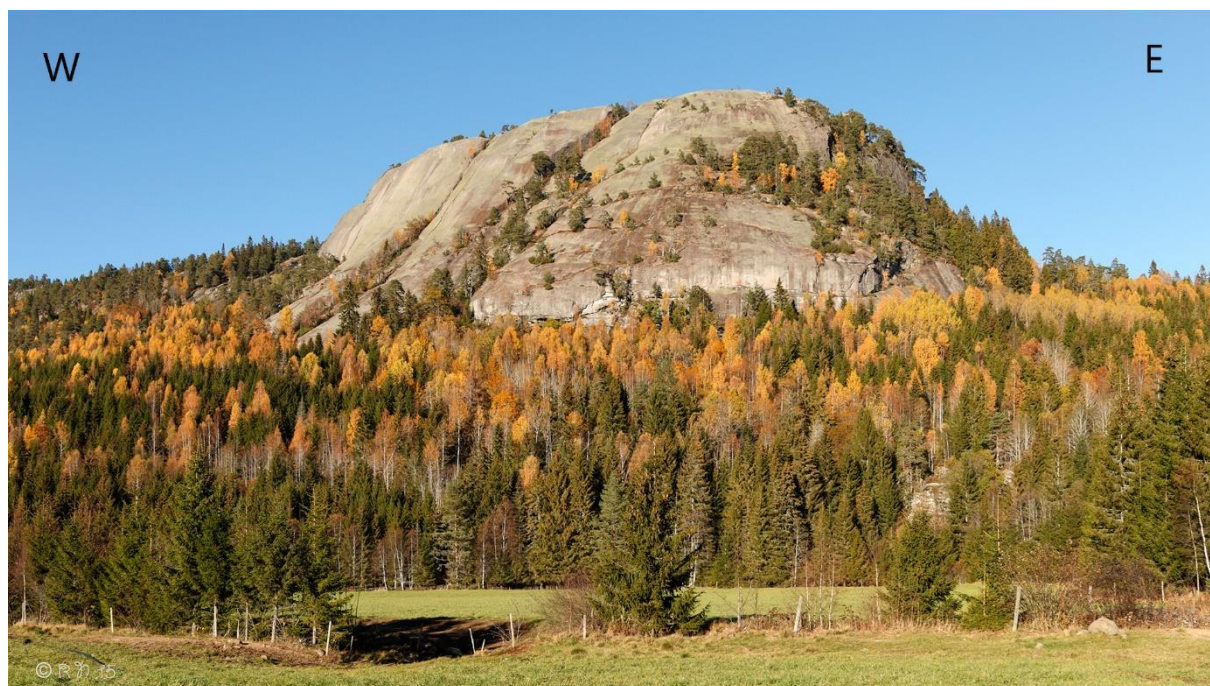


Figure 5-1: Skriua as seen from Kåsemyrene. The mountain consists of relatively homogeneous medium to coarse grained syenite. Foto from norgefoto.no with permission from Reidar Nordkveldmoen.



Approximately all medium to coarse grained syenitic samples have large negative Eu-anomalies (Figure 4-41), suggesting an origin from a melt depleted in Eu. This might be due to early crystal fractionation and removal of Ca-rich minerals which accommodated  $\text{Eu}^{2+}$ . Only sample 502 have a positive Eu-anomaly ( $\sim 1,55$ ). This sample is from key location Kåsemyrene, and the high anomalous value might be associated with the formation of Fe-Ti-P rich rock (Section 5.1.8).

Microprobe feldspar analysis of the medium to coarse grained syenite (536) reveal the feldspar is mainly anorthoclase, with zoned rims plotting as either K-feldspar or Na-feldspar. The alterations are especially pronounced around  $\mu\text{m}$  scale veins following feldspar grain boundaries and cutting feldspar crystals. The forming of veins and alteration with redistribution of alkalis imply sub solidus hydrothermal alteration (Pirajno, 2013).

The presence of a post solidus hydrothermal fluid is further supported by the observations of zonation in amphibole. The amphiboles occur in interstitial mafic enclaves and comprises of richterite cores with zonation of either blue green fluoro-richterite or blue green katophorite. The richterite cores are brown with prominent amphibole cleavage and are therefore interpreted to be primary crystals. The fluoro-richterite and katophorite does not have cleavage and show local fibrous habitus, and are therefore interpreted to be secondary.

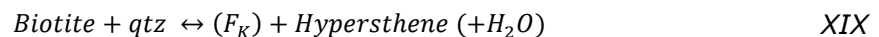
Last remark on the hydrothermal alteration is the high F content measured in apatite, phlogopite and amphibole in sample 536. The high F concentrations related to the zoned minerals and secondary mineral phases might imply the hydrothermal fluids were enriched with F volatiles. Larsen et al. (2008) remarked the rhomb porphyry magma were extremely enriched in F. Even though the rhomb porphyry and Siljan-Hvarnes Intrusion stem from separated magma sources, these observations might imply high concentrations of F was a common volatile in several magmas occurring in the Oslo Graben. Note that the observed alterations are not limited to sample 536 from Skriua, but are documented in in syenites mingling with Fe-Ti-P rich rock at Eiriks Gruve (thin sections 516, 517) and in coarse grained syenites east of Oppdalsvannet (TS 765).

#### 5.1.4 Very coarse-grained syenite

The very coarse grained syenite can be sub divided into two groups: First, sample 519 which plot marginally to the syenitic side of the monzonite- syenite border (59 wt.%, Figure 4-35), and secondly as sample 764 with a relatively high SiO<sub>2</sub> content (63 wt.%). Sample 511 has not been geochemically analysed but is considered to be a syenite based on field observations and geochemical analyses of associated rocks.

##### 5.1.4.1 Sample 519 - Larvikite

519 represent a larger outcrop of homogenous very-coarse grained syenite which bears few signs of weathering compared to other very coarse- grained rocks encountered in the field. It appears undistinguishable from Larvikite (monzonite with iridescent feldspars), and it plots consequently close to the other monzonite samples in the granitoid classification diagram. Thin sections reveal local anhedral interstitial pockets filled with quartz, which is most likely why this rock is slightly enriched with SiO<sub>2</sub> and does not plot as monzonite. The occurrence of quartz further suggests the last interstitial melts were highly evolved. Mineral alteration textures of feldspars and mafic minerals indicate the presence of late-stage fluids permeating through the network of interstitial space. These evolved fluids were notably in disequilibrium with the mafic minerals, which might have caused the alteration of pyroxene to amphibole to biotite (Figure 4-8). Disequilibrium is further evident in the symplectite which form during breakdown of unstable phases (Figure 4-9). The symplectite might represent the following eutectic transformation (Bard, 1986b):



F<sub>K</sub> represent free K<sup>+</sup> ions which might be transported from feldspars in a fluid phase.

519 stand out from practically all other samples by having the second highest measured Eu anomaly. This is most likely due to the rock being formed by accumulation. The possibility of a relative enrichment of Eu due to melt separation and apatite crystallization is ruled out as the REE content (Figure 4-43) is insignificantly lower compared to the other monzonites, and the sample is still relatively enriched in Mg, Ti, Ca, and P. Thus, this rock is has most likely not undergone large scale magma separation.

The very coarse-grained syenite in sample 519 is therefore assumed to be larvikite with highly evolved interstitial magma. Where it stems from is uncertain, it might be transported as a large unit of mingling magma or represent an individual intrusion from a nearby evolved larvikite magma chamber. No lithological contacts to the 519 unit were found, and field relations are therefore not included.

##### 5.1.4.2 Sample 764

Sample 764 were collected at key location Kåsemyrene – Parking (Chapter 4.2.2.1). Geochemical analysis of the sample reveal it plots similarly as the group of medium to coarse- grained syenites on the TAS, granitoid classification diagrams, Harker diagrams, and REE spider diagrams (Figure 4-35 to Figure 4-41). It is therefore likely the very coarse grained syenite originate from the same magma as the medium to coarse grained syenite. Sample 764 (Figure 5-2) might represent a local zone or pocket with a higher concentration of feldspars in the size range of 2 - 3 cm. The accumulation of large feldspars might be attributed to sorting of phenocrysts by density contrast and/ or internal convex flows (Winter, 2001)

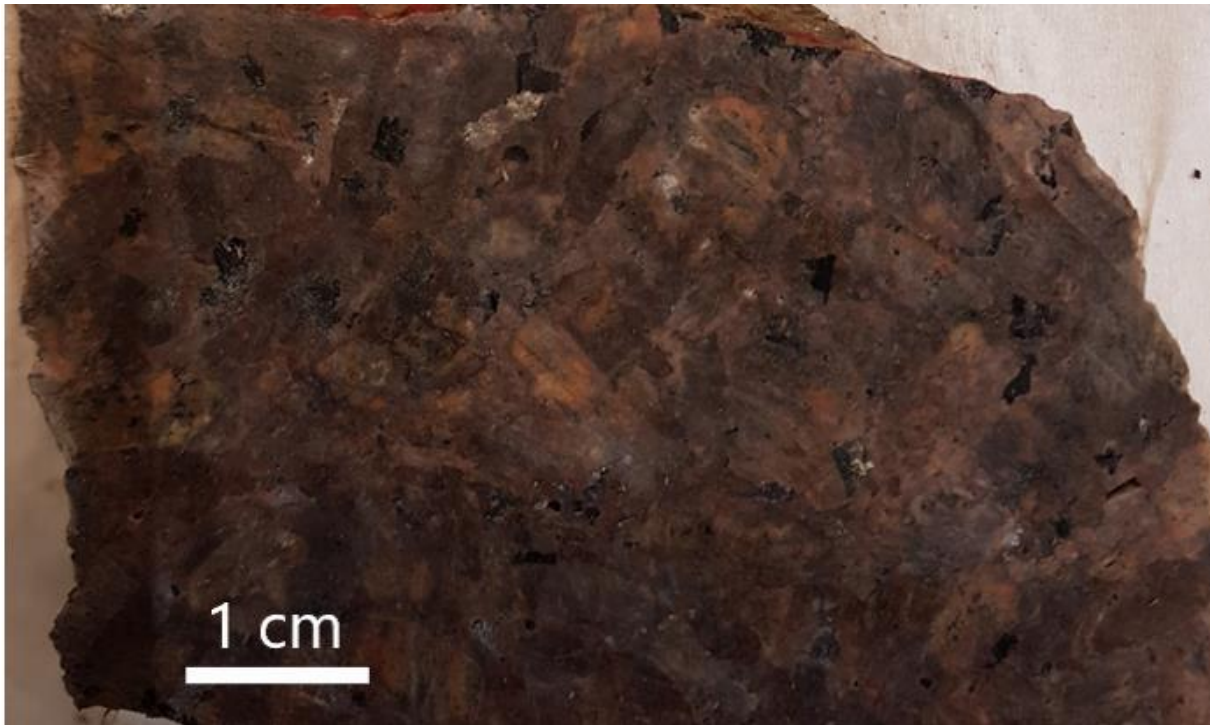


Figure 5-2: Cut slab of very coarse- grained syenite from Kåsemyrene, sample 764.

#### 5.1.4.3 Sample 511

Sample 511 were too small to for a whole rock analysis and have therefore not been geochemically analysed. The outcrop at Key- Location Sjøllandliene (chapter 4.2.3) reveal the very coarse-grained syenite is associated with the fine-grained quartz monzonite (512 B) which create a layer between the coarse grained syenite and the trachytic- porphyritic monzonite. Figure 4-31 and Figure 4-32 depicts a rectangular body of very-coarse grained syenite occurring as a xenolith in the porphyritic- trachytic monzonite, where red, fine-grained quartz monzonite create an interstitial network in the very coarse-grained syenite. Quartz monzonite additionally show branching of veins radiating out from the very-coarse grained syenite and into the porphyritic monzonite.

As discussed previously, the megacrystic rocks have most likely been transported from a different, deeper situated magma chamber. The relations at Key Location Sjøllandliene suggest the fine-grained quartz monzonite have been transported through a permeable network between the megacrysts, which created a solid network with interstitial melt. An induced high pressure might be the reason why the fine-grained quartz monzonite was squeezed out of the megacryst matrix and injected as veins into the surrounding porphyritic- trachytic monzonite.

#### 5.1.5 Porphyritic-trachytic quartz monzonite

This rock type appears to be location specific to Sjøllandliene, and only one sample (512 B) plot with quartz- monzonitic geochemistry (TAS-diagram and figure 512 B). As discussed in the previous paragraph; this rock show close field- relations to the very coarse-grained syenite where it forms an interstitial network, as well as a boundary layer to the porphyritic- trachytic monzonite. (Figure 4-28, Figure 4-30 and Figure 4-31). This rock may therefore represent magma being transported in the megacrystic mush, which created a permeable rigid network.

Bulk composition diagrams reveal this rock is as silica rich as the coarse grained syenites, but that is the end of the similarities; the quartz monzonite is rich in Mg, Fe, Ti, Ca, and P, and low in Na and K. Thin section study reveal the sample has more ternary feldspar than the syenitic samples, as well as ~10 modal% biotite and amphibole, and only minor amounts of oxides. Trace element analysis reveal the rock is relatively low in REEs, especially LREE ( $La_N$  values of ~ 350 compared ~600 for monzonites and ~430 for syenites). However, it is relatively enriched in HREE, with  $Lu_N$  values of 43 compared to 30 for syenites.

Apatite analyses reveal the quartz monzonite plot with higher Sr contents than the syenites, and extremely high amounts of Zr in apatite, even though zircon only is an accessory mineral in the thin section and whole rock analysis suggests the Zr values are moderate to low (~500 ppm) compared to the rest of the samples.

Relative high amounts of mafic associated major oxides, P, and Sr values suggests the quartz monzonite stem from a more primitive melt than the syenites. Thus, quartz monzonite might represent melt which were injected or transported into the magma chamber together with the very coarse- grained syenite. The argument of a deeper, more intermediate source is supported by the extraordinary high amounts of Zr in quartz monzonite apatites; Hoskin et al. (2000) suggest zircon is only likely to be a liquidus phase in felsic and some intermediate melts. Zircon associated with mafic melt is therefore likely to have crystallized in trapped melt pools far from liquidus. It is therefore a possibility that apatite crystallization predates zircon crystallization in this potential deep magma chamber and thus accommodated much of the Zr before it rose.

(Borg, 2011) studied quartz monzonite (akerite) situated in the Nordmarka- Hurdal Batholith north of Oslo. In terms of bulk composition, akerite is ferroan, metaluminous, alkali – calcic, while the Siljan-Hvarnes quartz-monzonite is ferroan, metaluminous, alkalic. Magma evolution modelling in MELTS indicated akerite could be a product of fractional crystallization of a  $B_1$  – type basalt down to 1070 °C and at ~5 kb (ibid). Geochemical analysis strongly suggests a common source for the rhomb porphyry/ larvikites and the akerite (ibid). Further, U-Pb dating of zircon in the akerite suggested an emplacement age of 279 Ma (ibid). This is approximately 2 Ma before the emplacement of the Siljan- Hvarnes intrusion (277.3 +/- 0,8 Ma (Pedersen et al., 1995)).

To assess if the Siljan- Hvarnes quartz- monzonite is an akerite, falls outside of the scope of this thesis. However, the evolution of an akeritic magma which has geochemical similarities and predates the Siljan-Hvarnes intrusion with 2 Ma suggests the quartz monzonite in Siljan might have formed under similar conditions. Field observations of mingling magmas (Figure 4-28, Figure 4-30 and Figure 4-31) further support the claim of a different magmatic evolutionary trend for the trachytic quartz- monzonite.

### 5.1.6 Monzodioritic dike

The monzodioritic dike (Figure 4-13 and Figure 4-14) cutting through the coarse-grained porphyritic syenite (508) has a 40 cm displacement with full separation between the two parts. The brittle fracturing of the dyke associated with the cut, in addition to the aphanitic grain size imply the monzodioritic dike were completely crystallized when it fractured. The homogeneous coarse grained syenite however, show practically no signs of strain, and must have been able to accommodate the movement. The structure of the syenite must therefore have been a solid-framework mush where phenocrysts rested onto each other but were able to move due to sufficient quantities of interstitial melt. Further arguments for this are that if the syenite magma had less phenocryst support, the dike would most likely mingle, and create semi- connected, elongated mafic blobs (Winter, 2001) and if the syenite were too consolidated it would show similar brittle fracturing and faulting. A similar observation was done 50 m south of sample point 512 (Søllandliene).

The remains of a mafic dike cutting through a porphyritic syenite with a sharp contact between the two lithologies further support the theory of monzodioritic dikes impregnating the pluton on a stage where it is semi- consolidated. Figure (Figure 5-3 B) represent the only documentation of an elongated mafic blob which might imply mafic dikes intruded on an early stage in the forming of the pluton. The observation was done 300 m south-east of Key location Kåsemyrene, in the driveway to Søilverød farm. The relatively sharp contact of the blob indicates a relatively rapid cooling in the syenitic melt.



Figure 5-3: (A) Remains of a mafic dike cutting through porphyritic syenite, Søllandliene. (B) Elongated mafic enclave in medium to coarse grained porphyritic syenite.

### 5.1.7 Porphyritic and trachytic syenite

The porphyritic and trachytic rocks are mainly found along a 1,5 km long sampling transect stretching from Rødstjønn in the north to Frotjenn in the south (Figure 4-1). The lithology along the transect varies drastically over distances of 10 – 100s of meters, with changes in phenocryst orientation, alteration, size, composition, and modality. The groundmass varies from medium-grained to fine-grained and trachytic.

Figure 4-10 (sample 539) depicts 1 – 2 cm large, rounded grey and partly iridescent feldspar phenocrysts with 1 – 2 mm zonation along the rim. Sample 535 (Figure 4-11) contain euhedral prismatic feldspar phenocrysts ca. 0,5 cm long, and an enclave containing fragments of an almost fully resorbed iridescent feldspar phenocryst. Figure (Figure 5-4 A) depicts a weakly rounded rhombohedral 1 cm long phenocryst. (B) is a thin section scan of a phenocryst from sample/ location 538 (Figure 4-10). The phenocryst has a rounded core, semi-rounded blocky second rim and an undulating weak third zonation containing multiple embayments. Figure 4-10 depicts the outcrop from where the sample was collected, and the rock contains zoned pheno- to megacrysts. Note that the crystal in the thin section is not a megacrysts. The megacrysts appear as semi-rounded, pale cores with grey 2 – 4 mm thick rims.

Zonation of the phenocrysts in the porphyritic syenite indicate different degrees of resorption and recrystallization. Figure 5-4 A and Figure 4-8 (sample 534 and 539, respectively) have occasional euhedral phenocrysts with moderate rounding of edges and thin to no rim along the grain boundaries. The weak rounding is probably due to disequilibrium between the phenocryst and the groundmass. Figure 4-11 and Figure 5-5 (sample 535) depicts an almost fully resorbed phenocryst, where the remains of the phenocrysts are separated fragments with pronounced resorption rims. This would signify a stronger disequilibrium between phenocryst and melt compared to sample 534 and 539. The trachytic fine to medium grained ground mass suggest a relatively rapid cooling (Winter, 2001; Robb, 2015).

Figure 4-12 (538 outcrop) depicts weakly rounded, euhedral megacrysts which have grown in at least two stages. This suggests the megacrysts was stable in the magma and continued to crystallize a new zone of feldspar. The thin section (Figure 5-4 B) is from the same outcrop but does not include any zoned megacryst. The outermost zone has a subhedral form with intergrowth texture with the fine-grained groundmass, which suggests the outermost rim and groundmass were in equilibrium

Trace element analysis (Figure 4-39 to Figure 4-41) depicts the porphyritic and trachytic syenites plotting over a wide range regarding LILE. Sample 508 and 539 have highest Sr and Ba values, and lowest Rb and Cs values. This coincides well with having the highest Ca, and lowest K values, as Sr and Ba substitute for Ca, and Rb and Cs substitute for K. Sample 539 have a high modal percent of grey feldspar (Figure 4-11), which most likely are ternary- or plagioclase series feldspar containing Ca. Sample 538 and 534 show the opposite trend, and are among the samples with highest K, Rb and Cs content of all samples.

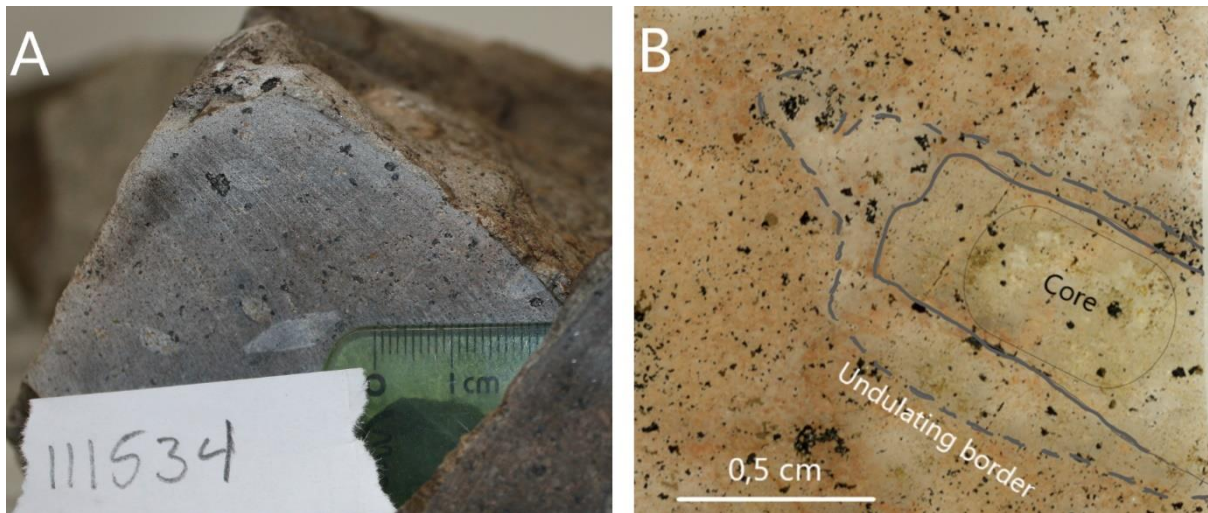


Figure 5-4: (A) rhombohedral feldspar phenocryst in sample 534. Ruler for scale. (B) Scan of thin section sample 538. Zoned feldspar phenocrysts in fine-grained matrix.

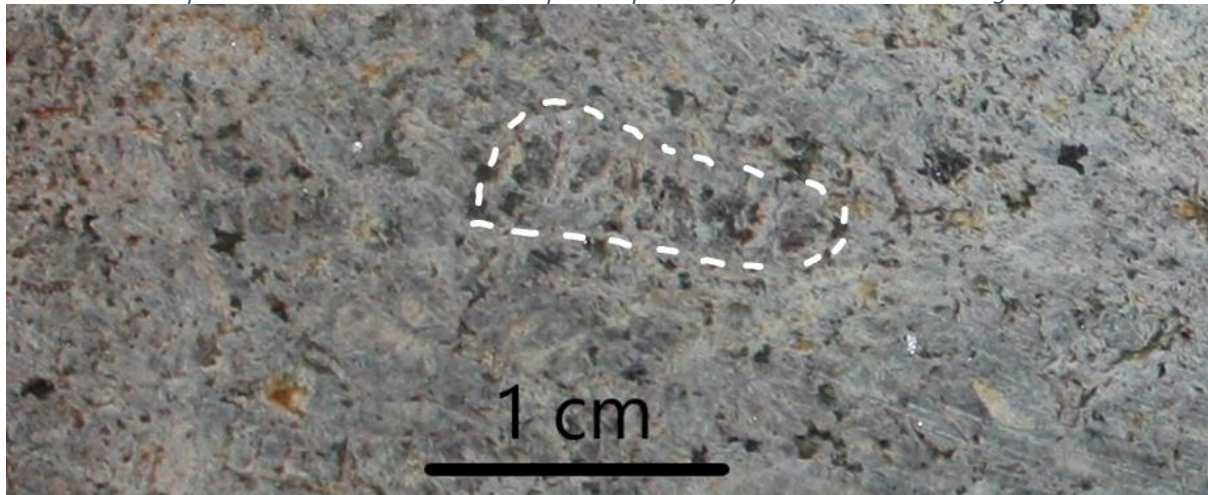


Figure 5-5: Highlighted area of the remains of a phenocryst almost completely resorbed along internal fractures (sample 535).

The porphyritic and trachytic syenites form a trend between the monzonites and the medium to coarse-grained syenite on both the TAS, iron-magnesian index, MALI, ASI and major oxides Harker diagrams. This suggests there could be an evolutionary trend from the monzonite, through the porphyritic syenites to the homogeneous medium to coarse-grained syenites.

Eu anomalies for the porphyritic and trachytic syenites is generally high, with positive value ( $>1$ ) for 508 and between 0,9 – 1,0 for 535, 538 and 539. (Note 508 is from Kåsemyrene, and not south of Rødstjønn like the rest of the trachytic and porphyritic syenites). High (positive) Eu- anomalies are usually ascribed to feldspar accumulation. While most of the trachytic to porphyritic samples have a low negative anomaly, the relative enrichment of Eu might imply porphyritic and trachytic syenites represent areas which accumulated early forming, thus slightly more primitive feldspars.

A plausible petrogenesis of the trachytic to fine grained syenite is that it formed early in the magma chamber and formed concentric zonation: Robb (2015), states concentric zonation is characterized by distal plutonic zones consisting of more mafic components compared to the central zones. This is largely attributed to the degree of fractionation the

magma underwent before crystallizing. When the granitoid pluton was emplaced at shallow depth, most of the heat was lost to side- and roof walls. This caused cooling and crystallization to commence along the boundaries of the magma- chamber and thus, the wall and roof zones crystallized with a less evolved composition.

However, this model alone does not explain the vast internal variations of major and trace elements observed in the trachytic and porphyritic syenites. (Figure 4-38, Figure 4-39 to Figure 4-41, and Figure 4-43). The pheno- and megacrysts are likely to be the products of partly crystallization of the magma at depth before the magma were transported and emplaced at current level. The great variance in phenocryst habitus, size, composition, and equilibria textures further suggests different crystalizing environments. As all key locations depict areas with magma mingling, it is not unreasonable to assume these rocks might be the product of either magma mixing and mingling. It is also not uncommon that granitoid systems consists of several magma pulses, which can be a contributing factor to magma mixing and/or mingling (Winter, 2001; Farina et al., 2012; Sommer and Kröner, 2019).

Lastly, the chemical variance of the trachytic and porphyritic syenites might be affected by metasomatic processes. The feldspars in thin section 538 are dusty and orange (Figure 5-4), which might be due to hydrothermal alteration. This might be one of the reasons why it plots with highly evolved composition. Additionally, sampling technique might represent a source for variance. E.g., sample 538 stem from a 50 m long outcrop containing pale megacrysts concentrated in zones by magma flow and accumulation. The analysed sample contained few to none of these megacrysts, and it is likely this affected the measured Ca content as the megacrysts are believed to be in the plagioclase series.



### 5.1.8 Fe- Ti- P rich rock

The Fe-Ti-P rich rock form m-scale mineralizations at Kåsemyrene, Eiriks Gruve and Jernskottet, and are encountered as ubiquitous smaller cm – dm scale veins, lenses, and patchy ores associated with syenites across the field area. The common traits of the occurrences appear to be that they accumulate at lithological contacts, with sharp contact to the footwall and often gradational contact to the hanging wall. Larger porphyritic ore bodies commonly show alignment of feldspar phenocrysts, where the crystals are oriented parallel to the lower contact (Figure 4-19 and Figure 4-23).

The Fe-Ti-P rich rock is characterized by feldspar phenocrysts surrounded by a fine to medium- grained mafic groundmass. The feldspar phenocrysts have oligoclase cores, and mm-scale anorthoclase rims. Anorthoclase is also found as an interstitial phase in the mafic groundmass. The mafic phase has modal composition of 20 – 50% augite, 20-30% ilmenite and titanomagnetites, 20-40% biotite and/or amphibole and 5-10% apatite. Monazite, olivine, sphene and sulfides are found as accessory minerals. Apatite represents a mineral phase found both as needle-like inclusions in feldspar phenocryst cores and as densely spaced subhedral to euhedral prismatic crystals in the mafic groundmass. It is therefore assumed to have reached liquidus at an early stage.

Geochemically, the Fe-Ti-P rich rock is extremely enriched in incompatible elements such as the REEs (especially LREE) compared to the host syenite. The whole- rock content of TREO is varying from 0,1 – 0,3 wt.% while TREE is up to 7 wt.% in apatite associated with porphyritic Fe-Ti-P rich rock in Eiriks Gruve. The content of Cr, Co, Ni, Cu, Pb and Zn, however, is often lower than the detection limit for XRF analysis.

#### *5.1.8.1 Review of petrogenetic processes*

A large body of Fe-Ti-P rich rock located in Kodal shares many of the chemical, textural and mineralogical properties as the Fe-Ti-P occurrences in Siljan (Jensen, 1991; Kragh, 1991; Ihlen et al., 2014). The origin of this deposit has been discussed over decades, and there is still not a unison consensus among academics (Bergstøl, 1972; Lindberg, 1985; Andersen, T., Seiersten, M., 1994; Ihlen et al., 2014). Since there are no articles discussing the occurrences in the Siljan intrusion, the petrological discussion of the Kodal deposit is deemed applicable as the systems are sufficiently alike.

##### 5.1.8.1.1 Fractional Crystallization

Lindberg (1985), argues the deposit stem from accumulation of mafic minerals fractionated in situ from a monzonitic parent. Andersen and Seiersten (1994) support the theory of fractional crystallization, but argues the fractionation took place at the middle to lower crust from an ijolitic parent magma. The mafic cumulates were then trapped in ascending monzonitic magma and emplaced at shallow depth.

There are some common geochemical patterns which can be expected in rocks created by fractional crystallization. Mafic minerals, which crystallize early, tend to be enriched in compatible elements, and incompatible elements such as REEs and HFSEs partition into the liquid phase. Thus, REE enrichment would be expected in the last mineral phases to crystallize. However, whole rock analysis from this thesis reveals strong contrasting results where the mafic Fe-Ti-P rich rock is the most enriched in REEs (Figure 4-42). This trend is also evident in Figure 5-6 (below), which reveal a moderate positive correlation between apatite concentration and TREE (Total Rare Earth Element) content, suggesting apatite is the main carrier for REEs. Thus, fractionation of apatite which settled with the mafic minerals could theoretically be the source for the high REE content in the Fe-Ti-P rich phase.

Fractional crystallization as a Fe-Ti-P forming process raises further complications as magmatic layering have not been observed in the field. Fractionation and settling of mafic minerals would ideally create layers following the Bowen's reaction series (Bowen, 1928; Winter, 2001; Tegner et al., 2006; Robb, 2015). However, all larger mineralizations of Fe-Ti-P rich rock appear to occur as lenses in medium to coarse grained syenites. A plausible model which can explain the lenses is disruption of magmatic layering by internal convectional flows and replenishment of magma. Thus, the traditional gradient from mafic to felsic composition is destroyed, and the mafic minerals would be rearranged to the lenses and patches observed today.

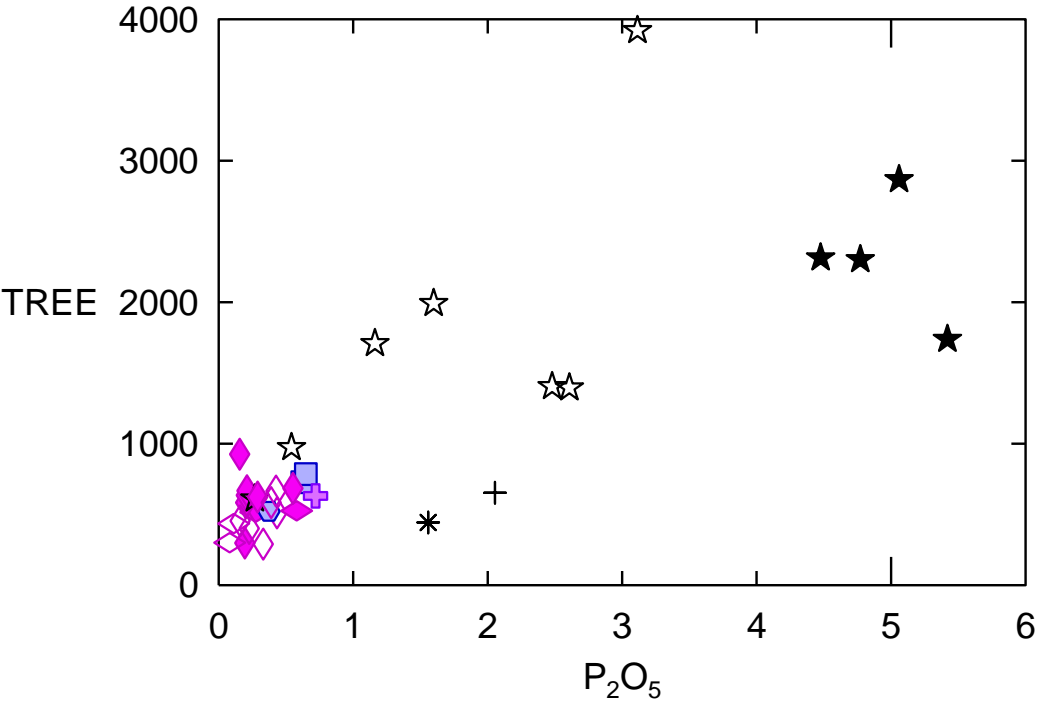


Figure 5-6: Bulk analysis of TREE (Total Rare Earth Elements) vs. P<sub>2</sub>O<sub>5</sub> content.

This form of mingling might also be a product of transportation of Fe-Ti-P rich magma. (Andersen, T., Seiersten, M., 1994), suggested the Fe-Ti-P rich rock originated from crystal fractionation of a deeply situated ijolite which were able to ascend to present level by being carried by intermediate magma. The petrogenesis from an ijolite appear unlikely in the Siljan-Hvarnes Intrusion as all samples are quartz normative. Further, the authors and (Ihlen et al., 2014), remarked the problematic aspect of a dense Fe-Ti-P rich cumulate being transported upwards in a less dense carrier- magma.

However, there are several indicators which suggest fractional crystallization probably not formed the Fe-Ti-P rich rock. Firstly, large-scale accumulation of mafic minerals is accredited to large systems with a basaltic parental melt (Robb, 2015). The settling of mafic minerals is promoted by the density contrast and the low viscosity in basaltic magmas, which enables crystals to gravitationally settle (The viscosity for basalt is commonly  $10^2$  Pa s, and  $10^6$  Pa s for felsic magmas) (ibid). Secondly, such a system would be expected to crystallize in a geochemical continuum of compositions (Bonnefoi et al., 1995; Robb, 2015). This is not reflected in sample compositions from Siljan (Figure 5-7). The gap between 30 wt.% and 58 wt.%  $\text{SiO}_2$  of the fine-grained Fe-Ti-P rich rock and the monzonite can hardly be explained trough fractional crystallization. (Namur et al., 2011) who studied the differentiation of tholeiitic basalt to A-type granite in the Sept Iles layered intrusion were inclined to suggest silicate liquid immiscibility as a possible cause for a far lower gap from 57 to 67 wt.%  $\text{SiO}_2$ .

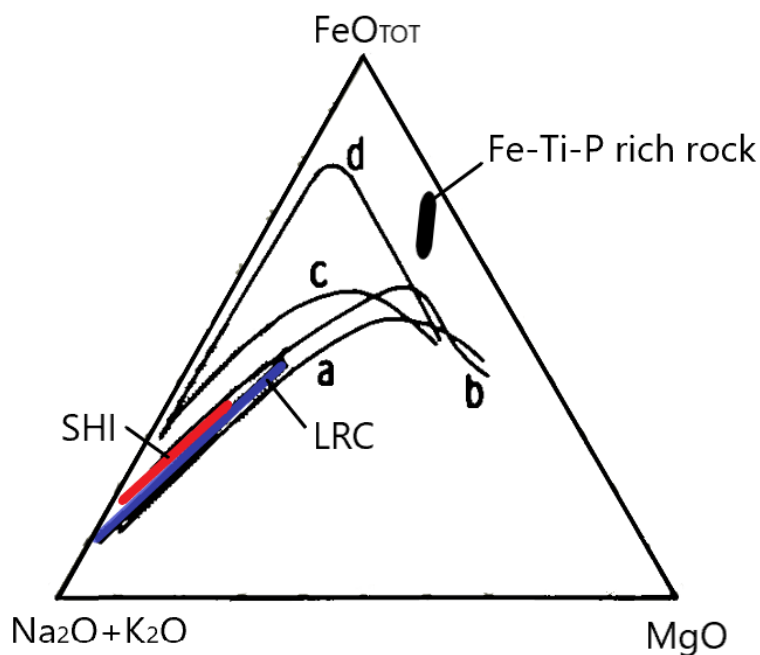


Figure 5-7: Alkali-  $\text{FeO}_{\text{TOT}}$ - $\text{MgO}$  variations of the Siljan- Hvarnes Intrusion (SHI) – and Larvik Ring Complex (LRC)- and Fe-Ti-P rich rocks. (a) Highly alkaline lavas and (b) plutonic rocks from Tahiti (McBirney & Aoki, 1968 in (Neumann, 1980)), (c) unsaturated alkaline volcanic rocks from East Otago, New Zealand (Coombs & Wilkinson, 1969 in (Neumann, 1980)), and (d) tholeiitic rocks in the Skaergaard intrusion (Carmichael et al., 1974 in (Neumann, 1980)). Figure adapted from (Neumann, 1980).

The most compelling argument against fractional crystallization is encountered in the study of the textural- and geochemical mineral relations:

The assessment of thin section 403B (Figure 4-44) revealed clinopyroxene occurring both as inclusions in the feldspar phenocryst and in the Fe-Ti-P rich groundmass. EPMA analysis plot both clinopyroxene types with almost indistinguishable chemical composition. Thus, both pyroxene types formed most likely under the same physical- and geochemical conditions. Textural relations suggest clinopyroxene were one of the first phases to crystallize, then feldspar formed with a relatively high growth rate which subsequently lead to the encapsulation of some pyroxenes. Those pyroxenes which were not entrapped continued to grow to  $\sim 10x$  the size of the enclosed.

Intergrowth textures between the anhedral anorthoclase rim and anhedral to interstitial phlogopite, pargasite, and Fe-Ti oxides suggest the mineral phases crystallized simultaneously (Figure 4-17 and Figure 4-44). Thus, the feldspar zonation observed in Fe-Ti-P rich rock cannot be accredited to a change in physiochemical environment during ascension of the magma. (Note, this observation applies only to the transition from Ca to Na in feldspar composition in porphyritic Fe-Ti-P rich rock. It does not exclude the possibility of phenocrysts and phenocryst cores originating from various deeper located magma chambers as discussed in previous sections).

To summarize, chemical and textural indicators suggest fractional crystallization is an unlikely petrogenic process for the Fe-Ti-P rich rock. (Bergstøl, 1972) along with (Jensen, 1991; Kragh, 1991) suggested the Fe-Ti-P rich rock was produced by the onset of liquid immiscibility between a silica rich- and Fe rich phase. Unfortunately, few studies were devoted to this rock forming process before the 2000's, so little literature could support these claims. However, immiscibility has been recognized as a far more common process in magmatic chambers over the last 20 years and sever experiments have been conducted on the onset of immiscibility during the tholeiitic line of descent (Markl, 2001; Holness et al., 2011; Namur et al., 2011; Charlier and Grove, 2012; Veksler and Charlier, 2015; Honour et al., 2019).

#### 5.1.8.1.2 Geochemical Indicators for Silicate Liquid Immiscibility

Jakobsen et al. (2005), were the first to prove silicate liquid immiscibility had occurred in the Skaergaard intrusion. The evidence came as melt inclusions of Fe-rich phase in apatite and silica phase in olivine. The Fe-rich inclusions consisted of plagioclase, ilmenite, magnetite, iron-rich biotite (lepidomelane) and a fine-grained matrix, while the less common silicic inclusions consisted of quartz, orthoclase, albite, minor magnetite and finely intergrown matrix (ibid). Charlier and Grove (2012), did also use trapped globules of Fe- and Si phases as evidence for two liquid system in synthetic immiscible experiments.

There has been no attempt in analysing and interpreting melt inclusions in apatite or olivine in this study, even though it is regarded as the most secure evidence for immiscibility. The argumentation for liquid immiscibility will rather be based on textural and chemical evidence. Figure 5-8 and Figure 5-9 represent figures adapted from Charlier and Grove (2012). In Figure 5-8 A,  $\text{Fe}_2\text{O}_3$  represent  $\text{FeO}_T$ , as it is based on XRF analysis. All three sub-figures (A-C) show a wide gap between the fine to medium grained Fe-Ti-P rich rock and the syenites. These observations are in concordance with the results produced by liquid immiscibility in Charlier and Grove (2012). In both figures plots the porphyritic Fe-T-P rich samples over a wide range of compositions between the fine-grained Fe-Ti-P rich rock and the Si- rich rock. This is believed to be a result of the distribution of feldspar phenocrysts and Fe-Ti-P groundmass. They do therefore not represent a chemical evolutionary trend from mafic Fe-Ti-P rich rock to felsic syenite. Two samples of porphyritic Fe-Ti-P rich rock plot as Fe- rich outliers in Figure 5-8 (A) and Mg-low, Ti- rich outliers in (B). These are from Eiriks Gruve, while the fine-grained Fe-Ti-P rich rock stem from the mines at Kåsemyrene.

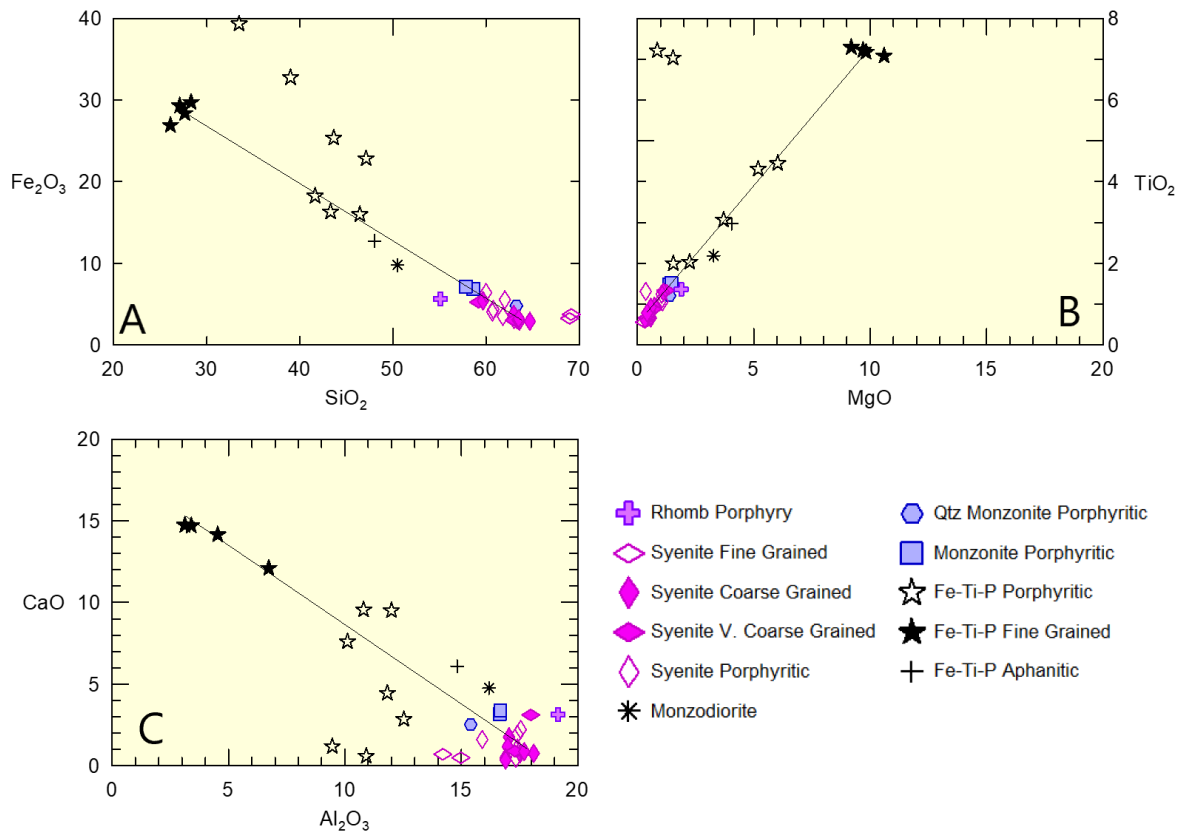


Figure 5-8: XY diagrams highlighting compositional differences between fine-grained Fe-Ti-P rich rocks and silicic rocks (Adapted from Charlier and Grove, 2012). The tie lines represent possible immiscible pairs and tie the fine-grained Fe-Ti-P rich rock with the most Fe, Ti, and Ca depleted samples.

Figure 5-8 A-C depict ternary diagrams where black lines represent interpreted two liquid stability fields. The diagrams plot indicative of liquid immiscibility (Charlier and Grove, 2012). The porphyritic Fe-Ti-P rich rock plot between the fine-grained Fe-Ti-P rich rock and syenitic rocks in figure A and B. This observation further supports the assertion of porphyritic Fe-Ti-P rich rock representing a chemical mix of Fe-Ti-P rich rock and feldspar phenocrysts.

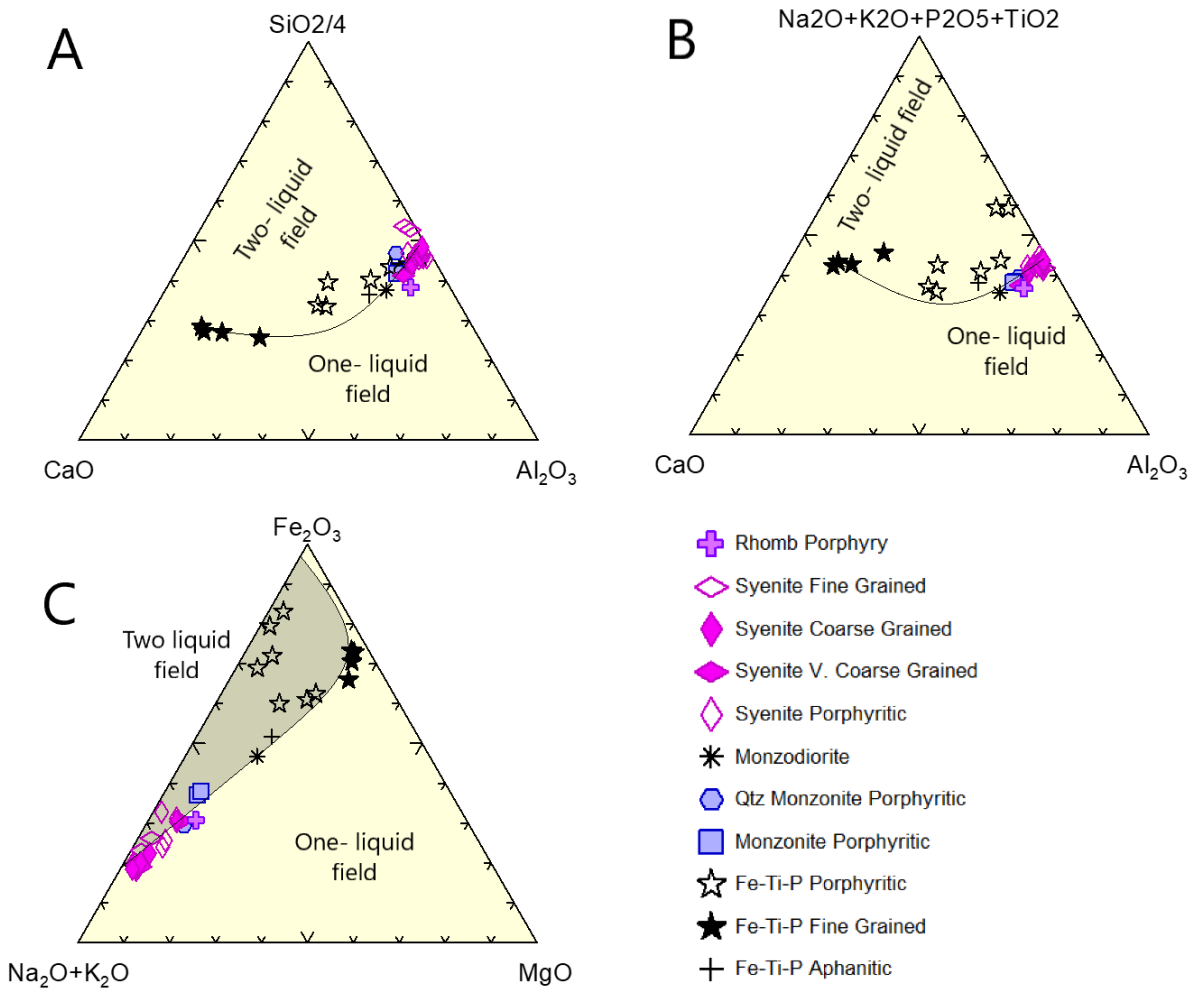


Figure 5-9: Ternary diagrams highlighting the potential one and two liquid stability fields (Adapted from (Charlier and Grove, 2012)).

Figure 2-6 depicts experimental values for element partitioning between the iron rich and silica rich phase during immiscibility. Charlier and Veksler (2015) conducted the experiment on a cooling synthetic magma under reduced conditions ( $f\text{O}_2$  from -8,3 to -8,7), and calculated the Nernst partition coefficient for major- and trace elements. The results yielded clear trends of Fe, Ti, P, REE's, HFSE and transition metals partitioning into the Fe- phase, while Si, Al, Sn, K, Rb, Cs and Sb partition into the silica phase. However, the experimental system does not include P or Mg, which are common and important components in natural silicate immiscibility systems. Charlier and Grove (2012), emphasized how P and Mg likely expanded the two liquid stability field. Regardless, enrichment in a mafic phase of Fe, Ti, P, REE's, HFSE and transition metals have been recognized as a valid characterization for silicate immiscibility in natural magmatic systems (Jakobsen et al., 2005; Holness et al., 2011; Charlier and Grove, 2012; Veksler and Charlier, 2015).

The geochemical analyses of this study do largely concord with the results of Charlier and Veksler (2015). The major oxides show a great dispersion between the silica rich and Fe rich samples (Figure 4-37 and Figure 5-8). The Fe-Ti-P rich rocks are generally enriched in REEs (Figure 4-42 and Figure 4-43), and the transition metals Cu and V (Figure 4-39). The largest deviances from the expected results are found in the plot of HFSE and LILE (Figure 4-40 and Figure 4-41, respectively). The HFSE values in the Fe-Ti-P rich samples are comparable to those from the silica rich rocks, and the monzonites are overall the most enriched rock in HFSE. Of the LILEs are Sr and Ba expected to partition into the Fe-phase and Cs and Rb expected to partition into the silica phase. The latter appear to be consistent with this study's results, however, the Sr content of the Fe-Ti-P rich rock plot generally between the monzonites and the syenites while the Ba content appear to follow no trend. The Sr content are highest for two porphyritic Fe-Ti-P rich samples. As the porphyritic samples are recognized with higher modal percent of feldspars, it is possible the Sr partitioned into the feldspar phase and caused an uneven distribution of this element. Thus, Sr is low for the fine to medium grained Fe-Ti-P rich rock which have minor components of interstitial feldspar.

To summarize, the geochemical analysis aligns better with the theory of the Fe-Ti-P rich rock originating from unmixing rather than fractional crystallization. However, a definite evidence in the form of trapped inclusions representing Fe-rich liquid and Si-rich liquid is not documented.

#### 5.1.8.1.3 Textural and Mineral Analyses Indicating Silicate Liquid Immiscibility

As discussed earlier, intergrowth textures in sample 403 B indicate anorthoclase and Fe-Ti-P groundmass minerals crystallized simultaneously. The zoning in the feldspar phenocrysts (Figure 4-17, Figure 4-44 and Figure 5-10 (below)) show a change in feldspar composition from oligoclase to anorthoclase, which imply a change from crystallization in a Ca- Na rich melt to Na - K rich melt. This change is not reflected in the adjacent Fe-Ti-P rock- forming minerals such as biotite, amphibole, and pyroxene. All three minerals can accommodate Ca, Na and K, still they remain Ca-rich and show no zonation related Na - K enrichment. Thus, it is likely the anorthoclase crystallized from a Si-rich liquid, while the Fe-Ti-P groundmass minerals crystallized from a Fe-rich liquid.

Figure 5-10 (below) depict the chemical change between the oligoclase core and anorthoclase rim as the jump from 21 wt.% to 19,5 wt.%  $Al_2O_3$ . This is expected as anorthoclase incorporate less Al (anorthoclase has chemical formula  $(Na,K)AlSi_3O_8$  while oligoclase has  $(Na,Ca)Al_{1-2}Si_{3-2}O_8$ ) (Deer et al., 1975). However, the sudden increase in Sr as anorthoclase forms is inconsistent with the prediction of Sr partitioning during silica immiscibility. According to Veksler and Charlier (2015), will Sr partition into the Fe-rich liquid. Maybe the unmixing caused a general redistribution of trace elements, which somehow initially caused Sr to partition into the crystallizing feldspar. However, the Sr concentration in feldspar drops rapidly, and the feldspar phases interpreted to crystallize last have stable, low values of Sr.

Figure 4-17 depicts subhedral needle- like phlogopite crystals radiating into the anorthoclase rim of a feldspar phenocryst. This observation further supports the claim of two immiscible liquids crystallizing simultaneously and suggests phlogopite were one of the last phases to crystallize.



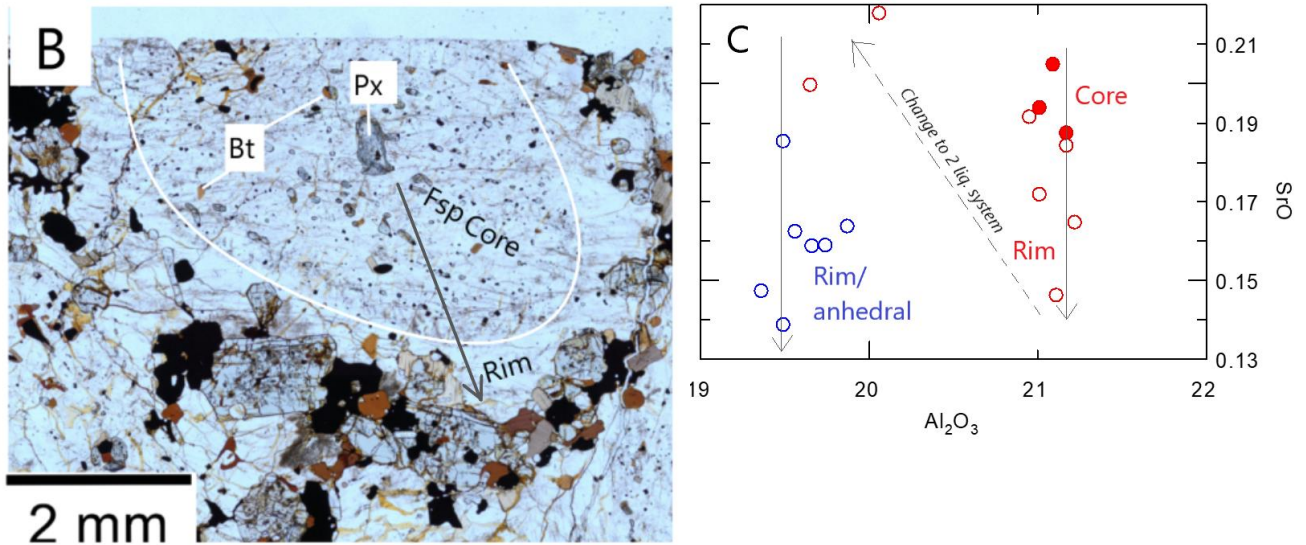


Figure 5-10: Photomicrograph of oligoclase phenocryst with anorthoclase rim in sample 403B and SrO vs  $Al_2O_3$  plot depicting the chemical change between the two phases. Arrows indicate crystallization pattern.

#### 5.1.8.2 The Onset of Liquid Immiscibility

Figure 5-10 might represent felspar formed from a Si-rich liquid while the Fe-Ti-P groundmass crystallized from a Fe-rich liquid. However, this study has not established a parent magma or any relations between Si-rich and Fe-rich melts.

Figure 5-11 compares the line of descent in the Siljan – Hvarnes intrusion and Larvik Ring Complex to the results from Charlier and Groves (2012) study. Their ternary diagram depicts two grey curves representing tholeiitic liquid line of descent of Toplis and Carroll (1995) and Juster et al. (1989). The grey stars represent the composition of the homogeneous synthetic melt before the onset of immiscibility. Black circles are Fe-rich immiscible melts, and white circles are Si-rich immiscible melts. Tie lines join the immiscible pairs.

Charlier and Grove (2012) have a defined homogeneous starting melt, however, it is uncertain what the composition was for the initial melt in Siljan. Additionally, all articles assessing immiscibility cited in this study applies to systems with a tholeiitic parent (Markl, 2001; Jakobsen et al., 2005; Holness et al., 2011; Charlier and Grove, 2012; Veksler and Charlier, 2015; Honour et al., 2019). There is therefore some level of uncertainty linked to the environment in the Siljan-Hvarnes intrusion triggering the immiscible process. E.g., it is unclear if any of the syenites represent immiscible pairs with any of the Fe-Ti-P rich rocks, and how the evolved magma entered the two-liquid stability field.

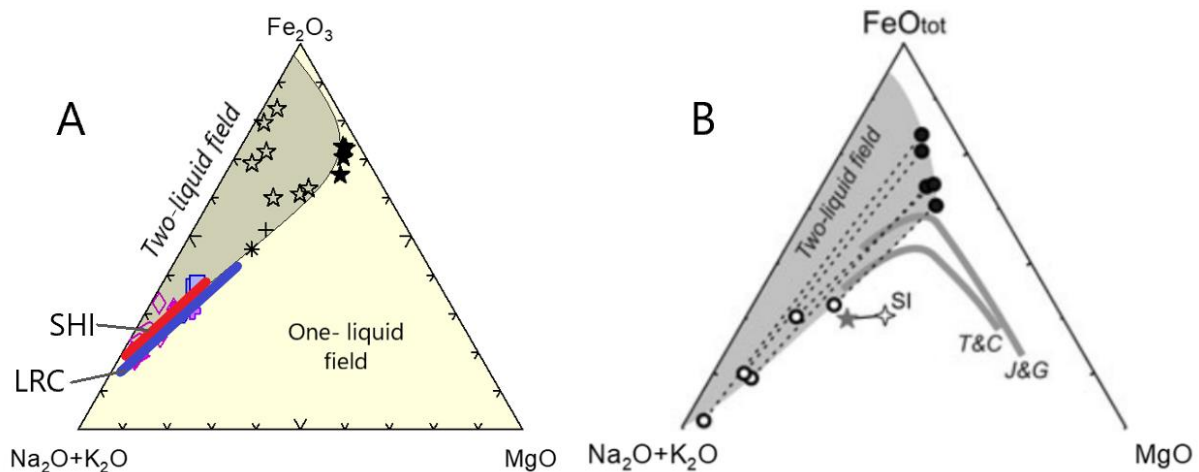


Figure 5-11: (A) Samples from this study with an interpreted two-liquid field and line of descent for the Siljan- Hvarnes Intrusion (SHI) – and Larvik Ring Complex (LRC) (Neumann, 1980). (B) Tholeiitic line of descent entering the two-liquid field (Charlier and Grove, 2012). Note figure B is cut at 30%  $FeO_T$ .

The Fe-Ti-P rich rock is commonly associated with the medium- to coarse-grained syenite, but it does not necessarily represent the immiscible pair. The medium- to-coarse grained syenite might have worked as a solid framework mush which allowed Fe- rich liquid to sieve through (Weinberg, 2006). The immiscible process possibly stems from more elevated parts of the magma chamber as the Fe-rich liquid is denser and has a lower viscosity than the Si-rich liquid at any given temperature (Honour et al., 2019). The viscosity of Fe rich liquid ranges from  $10^3$  to  $10^4$  Pa. s, while Si-rich liquids ranges from  $10^4$  to  $10^7$  Pa. s for the temperature interval  $1050^\circ\text{C}$  to  $955^\circ\text{C}$  (ibid). Thus, if enough Fe-rich liquid nucleate, it will most likely sink and pond at solid contacts within the magma chamber. This phenomenon is evident at Key- Location 520: where the Fe- Ti-P rich rock form a sharp contact to the underlying syenite and a gradational contact to the overlying medium to coarse grained syenite. Additionally, the phenocrysts are oriented parallel with the downwards flow direction, and the Fe-Ti-P rich rock accumulates in a concave pool in the lower contact. Thus, rocks representing the Si- rich immiscible pair might be located elsewhere in the pluton.

Additionally, small veins of Fe-Ti-P rich rock were found at several locations throughout the pluton. Figure 5-12 show a Fe-Ti-P vein in associated with a syenite intruding the rhomb porphyry. As small mineralizations appear ubiquitous, it is possible the onset of immiscibility occurred locally, and not as one major event in the magma chamber. The distinct variation in V, Zr,  $Eu^*$ , Sr, Y and TREE in apatite from Kåsemyrene and Eiriks Gruve might imply the Fe-Ti-P rich rock does not stem from a single, common source.



*Figure 5-12: Vein of Fe-Ti-P rich rock associated with syenite intruded in the rhomb porphyry sequence.*

One of the factors which might have promoted the immiscible process is the high content of Ti which are evident through chemical analyses. According to Charlier and Grove (2012), are Ti among the elements which will increase the stability field of two liquids and thus promote the onset of immiscibility. The generally high content of Ti is apparent in the bulk analysis Harker plot (Figure 4-37). Additionally, enrichment of Ti is apparent in amphiboles "rootname 4" and pargasite (Figure 4-65) and phlogopite (Figure 4-51). These two minerals occur anhedral to interstitial in the Fe-Ti-P rich rock and represent most likely the two last phases to crystallize. Thus, Ti was probably present in surplus during crystallization of all mineral phases crystallizing from the Fe- rich liquid. This is especially evident in Figure 4-51 D, plotting a trend where Fe content decreases as Ti content increases in phlogopite. Textural relations suggest the Fe-rich crystals formed early (as they occur as inclusions in feldspar), and the Ti rich samples crystallized last (as interstitial phases in the Fe-Ti-P rich groundmass). Thus, iron contents were gradually depleted while Ti were constantly in surplus.

Further supporting evidence for high Ti content might be presented in thin section 763A (Figure 4-22) from Kåsemyrene. The sample resembles Fe-Ti-P rich rock with mineral phases such as apatite, amphibole and Fe-Ti oxides. However, it has up to 40 modal% interstitial quartz and feldspar, 5 modal% euhedral zircon, and 5 modal% sphene. The quartz and sphene both form up to 2 mm long oikocrysts. This observation indicates quartz and sphene were the two last mineral phases to crystallize. Thus, if this sample represents rock formed by immiscibility, it witnesses Ti being in surplus until the last Ti-rich phase crystallized as sphene ( $\text{CaTiSiO}_5$ ).

To summarize, the Fe-Ti-P rich rock most likely formed by the onset of liquid immiscibility. Field observations suggest Fe-rich liquid pooled along internal solid boundaries in the magma chamber and formed the patchy ores observed today. The study has not established a parental magma for the Fe-Ti-P rich rock and neither a silicate immiscible pair. However, the shallow emplacement and enrichment of Ti in the system were probably promoting the onset of immiscibility (Charlier and Grove, 2012).

## 5.2 Geomagnetic Study

The geomagnetic study was conducted to assess if any of the Fe-Ti-P ores showed correlation with magnetic anomalies. The short analysis of the magnetic properties of the lithologies in the field area yielded promising results as the Fe-Ti-P rich rock have a high susceptibility and Q values from 15 – 25, while most of the syenites hosting the ore have a Q value between 1 and 10. Thus, A shallowly emplaced, sufficiently large magnetic body would most likely create an anomaly visible as a shift from high positive to low negative over a short distance which would contrast to the magnetic signature of the hosting rocks (Airo, 2015)

Examination of the geomagnetic map (Figure 5-15) reveal this is not the case. However, the Fe-Ti-P mineralizations appear to occur along zones with a shift from positive to negative, which can be correlated to the intrusive rings of the pluton. This observation might serve as further support for the theory of Fe-rich melt pooling and crystallizing along internal solid contacts. However, a more detailed study and modelling of the sub-surface is needed to rectify this claim as supporting evidence.

The second observation which drew attention on the magnetic map (Figure 5-15) were the strongly negative anomaly occurring in the middle of a contrastingly larger, strong positive anomaly. (Seen north in the field area, associated with the rhomb porphyry sequence). The results of the NRM analysis suggests the negative anomaly might be caused by the rhomb porphyry. The Q-plot (Figure 4-66) reveal how the rhomb porphyries (521, 524, 525) are extremely dominated by natural remanent magnetization. Additionally, is the strong magnetic vector of 524 oppositely directed to the present-day field (Figure 4-67). Sample 521 and 525 are not as contrastingly oriented but do attribute with SSE- directed vector.

The strong remanent vector in the rhomb porphyries is probably attributed to the elongated  $\mu\text{m}$  scale, oriented magnetite, titanomagnetite and ilmenite grains in the groundmass (Figure 5-13). This crystal shape and size is associated to single domain grains and contributes to forming a stable remanent magnetization (Harrison and Feinberg, 2009). Figure 5-14 depicts calculated size fractions and axial ratios which promote single domain state.

The main reason for the inability to observe the magnetic anomalies from the Fe-Ti-P rich ores is the coarse resolution of the magnetic map. The spatial resolution is 50 m, which means each cell representing a spatial value is 50m x 50m (Baranwal, 2015). Even though the mine locations were heavily vegetated and the extent of the ores could not be mapped, the size of the mines suggest the ores are in 1 – 10 m scale range. Thus, an appropriate resolution would be in the range 10 cm to no more than 1 m. This is probably best obtained with drone- or carried magnetometers.

Lastly, the NRM analysis of the Fe-Ti-P rich samples yielded results which may imply user source of error. Sample 504 had an angle of  $88,9^\circ$  between two vectors, and sample 505 had four vectors evenly distributed in two clusters separated by an angle of  $86,9^\circ$ . This consistent error is most likely caused by wrong sample cylinder marking by wrong instalment in the Agico Magnetometer. However, these errors do not affect the discussion or conclusion of the geomagnetic study in any matter.



Figure 5-13: Photomicrograph of rhomb porphyry ground mass (524). Note elongated felspar (transparent) and Fe-Ti-oxides (opaque) show moderate orientation.

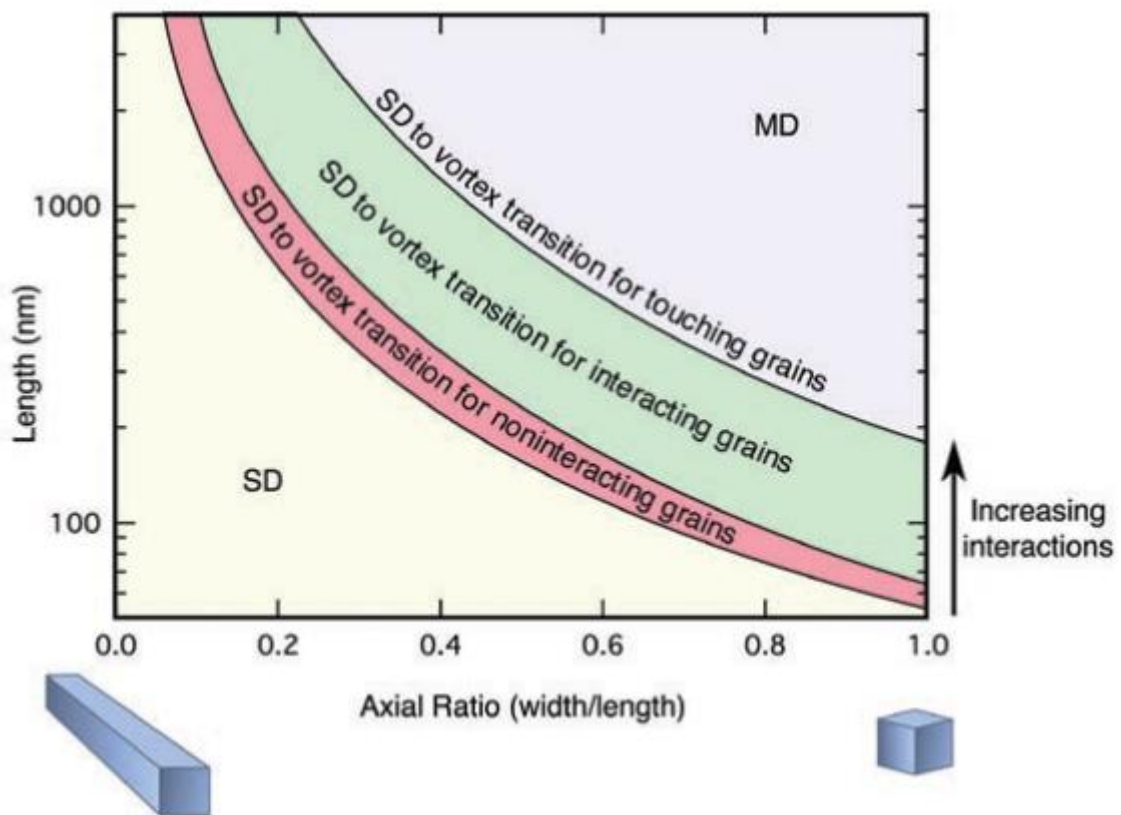
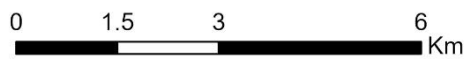
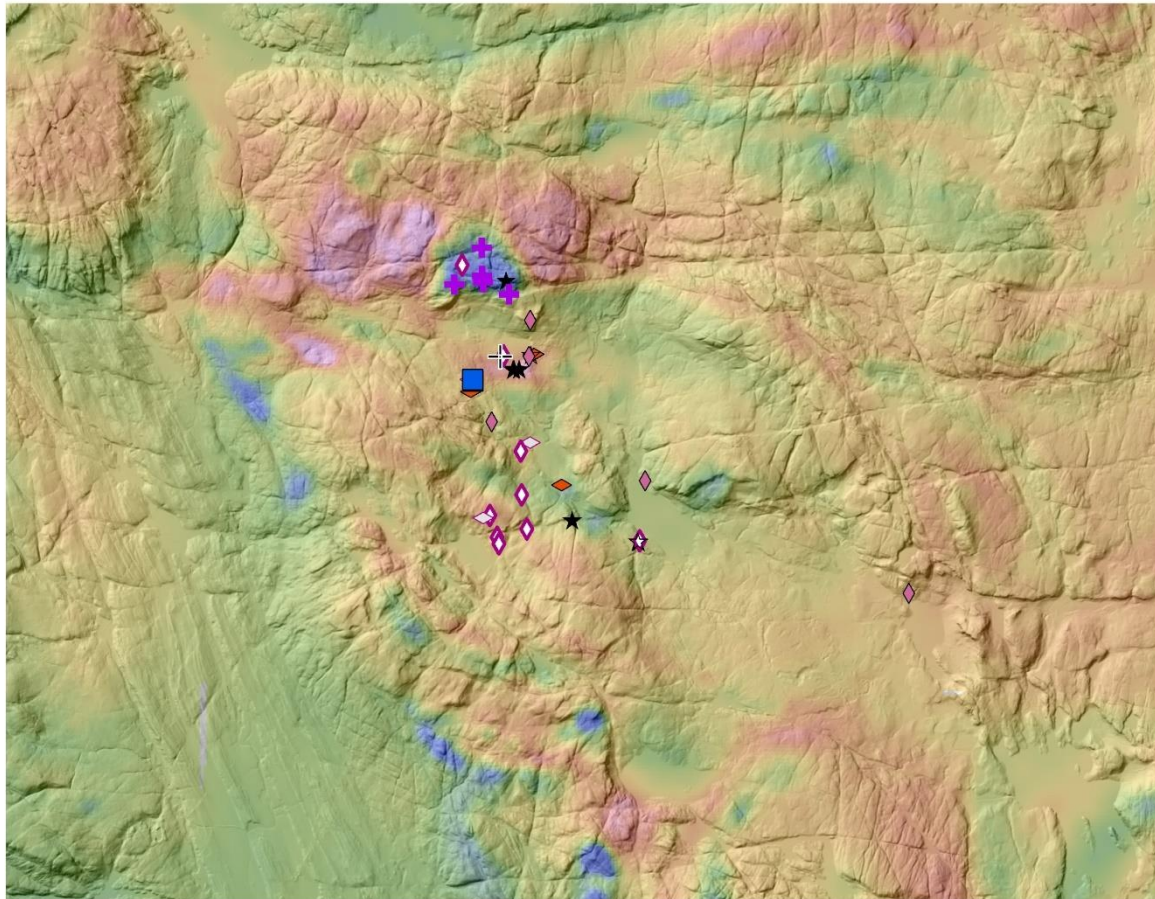


Figure 5-14: Magnetic domain based on particle size, shape, and interparticle spacing (Figure 8 in Harrison and Feinberg (2009)).



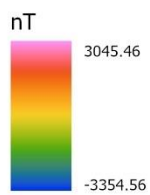
# GEOMAGNETIC MAP

## SILJAN INTRUSION



### Rock units

- |                      |                  |
|----------------------|------------------|
| ★ Fe-Ti-P F-Gr       | ◇ Syenite C-Gr   |
| ☆ Fe-Ti-P Porph.     | ◇ Syenite F-Gr   |
| ⊥ Monzodioritic Dike | ◇ Syenite Porph. |
| ■ Monzonite Porph.   | ◇ Syenite V.C-Gr |
| ⊕ RP                 |                  |



Spatial Reference  
PCS: ETRS 1989 UTM Zone 32N  
GCS: GCS ETRS 1989

By: Tord Andersen

Figure 5-15: Geomagnetic map imposed on top of DTM 10 hill shade.

## 6 Conclusion

The Siljan -Hvarnes Intrusion formed 277 Ma during the most active volcanic period of the rifting of Oslo Graben. The intrusion consists of several nested rings developing westwards over a span of ~20 km. Bulk rock analysis reveal all larger intruding lithologies are ferroan alkalic metaluminous granitoids and form a geochemical trend from monzonitic to syenitic composition. However, feldspar phenocryst analysis suggests the lithologies stem from various magma sources, and mixed/ mingled to various degree in the pluton.

Smaller, cm-scale Fe-Ti-P rich rock is encountered throughout the pluton as veins and blobs. Larger Fe-Ti-P ores are encountered at Kåsemyrene, Eiriks Gruve and Jernskottet. These mineralizations are mainly composed of augite, apatite, phlogopite, Ti- rich amphiboles ("Rootname 4" and Ti-rich pargasite), ilmenite, titanomagnetite and felspar phenocrysts. Bulk rock analysis reveal the Fe-Ti-P rich rock is extremely enriched in REEs (1500 ppm – 4000 ppm), especially LREE. Apatite is the main carrier for REEs and P<sub>2</sub>O<sub>5</sub> content of the fine to medium- grained Fe-Ti-P rich rock ranges from 4,4 – 5,4 wt.% and correlates positively with the REE content ranging from 1 wt.% - 3 wt.%. The highest REE contents (up to 7 wt.%) were measured in an apatite from porphyritic Fe-Ti-P rich rock collected at Eiriks Gruve.

Chemical and textural analysis suggest the Fe-Ti-P rich rock formed by immiscibility between a Si-rich and Fe-rich liquid. The Fe-rich liquid nucleated, sank, and pooled along internal solid contacts in the magma chamber.

The geomagnetic study revealed existing open-source geomagnetic maps have a too coarse resolution to depict anomalies from known Fe-Ti-P rich ores. However, all Fe-Ti-P mineralizations tend to accumulate along overlapping magnetic and K/ Th+U radiogenic boundaries interpreted to represent lithological contacts.

The large negative anomaly in the field area is most likely caused by strong, downwards directed NRM vector in the rhomb porphyry sequence.

## Recommendations for Future Work

Key location Kåsemyrene present itself as an area of cryptic textures and extremely interesting lithologies. Further studies in this area are needed to unveil the true size and mineralogical properties of this/ these ores. As concluded in this contribution, the Fe-Ti-P rich rock in the Siljan is most likely formed by pooling of Fe-rich liquid which leads to highly unpredictable shapes and sizes of Fe-Ti-P rich ores. This means there is a possibility that the Fe-Ti-P mineralization from the parking lot and through the two mine pits are connected. The high content of euhedral zircon (Figure 4-22) might also represent an opportunity to obtain age data.



## 7 References

- Airo, M.-L., 2015. Geophysical signatures of mineral deposit types in Finland, Special Paper 58, GEOLOGICAL SURVEY OF FINLAND.
- Andersen, T., Erambert, M., Larsen, A.O., Selbekk, R.S., 2014. Petrology of nepheline syenite pegmatites in the Oslo Rift, Norway: Zr and Ti mineral assemblages in miaskitic and agpaitic pegmatites in the Larvik Plutonic Complex. *Mineralogia* 44, 61–98. <https://doi.org/10.2478/mipo-2013-0007>
- Andersen, T., Seiersten, M., 1994. Deep cumulates in a shallow intrusion: origin and crystallization history of a pyroxenite (jacupirangite s.l.) body in the Larvik Pluton, Oslo Region, South Norway. *Neues Jb. Mineral. Monat* 6, 255–274.
- Ånestad, S., 2020. The Magnetic Petrological Expression of Slipesteinsberget, a Zoned Serpentinized Ultramafic Body In Trøndelag.
- Baranwal, V., 2015. Ngu report 2013.030.
- Bard, J.P., 1986a. *Microtextures of Igneous and Metamorphic Rocks*. D. Reidel Publishing Company.
- Bard, J.P., 1986b. *Microtextures of igneous and metamorphic rocks*, 1st ed. D. Reidel Publishing Company.
- Barth, T.F.W., 1945. Studies on the igneous rock complex of the Oslo region. II. Systematic petrology of the plutonic rocks: *Skr. Norske Vid.-Akad. i Oslo, I., Mat. Nat. Kl.*
- BAS, M.J.L.E., MAITRE, R.W.L.E., STRECKEISEN, A., ZANETTIN, B., Rocks, I.S. on the S. of I., 1986. A Chemical Classification of Volcanic Rocks Based on the Total Alkali-Silica Diagram. *Journal of Petrology* 27, 745–750. <https://doi.org/10.1093/petrology/27.3.745>
- Belousova, E.A., Griffin, W.L., O`Reilly, S.Y., Fisher, N.I., 2002. Apatite as an indicator mineral for moneral exploration: trace- element compositions and their relationship to host rock type. *Journal of Geochemical Exploration* 76, 46–69.
- Bergstøl, S., 1972. The jacupirangite at Kodal, Vestfold, Norway - A potential magnetite, ilmenite and apatite ore. *Mineralium Deposita* 7, 233–246. <https://doi.org/10.1007/BF00206786>
- Best, M.G., 2013. *Igneous and metamorphic petrology*. John Wiley & Sons.
- Bøen, Gunvor; Bøen, H., n.d. *Sølland I Siljan, Forfedrene til Peder Jakobsen og Karen Olava Edvardsdatter Sølland*.
- Bonnefoi, C.C., Provost, A., Albarède, F., 1995. The “Daly gap” as a magmatic catastrophe. *Nature* 378, 270–272. <https://doi.org/10.1038/378270a0>
- Borg, G., 2011. Petrology of akerite (quartz monzonite) in the Oslo Rift, SE Norway. 132.
- Bowen, N.L., 1928. *The Evolution of the Igneous Rocks*. Dover Publications.
- Brøgger, W.C., 1890. *Die Mineralien der Syenitpegmatitgänge der Südnorwegischen Augit- und Nephelinsyenite*. Verlag von Wilhelm Engelmann, Leipzig.

- Bruand, E., Storey, C., Fowler, M., 2016. An apatite for progress: Inclusions in zircon and titanite constrain petrogenesis and provenance. *Geology* 44, 91–94. <https://doi.org/10.1130/G37301.1>
- Butler, R.F., Butler, R.F., 1992. *Paleomagnetism: magnetic domains to geologic terranes*. Blackwell Scientific Publications Boston.
- Charlier, B., Grove, T.L., 2012. Experiments on liquid immiscibility along tholeiitic liquid lines of descent. *Contributions to Mineralogy and Petrology* 164, 27–44. <https://doi.org/10.1007/s00410-012-0723-y>
- Chew, D.M., Babechuk, M.G., Cogné, N., Mark, C., O’Sullivan, G.J., Henrichs, I.A., Doepke, D., McKenna, C.A., 2016. (LA, Q)-ICPMS trace-element analyses of Durango and McClure Mountain apatite and implications for making natural LA-ICPMS mineral standards. *Chemical Geology* 435, 35–48.
- Clark, D.A., 1997. Magnetic petrophysics and magnetic petrology: aids to geological interpretation of magnetic surveys. 17, 83–103.
- Corfu, F., Dahlgren, S., 2008. Perovskite U–Pb ages and the Pb isotopic composition of alkaline volcanism initiating the Permo-Carboniferous Oslo Rift. *Earth and Planetary Science Letters* 265, 256–269.
- Deer, W.A., R. A. Howie, Zussman., J., 1975. *An Introduction to the Rock Forming Minerals*. Eighth edition. London, Longmans. p.1-528., 2nd ed. Pearson Education Limited.
- Dekkers, M.J., 1988. Magnetic properties of natural pyrrhotite Part I: Behaviour of initial susceptibility and saturation-magnetization-related rock-magnetic parameters in a grain-size dependent framework. *Physics of the Earth and Planetary Interiors* 52, 376–393.
- Dentith, M., Mudge, S.T., 2014. *Geophysics for the mineral exploration geoscientist*. Cambridge University Press.
- DePaolo, D.J., 1981. Trace element and isotopic effects of combined wallrock assimilation and fractional crystallization. *Earth and Planetary Science Letters* 53, 189–202. [https://doi.org/10.1016/0012-821X\(81\)90153-9](https://doi.org/10.1016/0012-821X(81)90153-9)
- Farina, F., Stevens, G., Villaros, Arnaud., 2012. Multi-batch, incremental assembly of a dynamic magma chamber: the case of the Peninsula pluton granite (Cape Granite Suite, South Africa)., *Mineralogy and Petrology*. <https://doi.org/10.1007/s00710-012-0224-8>
- Freestone, I.C., 1990. LIQUID IMMISCIBILITY Liquid immiscibility. *Petrology*. Springer US, Boston, MA, 281–283. [https://doi.org/10.1007/0-387-30845-8\\_122](https://doi.org/10.1007/0-387-30845-8_122)
- Frost, B.R., Barnes, C.G., Collins, W.J., Arculus, R.J., Ellis, D.J., Frost, C.D., 2001. A geochemical classification for granitic rocks. *Journal of Petrology* 42, 2033–2048. <https://doi.org/10.1093/petrology/42.11.2033>
- Goldschmidt, V.M., 1937. The principles of distribution of chemical elements in minerals and rocks. The seventh Hugo Müller Lecture, delivered before the Chemical Society on March 17th, 1937. *Journal of the Chemical Society (Resumed)* 655–673.
- Harlov, D.E., Rakovan, J.F., 2015. *Apatite: A Mineral for All Seasons*.

- Harrison, R.J., Feinberg, J.M., 2009. Mineral magnetism: Providing new insights into geoscience processes. *Elements* 5, 209–215. <https://doi.org/10.2113/gselements.5.4.209>
- Hawthorne, F.C., Oberti, R., Harlow, G.E., Maresch, W. v., Martin, R.F., Schumacher, J.C., Welch, M.D., 2012. Ima report: Nomenclature of the amphibole supergroup. *American Mineralogist* 97, 2031–2048. <https://doi.org/10.2138/am.2012.4276>
- HFSE-LILE Diagram [WWW Document], 2018. Earth Science Beta. URL <https://bit.ly/2Ua0MQM>
- Holness, M.B., Stripp, G., Humphreys, M.C.S., Veksler, I. v., Nielsen, T.F.D., Tegner, C., 2011. Silicate liquid immiscibility within the crystal mush: late-stage magmatic microstructures in the skaergaard intrusion, east greenland. *Journal of Petrology* 52, 175–222. <https://doi.org/10.1093/petrology/egq077>
- Honour, V.C., Holness, M.B., Partridge, J.L., Charlier, B., 2019. Microstructural evolution of silicate immiscible liquids in ferrobasalts. *Contributions to Mineralogy and Petrology* 174. <https://doi.org/10.1007/s00410-019-1610-6>
- Hoskin, P.W.O., Ireland, T.R., 2000. Rare earth element chemistry of zircon and its use as a provenance indicator. *Geology* 28, 627–630. [https://doi.org/10.1130/0091-7613\(2000\)028<0627:REECOZ>2.3.CO;2](https://doi.org/10.1130/0091-7613(2000)028<0627:REECOZ>2.3.CO;2)
- Howell, J. v., 1957. Glossary og Geology and Related Sciences, Supplemen. ed. American Geological Institute.
- Ihlen, P.M., Schiellerup, H., Gautneb, H., Skår, Ø., 2014. Characterization of apatite resources in Norway and their REE potential - A review. *Ore Geology Reviews* 58, 126–147. <https://doi.org/10.1016/j.oregeorev.2013.11.003>
- Jahns, R.H., Burnham, C.W., 1969. Experimental Studies On Pegmatite Genesis. *Econ. Geol.* 64, 843–864.
- Jakobsen, J.K., Veksler, I. v., Tegner, C., Brooks, C.K., 2005. Immiscible iron- and silica-rich melts in basalts petrogenesis documented in the Skaergaard intrusion. *Geology* 33, 885–888. <https://doi.org/10.1130/G21724.1>
- Jennings, E.S., Marschall, H.R., Hawkesworth, C.J., Storey, C.D., 2011. Characterization of magma from inclusions in zircon: Apatite and biotite work well, feldspar less so. *Geology* 39, 863–866. <https://doi.org/10.1130/G32037.1>
- Jensen, O.A., 1991. En Petrologisk og geokemisk undersøgelse af Larvikit-Massiverne, Kodal, SydNorge.
- Juster, T.C., Grove, T.L., Perfit, M.R., 1989. Experimental constraints on the generation of FeTi basalts, andesites, and rhyodacites at the Galapagos Spreading Center, 85 W and 95 W. *Journal of Geophysical Research: Solid Earth* 94, 9251–9274.
- Kragh, K., 1991. En Petrologisk og Geokemisk undersøgelse af Koldalforekomsten Oslofeltet, SydNorge.
- Larsen, A.O., 1993. Fossum Jernverk [WWW Document], NGU Mineralressursdatabase. URL <http://geo.ngu.no/api/faktaark/mineralressurser/visProvins.php?more=false&objid=19508&lang=nor>

- Larsen, B.T., 1978. Krokskogen Lava Area. Paleorift: A Review and Guide to Excursions. Norges Geologiske Undersøkelse Bulletin, 337. 143–162.
- Larsen, B.T., Olaussen, S., Sundvoll, B., Heeremans, M., 2008. The permo-carboniferous Oslo rift through six stages and 65 million years. Episodes 31, 52–58. <https://doi.org/10.18814/epiiugs/2008/v31i1/008>
- Li, X., Zhang, C., Behrens, H., Holtz, F., 2020. Calculating biotite formula from electron microprobe analysis data using a machine learning method based on principal components regression. Lithos 356–357, 105371. <https://doi.org/10.1016/j.lithos.2020.105371>
- Lindberg, P.A., 1985. Fe-Ti-P mineralizations in the larvikite-lardalite complex, Oslo Rift. Norges Geologiske Undersøkelse Bulletin 402, 93–98.
- Lindqvist, K., Suominen, V., 2017. Mirolitic cavities in rapakivi granite on Hästholmen, Loviisa, southeastern Finland. Bulletin of the Geological Society of Finland 59, 71–75. <https://doi.org/10.17741/bgsf/59.1.005>
- Locock, A.J., 2014. An Excel spreadsheet to classify chemical analyses of amphiboles following the IMA 2012 recommendations. Computers and Geosciences 62, 1–11. <https://doi.org/10.1016/j.cageo.2013.09.011>
- Markl, G., 2001. A new type of silicate liquid immiscibility in peralkaline nepheline syenites (lujavrites) of the Ilimaussaq complex, South Greenland. Contributions to Mineralogy and Petrology 141, 458–472. <https://doi.org/10.1007/s004100100252>
- McEnroe, S.A., Fabian, K., Robinson, P., Gaina, C., Brown, L.L., 2009. Crustal magnetism, lamellar magnetism and rocks that remember. Elements 5, 241–246.
- Merrill, R.; McElhinny, M.; and McFadden, P.L., 1996. The magnetic field of the earth: paleomagnetism, the core, and the deep mantle. International Geophysics Series: Academic Press 63.
- Middlemost, E.A.K., 1994. Naming materials in the magma/igneous rock system. Earth-Science Reviews 37, 215–224.
- MORIMOTO, N., 1988. Nomenclature of pyroxenes: subcommittee on pyroxenes Commission on New Minerals and Mineral Names (CNMMN) International Mineral Association (IMA). Schweizerische Mineralogische Und Petrographische Mitteilungen 68, 95–111.
- Namur, O., Charlier, B., Toplis, M.J., Higgins, M.D., Hounsell, V., Liégeois, J.P., Auwera, J. vander, 2011. Differentiation of tholeiitic basalt to A - type granite in the Sept Iles layered intrusion, Canada. Journal of Petrology 52, 487–539. <https://doi.org/10.1093/petrology/egq088>
- NCEI, 2020. Magnetic Field Estimated Values [WWW Document]. URL <https://www.ngdc.noaa.gov/geomag/calculators/magcalc.shtml#igrfwmm>
- Neumann, E., 1980. Petrogenesis of the Oslo region larvikites and associated rocks. Journal of Petrology 21, 499–531. <https://doi.org/10.1093/petrology/21.3.499>
- Neumann, E.R., Wilson, M., Heeremans, M., Spencer, E.A., Obst, K., Timmerman, M.J., Kirstein, L., 2004. Carboniferous-Permian rifting and magmatism in southern

- Scandinavia, the North Sea and northern Germany: A review. Geological Society Special Publication 223, 11–40. <https://doi.org/10.1144/GSL.SP.2004.223.01.02>
- NGU kommunikasjon & samfunn, 2019. Mineraler for det grønne skiftet, NGU TEMA n. ed. NGU.
- Olaussen, S., Dahlgren, S., 2007. Environmental setting of the southernmost outcrop of the Carboniferous in the Oslo Rift. An arid syn-tectonic lacustrine and alluvial deposit with possible marine incursions. *Vinterkonferansen* 1, 70–71.
- Parsons, I., 2010. Feldspars defined and described: a pair of posters published by the Mineralogical Society. Sources and supporting information. *Mineralogical Magazine* 74, 529–551. <https://doi.org/10.1180/minmag.2010.074.3.529>
- Pasero, M., Kampf, A.R., Ferraris, C., Pekov, I. v., Rakovan, J., White, T.J., 2010. Nomenclature of the apatite supergroup minerals. *European Journal of Mineralogy* 22, 163–179. <https://doi.org/10.1127/0935-1221/2010/0022-2022>
- Pedersen, L.E., Heaman, L.M., Holm, P.M., 1995. Further constraints on the temporal evolution of the Oslo Rift from precise U-Pb zircon dating in the Siljan-Skrim area. *Lithos* 34, 301–315. [https://doi.org/10.1016/0024-4937\(94\)00014-S](https://doi.org/10.1016/0024-4937(94)00014-S)
- Petersen, J.S., 1978. Structure of the larvikite-lardalite complex, Oslo-region, Norway, and its evolution. *Geologische Rundschau* 67, 330–342.
- Pettke, T., Oberli, F., Audétat, A., Guillong, M., Simon, A.C., Hanley, J.J., Klemm, L.M., 2012. Recent developments in element concentration and isotope ratio analysis of individual fluid inclusions by laser ablation single and multiple collector ICP-MS. *Ore Geology Reviews* 44, 10–38.
- Pirajno, F., 2013. Effects of Metasomatism on Mineral Systems and Their Host Rocks: Alkali Metasomatism, Skarns, Greisens, Tourmalinites, Rodingites, Black-Wall Alteration and Listvenites. *Metasomatism and the Chemical Transformation of Rock*. Springer, 204–246. [https://doi.org/10.1007/978-3-642-28394-9\\_7](https://doi.org/10.1007/978-3-642-28394-9_7)
- Potter, D.K., Al-Ghamdi, T.M., Ivakhnenko, O.P., 2011. Sensitive carbonate reservoir rock characterization from magnetic hysteresis curves and correlation with petrophysical properties. *Petrophysics-The SPWLA Journal of Formation Evaluation and Reservoir Description* 52, 50–57.
- Pracejus, B., 2015. *The Ore Minerals Under the Microscope*, Volume 3, 2nd ed. Elsevier Science.
- Ramberg, I.B., 1974. Gravity interpretation of the Oslo Graben and associated igneous rocks. Department of Geology, University of Oslo.
- Rasmussen, E., Neumann, E.-R., Andersen, T., Sundvoll, B., Fjerdingsstad, V., Stabel, A., 1988. Petrogenetic processes associated with intermediate and silicic magmatism in the Oslo rift, south-east Norway. *Mineralogical Magazine* 52, 293–307.
- Reynolds, J.M., 2011. *An introduction to applied and environmental geophysics*. John Wiley & Sons.
- Richards, S.W., Collins, W.J., 2002. The Cooma Metamorphic Complex, a low-P, high-T (LPHT) regional aureole beneath the Murrumbidgee Batholith. *Journal of Metamorphic*

- Geology 20, 119–134. <https://doi.org/https://doi.org/10.1046/j.0263-4929.2001.00360.x>
- Robb, L., 2015. *Introduction to Ore- Forming Processes*, 15th ed. Blackwell Publishing.
- Shand, S.J., 1943. *The Eruptive Rocks*, 2nd ed. New York: John Willey.
- Skienatlas, n.d. Produksjon og bruk av trekull [WWW Document]. URL <http://www.skienatlas.org/content/download/2488/15559/file/KULLBRENNING+MV.pdf>
- Skilbred, J.E., 2016. Eiriks Gruve [WWW Document], Kulturminnesøk. URL <https://bit.ly/3gj8ila>
- Sommer, H., Kröner, A., 2019. Igneous petrology, zircon geochronology and geochemistry of multiply emplaced granitoid bodies from the Palaeoproterozoic Usagaran domain in central Tanzania. *Journal of African Earth Sciences* 150, 626–656. <https://doi.org/10.1016/j.jafrearsci.2018.09.017>
- Streckeisen, A., 1974. Classification and nomenclature of plutonic rocks recommendations of the IUGS subcommission on the systematics of Igneous Rocks. *Geologische Rundschau* 63, 773–786. <https://doi.org/10.1007/BF01820841>
- Sun, S.S., McDonough, W.F., 1989. Chemical and isotopic systematics of oceanic basalts: Implications for mantle composition and processes. *Geological Society , London, Special Publications* 42, 313–345. <https://doi.org/10.1144/GSL.SP.1989.042.01.19>
- Sundvoll, B., Neumann, E.R., Larsen, B.T., Tuen, E., 1990. Age relations among Oslo Rift magmatic rocks: implications for tectonic and magmatic modelling. *Tectonophysics* 178, 67–87. [https://doi.org/10.1016/0040-1951\(90\)90460-P](https://doi.org/10.1016/0040-1951(90)90460-P)
- Tegner, C., Wilson, J., Robins, B., 2006. Role of Assimilation and Fractional Crystallisation in Crustal Magma Transfer. AGU Fall Meeting Abstracts. V22A-05.
- Toplis, M.J., Carroll, M.R., 1995. An experimental study of the influence of oxygen fugacity on Fe-Ti oxide stability, phase relations, and mineral—melt equilibria in ferro-basaltic systems. *Journal of Petrology* 36, 1137–1170.
- Vaagland, L., 2016. Avsølskås [WWW Document], Kulturminnesøk. URL <https://bit.ly/3vcXE3z>
- van Kauwenbergh, S.J., 2010. *World Phosphate Rock Reserves and Resources*, Technical Bulletin IFDC-T-75.
- Veksler, I. v, Charlier, B., 2015. Silicate Liquid Immiscibility in Layered Intrusions. In: Charlier, B., Namur, O., Latypov, R., Tegner, C. (Eds.), *Layered Intrusions*. Springer Netherlands, Dordrecht, 229–258. [https://doi.org/10.1007/978-94-017-9652-1\\_5](https://doi.org/10.1007/978-94-017-9652-1_5)
- Webster, J.D., Piccoli, P.M., 2015. Magmatic apatite: A powerful, yet deceptive, mineral. *Elements* 11, 177–182.
- Weinberg, R.F., 2006. Melt segregation structures in granitic plutons. *Geology* 34, 305–308. <https://doi.org/10.1130/G22406.1>
- Winter, J.D., 2001. *An introduction to Igneous and Metamorphic Petrology*, 1. ed. Prentice Hall.

Yoder, H.S.; Tilley, C.E., 1962. Origin of Basalt Magmas: An Experimental Study of Natural and Synthetic Rock Systems. *Journal of Petrology* 3, 342–532.  
<https://doi.org/10.1093/petrology/3.3.342>

# Appendix

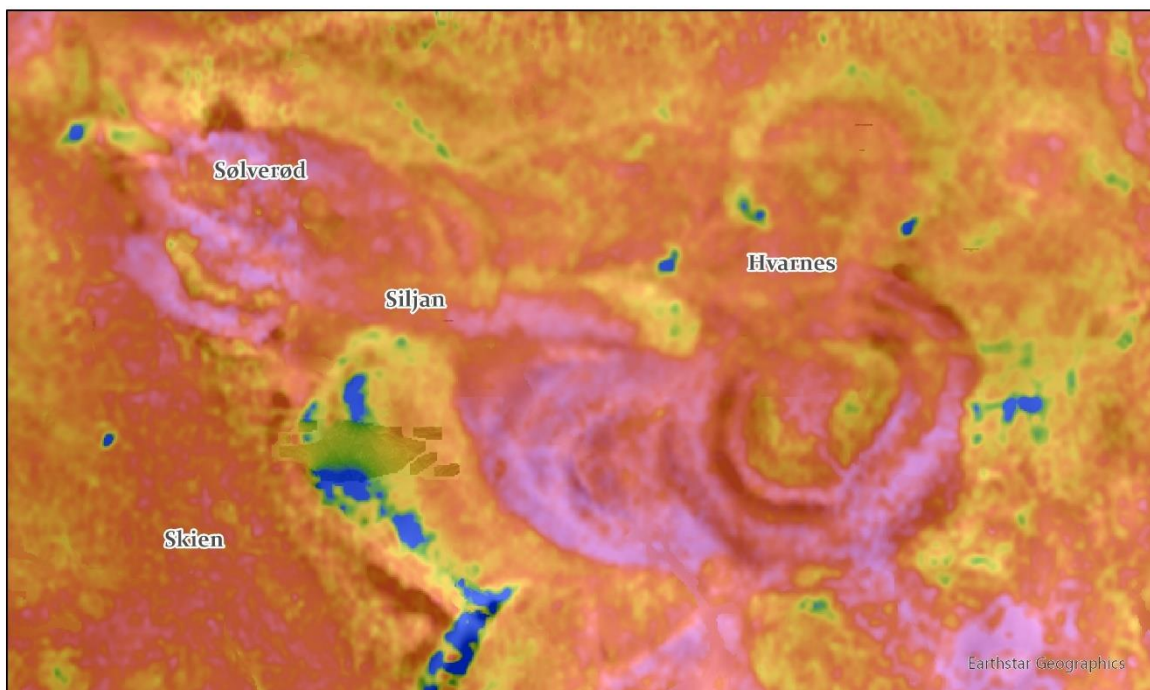


# APPENDIX A: Geomagnetism



## COMBINED GEOPHYSICS

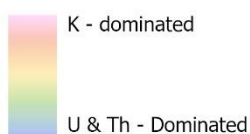
### SILJAN - HVARNES INTRUSION



0 3 6 12 Km

Spatial Reference  
PCS: ETRS 1989 UTM Zone 32N  
GCS: GCS ETRS 1989  
By: Tord Andersen

Combined radiometric  
maps



Geomagnetic map

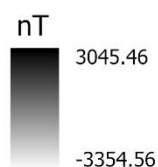


Figure 0-1: Experimental map of K – Th&U ratio layered on top of the geomagnetic map in monochrome created to differentiate pulses of intrusions. Ring-structures south of Hvarnes is a lardalite complex. Siljan-Hvarnes intrusion stretches E-W and ends at Sølverød. Blue areas in the east are river sediments, while blue section south of Siljan corresponds to the U-rich Alun-shale. Rocks to the west of the Alun-shale are mainly Ordovician sedimentary rocks. (The resolution of the radiometric maps was unfortunately too low to create a map of the field area).

Magnetic field for Siljan calculated by WMM-2020 and IGRF 2020.

Magnetic Field							
<b>Model Used:</b> WMM-2020							
<b>Latitude:</b> 59.318935° N							
<b>Longitude:</b> 9.634012° E							
<b>Elevation:</b> 0.0 km Mean Sea Level							
Date	Declination (+ E   - W )	Inclination (+ D   - U )	Horizontal Intensity	North Comp (+ N   - S)	East Comp (+ E   - W)	Vertical Comp (+ D   - U)	Total Field
2020-06-01	3.3691°	72.4294°	15,439.5 nT	15,412.8 nT	907.3 nT	48,758.1 nT	51,144.2 nT
<b>Change/Year</b>	0.2159°/yr	0.0190°/yr	-1.7 nT/yr	-5.1 nT/yr	58.0 nT/yr	50.7 nT/yr	47.8 nT/yr
<b>Uncertainty</b>	0.45°	0.21°	128 nT	131 nT	94 nT	157 nT	145 nT

Magnetic Field							
<b>Model Used:</b> IGRF2020							
<b>Latitude:</b> 59.318935° N							
<b>Longitude:</b> 9.634012° E							
<b>Elevation:</b> 0.0 km Mean Sea Level							
Date	Declination (+ E   - W )	Inclination (+ D   - U )	Horizontal Intensity	North Comp (+ N   - S)	East Comp (+ E   - W)	Vertical Comp (+ D   - U)	Total Field
2020-06-01	3.4222°	72.4352°	15,439.4 nT	15,411.9 nT	921.6 nT	48,775.1 nT	51,160.4 nT
<b>Change/Year</b>	0.2224°/yr	0.0178°/yr	0.9 nT/yr	-2.7 nT/yr	59.9 nT/yr	55.6 nT/yr	53.2 nT/yr

Dip-direction and dip for oriented samples

<b>Sample nr</b>	<b>Dipdir/dip</b>
111501	345/32
111502	278/90
111503	270/90
111504	305/86
111505	041/64
111510	330/84
111512	304/06
111514	148/75W
111515	026/88
111519	230/80
111520	209/85
111521	343/78
111522	350/60
111523	151/55
111524	213/40
111525	340/80
111526	298/76
111527	281/85
111528	240/78
111529	011/68
111530	191/90
111531	213/70
111532	292/86
111533	182/81
111535	158/72
111536	110/85
111537	350/82
111538	034/75
111539	174/74

Sample coordinates

<b>SAMPLE</b>	<b>Coordinate (lat/lon)</b>	<b>UTM (32V E, N)</b>
111501	6587762.265928 195067.94592	32V 536382 6575654
111502	6587742.414608 195035.842723	32V 536352 6575632
111503	6587569.259856 194874.546371	32V 536207 6575445
111504	6587567.005407 194876.863199	32V 536209 6575443
111505	6587582.249693 194797.940338	32V 536129 6575451
111506	6587571.820053 194791.065038	32V 536124 6575440
111507	6587571.613187 194783.565303	32V 536116 6575439
111508	6587786.0219 194658.172881	32V 535972 6575641
111509	6587776.251672 194610.689682	32V 535926 6575627
111510	6587480.062807 194134.177953	32V 535478 6575290
111511	6587298.407553 194126.434087	32V 535487 6575108
111512	6587453.800716 194174.824505	32V 535521 6575267
111513	6587473.804616 194173.020118	32V 535518 6575287
111514	6584854.181073 196407.978759	32V 537976 6572882
111515	6584868.892796 196424.182548	32V 537991 6572898
111516	6584866.256129 196396.803218	32V 537964 6572893
111517	6584863.063271 196397.550615	32V 537965 6572890
111518	6584861.574193 196398.723237	32V 537966 6572888
111519	6585798.045862 195345.07299	32V 536834 6573725
111520	6586467.732556 194936.691357	32V 536368 6574355
Jernskottet	6585264.437478 195455.741234	32V 536992 6573204
111521	6589410.9403 194484.285488	32V 535653 6577242
111522	6589180.049621 194170.531985	32V 535362 6576984
111523	6588904.509034 194031.111378	32V 535248 6576697
111524	6588900.638346 194458.102399	32V 535673 6576732
111525	6588995.832463 194452.938583	32V 535659 6576826
111526	6588894.03742 194799.831739	32V 536013 6576756

Sample coordinates

<b>SAMPLE</b>	<b>Coordinate (lat/lon)</b>	<b>UTM (32V E, N)</b>
111530	6586353.035047 194788.220532	32V 536230 6574227
111531	6586825.947675 194396.651402	32V 535798 6574662
111532	6585443.476255 194246.138799	32V 535773 6573274
111533	6585415.899693 194143.432446	32V 535673 6573237
111534	6585111.216211 194323.721278	32V 535880 6572950
111535	6585012.998669 194340.610575	32V 535905 6572854
111536	6588274.860992 195101.928819	32V 536370 6576167
111537	6588687.615579 194823.558291	32V 536056 6576553
111538	6585706.741742 194742.767641	32V 536243 6573580
111539	6585193.361812 194773.094902	32V 536319 6573072
195763	6587761.488734 195098.640034	32V 536412 6575656
195764	6587769.206484 195111.453276	32V 536425 6575665
195765	6585749.488583 196584.790063	32V 538072 6573788
195766	6583734.99644 200329.947824	32V 541979 6572121
195767	6584680.227304 204376.299498	32V 545919 6573425

Density calculations part 1

<b>Sample</b>	<b>W_immersed</b>	<b>W_dry</b>	<b>W_(DisplacedFluid)</b>	<b>Vol_rock</b>	<b>density_rock</b>
510_1A	15.598	25.1339	9.5359	9.55280847	2.631048249
510_1B	15.1613	24.4427	9.2814	9.29785721	2.62885302
510_2A	15.0525	24.3271	9.2746	9.29104515	2.618338369
510_2B	14.6829	2.37E+01	9.0135	9.02948218	2.624336537
512_1A	16.7836	2.66E+01	9.8572	9.87467818	2.697890454
512_1B	16.7641	26.5291	9.765	9.7823147	2.711945058
512_2A	18.644	29.6056	10.9616	10.9810364	2.696066093
514_1A	19.5475	28.6667	9.1192	9.1353696	3.137990168
514_1B	20.296	29.7844	9.4884	9.50522425	3.133476836
514_2A	19.8504	29.6901	9.8397	9.85714715	3.012037819
514_2B	20.5679	30.8901	10.3222	10.3405027	2.987291907
514_2C	20.0558	30.2186	10.1628	10.1808201	2.968189188
515_1	15.7508	25.3949	9.6441	9.66120032	2.62854502
515_2	16.6241	26.8069	10.1828	10.2008555	2.627907038
520	15.6747	25.7491	10.0744	10.0922633	2.551370215
521_1A	16.9139	26.6867	9.7728	9.79012853	2.725878412
521_1B	16.7125	26.3295	9.617	9.63405227	2.732962128
521_2A	15.7978	24.8546	9.0568	9.07285896	2.739445208
521_2B	17.4125	27.3943	9.9818	9.99949911	2.739567221
524_A	17.4912	27.5955	10.1043	10.1222163	2.726231007
524_B	17.6588	27.9831	10.3243	10.3426064	2.705613932
525_1A	17.7428	28.0867	10.3439	10.3622412	2.710485072
525_1B	17.6981	28.0003	10.3022	10.3204672	2.713084532
525_1C	17.4578	27.7113	10.2535	10.2716809	2.697834983
525_2A	17.8791	28.3542	10.4751	10.4936738	2.702027958
525_2B	17.7087	28.0361	10.3274	10.3457119	2.709924676
525_2c	17.681	27.9682	10.2872	10.3054406	2.713925683
526_1A	20.3704	31.0522	10.6818	10.7007403	2.901873992
526_1B	19.7891	30.1478	10.3587	10.3770674	2.905233127
526_1C	19.1039	29.0764	9.9725	9.99018262	2.910497345
526_2A	18.8278	28.6953	9.8675	9.88499644	2.90291455
526_2B	20.6017	31.4002	10.7985	10.8176472	2.902682932
527_1	16.1373	26.0885	9.9512	9.96884486	2.617003312
527_2	15.847	25.7391	9.8921	9.90964006	2.597379909
528_A	17.0978	27.1937	10.0959	10.1138014	2.688771397
528_B	15.2279	24.185	8.9571	8.97298218	2.6953135
529_1A	19.2971	29.649	10.3519	10.3702554	2.859042424
529_1B	18.3157	28.2491	9.9334	9.95101329	2.838816427
529_2A	20.2724	31.0977	10.8253	10.8444948	2.867602475
529_2B	19.8572	30.4972	10.64	10.6588662	2.861204883
529_2C	18.6681	28.7589	10.0908	10.1086924	2.844967371
530_1A	16.1844	26.2595	10.0751	10.0929645	2.60176283

Density calculations part 2

<b>Sample</b>	<b>W_immersed</b>	<b>W_dry</b>	<b>W_(DisplacedFluid)</b>	<b>Vol_rock</b>	<b>density_rock</b>
530_1B	14.9697	24.2298	9.2601	9.27651944	2.611949466
530_1C	15.7171	25.404	9.6869	9.70407621	2.617868969
530_2A	15.223	24.6181	9.3951	9.41175881	2.615674763
530_2B	15.6144	25.594	9.9796	9.99729521	2.560092451
531_1A	15.3374	24.5603	9.2229	9.23925348	2.658255892
531_1B	15.6304	24.9738	9.3434	9.35996714	2.668150392
531_1C	15.3529	24.4764	9.1235	9.13967723	2.67803768
531_2A	14.9354	23.9441	9.0087	9.02467367	2.653181807
531_2B	16.8207	26.9277	10.107	10.1249211	2.659546648
532_A	16.7566	26.9325	10.1759	10.1939433	2.642009992
532_B	15.975	25.6199	9.6449	9.66200174	2.651614094
533	15.8433	25.7583	9.915	9.93258067	2.593313949
535_A	16.2265	26.265	10.0385	10.0562997	2.611795682
535_B	15.9644	25.8541	9.8897	9.90723581	2.60961791
536	16.2929	26.383	10.0901	10.1079911	2.61011309
537_A	16.8232	26.5671	9.7439	9.76117728	2.721710633
537_B	16.4601	25.8793	9.4192	9.43590155	2.742642012
538_1A	16.8044	27.2564	10.452	10.4705328	2.603153097
538_2	17.0848	27.7699	10.6851	10.7040462	2.594336719
539_1A	14.8038	23.7542	8.9504	8.9662703	2.649284397
539_1B	17.0208	27.2764	10.2556	10.2737846	2.654951516
539_1C	16.6879	26.8923	10.2044	10.2224938	2.630698584
539_2A	16.201	25.9413	9.7403	9.7575709	2.658581758
539_2B	17.2741	27.6389	10.3648	10.3831782	2.661892091
501A	18.1787	28.8635	10.6848	10.7037456	2.696579403
501B	17.3629	27.4623	10.0994	10.1173076	2.714388155
501C	16.7609	26.5906	9.8297	9.84712942	2.700340258
501D	17.9271	28.5573	10.6302	10.6490488	2.681676128
501E	17.9222	28.4073	10.4851	10.5036915	2.704506307
502A	17.1918	28.0271	10.8353	10.8545125	2.582068981
502B	16.8391	27.4302	10.5911	10.6098795	2.585345105

Density calculations part 3

<b>Sample</b>	<b>W_immersed</b>	<b>W_dry</b>	<b>W_(DisplacedFluid)</b>	<b>Vol_rock</b>	<b>density_rock</b>
504A	26.4629	37.085	10.6221	10.6409345	3.485126251
504B	25.3548	35.4135	10.0587	10.0765355	3.514451977
504C	24.8067	34.9555	10.1488	10.1667952	3.438202424
505A	26.2759	36.6456	10.3697	10.3880869	3.527656276
505B	25.6548	35.8229	10.1681	10.1861294	3.516831411
505C	26.4332	36.8606	10.4274	10.4458892	3.528718256
505D	24.3498	33.9229	9.5731	9.59007443	3.537292671
519A	17.4322	27.6608	10.2286	10.2467367	2.699474061
519B	17.7472	28.3442	10.597	10.6157899	2.670003847
519C	16.1887	25.863	9.6743	9.69145387	2.668639849
522A	17.7228	28.1767	10.4539	10.4724362	2.690558284
522B	18.4797	29.4111	10.9314	10.9507829	2.685753184
522C	18.3494	29.1283	10.7789	10.7980125	2.697561245



Induced magnetization and Norm. modulus calculation Part 1

Sample	Density Lab		SUSC MEASUREMENTS			NRM MEASUREMENTS	
Sample	Vol <sub>rock</sub>	density <sub>rock</sub>	KRe[SI]	Kvol[SI]	Induced mag [A/m]	Modulus [A/m]	Norm. Modulus [A/m]
				Kre*(1/Vol <sub>rock</sub> )	Kvol*H		(Modulus*11.15)/Vol <sub>rock</sub>
501_A	10.70375	2.696579	9.03E-02	8.44E-03	0.00E+00	0.3888806	0.405094
501_B	10.11731	2.714388	1.01E-01	9.95E-03	0.00E+00	1.17959	1.299993
501_C	9.847129	2.70034	9.98E-02	1.01E-02	0.00E+00	0.9988211	1.130975
501_D	10.64905	2.681676	7.84E-02	7.36E-03	0.00E+00	1.65375	1.731545
501_E	10.50369	2.704506	9.25E-02	8.81E-03	0.00E+00	1.160642	1.232058
502_A	10.85451	2.582069	3.10E-02	2.86E-03	0.00E+00	0.4617651	0.474336
502_B	10.60988	2.585345	2.98E-02	2.80E-03	0.00E+00	0.5054503	0.531181
504_A	10.64093	3.485126	5.02E-01	4.72E-02	0.00E+00	37.00784	38.77831
504_B	10.07654	3.514452	4.77E-01	4.73E-02	0.00E+00	29.81359	32.98966
504_C	10.1668	3.438202		0.00E+00	0.00E+00	11.81688	12.95966
505_A	10.38809	3.527656	4.38E-01	4.22E-02	0.00E+00	39.82424	42.74514
505_B	10.18613	3.516831	4.16E-01	4.08E-02	0.00E+00	31.29633	34.25777
505_C	10.44589	3.528718	4.30E-01	4.12E-02	0.00E+00	23.5669	25.15544
505_D	9.590074	3.537293	3.99E-01	4.16E-02	0.00E+00	8.969398	10.42836
510_1A	9.552808	2.631048	3.57E-02	3.73E-03	0.00E+00	0.7115061	0.830467
510_1B	9.297857	2.628853	3.29E-02	3.54E-03	0.00E+00	0.5503317	0.659958
510_2A	9.291045	2.618338	3.42E-02	3.68E-03	0.00E+00	0.729913	0.875954
510_2B	9.029482	2.624337	3.42E-02	3.79E-03	0.00E+00	0.716758	0.885084
512_1A	9.874678	2.69789	2.48E-02	2.51E-03	0.00E+00	0.4025245	0.454511
512_1B	9.782315	2.711945	3.30E-02	3.37E-03	0.00E+00	0.5834732	0.66505
512_2A	10.98104	2.696066	2.04E-02	1.86E-03	0.00E+00	0.2889446	0.293391
514_1A	9.13537	3.13799	5.63E-01	6.16E-02	0.00E+00	6.035296	7.366265
514_1B	9.505224	3.133477	5.81E-01	6.11E-02	0.00E+00	6.646811	7.796969
514_2A	9.857147	3.012038	4.63E-01	4.69E-02	0.00E+00	1.665667	1.884134
514_2B	10.3405	2.987292	4.72E-01	4.56E-02	0.00E+00	2.823863	3.044927
514_2C	10.18082	2.968189	4.33E-01	4.26E-02	0.00E+00	3.111029	3.407189
515_1	9.6612	2.628545	2.35E-02	2.43E-03	0.00E+00	0.248423	0.286705

Induced magnetization and Norm. modulus calculation Part 2

Sample	Density Lab		SUSC MEASUREMENTS			NRM MEASUREMENTS	
Sample	Vol <sub>rock</sub>	density <sub>rock</sub>	KRe[SI]	Kvol[SI]	Induced mag [A/m]	Modulus [A/m]	Norm. Modulus [A/m]
				Kre*(1/Vol <sub>rock</sub> )	Kvol*H		(Modulus*11.15)/Vol <sub>rock</sub>
515_2	10.20086	2.627907	2.39E-02	2.34E-03	0.00E+00	0.2386399	0.260844
519_A	10.24674	2.699474	3.68E-02	3.59E-03	0.00E+00	0.5979716	0.650684
519_B	10.61579	2.670004	2.73E-02	2.57E-03	0.00E+00	0.7653365	0.80385
519_C	9.691454	2.66864	2.14E-02	2.21E-03	0.00E+00	0.7075316	0.814014
520	10.09226	2.55137	3.61E-02	3.58E-03	0.00E+00	0.1016522	0.112306
521_1A	9.790129	2.725878	2.64E-04	2.70E-05	0.00E+00	2.803587	3.193012
521_1B	9.634052	2.732962	3.07E-04	3.19E-05	0.00E+00	2.652961	3.070413
521_2A	9.072859	2.739445	2.51E-04	2.77E-05	0.00E+00	2.327445	2.86029
521_2B	9.999499	2.739567	2.78E-04	2.78E-05	0.00E+00	3.288799	3.667195
522_A	10.47244	2.690558	6.35E-02	6.06E-03	0.00E+00	0.9879621	1.051883
522_B	10.95078	2.685753	5.76E-02	5.26E-03	0.00E+00	1.614505	1.643876
522_C	10.79801	2.697561	6.86E-02	6.35E-03	0.00E+00	0.7934362	0.8193
524_A	10.12222	2.726231	2.98E-04	2.95E-05	0.00E+00	4.290804	4.726481
524_B	10.34261	2.705614	2.91E-04	2.82E-05	0.00E+00	4.249353	4.581078
525_1A	10.36224	2.710485	1.83E-04	1.77E-05	0.00E+00	3.979598	4.282135
525_1B	10.32047	2.713085	2.05E-04	1.98E-05	0.00E+00	3.781653	4.085613
525_1C	10.27168	2.697835	1.81E-04	1.76E-05	0.00E+00	3.150429	3.419818
525_2A	10.49367	2.702028	1.90E-04	1.81E-05	0.00E+00	3.138312	3.334598
525_2B	10.34571	2.709925	1.86E-04	1.79E-05	0.00E+00	3.660068	3.944606
525_2C	10.30544	2.713926	1.83E-04	1.78E-05	0.00E+00	3.728498	4.034059
526_1A	10.70074	2.901874	1.14E-01	1.07E-02	0.00E+00	2.929061	3.052035
526_1B	10.37707	2.905233	1.08E-01	1.04E-02	0.00E+00	2.862342	3.075543
526_1C	9.990183	2.910497	1.03E-01	1.04E-02	0.00E+00	3.333902	3.720954
526_2A	9.884996	2.902915	1.21E-01	1.22E-02	0.00E+00	1.565638	1.765996
526_2B	10.81765	2.902683	1.21E-01	1.12E-02	0.00E+00	1.879707	1.937458
527_1	9.968845	2.617003	2.86E-02	2.87E-03	0.00E+00	0.1115117	0.124724
527_2	9.90964	2.59738	1.92E-02	1.93E-03	0.00E+00	0.1722993	0.193865

Induced magnetization and Norm. modulus calculation Part 3

Sample	Density Lab		SUSC MEASUREMENTS			NRM MEASUREMENTS	
Sample	Vol <sub>rock</sub>	density <sub>rock</sub>	KRe[SI]	Kvol[SI]	Induced mag [A/m]	Modulus [A/m]	Norm. Modulus [A/m]
				Kre*(1/Vol <sub>rock</sub> )	Kvol*H		(Modulus*11.15)/Vol <sub>rock</sub>
528_A	10.1138	2.688771	4.59E-02	4.53E-03	0.00E+00	10.37	11.43245
528_B	8.972982	2.695313	4.75E-02	5.30E-03	0.00E+00	10.28475	12.78003
529_1A	10.37026	2.859042	1.49E-01	1.44E-02	0.00E+00	1.142483	1.228387
529_1B	9.951013	2.838816	1.38E-01	1.39E-02	0.00E+00	1.413649	1.583978
529_2A	10.84449	2.867602	1.54E-01	1.42E-02	0.00E+00	0.9484835	0.975204
529_2B	10.65887	2.861205	1.54E-01	1.45E-02	0.00E+00	1.253739	1.311508
529_2C	10.10869	2.844967	1.43E-01	1.41E-02	0.00E+00	1.685747	1.859398
530_1A	10.09296	2.601763	7.07E-02	7.00E-03	0.00E+00	1.513884	1.672433
530_1B	9.276519	2.611949	7.52E-02	8.11E-03	0.00E+00	1.386608	1.666647
530_1C	9.704076	2.617869	8.86E-02	9.13E-03	0.00E+00	1.778747	2.043783
530_2A	9.411759	2.615675	7.27E-02	7.73E-03	0.00E+00	2.039106	2.415705
530_2B	9.997295	2.560092	7.68E-02	7.69E-03	0.00E+00	1.842576	2.055028
531_1A	9.239253	2.658256	3.36E-02	3.64E-03	0.00E+00	1.075771	1.298248
531_1B	9.359967	2.66815	3.49E-02	3.73E-03	0.00E+00	1.040868	1.239927
531_1C	9.139677	2.678038	3.37E-02	3.69E-03	0.00E+00	1.202711	1.467254
531_2A	9.024674	2.653182	3.03E-02	3.36E-03	0.00E+00	0.893492	1.103911
531_2B	10.12492	2.659547	3.50E-02	3.46E-03	0.00E+00	0.9661362	1.063951
532_A	10.19394	2.64201	3.70E-02	3.63E-03	0.00E+00	0.2166217	0.236938
532_B	9.662002	2.651614	3.42E-02	3.54E-03	0.00E+00	0.2082461	0.240317
533	9.932581	2.593314	6.23E-02	6.27E-03	0.00E+00	4.459159	5.00571
535_A	10.0563	2.611796	2.58E-02	2.57E-03	0.00E+00	0.106246	0.117801
535_B	9.907236	2.609618	2.35E-02	2.37E-03	0.00E+00	0.0643205	0.072389
536	10.10799	2.610113	2.75E-02	2.72E-03	0.00E+00	0.5614597	0.619339
537_A	9.761177	2.721711	1.08E-01	1.11E-02	0.00E+00	1.701416	1.943494
537_B	9.435902	2.742642	1.35E-01	1.43E-02	0.00E+00	1.656506	1.957422
538_1A	10.47053	2.603153	5.54E-02	5.29E-03	0.00E+00	0.8926024	0.950526
538_2	10.70405	2.594337	6.79E-02	6.34E-03	0.00E+00	0.8850813	0.921956
539_1A	8.96627	2.649284	3.67E-02	4.09E-03	0.00E+00	0.2189755	0.272307
539_1B	10.27378	2.654952	4.02E-02	3.91E-03	0.00E+00	0.2949678	0.320125
539_1C	10.22249	2.630699	4.26E-02	4.16E-03	0.00E+00	0.3044257	0.332047
539_2A	9.757571	2.658582	3.71E-02	3.80E-03	0.00E+00	0.331658	0.378986
539_2B	10.38318	2.661892	4.21E-02	4.05E-03	0.00E+00	0.3627795	0.389572

Q-values part 1

Sample	Rock Type	Induced [A/m]	mag	Norm. Modulus [A/m]	Q
526_1A	Fe-Ti-P Aph.	0.433725638		3.052034645	7.04
526_1B	Fe-Ti-P Aph.	0.422537378		3.07554264	7.28
526_1C	Fe-Ti-P Aph.	0.421377341		3.72095373	8.83
526_2A	Fe-Ti-P Aph.	0.497936372		1.765995951	3.55
526_2B	Fe-Ti-P Aph.	0.454253751		1.937457618	4.27
504_A	Fe-Ti-P F-Gr.	1.919883854		38.77830634	20.20
504_B	Fe-Ti-P F-Gr.	1.92762365		32.98966491	17.11
504_C	Fe-Ti-P F-Gr.	0		12.95966025	#DIV/0!
505_A	Fe-Ti-P F-Gr.	1.716182377		42.74514448	24.91
505_B	Fe-Ti-P F-Gr.	1.662278534		34.25776996	20.61
505_C	Fe-Ti-P F-Gr.	1.676285908		25.15543956	15.01
505_D	Fe-Ti-P F-Gr.	1.693425619		10.42836408	6.16
514_1A	Fe-Ti-P Porph.	2.509478457		7.366264674	2.94
514_1B	Fe-Ti-P Porph.	2.488501074		7.796969406	3.13
514_2A	Fe-Ti-P Porph.	1.910225176		1.884134097	0.99
514_2B	Fe-Ti-P Porph.	1.856761882		3.044926673	1.64
514_2C	Fe-Ti-P Porph.	1.73232652		3.407188534	1.97
529_1A	Mafic dike	0.58613064		1.228386864	2.10
529_1B	Mafic dike	0.564593465		1.583978022	2.81
529_2A	Mafic dike	0.578518675		0.975203664	1.69
529_2B	Mafic dike	0.589357729		1.311508147	2.23
529_2C	Mafic dike	0.57391021		1.859397668	3.24
521_1A	Rhomb Porphyry	0.001099089		3.193011712	2905.14
521_1B	Rhomb Porphyry	0.001298607		3.070412565	2364.39
521_2A	Rhomb Porphyry	0.001127196		2.86029044	2537.53
521_2B	Rhomb Porphyry	0.001132669		3.66719457	3237.66
524_A	Rhomb Porphyry	0.001199378		4.726481145	3940.78
524_B	Rhomb Porphyry	0.001147053		4.581077927	3993.78
525_1A	Rhomb Porphyry	0.000720166		4.282135205	5946.04
525_1B	Rhomb Porphyry	0.000807106		4.085612601	5062.05
525_1C	Rhomb Porphyry	0.0007174		3.419818409	4766.96
525_2A	Rhomb Porphyry	0.00073714		3.334597535	4523.70
525_2B	Rhomb Porphyry	0.000730761		3.944606089	5397.94
525_2C	Rhomb Porphyry	0.000722951		4.034058726	5579.99
537_A	Rhomb Porphyry	0.452117325		1.943493889	4.30
537_B	Rhomb Porphyry	0.583765551		1.957422066	3.35
528_A	Rhomb Porphyry	0.184564846		11.43244712	61.94
528_B	Rhomb Porphyry	0.215652788		12.78002789	59.26
536	Syenite C-Gr	0.11084284		0.61933925	5.59

Q-values part 2

Sample	Rock Type	Induced [A/m]	mag	Norm. Modulus [A/m]	Q
531_1A	Syenite C-Gr	0.148056154		1.298248465	8.77
531_1B	Syenite C-Gr	0.151931676		1.239927237	8.16
531_1C	Syenite C-Gr	0.15020375		1.467253965	9.77
531_2A	Syenite C-Gr	0.136734623		1.103910918	8.07
531_2B	Syenite C-Gr	0.140814884		1.063950871	7.56
502_A	Syenite C-Gr	0.116272079		0.474335524	4.08
502_B	Syenite C-Gr	0.114194857		0.531181419	4.65
510_1A	Syenite F-Gr	0.152018382		0.830467086	5.46
510_1B	Syenite F-Gr	0.143970331		0.659958345	4.58
510_2A	Syenite F-Gr	0.149728501		0.875954192	5.85
510_2B	Syenite F-Gr	0.154155961		0.885084165	5.74
520	Syenite F-Gr	0.145627266		0.11230603	0.77
533	Syenite F-Gr	0.255399309		5.005710451	19.60
527_1	Syenite F-Gr	0.11688233		0.124724125	1.07
527_2	Syenite F-Gr	0.07871576		0.193865487	2.46
538_1A	Syenite Porph.	0.215370715		0.950526292	4.41
538_2	Syenite Porph.	0.258101156		0.921955712	3.57
501_A	Syenite Porph.	0.343421864		0.405093585	1.18
501_B	Syenite Porph.	0.405217863		1.29999294	3.21
501_C	Syenite Porph.	0.412449576		1.130974804	2.74
501_D	Syenite Porph.	0.29984407		1.731545495	5.77
501_E	Syenite Porph.	0.358528629		1.232058106	3.44
515_1	Syenite Porph.	0.098944367		0.286705208	2.90
515_2	Syenite Porph.	0.09530634		0.260844287	2.74
530_1A	Syenite Porph.	0.285183722		1.672432963	5.86
530_1B	Syenite Porph.	0.330164268		1.666646559	5.05
530_1C	Syenite Porph.	0.37170944		2.043783314	5.50
530_2A	Syenite Porph.	0.314519389		2.415704902	7.68
530_2B	Syenite Porph.	0.312876096		2.055028081	6.57
532_A	Syenite Porph.	0.147888896		0.236937943	1.60

Q-values part 3

Sample	Rock Type	Induced [A/m]	mag	Norm. Modulus [A/m]	Q
532_B	Syenite Porph.	0.14423274		0.240317077	1.67
512_1A	Syenite Porph.	0.102123837		0.45451083	4.45
512_1B	Syenite Porph.	0.137381408		0.665049774	4.84
512_2A	Syenite Porph.	0.075558776		0.293390547	3.88
522_A	Syenite Porph.	0.246859627		1.05188298	4.26
522_B	Syenite Porph.	0.214216122		1.643876145	7.67
522_C	Syenite Porph.	0.258645161		0.819300186	3.17
535_A	Syenite Porph.	0.104530277		0.117801074	1.13
535_B	Syenite Porph.	0.09636391		0.072388867	0.75
539_1A	Syenite Porph.	0.166412605		0.27230685	1.64
539_1B	Syenite Porph.	0.159222172		0.320124579	2.01
539_1C	Syenite Porph.	0.169539486		0.332046819	1.96
539_2A	Syenite Porph.	0.154586144		0.378986403	2.45
539_2B	Syenite Porph.	0.165072928		0.389571607	2.36
519_A	Syenite VC-Gr	0.14625284		0.65068358	4.45
519_B	Syenite VC-Gr	0.104543636		0.803849927	7.69
519_C	Syenite VC-Gr	0.090023793		0.814013815	9.04

Measured NRM Vectors

Specimen	Module [A/m]	Dec	Inc
501A	0.3888806	26.7	17.2
501B	1.17959	301.4	61.3
501C	0.9988211	281.5	-7.7
501D	1.65375	23.9	66.4
501E	1.160642	349.1	69
502A	0.4617651	218.8	44.4
502B	0.5054503	308.2	48.7
504	11.81688	290.6	-25.2
504A	37.00784	266.3	-41.9
504B	29.81359	254.5	46.4
505A	39.82424	200.5	-49.8
505B	31.29633	184.8	-60
505C	23.5669	192.1	47.8
505D	8.969398	166.9	38.5
510_1A	0.7115061	3.7	0.4
510_1B	0.5503317	355.4	-2.6
510_2A	0.729913	16.9	10.7
510_2B	0.716758	9.2	4.9
512_1A	0.4025245	192.9	44.7
512_1B	0.5834732	198	-0.4
512_2A	0.2889446	174.2	37.5
514_1A	6.035296	337.2	29.2
514_1B	6.646811	319.4	45.5
514_2A	1.665667	329.1	22.7
514_2B	2.823863	7.7	48.3
514_2C	3.111029	41.1	66.4
515_1	0.248423	197.8	68.4
515_2	0.2386399	210.2	74.5
519A	0.5979716	205.3	-63
519B	0.7653365	244	-28.9
519C	0.7075316	211.7	-43.6
520	0.1016522	354.5	35.5
521_1A	2.803587	160.8	-4.3
521_1B	2.652961	158.9	-6.3
521_2A	2.327445	159	-6.2
521_2B	3.288799	162.8	-4.9
522A	0.9879621	175.3	42.2
522B	1.614505	183.1	-10.7
522C	0.7934362	179.9	8.8
524_A	4.290804	191.3	-77
524_B	4.249353	221.9	-77.6
525_1A	3.979598	154.2	-18.5
525_1B	3.781653	155.4	-19.6

Specimen	Module [A/m]	Dec	Inc
525_1C	3.150429	155.5	-20.8
525_2A	3.138312	154.2	-20.3
525_2B	3.660068	157.7	-19.1
525_2C	3.728498	156.1	-19.1
526_1A	2.929061	248.5	-3.7
526_1B	2.862342	253	-8
526_1C	3.333902	250	-11.4
526_2A	1.565638	236.7	7.2
526_2B	1.879707	239.4	12.3
527_1	0.111512	348	80.6
527_2	0.172299	314.4	39.2
528_A	10.37	129.6	9.7
528_B	10.28475	127.4	11.4
529_1A	1.142483	95.1	53.8
529_1B	1.413649	45.5	62
529_2A	0.948484	123.8	77
529_2B	1.253739	33.1	71.8
529_2C	1.685747	39.3	65.1
530_1A	1.513884	22.9	55
530_1B	1.386608	33.9	53.5
530_1C	1.778747	4.1	25.9
530_2A	2.039106	17.4	49.6
530_2B	1.842576	0.6	40.3
531_1A	1.075771	254.5	-58.7
531_1B	1.040868	273.9	-61.5
531_1C	1.202711	259.3	-50.8
531_2A	0.893492	292.5	-76.8
531_2B	0.966136	240.5	-56.4
532_A	0.216622	5.6	56.2
532_B	0.208246	12.6	33.2
533	4.459159	207.2	-26.8
535_A	0.106246	48.1	39.7
535_B	0.064321	103	-5.4
536	0.56146	156.8	25.4
537_A	1.701416	351	22.5
537_B	1.656506	8.5	-15.2
538_1A	0.892602	129.8	63.2
538_2	0.885081	106.3	22.5
539_1A	0.218976	290.4	56.4
539_1B	0.294968	276.5	59.4
539_1C	0.304426	350.2	84.5
539_2A	0.331658	320.4	76.9
539_2B	0.36278	308.7	82.9

## APPENDIX B: EPMA Analysis



EPMA Apatite part 1

Sample	MgO	Na2O	F	Al2O3	SiO2	Ce2O3	SrO	TiO2	Cr2O3	FeO	La2O3	K2O	Nd2O3	Cl	P2O5	CaO	Total
403B-Z1-Ap-01-c1	0.0338	0.2303	3.28	0.0016	0.448	1.2	0.0572	0	0.0049	0.1622	0.4686	0.0141	0.44	0.3619	40.84	51.48	98.9682
403B-Z1-Ap-02-c1	0.0148	0.262	2.66	0.0089	0.2683	1.0041	0.0423	0.0664	0.0008	0.4863	0.4295	0.0049	0.3463	0.3494	41.44	51.98	99.2923
403B-Z1-Ap-02-c2	0.0402	0.2839	2.88	0.0042	0.3184	1.0819	0.0631	0.023	0.0024	0.3859	0.403	0.001	0.3556	0.3534	41.21	51.74	99.0752
403B-Z1-Ap-03-c1	0.0176	0.2863	2.19	0.006	0.8111	1.94	0.0128	0.0122	0.0049	0.0747	0.7577	0.1183	0.5889	0.3204	40.64	51.92	99.6474
403B-Z1-Ap-04-c1	0.0102	0.2722	3.38	0	0.3173	1.0563	0.0492	0.0088	0.0303	0.3603	0.4087	0	0.3543	0.3179	41.55	52.03	100.0962
403B-Z1-Ap-04-r1	0	0.2579	3.28	0.0014	0.2852	1.0524	0.0571	0.0007	0	0.11	0.4304	0.0031	0.3525	0.3762	41.54	51.98	99.7217
403B-Z1-Ap-05-c1	0.0477	0.2355	3.4	0.0029	0.4201	1.23	0.0482	0.0129	0	0.1184	0.4474	0	0.3996	0.3036	41.67	51.66	99.9328
403B-Z1-Ap-06-c1	0	0.2935	1.95	0.0074	0.3835	1.23	0.1339	0.0111	0	0.3672	0.4896	0.0313	0.4277	0.4899	41.41	52.59	99.7966
403B-Z1-Ap-07-c1	0.0142	0.2826	2.45	0.0085	0.3832	1.17	0.0708	0.0093	0	0.1013	0.4512	0.0007	0.3868	0.326	41.25	51.38	98.2519
403B-Z2-Ap-01-c1	0.0253	0.2597	2.83	0.0027	0.3811	1.19	0.0847	0.0085	0.0196	0.1686	0.4642	0.0151	0.4155	0.2387	41.2	51.72	98.9525
403B-Z2-Ap-02-c1	0.0245	0.2506	2.75	0	0.6387	1.44	0.0877	0	0.0131	0.2166	0.5442	0.003	0.5082	0.2357	41.06	51.44	99.1717
403B-Z2-Ap-02-r1	0.0073	0.2698	2.89	0	0.8211	1.68	0.0593	0.0187	0.0073	0.589	0.6245	0.0218	0.6311	0.2674	40.07	50.66	98.584
403B-Z2-Ap-03-c1	0.0125	0.2651	2.53	0.0091	0.9901	1.93	0.082	0	0	0.1047	0.6781	0	0.683	0.2729	39.71	50.26	97.5059
403B-Z2-Ap-03-r1	0.0113	0.254	2.75	0	0.4938	1.24	0.0472	0.0197	0	0.2216	0.4885	0	0.4518	0.2754	40.92	50.49	97.5851
503-Z1-Ap-01-c	0	0.2003	1.85	0	0.6411	1.37	0.135	0.004	0.0107	0.1065	0.4924	0	0.4968	0.1976	40.97	49.29	95.7497
503-Z1-Ap-01-r	0	0.221	2.07	0	0.397	0.981	0.1359	0.0019	0.0141	0.1496	0.3758	0	0.3806	0.2118	41.97	53.06	99.9527
503-Z1-Ap-02-c	0	0.2124	2.23	0.0219	0.7418	1.35	0.1632	0	0	0.094	0.4984	0.0123	0.5759	0.2186	41.55	52.22	99.8543
503-Z1-Ap-02-r	0	0.2059	2.79	0	0.4171	1.0021	0.1032	0.0162	0	0.1315	0.351	0.0242	0.3736	0.2038	41.66	52.3	99.5624
503-Z1-Ap-03-c	0.0518	0.1469	2.97	0.0046	0.3758	0.7925	0.2123	0.0155	0	0.3103	0.291	0.0009	0.2994	0.1413	42.17	52.82	100.5295
503-Z1-Ap-03-r	0.0345	0.1405	3.11	0	0.379	0.7737	0.2087	0.1264	0	0.293	0.3076	0.0078	0.3771	0.1352	42.28	53.09	101.2212

EPMA Apatite part 2

Sample	MgO	Na2O	F	Al2O3	SiO2	Ce2O3	SrO	TiO2	Cr2O3	FeO	La2O3	K2O	Nd2O3	Cl	P2O5	CaO	Total
503-Z1-Ap-04-c	0.0185	0.1231	3.12	0.0032	0.3728	0.8261	0.2314	0.0383	0.0033	0.1505	0.2967	0.0028	0.3801	0.1342	42.23	52.63	100.5332
536-Z1-Ap-01-c1	0	0.8266	3.94	0	0.534	2.05	0.0457	0	0	0	0.7733	0	0.8309	0.0335	39.66	48.79	97.484
536-Z1-Ap-01-m1	0	0.815	3.76	0.0066	0.6062	1.97	0.0496	0.0023	0.0147	0.0035	0.706	0.0029	0.8913	0.0317	39.75	48.61	97.1898
536-Z1-Ap-01-r1	0	0.606	3.94	0	0.2982	1.18	0.0326	0	0	0.0886	0.5291	0	0.4517	0.0173	40.58	50.37	98.0609
536-Z1-Ap-02-c1	0	1.1885	4.09	0	0.2963	2.5	0.0577	0	0	0.0042	0.8726	0.008	0.9997	0.0418	39.77	47.56	97.3766
536-Z1-Ap-02-m2	0	1.2307	4.25	0	0.5141	3.04	0.0398	0	0.0113	0	1.0685	0.0067	1.1554	0.0448	39.38	46.52	97.2035
536-Z1-Ap-02-r1	0	0.8499	4.33	0	0.8058	2.13	0.0377	0	0	0	0.7214	0.0107	1.0434	0.0226	39.4	48.42	97.7231
536-Z1-Ap-03-c1	0	0.5175	3.38	0.0014	1.1434	2.6	0.0257	0.0426	0.0153	0.1042	1.0896	0.0021	0.7741	0.0354	39.31	49.09	98.0868
536-Z1-Ap-03-r1	0	0.514	3.09	0.0021	0.4401	1.71	0.0413	0.03	0.0146	0.0661	0.7219	0.0153	0.4624	0.0194	40.8	50.92	98.7592
536-Z1-Ap-04-c1	0	0.5136	3.72	0	1.089	2.37	0.0138	0	0.0024	0	0.9212	0.0038	0.9268	0.0254	39.05	49.6	98.216
536-Z1-Ap-04-r1	0	0.5251	3.52	0.0072	1.8736	3.11	0.0189	0.0114	0.0234	0	1.0439	0.0109	1.21	0.0177	37.56	48.41	97.2703
536-Z2-Ap-01-c1	0	1.1934	3.18	0	0.5512	1.5	0.0779	0.0074	0	0.1758	0.3244	0.0104	0.967	0.0329	39.6	47.59	95.1926
761-Z2-Ap-01-c1	0.0003	0.1741	3.14	0	0.5166	1.1149	0.0503	0.0137	0	0.0892	0.3924	0.0094	0.4599	0.1708	41.05	52	99.1582
761-Z2-Ap-02-c1	0.058	0.1792	3.37	0.0098	0.4601	1.0394	0.0591	0	0.0196	0.0646	0.3555	0.0036	0.4103	0.1467	40.55	51.8	98.4349
761-Z2-Ap-03-c1	0.0075	0.1584	2.37	0.0117	0.386	0.9652	0.0718	0.0118	0	0.0534	0.388	0.0158	0.2763	0.1649	41.13	52.69	98.6698
761-Z2-Ap-04-c1	0.0209	0.1754	2.38	0	0.2821	0.8344	0.116	0.0089	0.0041	0.2595	0.3132	0	0.2976	0.1476	41.66	53.45	99.9158
761-Z2-Ap-05-c1	0.0213	0.1918	2.98	0.0049	0.4281	0.9896	0.1302	0.0094	0	0.2254	0.3589	0	0.3943	0.1633	41.41	52.23	99.5016
761-Z2-Ap-05-c2	0.0324	0.1599	3.06	0.0139	0.6093	0.9627	0.1206	0.0073	0	0.446	0.3438	0.002	0.369	0.1646	41.24	52.58	100.0559
761-Z2-Ap-06-c1	0.017	0.1925	2.93	0.0096	0.3523	0.9026	0.1391	0.0107	0	0.1176	0.3544	0.0129	0.3368	0.1416	41.72	52.28	99.4669
761-Z2-Ap-06-r1	0.0361	0.1716	3.33	0.0065	0.329	0.8258	0.1135	0.0071	0.0181	0.116	0.3048	0.0231	0.3762	0.1663	41.34	52.8	99.8963
761-Z2-Ap-07-c1	0.0262	0.1839	2.92	0	0.3292	0.8199	0.1557	0.0095	0	0.2738	0.3072	0.0003	0.3538	0.1531	41.12	52.11	98.7266
761-Z2-Ap-08-c1	0.0329	0.1961	2.96	0	0.4588	0.9561	0.1311	0.0096	0.0156	0.1174	0.3388	0.0008	0.401	0.1623	41	52.42	99.1416

## EPMA Amphibole Analysis

Sample	SiO2	TiO2	Al2O3	Cr2O3	MnO	FeO	MgO	CaO	Na2O	K2O	F	Cl	Total intital
503-Z1-amp-1-c	43.01	4.59	10.11	0.04	0.4388	11.11	13.78	11.04	2.85	1.0658	0.3485	0.0142	98.2473
503-Z1-amp-1-m	42.96	4.64	10.04	0.04	0.4487	11.29	13.76	11.06	2.87	1.0495	0.3257	0.017	98.3609
503-Z1-amp-1-r	43	4.4	9.98	0.04	0.4237	10.7	14.1	11	2.89	1.059	0.3343	0.0232	97.8002
503-Z1-amp-2-c	42.7	4.66	10.04	0.04	0.4262	11.11	13.72	11.08	2.9	1.0624	0.3189	0.0161	97.9336
503-Z1-amp-2-r	43.06	4.5	9.91	0.04	0.4348	10.67	13.94	11.11	2.95	1.0635	0.3422	0.018	97.8885
503-Z1-amp-3-c	42.9	4.67	10.18	0.04	0.43	10.94	13.78	11.08	2.95	1.0825	0.3087	0.0172	98.2484
503-Z1-amp-3-m	42.66	4.6	10.09	0.04	0.438	11.15	13.85	11.05	2.9	1.0826	0.3168	0.0129	98.0503
503-Z1-amp-3-r	42.7	4.59	10.05	0.04	0.4203	11.03	13.95	10.99	2.89	1.0848	0.3062	0.0122	97.9335
536-Z1-Amp-01-c1	53.85	1.0153	1.1999	0.04	1.46	11.9	14.91	5.2	6.19	1.1336	1.95		98.0288
536-Z1-Amp-01-c2	53.76	0.9962	1.0932	0.04	1.4	11.72	14.87	5.03	6.02	1.1322	1.79	0.0172	97.1088
536-Z1-Amp-02-c1	55.53	0.5437	0.8385	0.04	1.2717	11.45	14.85	4.5	6.16	1.118	2.19		97.5719
536-Z1-Amp-02-c2	55.09	0.5569	1.0429	0.04	1.1434	11.25	14.86	4.4	6.3	1.0716	2.3		97.0848
536-Z1-Amp-03-c1	52.68	1.3639	0.907	0.04	1.76	13.65	13.45	4.13	6.74	1.1008	1.77		96.8417
536-Z1-Amp-03-r1	53.98	0.896	0.8915	0.04	1.63	13.71	13.41	3.66	6.84	1.0407	1.73		97.0982
536-Z1-Amp-04-c1	51.24	1.4439	2.71	0.04	1.1563	10.02	16.23	7.3	5.26	1.1016	1.83	0.0129	97.5747
536-Z1-Amp-05-c1	50.86	1.3658	3.26		1.1991	9.8	16.04	7.7	4.98	1.1899	1.92		97.5048
536-Z1-Amp-05-m1	51.86	0.7431	2.75		1.203	9.76	16.6	7.28	4.93	1.162	1.92		97.3981
536-Z1-Amp-06-c1	53.06	0.4337	2.82		1.2101	9.1	16.57	7.21	4.99	1.1143	2.19		97.7781
536-Z2-Amp-01-c1	51.77	1.3681	1.1787		1.86	14.01	13.05	4.74	6.37	1.0034	1.65		96.3102

## EPMA Biotite Analysis

Sample label	SiO2	TiO2	Al2O3	FeOT	MnO	MgO	CaO	Na2O	K2O	F	Cl	?=F+Cl	Totalinitial
403B-Z1-bt-01-c1	38.34	6.62	12.97	11.52	0.1914	16.18	0.0401	0.1761	9.53	0.7846	0.0315	0.34	96.05
403B-Z1-bt-02-c1	38.4	7.04	13.37	9.83	0.1499	17.21		0.2637	9.54	0.8462	0.0319	0.36	96.32
403B-Z1-bt-03-c1	38.01	6.89	12.86	11.53	0.2029	16.3	0.0556	0.2477	9.49	0.7774	0.0425	0.34	96.07
403B-Z1-bt-04-c1	38.3	7.27	12.92	11.28	0.2096	15.94		0.2963	9.28	0.8056	0.0335	0.35	95.99
403B-Z1-bt-04-c2	38.09	6.94	12.66	12.02	0.1835	16.21	0.0835	0.3555	8.79	0.7949	0.0331	0.34	95.82
403B-Z1-bt-05-c1	38.57	7.13	13.25	10.28	0.1613	16.69	0.061	0.3702	9.12	0.7682	0.0325	0.33	96.10
403B-Z2-bt-01-c1	38.83	7.43	13.13	9.53	0.1549	16.96	0.1297	0.5962	8.5	0.8507	0.0234	0.36	95.77
403B-Z2-bt-01-c2	38.89	7.33	13.08	9.22	0.1491	17.21	0.1115	0.6113	8.66	0.824	0.0236	0.35	95.76
403B-Z2-bt-01-r1	38.53	7.43	13.05	9.6	0.1499	16.73	0.1849	0.4958	8.51	0.7857	0.0186	0.34	95.15
503-Z1-bt-1-c	38.34	6.57	14.09	8.55	0.1048	18.39	0.0221	1.1734	8.27	0.5654	0.0152	0.24	95.85
503-Z1-bt-1-r	38.55	6.43	14.13	8.45	0.1172	18.55	0.0793	1.1129	8.21	0.5941	0.0154	0.25	95.99
503-Z1-bt-2-c	38.42	6.69	13.98	9.15	0.1231	17.76	0.0365	1.0905	8.26	0.617		0.26	95.87
503-Z1-bt-2-r	38.28	6.61	14.11	8.96	0.1389	17.86	0.0323	1.0481	8.29	0.5862	0.0115	0.25	95.68
536-Z1-Bt-01-c1	42.34	2.39	10.25	8	0.503	20.12	0.0792	0.2775	9.46	2.75	0.0262	1.16	95.03
536-Z1-Bt-01-r1	42.7	2.31	10.44	6.35	0.4333	21.24	0.1168	0.2471	9.48	2.91	0.0229	1.23	95.02
761-Z1-Bt-01-c1	38.06	8.05	13.49	10.19	0.1415	16.05		0.2509	9.52	0.8264	0.0127	0.35	96.24
761-Z1-Bt-02-c1	37.93	8.2	13.42	10.27	0.1614	15.89		0.5294	9.02	0.8436	0.0125	0.36	95.92
761-Z1-Bt-02-r1	37.88	7.96	13.56	10.17	0.1391	16.05		0.1442	9.54	0.7868	0.0168	0.34	95.91
761-Z2-Bt-01-c1	37.7	7.78	13.23	11.77	0.1797	15.41		0.2439	9.53	0.8457	0.0173	0.36	96.35
761-Z2-Bt-02-c1	37.83	7.91	13.31	11.28	0.1506	15.37		0.2197	9.3	0.7734	0.013	0.33	95.83
761-Z2-Bt-03-c1	37.45	7.84	13.51	10.51	0.1588	15.54		0.2019	9.34	0.752	0.0175	0.32	95.00
761-Z2-Bt-04-c1	38.01	8.27	13.47	9.87	0.1151	16.07	0.0524	0.634	8.66	0.7612	0.0168	0.32	95.61
761-Z2-Bt-05-c1	38.15	8.22	13.56	9.93	0.1097	16.21	0.021	0.5538	8.8	0.7821	0.0192	0.33	96.02
761-Z2-Bt-05-c2	37.93	8.27	13.65	10.16	0.142	16.11		0.5097	9	0.7627	0.017	0.33	96.23
761-Z2-Bt-06-c1	37.69	7.97	13.34	10.71	0.1553	15.85	0.0245	0.2337	9.47	0.825	0.0153	0.35	95.93
761-Z2-Bt-06-c2	37.51	8.01	13.35	11.2	0.1674	15.71		0.2582	9.41	0.8071	0.0122	0.34	96.09

EPMA Feldspar analysis part 1

Sample	Rb2O	SrO	SiO2	TiO2	Al2O3	FeO	MgO	CaO	Na2O	K2O	Total	albite	anorthite	orthoclase	total
403B-Z1-flid-01-c1	0	0.2049	64.93	0.092	21.09	0.2176		2.89	9.05	1.44	99.71	81.38	14.36	4.26	100
403B-Z1-flid-01-c2	0	0.1939	65.1	0.0819	21.01	0.198		2.67	9.24	1.41	99.71	82.65	13.20	4.15	100
403B-Z1-flid-01-c3	0	0.1875	65.15	0.0842	21.17	0.2575		2.89	9.15	1.1962	99.90	82.13	14.34	3.53	100
403B-Z1-flid-01-m1	0	0.1916	64.98	0.0921	20.95	0.222		2.73	9.15	1.55	99.67	81.93	13.51	4.57	100
403B-Z1-flid-01-m2	0	0.1463	65.2	0.0986	21.11	0.2043		2.71	9.31	1.23	99.86	83.03	13.36	3.61	100
403B-Z1-flid-01-m3	0	0.1648	64.8	0.0827	21.22	0.2094		2.79	9.32	1.1052	99.53	83.03	13.73	3.24	100
403B-Z1-flid-01-r1	0	0.1388	65.79	0.0624	19.49	0.2031		1.2624	6.03	7.23	100.07	66.22	7.66	26.12	100
403B-Z1-flid-01-r2	0	0.159	66.01	0.0694	19.74	0.244		1.41	7.16	5.43	100.06	73.62	8.01	18.37	100
403B-Z1-flid-01-r3	0	0.1474	66.16	0.0932	19.36	0.2658		1.3159	6.58	6.16	99.93	70.50	7.79	21.71	100
403B-Z1-flid-02-c1	0	0.1719	65.16	0.0744	21.01	0.2178		2.65	9.55	1.0648	99.73	84.03	12.89	3.08	100
403B-Z1-flid-02-c2	0	0.2179	64.43	0.0696	20.06	0.1959		1.99	4.95	7.83	99.53	57.39	12.75	29.86	100
403B-Z1-flid-02-m1	0	0.1843	65.02	0.0788	21.17	0.2459		2.87	9.17	1.28	99.83	82.04	14.19	3.77	100
403B-Z1-flid-02-m2	0	0.1997	65.14	0.0678	19.65	0.1625		1.55	5.64	7.33	99.54	63.31	9.62	27.07	100
403B-Z1-flid-02-r1	0.0268	0.1854	65.52	0.0779	19.49	0.186		1.3311	6.22	6.81	99.64	67.64	8.00	24.36	100
403B-Z1-flid-02-r2	0	0.1588	66.46	0.0778	19.66	0.2524		1.3849	7.3	5.31	100.45	74.40	7.80	17.80	100
403B-Z2-flid-01-c1	0	0.1638	65.41	0.0768	19.87	0.1628		1.55	6.98	5.57	99.62	72.19	8.86	18.95	100
403B-Z2-flid-01-c2	0	0.1625	65.47	0.0649	19.56	0.157		1.3639	6.48	6.47	99.57	69.21	8.05	22.74	100
536-Z1-flid-01-c1	0	0	66.92	0.1115	18.5	0.4279		0.2416	6.08	7.81	100.09	69.23	1.52	29.25	100
536-Z1-flid-01-c2	0	0	66.95	0.1201	18.59	0.4268		0.267	7.64	5.71	99.70	79.04	1.53	19.43	100
536-Z1-flid-01-c3	0.029	0	66.72	0.0939	18.37	0.4712		0.1873	7.46	6.02	99.32	78.16	1.08	20.75	100
536-Z1-flid-02-r1	0	0.0208	67.87	0.1431	19.13	0.3008		0.4114	11.16	0.3513	99.37	97.02	1.98	1.00	100
536-Z1-flid-02-r2	0	0	68.54	0.138	19.17	0.2967		0.3743	11.39	0.4208	100.33	97.06	1.76	1.18	100
536-Z1-flid-02-r3	0	0.0212	68.01	0.0835	19.07	0.2508		0.3999	11.67	0.1736	99.66	97.67	1.85	0.48	100
536-Z1-flid-03-r1	0.038	0	66.8	0.1001	18.43	0.4649		0.1957	7.3	6.22	99.51	77.21	1.14	21.64	100
536-Z1-flid-04-c1	0	0	67.48	0.123	18.65	0.4156		0.3275	7.65	5.62	100.2661	79.03	1.87	19.10	100
536-Z1-flid-04-c2	0	0.0234	66.8	0.0946	18.39	0.4581		0.2263	6.63	7.15	99.749	72.80	1.37	25.83	100
536-Z1-flid-04-m1	0	0	67.1	0.147	18.7	0.3528		0.3553	7.37	5.93	99.9551	77.44	2.06	20.50	100

EPMA Feldspar analysis part 2

Sample	Rb2O	SrO	SiO2	TiO2	Al2O3	FeO	MgO	CaO	Na2O	K2O	Total	albite	anorthite	orthoclase	total
536-Z1-flid-04-r1	0.034	0.0216	66.77	0.0849	18.3	0.5423		0.1225	7.08	6.88	99.7797	75.23	0.72	24.05	100
536-Z1-flid-05-c1	0.044	0	66.74	0.1069	18.48	0.4152		0.2507	7.67	5.65	99.3128	79.34	1.43	19.23	100
536-Z1-flid-05-m1	0	0	66.88	0.113	18.49	0.4379		0.2106	7.31	6.29	99.7315	76.98	1.23	21.79	100
536-Z1-flid-05-r1	0.0613	0	100.93	0	0	0		0.0204	0	0	#VALUE!	#VALUE!	#VALUE!	#VALUE!	#VALUE!
536-Z2-Flid-01-c1	0	0	68.48	0	18.12	1.68		0	11.81	0.0871	#VALUE!	#VALUE!	#VALUE!	#VALUE!	#VALUE!
536-Z2-Flid-01-c2	0	0	68.79	0.0236	17.78	1.59		0.0235	11.59	0.0679	99.865	99.70	0.11	0.19	100
536-Z2-Flid-01-c3	0.0805	0	65.23	0.0262	17.03	1.1569		0	0.2208	15.96	#VALUE!	#VALUE!	#VALUE!	#VALUE!	#VALUE!
536-Z2-Flid-01-c4	0.0931	0	64.99	0.0138	16.99	0.4646		0.0232	0.1503	16.1	98.7319	2.75	0.23	97.01	100
536-Z2-Flid-02-c1	0.0741	0	65.29	0.0254	16.2	1.98		0	0.349	15.74	#VALUE!	#VALUE!	#VALUE!	#VALUE!	#VALUE!
761-Z1-flid-01-c1	0	0.2667	63.53	0.0868	22.12	0.2519		4.03	8.25	1.71	99.9787	74.73	20.17	5.10	100
761-Z1-flid-01-c2	0	0.2427	62.86	0.0894	22.05	0.2085		4.12	8.02	1.55	98.8979	74.21	21.07	4.72	100
761-Z1-flid-01-c3	0	0.2573	62.36	0.0901	21.96	0.2524		4.02	8.16	1.63	98.4725	74.74	20.35	4.91	100
761-Z1-flid-02-c1	0	0.2473	63.4	0.0978	22.02	0.2653		4.06	8.07	1.84	99.7531	73.91	20.55	5.54	100
761-Z1-flid-02-c2	0	0.2587	63.07	0.0941	22.25	0.2553		4.21	8.2	1.45	99.5294	74.52	21.14	4.34	100
761-Z1-flid-03-c1	0	0.2319	62.77	0.091	22.15	0.2454		4.18	8.29	1.47	99.1964	74.80	20.84	4.36	100
761-Z1-flid-03-c2	0	0.2588	62.15	0.098	22.03	0.2202		3.97	8.06	1.85	98.3782	74.20	20.20	5.60	100
761-Z1-flid-04-c1	0	0.223	63.25	0.0996	21.81	0.2877		3.59	8.38	1.83	99.2473	76.42	18.09	5.49	100
761-Z1-flid-04-m1	0	0.2479	62.89	0.0993	22.06	0.2592		3.96	8.21	1.62	99.0985	75.11	20.02	4.88	100
761-Z1-flid-04-r1	0	0.2609	62.57	0.0842	22.48	0.2471	0.0116	4.27	8.1	1.4	99.1629	74.17	21.61	4.22	100
761-Z2-flid-01-c1	0	0.2274	63.83	0.1011	22	0.2222		3.78	8.47	1.51	99.9133	76.61	18.89	4.49	100
761-Z2-flid-01-c2	0	0.2525	62.93	0.098	21.89	0.2332		3.79	8.39	1.7	99.0312	75.97	18.96	5.06	100
761-Z2-flid-02-c1	0	0.2185	59.98	0.1178	24.28	0.2017		6.49	7.43	0.6088	99.1083	66.24	31.97	1.79	100
761-Z2-flid-02-c2	0	0.2249	61.36	0.1326	23.53	0.2341	0.0101	5.63	7.77	0.851	99.5178	69.62	27.87	2.51	100
761-Z2-flid-03-c1	0	0.2467	62.62	0.0929	22.29	0.2185		4.23	8.19	1.5	99.1414	74.31	21.21	4.48	100
761-Z2-flid-04-c1	0	0.2777	62.98	0.0896	21.52	0.2543		3.79	8.2	1.85	98.6839	75.21	19.21	5.58	100
761-Z2-flid-04-m1	0	0.2317	62.45	0.0977	21.96	0.2145		3.97	8.26	1.57	98.5222	75.29	20.00	4.71	100
761-Z2-flid-04-r1	0	0.3218	63.02	0.0834	21.77	0.2484		3.7	8.19	2.07	99.0818	75.03	18.73	6.24	100

EPMA Pyroxene Part 1

Sample	SiO2	TiO2	Al2O3	FeO	MnO	MgO	CaO	Na2O	Total	Wo	En	Fs	Q	J	join Q à J	join Q + J
403B-Z1-px-02-c1	52.2	0.4893	1.1439	8.35	0.8726	14.5	20.77	0.6918	99.02	43.13	41.90	14.97	1.84	0.10	0.05	1.94
403B-Z1-px-03-c1	52.12	0.5954	1.2815	8.54	0.8347	14.11	20.84	0.7918	99.11	43.60	41.07	15.33	1.83	0.11	0.06	1.94
403B-Z1-px-04-c1	52.07	0.5809	1.3412	8.44	0.8918	14.18	20.88	0.7458	99.13	43.59	41.19	15.22	1.83	0.11	0.06	1.94
403B-Z1-px-05-c1	52.2	0.4875	1.1845	8.52	0.8847	14.36	20.79	0.7495	99.18	43.20	41.52	15.27	1.83	0.11	0.06	1.94
403B-Z1-px-06-c1	52.49	0.485	1.1844	8.49	0.853	14.39	20.7	0.7314	99.32	43.10	41.69	15.20	1.84	0.11	0.05	1.95
403B-Z1-px-07-c1	52.01	0.5092	1.2243	8.53	0.8283	14.21	20.71	0.7482	98.77	43.33	41.37	15.30	1.83	0.11	0.06	1.94
403B-Z1-px-08-c1	52.44	0.7089	1.4246	8.5	0.868	14.22	20.55	0.755	99.47	43.12	41.52	15.36	1.84	0.11	0.06	1.95
403B-Z1-px-08-r1	52.23	0.5956	1.3055	8.25	0.8155	14.31	20.63	0.7539	98.89	43.32	41.81	14.87	1.84	0.11	0.06	1.95
403B-Z1-px-09-c1	52.51	0.4794	1.2041	8.2	0.9034	14.43	20.87	0.7097	99.31	43.42	41.77	14.80	1.84	0.10	0.05	1.94
403B-Z1-px-10-c1	52.14	0.5596	1.2426	8.52	0.866	14.25	20.71	0.7343	99.02	43.26	41.42	15.32	1.84	0.11	0.05	1.94
403B-Z1-px-11-c1	52.41	0.4675	1.1114	8.51	0.8754	14.11	20.9	0.7523	99.14	43.66	41.01	15.32	1.84	0.11	0.06	1.95
403B-Z1-px-11-r1	52.83	0.4825	1.0271	8.38	0.8381	14.35	20.97	0.7459	99.62	43.56	41.48	14.96	1.85	0.11	0.06	1.95
403B-Z1-px-12-c1	53.08	0.4549	1.0837	8.59	0.8355	14.24	20.79	0.7995	99.87	43.34	41.30	15.35	1.84	0.12	0.06	1.96
403B-Z1-px-12-c2	52.98	0.4951	1.0759	8.8	0.8609	14.27	20.6	0.8294	99.91	42.91	41.36	15.73	1.84	0.12	0.06	1.96
403B-Z1-px-12-m1	52.67	0.4822	1.003	8.59	0.8691	14.3	20.87	0.729	99.51	43.34	41.32	15.35	1.85	0.11	0.05	1.95
403B-Z1-px-12-r1	53.03	0.4314	0.9137	8.79	0.8603	14.28	21.11	0.671	100.09	43.51	40.95	15.54	1.86	0.10	0.05	1.95
403B-Z2-px-01-c1	52.54	0.4775	1.2228	8.66	0.8148	14.12	20.75	0.8334	99.42	43.41	41.10	15.49	1.83	0.12	0.06	1.95
403B-Z2-px-01-c2	52.73	0.4976	1.0761	8.65	0.8479	14.13	20.83	0.7535	99.52	43.48	41.03	15.49	1.85	0.11	0.06	1.96
403B-Z2-px-01-m1	52.13	0.5632	1.1332	8.33	0.8127	14.2	21.03	0.7572	98.96	43.87	41.22	14.91	1.83	0.11	0.06	1.94

## EPMA Pyroxene Part 2

Sample	SiO2	TiO2	Al2O3	FeO	MnO	MgO	CaO	Na2O	Total	Wo	En	Fs	Q	J	join Q à J	join Q + J
403B-Z2-px-01-r1	52.95	0.4871	0.9631	8.44	0.7766	14.34	21.01	0.734	99.7	43.62	41.43	14.95	1.85	0.11	0.05	1.96
503-Z1-px-01	53.28	0.5682	0.9703	7.96	0.8736	15.04	20.8	0.587	100.08	42.77	43.03	14.20	1.88	0.08	0.04	1.96
503-Z1-px-2-c	53.48	0.5895	1.2841	7.99	0.8098	14.95	20.69	0.6816	100.48	42.78	43.01	14.22	1.86	0.10	0.05	1.96
503-Z1-px-2-m	53.25	0.6179	1.2982	7.75	0.6969	14.97	21.39	0.6519	100.62	43.81	42.67	13.52	1.86	0.09	0.05	1.95
503-Z1-px-2-r	53.47	0.5959	1.3705	7.61	0.6884	14.92	21.54	0.6142	100.81	44.15	42.55	13.29	1.87	0.09	0.04	1.96
503-Z1-px-3-c	53.33	0.5724	0.961	7.85	0.75	14.99	21.02	0.6371	100.11	43.25	42.92	13.83	1.87	0.09	0.05	1.96
503-Z1-px-3-r	53.67	0.5379	1.027	7.45	0.6586	15.1	21.53	0.5659	100.54	44.05	42.99	12.96	1.89	0.08	0.04	1.97
503-Z1-px-4-c	52.89	0.657	1.546	7.65	0.6302	14.76	21.47	0.6647	100.27	44.29	42.36	13.35	1.85	0.10	0.05	1.95
503-Z1-px-4-r	52.9	0.675	1.5025	7.76	0.6405	14.78	21.52	0.6193	100.4	44.24	42.27	13.49	1.86	0.09	0.05	1.95
503-Z1-px-r-02	53.1	0.5768	1.0964	7.77	0.6993	15.1	21.3	0.5578	100.2	43.53	42.94	13.53	1.87	0.08	0.04	1.95
761-Z1-Px-01-c1	52.35	0.6278	1.5772	7.71	0.6745	14.66	20.83	0.6507	99.08	43.60	42.69	13.71	1.86	0.09	0.05	1.95
761-Z1-Px-01-r1	52.2	0.7243	1.6115	7.68	0.6578	14.77	20.9	0.6534	99.2	43.57	42.85	13.58	1.85	0.09	0.05	1.95
761-Z1-Px-02-c1	52.36	0.7854	1.6124	8.06	0.6542	14.69	20.78	0.6512	99.59	43.27	42.56	14.18	1.85	0.09	0.05	1.95
761-Z1-Px-03-c1	52.73	0.6045	1.2927	7.88	0.686	14.93	20.81	0.6687	99.6	43.11	43.03	13.86	1.86	0.10	0.05	1.95
761-Z1-Px-04-c1	52.95	0.652	1.4068	8.02	0.6889	15.07	20.54	0.6873	100.02	42.51	43.40	14.08	1.86	0.10	0.05	1.95
761-Z1-Px-04-r1	52.86	0.5897	1.3188	7.99	0.7029	15.09	20.85	0.608	100.01	42.87	43.17	13.96	1.86	0.09	0.04	1.95
761-Z2-Px-01-c1	52.54	0.7727	1.6137	8.07	0.6698	14.92	20.74	0.6584	99.98	42.91	42.96	14.13	1.85	0.09	0.05	1.95
761-Z2-Px-02-c1	53.15	0.6298	1.4855	7.15	0.6613	14.87	21.34	0.6168	99.9	44.33	42.98	12.68	1.87	0.09	0.05	1.96
761-Z2-Px-03-c1	52.77	0.6049	1.3976	7.29	0.6464	14.91	20.96	0.6099	99.19	43.75	43.30	12.94	1.87	0.09	0.04	1.96
761-Z2-Px-04-c1	52.54	0.6842	1.4326	8.04	0.7415	14.85	20.61	0.6629	99.56	42.82	42.93	14.26	1.85	0.10	0.05	1.95
761-Z2-Px-04-m1	52.93	0.6171	1.2815	7.96	0.7074	15.17	20.7	0.6237	99.99	42.61	43.45	13.94	1.86	0.09	0.05	1.95
761-Z2-Px-04-r1	52.61	0.631	1.3314	7.87	0.7147	15.06	20.78	0.6357	99.63	42.90	43.26	13.85	1.86	0.09	0.05	1.95



## APPENDIX C: XRF Analysis

Splitting of XRF table

	a	b
1	1a	
2		2b

## Bulk Rock Major Oxides Part 1a

Sample	LOI (%) 1000°C	Sum	Al2O3	BaO	CaO	Cr2O3	CuO	Fe2O3	FeO	HfO2	K2O	MgO
		(%)	(%)	(%)	(%)	(%)	(%)	(%)	(%)	(%)	(%)	(%)
111501	0.687	99.46	10.108	0.230	7.605	NA	NA	15.972	14.372	0.005	3.442	3.704
111502	0.438	99.96	18.110	0.147	0.758	0.003	NA	2.884	2.595	NA	6.297	0.576
111503	0.180	99.88	4.535	0.200	14.146	NA	0.001	28.371	25.528	NA	1.346	9.827
111505	-0.004	99.88	3.127	0.192	14.735	NA	0.004	29.720	26.742	NA	0.984	9.695
111507	0.599	99.82	10.800	0.216	9.544	0.004	0.003	18.240	16.412	NA	1.741	6.029
111508	0.188	99.67	17.548	0.149	2.216	0.003	NA	4.346	3.910	NA	5.451	1.062
111509	3.071	99.73	16.190	0.148	4.758	NA	0.002	9.763	8.784	NA	2.742	3.283
111510	0.526	99.96	14.207	0.085	0.700	0.005	NA	3.737	3.363	0.001	5.236	0.426
111512 A	0.411	99.97	15.403	0.120	2.515	NA	0.002	4.795	4.315	NA	4.892	1.383
111512 B	0.304	99.99	16.646	0.140	3.164	0.002	NA	6.860	6.173	NA	4.576	1.387
111513	0.212	99.70	16.672	0.144	3.382	0.001	NA	7.132	6.417	0.002	4.501	1.461
111514	-0.148	99.82	12.533	0.154	2.847	0.001	NA	22.826	20.539	NA	3.919	1.544
111515	0.356	99.48	17.484	0.040	0.854	NA	NA	3.131	2.817	NA	6.411	0.617
111516 A	0.347	98.97	17.532	0.113	0.749	0.001	0.002	3.114	2.802	NA	5.603	0.335
111516 B	-0.828	99.66	9.457	0.094	1.179	NA	0.004	39.330	35.389	NA	3.032	1.535
111517	-0.264	99.96	10.919	0.081	0.586	0.003	0.002	32.744	29.463	0.001	3.425	0.859

Bulk Rock Major Oxides Part 1b

Sample	Mn3O4	Na2O	NiO	P2O5	PbO	SiO2	SO3	SrO	TiO2	V2O5	ZnO	ZrO2
	(%)	(%)	(%)	(%)	(%)	(%)	(%)	(%)	(%)	(%)	(%)	(%)
111501	0.793	3.520	0.002	3.115	NA	46.448	0.027	0.017	3.061	0.031	0.080	0.609
111502	0.089	6.150	NA	0.195	NA	63.562	NA	0.031	0.661	0.003	0.009	0.049
111503	0.723	0.700	0.004	4.772	NA	27.646	0.011	0.029	7.175	0.090	0.069	0.058
111505	0.782	0.407	NA	4.476	NA	28.326	0.011	0.023	7.222	0.089	0.065	0.029
111507	0.487	3.211	0.001	2.608	NA	41.644	0.014	0.106	4.448	0.058	0.045	0.020
111508	0.148	6.103	NA	0.434	0.005	60.779	NA	0.028	1.127	0.006	0.011	0.064
111509	0.181	5.114	0.002	1.558	0.005	50.490	0.071	0.089	2.185	0.017	0.023	0.038
111510	0.102	4.871	NA	0.112	0.004	69.132	NA	0.004	0.664	0.005	0.009	0.137
111512 A	0.198	5.300	NA	0.374	0.004	63.255	NA	0.029	1.205	0.005	0.015	0.068
111512 B	0.190	5.695	NA	0.622	NA	58.630	NA	0.046	1.490	0.011	0.019	0.203
111513	0.186	5.680	0.001	0.648	0.004	57.825	NA	0.057	1.519	0.011	0.015	0.250
111514	0.801	4.844	NA	1.162	NA	47.113	0.011	0.022	1.995	0.015	0.099	0.085
111515	0.150	6.311	NA	0.160	0.003	63.009	0.002	0.001	0.847	0.004	0.008	0.092
111516 A	0.095	6.795	NA	0.211	0.002	63.330	0.002	0.018	0.635	0.002	0.010	0.079
111516 B	1.126	3.445	NA	0.542	NA	33.478	0.005	0.011	7.032	0.014	0.129	0.073
111517	0.740	4.199	NA	0.269	0.005	39.010	NA	0.005	7.208	0.006	0.073	0.091

## Bulk Rock Major Oxides Part 2a

Sample	LOI (%) 1000°C	Sum	Al2O3	BaO	CaO	Cr2O3	CuO	Fe2O3	FeO	HfO2	K2O	MgO
111518	-0.220	99.88	11.823	0.187	4.447	0.001	NA	25.338	22.799	NA	2.933	2.244
111519	0.352	100.26	17.985	0.208	3.106	0.003	NA	5.234	4.709	NA	4.402	1.233
111520	0.439	99.85	14.982	0.126	0.491	0.003	NA	3.247	2.921	NA	5.575	0.315
111525	1.212	99.64	19.158	0.162	3.128	NA	0.001	5.630	5.066	0.002	6.623	1.887
111526	0.691	99.90	14.821	0.163	6.090	NA	0.001	12.721	11.447	NA	3.459	4.048
111531	0.901	99.60	17.051	0.118	1.765	NA	NA	5.409	4.867	NA	5.449	1.135
111534	0.579	100.07	15.896	0.108	1.601	0.004	NA	5.530	4.976	0.004	5.786	1.049
111535	0.551	98.81	17.408	0.084	1.079	0.003	NA	3.492	3.142	NA	6.144	0.703
111536	0.306	99.89	16.993	0.123	1.169	0.003	0.001	3.759	3.383	NA	5.874	0.735
111538	0.401	99.77	17.347	0.115	0.449	0.001	NA	6.406	5.764	NA	7.210	0.363
111539	0.496	99.20	17.404	0.148	1.918	0.003	NA	4.034	3.630	NA	5.585	1.085
195759	-0.085	98.7	6.73	0.249	12.1	0.002	NA	26.9	24.205	0.0005047	2.88	10.6
195760	-0.435	97.8	3.40	0.122	14.7	0.000	NA	29.3	26.364	0.0015685	1.34	9.19
195761	0.230	99.0	12.0	0.194	9.50	0.001	NA	16.3	14.667	0.0006144	1.71	5.19
195764	0.515	98.9	17.3	0.083	0.894	0.001	NA	3.02	2.717	0.0008019	5.88	0.66
195765	0.405	99.7	17.7	0.042	0.864	0.001	NA	3.09	2.780	0.0019576	6.19	0.53
195766	0.679	98.9	16.9	0.004	0.489	0.000	NA	3.22	2.897	0.0009246	6.04	0.58
195767	0.420	99.2	16.9	0.011	0.352	0.000	NA	2.90	2.609	0.0020048	6.34	0.42

## Bulk Rock Major Oxides Part 2b

Sample	Mn3O4	Na2O	NiO	P2O5	PbO	SiO2	SO3	SrO	TiO2	V2O5	ZnO	ZrO2
111518	0.915	4.704	NA	1.599	NA	43.648	0.015	0.036	2.030	0.020	0.125	0.038
111519	0.155	6.295	NA	0.580	NA	59.200	NA	0.080	1.336	0.007	0.014	0.071
111520	0.084	4.899	NA	0.082	0.006	68.960	NA	0.002	0.557	0.004	0.011	0.070
111525	0.196	4.189	0.002	0.721	0.006	55.109	NA	0.080	1.358	0.013	0.015	0.147
111526	0.275	4.391	NA	2.055	-0.004	48.026	0.006	0.088	2.968	0.028	0.024	0.053
111531	0.166	5.841	NA	0.552	-0.001	59.671	0.007	0.023	1.289	0.009	0.015	0.202
111534	0.232	5.376	NA	0.427	-0.004	62.018	NA	0.018	1.245	0.009	0.007	0.188
111535	0.150	6.165	NA	0.227	0.005	61.801	NA	0.006	0.900	0.007	0.010	0.081
111536	0.198	6.428	NA	0.290	NA	62.976	0.011	0.010	0.948	0.007	0.009	0.053
111538	0.052	5.578	NA	0.332	NA	59.992	0.041	0.015	1.312	0.005	0.005	0.151
111539	0.163	6.106	NA	0.390	0.008	60.670	0.011	0.022	1.063	0.008	0.015	0.075
195759	0.494	0.41	NA	5.42	NA	26.1	NA	0.037015	7.08	0.089796	NA	0.018911
195760	0.749	0.18	NA	5.06	NA	27.1	NA	0.028501	7.29	0.077478	NA	0.073348
195761	0.394	3.54	NA	2.48	NA	43.3	NA	0.120625	4.31	0.045701	NA	0.023774
195764	0.152	6.29	NA	0.275	NA	63.0	NA	0.015019	0.877	0.005016	NA	0.03404
195765	0.123	6.42	NA	0.201	NA	63.4	NA	0.008704	0.802	0.005356	NA	0.103201
195766	0.139	6.25	NA	0.206	NA	63.5	NA	0.004021	0.922	0.006837	NA	0.040794
195767	0.146	6.07	NA	0.156	NA	64.7	NA	0.00123	0.781	0.004802	NA	0.118465

## APPENDIX D: Bulk Rock Trace Element Analysis

Splitting of trace element table

	a	b	c	d
1	1a			
2		2b		

Bulk Rock Trace Element Part 1a

Sample	Ag (ppm)	As (ppm)	Ba ppm	Be (ppm)	Bi (ppm)	Br (ppm)	Cd (ppm)	Ce ppm	Co (ppm)	Cr ppm	Cs ppm	Cu (ppm)	Dy ppm	Er ppm	Eu ppm	Ga ppm
195759	0	0	2230	0.000	0	0	0	696	0	11.4	0.56	0	32.1	15.0	12.5	20.3
195760	0	0	1090	0.000	0	0	0	1170	0	<5	<0.4	0	56.2	27.0	15.6	17.9
195761	0	0	1740	0.000	0	0	0	522	0	9.5	<0.4	0	30.1	14.5	11.2	22.2
195764	0	0	739	3.4	0	0	0	190	0	8.0	1.49	0	11.1	5.74	3.93	27.4
195765	0	0	379	3.5	0	0	0	227	0	5.5	0.80	0	10.3	5.81	3.45	30.4
195766	0	0	33.4	3.5	0	0	0	260	0	<5	0.63	0	8.60	3.96	2.84	33.5
195767	0	0	96.2	17.2	0	0	0	397	0	<5	0.87	0	11.4	6.02	3.02	32.1
111501	1.8	13	526	0	2.9	1.2	1.4	1550	20.8	20	0.64	5.3	71.5	36.6	17	29.6
111502	0.5	2.3	1300	0	0.8	0.3	0	116.5	11.2	10	0.48	2.6	5.3	2.64	3.62	26.3
111503	3.1	0	903	0	0	0	2.7	865	35.3	0	0.27	25.8	47.6	22.2	14.55	31.7
111505	2.5	0.9	870	0	0	0	2	865	30.8	10	0.33	35.8	46.3	23	14.65	30.1
111507	1.4	3	1420	0	1	0.3	0.7	527	34.5	0	0.42	29.6	28.3	14.15	10.65	29.1
111508	0.9	3.5	1230	0	0.7	0.3	0.4	203	12.9	10	0.42	3.8	8.36	4.28	4.56	29.7
111509	0.7	2.5	1255	0	0.4	0.3	0.4	170	16.7	0	1	6.4	7.65	3.47	4.68	23.1
111510	0.6	9.2	647	0	1.5	0.6	0	166	31.9	10	3.87	2.8	12.35	8.69	2.23	30.3
111512 A	0.7	6.6	930	0	1.2	1	0	194	21.9	10	1.71	8.6	11.95	7.33	3.57	27.1
111512 B	1.1	7.1	1010	0	1.2	0.7	0.7	289	24.4	0	1.15	8	13.75	7.58	4.4	31.5

## Bulk Rock Trace Element Part 1b

Sample	Gd	Ge	Hf	Ho	I	La	Lu	Mn	Mo	Nb	Nd	Ni	Pb	Pr
	ppm	(ppm)	ppm	ppm	(ppm)	ppm	ppm	(ppm)	(ppm)	ppm	ppm	(ppm)	(ppm)	ppm
195759	44.4	0	4.28	6.14	0	290	1.34	0	0	96.1	328	0	0	80.6
195760	69.3	0	13.3	10.4	0	497	2.96	0	0	149	500	0	0	127
195761	37.4	0	5.21	5.59	0	252	1.51	0	0	106	258	0	0	63.2
195764	12.1	0	6.80	2.20	0	103	0.731	0	0	122	84.0	0	0	21.6
195765	11.1	0	16.6	2.00	0	126	0.849	0	0	115	92.2	0	0	24.8
195766	11.5	0	7.84	1.60	0	143	0.603	0	0	110	108	0	0	28.7
195767	13.7	0	17.0	2.18	0	223	0.897	0	0	118	137	0	0	40.0
111501	88.2	0.8	87.9	13.5	0	734	4.31	5719.3	3.9	216	672	7.2	11.8	181.5
111502	6.04	0.5	9	0.98	1.1	59.6	0.35	558	0.9	50.5	46.6	3.8	12.5	13.2
111503	63.5	0.5	11.7	8.85	0	374	2.38	4738	1.6	174	431	10	0	108
111505	63	0.5	9	8.78	0	390	2.42	5577.8	1.8	174	422	15.5	0.1	108.5
111507	37.7	0.2	5.6	5.38	0	242	1.58	3331.8	0.9	113	248	15.3	2.4	64.2
111508	11.2	0.6	10.1	1.59	0	103	0.58	885.2	1.2	65.9	83.1	3.2	9.7	22.9
111509	11.75	0.4	6.7	1.43	0	82.5	0.41	1357.1	2.9	68.3	77.7	2.5	10	19.95
111510	9.8	1.2	31.7	2.61	0	65.2	1.42	725.3	4.2	317	52.1	5	31.6	15.1
111512 A	12.45	0.5	15.2	2.42	0.3	88.2	1.13	1372.6	5.8	238	78.4	4.5	24.7	21.7
111512 B	16.3	0.6	35.6	2.8	0.2	138	1.22	1324.4	8.5	227	111.5	4.1	19.2	31.9



Bulk Rock Trace Element Part 1c

Sample	Rb	Sb	Sc	Se	Sm	Sn	Sr	Ta	Tb	Te	Th	Tl
	ppm	(ppm)	(ppm)	(ppm)	ppm	ppm	ppm	ppm	ppm	(ppm)	ppm	(ppm)
195759	90.2	0	0	0	59.4	5.1	313	4.63	6.35	0	4.26	0
195760	49.5	0	0	0	89.9	7.3	241	7.90	10.3	0	5.37	0
195761	21.7	0	0	0	48.7	<5	1020	6.05	5.50	0	2.61	0
195764	151	0	0	0	15.5	<5	127	6.66	2.01	0	9.35	0
195765	113	0	0	0	15.5	<5	73.6	6.98	1.84	0	10.1	0
195766	119	0	0	0	16.1	<5	34.0	5.95	1.67	0	11.2	0
195767	182	0	0	0	20.7	<5	10.4	5.66	2.02	0	30.0	0
111501	82	0	27.1	2.2	111.5	10	193.5	9.2	13.05	0	16.6	4.2
111502	107	1.7	4	0.6	7.9	1	359	2.8	0.9	0	4.25	1.5
111503	40.1	0	33.5	0.2	77.3	7	315	8.9	8.87	0	5.96	0.4
111505	36	0	33.7	0	77.9	8	254	9	8.59	0	4.54	0.8
111507	31.4	0	17.5	0.5	44.4	4	918	3.6	5.3	0	2.38	2.1
111508	84.6	0.8	5.3	0.7	13.6	3	348	3.5	1.53	0	2.83	1.4
111509	46.1	0.5	6.1	0.5	13.75	3	829	3.3	1.46	0	5.64	0.8
111510	279	0.7	4.2	1.1	11	11	124.5	16.8	1.81	0	72.8	2.2
111512 A	152	0.6	8.9	0.8	15.3	6	278	14	2	0	33	1.7
111512 B	132.5	0.7	7.7	1	19.25	6	440	11	2.31	0	22.3	2

## Bulk Rock Trace Element Part 1d

Sample	Tm	U	V	W	Y	Yb	Zn	Zr	TREE
	ppm	ppm	ppm	ppm	ppm	ppm	(ppm)	ppm	ppm
195759	1.84	1.21	503	<0.2	154	10.4	0	140	1738.07
195760	3.54	1.39	434	<0.2	267	20.3	0	543	2866.50
195761	1.85	0.693	256	<0.2	142	10.5	0	176	1404.05
195764	0.826	2.60	28.1	1.48	57.7	4.91	0	252	515.35
195765	0.819	2.37	30.0	1.28	56.7	5.07	0	764	583.44
195766	0.577	2.69	38.3	1.45	44.0	3.48	0	302	634.63
195767	0.946	1.92	26.9	2.15	61.7	5.88	0	877	925.46
111501	5.01	4.36	193	69	366	29.6	727.7	4830	3920.87
111502	0.37	1.24	30	79	27.3	2.47	75.3	436	297.77
111503	2.97	1.36	617	24	224	17.05	349.5	417	2300.77
111505	2.97	1.07	593	35	229	18.15	411	273	2313.96
111507	1.84	0.53	342	35	136.5	10.9	300.6	197	1395.40
111508	0.68	0.97	49	83	42.7	3.95	82.7	485	510.33
111509	0.5	1.49	109	11	38.2	3.06	177.2	288	442.61
111510	1.39	23.8	32	286	71.8	9.35	88.7	1020	435.05
111512 A	1.16	10.85	40	143	65.6	8.01	117.4	534	522.12
111512 B	1.22	8.57	67	90	72.1	8.06	145	1510	727.09

## Bulk Rock Trace Element Part 2a

Sample	Ag	As	Ba	Be	Bi	Br	Cd	Ce	Co	Cr	Cs	Cu	Dy	Er	Eu	Ga
	(ppm)	(ppm)	ppm	(ppm)	(ppm)	(ppm)	(ppm)	ppm	(ppm)	ppm	ppm	(ppm)	ppm	ppm	ppm	ppm
111513	0.6	7.5	1005	0	1.4	1.1	0.2	309	16.2	10	1.26	7.8	15.05	8.71	4.64	32.4
111514	1.7	2.3	640	0	0	0.2	1.1	698	22.6	10	0.73	5.2	27.1	12.65	7.41	37.6
111515	0.3	2.7	219	0	0.6	0.1	0	186.5	18.9	0	0.63	2.8	7.52	3.92	2.85	34.6
111516 A	0.6	5.7	792	0	0.4	0.6	0.1	280	32.4	40	2.06	2.3	10.05	5.77	2.83	37.6
111516 B	3.1	0.4	434	0	0	0.3	1.8	403	3.8	10	1.35	9.1	14.25	7.09	3.85	36.7
111517	1.8	1.2	493	0	0	0	1	250	8	10	1.13	8.8	8.07	4.28	2.23	30.4
111518	2.5	0.5	881	0	0	0	0.5	812	11.7	10	1.22	4.6	31.4	14.15	9.47	36.5
111519	0.5	5.9	1720	0	1.7	0.9	0	207	15.3	10	1.45	4.8	9.01	4.9	5.31	30.6
111520	0.6	5.3	1070	0	0.5	0.4	0	129.5	48.4	10	1.79	1.2	4.58	2.88	1.56	23.9
111525	0.8	5.8	1235	0	1.4	0.6	0.2	264	15.9	10	2.55	23.9	9.62	5.58	3.96	28.4
111526	1.8	4.5	1230	0	0.7	0.5	1.2	242	31.3	0	6.78	7.2	13.05	6.16	6.34	24.7
111531	1	5.7	822	0	1.2	1	0.2	277	11.6	0	2.31	4.9	11.15	6.69	4.08	32.4
111534	0.4	8.7	715	0	1.4	0.9	0	266	17.2	10	4.31	4.5	12.55	7.58	3.77	32
111535	0.7	5.5	616	0	0.6	0.7	0	153	27.2	0	0.92	2.6	7.67	4.24	3.44	30.3
111536	0.5	3.9	902	0	0.7	0.3	0	238	16.1	10	1.04	4.9	12.6	6.88	4.66	32
111538	0.6	8.5	946	0	3.2	0.6	0	111	19.3	10	1.26	4.5	4.84	3.18	1.89	32.8
111539	0.6	3.3	1145	0	0.6	0.1	0	237	13	70	0.62	2.5	9.22	4.59	4.35	29.1

Bulk Rock Trace Element Part 2b

Sample	Gd	Ge	Hf	Ho	I	La	Lu	Mn	Mo	Nb	Nd	Ni	Pb	Pr
	ppm	(ppm)	ppm	ppm	(ppm)	ppm	ppm	(ppm)	(ppm)	ppm	ppm	(ppm)	(ppm)	ppm
111513	17.2	0.5	42.3	3.02	0.3	150.5	1.35	1278.3	20.2	252	119	4.6	21.6	33.7
111514	36.3	0.7	15.7	5	0	340	1.37	5400.9	3	90.8	288	7.3	11	80.1
111515	8.72	0.8	13.5	1.46	0.1	88.3	0.58	959.7	1.9	86.6	73.1	2.5	11.2	20.6
111516 A	11.4	0.9	14.8	2	0	148.5	0.85	544.9	6.8	120.5	96.2	4.3	17.3	29.1
111516 B	18.45	0	14.2	2.71	0	201	0.92	6742.2	6.9	363	156.5	5.4	11.3	45
111517	10.45	0	17.5	1.61	0	131.5	0.72	4749.8	3.6	349	92.6	6.6	10.4	27.4
111518	44.3	0.3	6.7	5.64	0	393	1.5	5957.7	2.4	55.2	343	7.8	9.3	94.4
111519	11.3	0.4	14	1.68	0.7	106.5	0.7	995.4	3.8	108.5	83.1	4.5	10.4	23.1
111520	4.95	0.7	13	1	1	65.1	0.45	633.8	3.8	70.4	37.9	5.1	27.9	11.35
111525	11.4	0.7	25.1	1.98	0	129	0.92	1561.6	1.6	269	95.6	5.6	7	28.3
111526	18.35	0.2	10.7	2.41	0	110.5	0.75	1815	6.7	78.7	119.5	4.3	6.9	29.4
111531	12.85	0.5	31.1	2.25	0.4	141	0.99	1192.6	6.8	182	103.5	4.3	20.3	29.7
111534	13.3	0.8	30	2.54	0.8	125	1.24	1537.8	5.8	214	98.3	4.1	25.7	28.2
111535	9.32	0.8	15	1.56	2.2	71.8	0.54	901.2	3.4	100.5	67.4	3.1	13.5	17.85
111536	14.3	0.8	12.9	2.58	0.9	115	0.85	1052.8	1.4	118	99.8	4	11.6	27.1
111538	5.43	1.4	28.7	1.07	0.7	59.7	0.67	297.9	2.2	199.5	39.2	4.6	74.2	11.75
111539	11.7	0.6	12.3	1.67	1	120	0.62	907.7	2.4	82.3	93	4.5	9.6	26

## Bulk Rock Trace Element Part 2c

Sample	Rb	Sb	Sc	Se	Sm	Sn	Sr	Ta	Tb	Te	Th	Tl
	ppm	(ppm)	(ppm)	(ppm)	ppm	ppm	ppm	ppm	ppm	(ppm)	ppm	(ppm)
111513	136.5	0	8.3	1.2	20.9	7	450	12.3	2.56	0	47.8	2.4
111514	72.2	0	15.6	0	48	19	196	4.5	4.88	0	11.6	1.4
111515	119	0.4	6.7	0.5	12.15	3	44.8	4.5	1.29	0	6.15	1.1
111516 A	119	1.3	3.7	0.5	15.75	7	186.5	7.1	1.66	0	24.7	1.4
111516 B	76.5	0	13.8	0	25.1	57	106.5	17.1	2.71	0	10.95	2.1
111517	70.2	0	14.6	0	14.25	85	104.5	14.2	1.47	0	20.5	2
111518	46.1	0	17.5	0	58.3	19	339	2.4	5.86	0	6.35	1
111519	90	0.3	5.3	1.1	14.1	3	668	5.9	1.5	0	9.29	2
111520	209	0.5	4.6	0.5	6.15	5	136.5	3.1	0.8	0	19.3	1.5
111525	187	0	4.7	1.3	15.2	5	758	15	1.69	0	25.5	2.1
111526	99.3	0.5	11.6	0.7	22.1	3	794	4	2.37	0	3.64	1.7
111531	181	1.1	7.8	1.2	17.3	6	234	9.4	2	0	23.8	1.5
111534	175	0	8.4	1.1	17.15	7	148.5	11.5	2.21	0	28.2	2.8
111535	143.5	0.6	7	0.7	12.15	4	133	5.3	1.27	0	10.25	2.1
111536	118.5	1	8.3	0.6	18.1	4	110.5	5.6	2.29	0	15	1.5
111538	185.5	0	10	1.1	6.51	29	168	10.7	0.79	0	27.6	2.9
111539	91.6	0.2	6.7	0.5	15.85	3	310	4.2	1.71	0	4.89	0.9

## Bulk Rock Trace Element Part 2d

Sample	Tm	U	V	W	Y	Yb	Zn	Zr	TREE
	ppm	ppm	ppm	ppm	ppm	ppm	(ppm)	ppm	ppm
111513	1.28	13.55	71	67	80.3	9.44	118.6	1830	784.95
111514	1.72	2.46	91	77	131	10.4	736.3	659	1707.53
111515	0.57	1.42	30	109	36.7	3.78	60.7	651	454.74
111516 A	0.82	6.48	8	192	52.9	5.62	71.1	499	667.15
111516 B	1.01	3.38	100	45	71.9	6.21	972.6	513	973.50
111517	0.68	5.03	67	72	45.2	4.73	546.4	664	609.79
111518	1.81	1.25	131	47	149	10.35	984.8	257	1991.68
111519	0.77	3.02	55	83	46.6	4.69	102.5	596	525.56
111520	0.45	3.68	24	403	25.8	2.96	87.3	485	300.03
111525	0.82	4.14	90	68	50.9	6.06	125.7	1070	629.73
111526	0.86	1.27	169	39	62.6	5.01	192.3	426	653.00
111531	1.03	7.16	51	43	59.5	6.92	122.6	1430	683.76
111534	1.16	6.45	42	110	68.9	8.44	69.8	1300	664.74
111535	0.64	2.97	34	155	38.8	3.89	79	677	400.57
111536	1.01	2.61	36	109	63.8	6.47	79.4	556	621.74
111538	0.57	2.58	29	112	28.8	4.49	45.4	1170	289.89
111539	0.66	1.3	42	88	46.9	4.03	112.6	565	584.00

### Chondrite Normalization Values (Sun and McDonough, 1989)

Sample	La	Ce	Pr	Nd	Sm	Eu	Gd	Tb	Dy	Ho	Er	Tm	Yb	Lu
C1 Sun and McDonough 1989	0.24	0.61	0.1	0.47	0.15	0.06	0.21	0.04	0.25	0.06	0.17	0.03	0.17	0.03

### Calculation of chondrite normalized Eu- anomaly and Yb/Gd ratio Part 1

Sample	Eu	Gd	Sm	Yb	Yb <sub>N</sub>	Eu <sub>N</sub>	Gd <sub>N</sub>	Sm <sub>N</sub>	Eu* <sub>N</sub>	(Yb/Gd) <sub>N</sub>
	ppm	ppm	ppm	ppm						
195759	12.5	44.4	59.4	10.4	346.7	59.5	1110.0	990.0	0.06	0.31
195760	15.6	69.3	89.9	20.3	676.7	74.3	1732.5	1498.3	0.05	0.39
195761	11.2	37.4	48.7	10.5	350.0	53.3	935.0	811.7	0.06	0.37
195764	3.93	12.1	15.5	4.91	163.7	18.7	302.5	258.3	0.07	0.54
195765	3.45	11.1	15.5	5.07	169.0	16.4	277.5	258.3	0.06	0.61
195766	2.84	11.5	16.1	3.48	116.0	13.5	287.5	268.3	0.05	0.40
195767	3.02	13.7	20.7	5.88	196.0	14.4	342.5	345.0	0.04	0.57
111501	17	88.2	111.5	29.6	986.7	81.0	2205.0	1858.3	0.04	0.45
111502	3.62	6.04	7.9	2.47	82.3	17.2	151.0	131.7	0.12	0.55
111503	14.55	63.5	77.3	17.05	568.3	69.3	1587.5	1288.3	0.05	0.36
111505	14.65	63	77.9	18.15	605.0	69.8	1575.0	1298.3	0.05	0.38
111507	10.65	37.7	44.4	10.9	363.3	50.7	942.5	740.0	0.06	0.39
111508	4.56	11.2	13.6	3.95	131.7	21.7	280.0	226.7	0.09	0.47
111509	4.68	11.75	13.75	3.06	102.0	22.3	293.8	229.2	0.09	0.35
111510	2.23	9.8	11	9.35	311.7	10.6	245.0	183.3	0.05	1.27
111512 A	3.57	12.45	15.3	8.01	267.0	17.0	311.3	255.0	0.06	0.86
111512 B	4.4	16.3	19.25	8.06	268.7	21.0	407.5	320.8	0.06	0.66

Calculation of chondrite normalized Eu- anomaly and Yb/Gd ratio Part 2

Sample	Eu	Gd	Sm	Yb	Yb <sub>N</sub>	Eu <sub>N</sub>	Gd <sub>N</sub>	Sm <sub>N</sub>	Eu* <sub>N</sub>	(Yb/Gd) <sub>N</sub>
	ppm	ppm	ppm	ppm						
111513	4.64	17.2	20.9	9.44	314.7	22.1	430.0	348.3	0.06	0.73
111514	7.41	36.3	48	10.4	346.7	35.3	907.5	800.0	0.04	0.38
111515	2.85	8.72	12.15	3.78	126.0	13.6	218.0	202.5	0.06	0.58
111516 A	2.83	11.4	15.75	5.62	187.3	13.5	285.0	262.5	0.05	0.66
111516 B	3.85	18.45	25.1	6.21	207.0	18.3	461.3	418.3	0.04	0.45
111517	2.23	10.45	14.25	4.73	157.7	10.6	261.3	237.5	0.04	0.60
111518	9.47	44.3	58.3	10.35	345.0	45.1	1107.5	971.7	0.04	0.31
111519	5.31	11.3	14.1	4.69	156.3	25.3	282.5	235.0	0.10	0.55
111520	1.56	4.95	6.15	2.96	98.7	7.4	123.8	102.5	0.07	0.80
111525	3.96	11.4	15.2	6.06	202.0	18.9	285.0	253.3	0.07	0.71
111526	6.34	18.35	22.1	5.01	167.0	30.2	458.8	368.3	0.07	0.36
111531	4.08	12.85	17.3	6.92	230.7	19.4	321.3	288.3	0.06	0.72
111534	3.77	13.3	17.15	8.44	281.3	18.0	332.5	285.8	0.06	0.85
111535	3.44	9.32	12.15	3.89	129.7	16.4	233.0	202.5	0.08	0.56
111536	4.66	14.3	18.1	6.47	215.7	22.2	357.5	301.7	0.07	0.60
111538	1.89	5.43	6.51	4.49	149.7	9.0	135.8	108.5	0.07	1.10
111539	4.35	11.7	15.85	4.03	134.3	20.7	292.5	264.2	0.07	0.46



## APPENDIX E: Apatite LA-ICP-MS Analysis

Splitting of apatite LA-ICP-MS table

	a	b	c
1	Part 1a		
2		Part 2b	
3			Part 3c
4			
5			
6			

Apatite LA-ICP-MS analysis Part 1a

Sample	P	Cl	Ca	Ca44	Ti	V	Mn	As	Sr	Y	Zr	Cd	Ba	La
	(ppm)	(ppm)	(ppm)	(ppm)	(ppm)	(ppm)	(ppm)	(ppm)	(ppm)	(ppm)	(ppm)	(ppm)	(ppm)	(ppm)
111511_Z1_AP1	124210	2996	400000	401731	9.30	12.42	1104.29	37.79	346.59	1911.43	19.58	0.23	0.80	5629.36
111511_Z1_AP2	130600	3860	400000	416038	9.09	11.22	1130.44	38.30	323.16	1995.32	16.74	0.21	0.50	6046.86
111511_Z1_AP3	125316	2777	400000	402876	9.57	9.96	1090.10	41.32	348.83	1845.54	7.63	0.07	0.50	5372.69
111511_Z1_AP4	127962	4389	400000	423317	9.53	11.99	1135.34	39.13	400.92	1939.95	12.92	0.25	1.65	5873.35
111511_Z1_AP5_core	128713	4648	400000	402482	9.50	9.47	1164.07	41.41	277.36	1942.33	8.39	0.28	0.50	5905.65
111511_Z1_AP5_rim	130022	4700	400000	404577	8.79	7.98	1232.38	53.02	235.89	2111.52	7.52	0.27	0.34	6381.58
111511_Z1_AP6	131714	3840	400000	419505	6.95	12.80	1023.39	39.64	267.92	1967.94	8.26	0.27	0.35	5672.63
111511_Z1_AP7	129379	4078	400000	405671	9.65	13.28	1005.07	39.17	264.81	1933.29	8.11	0.24	0.68	5530.53
111511_Z2_AP1	128225	5578	400000	413747	8.66	6.43	1048.67	35.42	246.95	1631.13	8.11	0.34	0.78	5333.47
111511_Z2_AP10	129264	679	400000	410366	7.72	1.27	251.52	11.25	303.52	540.27	0.42	-0.08	0.11	790.53
111511_Z2_AP2	128242	5690	400000	422523	9.79	3.83	1046.30	49.27	258.00	1832.42	6.15	0.25	0.57	5893.31
111511_Z2_AP3_core	127615	4748	400000	400081	9.12	12.55	969.46	36.91	224.35	1783.54	10.81	0.16	0.71	5155.07
111511_Z2_AP3_rim	125293	5142	400000	406753	8.27	7.23	974.06	42.19	231.39	1825.46	9.38	0.21	0.70	5752.78
111511_Z2_AP4	132195	3686	400000	417569	10.43	3.56	1085.35	52.47	246.59	2036.77	2.42	0.09	0.50	5310.32
111511_Z2_AP5	128795	3531	400000	431061	8.17	7.52	1127.33	50.16	254.28	2209.45	8.57	0.10	0.61	5893.80
111511_Z2_AP6	126791	746	400000	407436	7.92	1.06	183.70	24.74	393.59	535.23	2.09	0.03	0.05	624.55
111511_Z2_AP7	133118	3817	400000	400435	9.34	3.59	1073.50	42.10	260.33	1801.30	3.16	0.24	0.49	5366.42
111511_Z2_AP8	139980	3930	400000	415787	8.63	8.34	1082.78	38.86	280.83	1878.96	4.92	0.14	0.79	5401.63
111512_Z1_AP1	133122	2165	400000	395916	9.96	4.17	766.30	25.22	314.56	1360.66	1.31	-0.01	0.66	3527.30
111512_Z1_AP2_core	140140	2085	400000	409269	14.75	18.55	801.48	25.85	343.31	1309.80	28.98	0.03	1.17	3663.47
111512_Z1_AP2_rim	134931	2201	400000	414690	9.27	8.74	787.81	25.19	313.95	1369.89	48.58	0.04	0.99	3495.85
111512_Z1_AP3	137065	1807	400000	403370	9.05	3.98	737.35	26.72	309.40	1258.56	1.35	-0.04	1.15	3607.93
111512_Z1_AP4	140289	2315	400000	408938	9.47	4.26	784.60	26.77	302.03	1417.09	0.64	0.06	0.69	4086.99
111512_Z2_AP1_core	137785	2154	400000	412815	8.98	7.64	1128.51	28.91	366.56	1363.70	46.39	0.05	1.17	4467.25
111512_Z2_AP1_rim	142596	2194	400000	413582	9.27	6.57	1056.01	29.00	356.33	1345.18	25.32	0.04	0.85	4367.88
111512_Z2_AP2	136018	2201	400000	401290	8.50	6.84	928.60	26.02	340.17	1257.87	11.37	0.14	1.44	4080.14

Apatite LA-ICP-MS analysis Part 1b

Sample	Ce	Pr	Nd	Sm	Eu	Gd	Tb	Dy	Ho	Er	Tm	Yb	Lu	Pb206
	(ppm)	(ppm)	(ppm)	(ppm)	(ppm)	(ppm)	(ppm)	(ppm)	(ppm)	(ppm)	(ppm)	(ppm)	(ppm)	(ppm)
111511_Z1_AP1	11549.43	1209.68	4204.60	654.73	48.85	461.34	66.00	384.34	69.92	189.56	24.39	154.16	19.52	7.56
111511_Z1_AP2	12150.96	1330.31	4455.67	700.93	53.36	502.71	70.84	396.00	73.19	196.80	26.33	164.28	20.96	9.64
111511_Z1_AP3	11290.31	1210.07	4063.33	603.73	45.76	457.64	62.83	361.18	70.17	188.46	24.12	144.39	19.28	12.01
111511_Z1_AP4	11993.68	1298.28	4332.32	646.96	52.37	486.68	69.71	394.10	73.33	188.36	25.98	157.04	20.26	10.84
111511_Z1_AP5_core	12037.44	1242.67	4181.21	632.86	46.89	483.72	69.36	379.19	73.08	194.04	24.79	159.81	20.26	9.69
111511_Z1_AP5_rim	12554.08	1380.93	4631.34	673.60	45.68	526.52	74.15	422.94	80.62	212.81	28.74	171.18	21.75	14.76
111511_Z1_AP6	11311.30	1206.44	3988.64	607.47	38.23	458.37	69.59	379.28	71.49	190.01	24.86	143.96	18.00	9.79
111511_Z1_AP7	11141.96	1190.12	3923.71	589.45	36.49	461.76	62.39	353.68	67.51	178.13	23.66	142.66	17.58	10.18
111511_Z2_AP1	10571.03	1114.96	3728.76	550.07	36.74	415.53	57.88	319.26	60.30	157.67	20.88	129.62	16.31	8.56
111511_Z2_AP10	1870.57	196.12	627.52	106.95	11.52	102.59	14.76	94.26	19.37	54.00	6.28	34.21	4.18	1.91
111511_Z2_AP2	11836.85	1239.81	4080.52	610.26	37.01	445.29	62.96	335.50	63.84	170.46	23.12	139.99	18.01	5.54
111511_Z2_AP3_core	10486.49	1186.01	3879.51	589.84	34.44	452.35	62.90	344.74	63.17	167.87	22.09	138.92	18.17	7.56
111511_Z2_AP3_rim	11839.28	1266.61	4298.50	639.39	37.93	490.13	67.58	359.19	68.32	178.96	23.48	144.54	18.99	8.76
111511_Z2_AP4	11199.22	1234.95	4237.51	648.22	42.32	510.94	71.59	389.82	76.14	201.10	25.72	160.92	20.04	13.69
111511_Z2_AP5	12804.21	1390.66	4888.86	736.97	48.61	572.04	78.35	449.63	82.51	219.26	29.31	177.83	23.04	15.49
111511_Z2_AP6	1334.82	147.96	525.29	93.28	12.55	93.85	14.93	92.68	19.81	54.95	6.68	36.69	4.28	1.61
111511_Z2_AP7	10884.99	1216.56	4013.43	629.71	42.13	472.23	64.99	363.84	68.33	181.32	23.41	146.99	18.37	13.80
111511_Z2_AP8	11343.67	1226.65	3977.14	608.06	44.34	491.16	66.47	350.04	68.09	180.13	23.53	141.52	18.02	10.31
111512_Z1_AP1	7282.11	811.15	2707.84	428.97	39.25	360.44	49.79	268.15	50.28	129.20	16.12	94.09	12.28	6.95
111512_Z1_AP2_core	7344.32	811.66	2596.30	416.13	38.08	333.60	44.71	242.11	46.17	117.83	15.07	89.08	11.08	6.70
111512_Z1_AP2_rim	7381.17	798.69	2712.70	442.05	39.07	346.46	46.53	254.51	48.99	130.24	16.36	94.03	12.06	5.95
111512_Z1_AP3	7171.66	765.19	2489.17	387.56	39.66	307.11	41.24	230.83	44.66	118.19	15.18	91.58	11.50	9.51
111512_Z1_AP4	8417.29	862.77	2748.52	436.55	42.34	350.15	46.77	256.52	50.11	130.53	17.14	99.28	12.54	7.70
111512_Z2_AP1_core	8616.36	940.28	3055.63	474.55	40.91	363.30	48.82	260.54	48.76	128.34	16.53	92.46	11.96	7.70
111512_Z2_AP1_rim	8539.55	914.77	3007.00	453.63	43.85	360.20	47.10	257.17	47.43	126.49	15.66	92.88	11.86	8.07
111512_Z2_AP2	8021.58	851.37	2766.20	426.98	41.15	335.61	44.24	235.53	45.94	114.69	14.90	87.08	10.99	7.06

Apatite LA-ICP-MS analysis Part 1c

Sample	Pb207	Pb208	Th	U	Pb	TREE	(Ce/Yb)N	Eu*
	(ppm)	(ppm)	(ppm)	(ppm)	(ppm)	(wt.%)		
111511_Z1_AP1	3.89	4.82	64.05	22.68	5.31	2.66	20.9	0.26
111511_Z1_AP2	3.76	6.70	141.34	35.99	6.77	2.82	20.6	0.27
111511_Z1_AP3	4.38	8.27	185.19	47.28	8.33	2.58	21.8	0.26
111511_Z1_AP4	4.42	7.44	151.23	40.01	7.70	2.76	21.3	0.28
111511_Z1_AP5_core	3.27	5.94	132.23	40.20	6.20	2.74	21.0	0.25
111511_Z1_AP5_rim	3.32	9.33	278.65	75.12	9.36	2.93	20.4	0.23
111511_Z1_AP6	3.05	5.28	115.16	39.35	5.98	2.61	21.9	0.21
111511_Z1_AP7	4.37	6.28	115.24	39.56	7.04	2.57	21.8	0.21
111511_Z2_AP1	3.45	6.89	153.17	32.81	6.54	2.41	22.7	0.23
111511_Z2_AP10	0.64	1.43	37.98	9.38	1.41	0.45	23.6	0.33
111511_Z2_AP2	2.39	6.56	196.01	22.32	5.41	2.68	21.0	0.21
111511_Z2_AP3_core	3.94	6.50	136.52	26.35	6.21	2.44	22.8	0.20
111511_Z2_AP3_rim	3.32	8.42	242.48	34.47	7.36	2.70	19.4	0.20
111511_Z2_AP4	3.22	9.84	324.91	67.03	9.32	2.62	20.1	0.22
111511_Z2_AP5	3.28	11.50	401.70	83.10	10.65	2.96	10.1	0.22
111511_Z2_AP6	0.76	1.59	36.97	5.71	1.40	0.36	20.6	0.40
111511_Z2_AP7	3.50	9.79	317.20	68.86	9.38	2.53	22.3	0.23
111511_Z2_AP8	3.22	7.50	221.47	49.93	7.24	2.58	15.2	0.24
111512_Z1_AP1	3.54	4.03	24.72	20.44	4.64	1.71	21.6	0.30
111512_Z1_AP2_core	4.98	5.84	31.22	9.59	5.90	1.71	23.0	0.30
111512_Z1_AP2_rim	3.89	4.37	36.29	12.78	4.62	1.72	21.9	0.30
111512_Z1_AP3	5.07	5.39	27.70	22.51	6.25	1.66	21.8	0.34
111512_Z1_AP4	3.58	4.07	32.58	24.35	4.87	1.90	23.6	0.32
111512_Z2_AP1_core	5.57	5.90	42.11	12.82	6.34	1.99	26.0	0.29
111512_Z2_AP1_rim	4.74	5.74	34.75	15.14	6.09	1.96	25.6	0.32
111512_Z2_AP2	4.43	5.24	35.24	11.92	5.53	1.83	25.7	0.32

Apatite LA-ICP-MS analysis Part 2a

Sample	P	Cl	Ca	Ca44	Ti	V	Mn	As	Sr	Y	Zr	Cd	Ba	La
	(ppm)	(ppm)	(ppm)	(ppm)	(ppm)	(ppm)	(ppm)	(ppm)	(ppm)	(ppm)	(ppm)	(ppm)	(ppm)	(ppm)
111512_Z2_AP3	141222	2091	400000	411897	9.27	7.49	1073.98	28.55	370.58	1327.42	9.90	0.03	1.00	4354.64
111512_Z2_AP4	148520	1897	400000	421092	7.83	6.31	1081.26	29.09	369.74	1423.35	12.52	0.13	0.64	4652.00
111512_Z3_AP1_core	144649	2291	400000	401906	9.25	6.52	873.45	25.78	309.43	1357.14	2.37	0.06	0.87	3605.19
111512_Z3_AP1_rim	145131	2151	400000	401811	10.36	10.02	847.30	25.51	298.05	1364.44	32.91	0.05	0.82	3656.66
111512_Z3_AP2_core	147091	2594	400000	396720	10.15	10.28	842.14	26.15	315.90	1464.50	31.53	0.10	0.80	3691.96
111512_Z3_AP2_rim	147660	2203	400000	392900	8.61	8.90	717.60	25.39	281.42	1334.13	0.54	0.08	0.65	3631.48
111512_Z3_AP3	148008	2382	400000	403683	12.77	5.33	752.95	24.92	272.98	1476.89	20.72	-0.01	1.28	3733.20
111512_Z3_AP4_core	149249	2549	400000	399421	12.17	11.08	782.14	23.82	306.12	1442.47	42.20	0.01	1.08	3522.93
111512_Z3_AP4_rim	148325	2351	400000	409861	8.62	5.89	734.65	25.19	278.97	1450.73	0.67	0.01	0.52	3666.36
111514_Z1_AP1	147043	4418	400000	413708	8.29	15.12	2301.41	211.47	549.08	6046.49	6.48	2.48	2.06	7844.76
111514_Z1_AP10	156339	5445	400000	417412	7.80	28.39	2851.48	93.72	616.91	4235.95	15.78	1.18	1.81	12718.04
111514_Z1_AP2	150028	5974	400000	411725	8.04	30.09	2750.15	101.67	591.13	4459.23	15.96	2.33	1.47	13279.29
111514_Z1_AP4	155382	6008	400000	414450	8.28	16.56	2700.55	62.38	567.21	2949.64	3.97	2.13	1.92	8415.82
111514_Z1_AP5	157383	4881	400000	414666	9.20	33.19	2272.62	66.04	654.49	2892.02	1.97	1.73	2.06	8549.69
111514_Z1_AP6	151693	3917	400000	407557	8.16	26.06	2580.68	73.55	589.74	3094.34	1.26	1.58	1.52	5600.99
111514_Z1_AP7	158537	4097	400000	411986	7.82	26.92	2497.18	79.81	499.03	2859.72	5.15	2.26	1.49	9160.46
111514_Z1_AP8	157362	2800	400000	409882	7.73	26.27	2052.54	75.09	576.32	2464.04	4.66	1.61	1.09	4530.11
111514_Z1_AP9	154129	4461	400000	409994	8.57	28.19	3189.31	92.01	609.21	5206.24	22.59	1.93	1.43	6973.84
111514_Z2_AP1_core	157389	2043	400000	422288	8.12	20.23	2257.94	63.32	700.63	2907.55	4.52	1.92	2.03	6108.90
111514_Z2_AP1_rim	150876	2544	400000	407380	8.83	25.01	2149.02	66.51	669.11	2910.26	2.33	1.75	1.79	5802.76
111514_Z2_AP2_core	157300	2186	400000	414446	8.74	28.51	2149.52	67.10	658.38	3329.40	2.77	1.93	1.35	6210.83
111514_Z2_AP3	155186	2224	400000	416608	8.66	23.47	2154.22	66.57	674.50	3897.40	10.37	1.96	2.20	6316.43
111514_Z2_AP4	148511	2249	400000	404781	9.57	25.69	2285.30	79.02	651.61	4744.09	11.93	2.22	1.92	6638.40
111514_Z2_AP5	158103	2416	400000	404851	8.34	31.51	2365.84	87.57	677.63	5175.33	10.05	2.70	1.82	7699.14
111514_Z2_AP6	160762	2588	400000	419149	6.76	20.98	2128.28	60.17	666.67	3174.77	3.16	2.23	1.73	5835.82
111514_Z2_AP7	156373	2194	400000	417393	8.33	23.05	2016.93	57.05	659.87	3139.60	2.82	1.83	1.80	5459.45

Apatite LA-ICP-MS analysis Part 2b

Sample	Ce	Pr	Nd	Sm	Eu	Gd	Tb	Dy	Ho	Er	Tm	Yb	Lu	Pb206
	(ppm)	(ppm)	(ppm)	(ppm)	(ppm)	(ppm)	(ppm)	(ppm)	(ppm)	(ppm)	(ppm)	(ppm)	(ppm)	(ppm)
111512_Z2_AP3	8323.14	879.93	2923.72	461.05	41.39	359.74	46.51	250.63	48.04	122.40	15.20	86.90	11.11	6.98
111512_Z2_AP4	9089.06	929.74	3091.76	461.13	44.10	367.10	48.65	263.38	50.80	129.22	16.06	96.58	12.44	7.38
111512_Z3_AP1_core	7724.80	825.40	2666.51	431.82	33.34	341.35	46.06	249.60	49.24	125.88	16.10	96.64	12.34	7.03
111512_Z3_AP1_rim	7576.16	822.98	2738.46	434.58	35.28	342.91	46.23	261.30	49.53	129.19	16.59	96.89	12.39	6.72
111512_Z3_AP2_core	7743.70	834.52	2761.16	443.52	36.64	348.63	46.86	264.90	50.35	132.99	17.02	101.45	12.99	7.06
111512_Z3_AP2_rim	7731.67	823.79	2707.15	427.41	35.26	331.81	46.16	255.16	48.27	128.92	16.29	93.14	11.99	7.23
111512_Z3_AP3	7921.90	860.47	2804.70	451.71	38.45	360.37	50.10	275.07	53.51	142.01	17.77	104.40	13.54	6.51
111512_Z3_AP4_core	7331.87	811.31	2671.78	442.25	38.89	345.06	49.88	276.06	52.12	139.06	17.38	102.34	12.87	6.47
111512_Z3_AP4_rim	7751.37	831.73	2729.66	461.54	38.48	355.72	49.89	275.00	52.62	139.79	17.58	103.03	13.14	7.45
111514_Z1_AP1	19763.36	2638.92	10154.54	1866.09	272.32	1486.07	213.52	1224.83	223.88	561.29	67.02	355.28	39.11	20.54
111514_Z1_AP10	25833.96	2878.10	9951.18	1574.17	215.73	1228.24	165.35	881.19	155.37	390.91	45.78	254.26	31.51	14.97
111514_Z1_AP2	27486.08	3248.57	11283.45	1713.19	224.15	1262.84	166.52	899.52	165.33	414.45	50.30	270.52	30.87	15.56
111514_Z1_AP4	17545.66	2004.21	7167.02	1094.83	148.50	852.41	111.71	598.36	106.90	264.37	31.32	165.59	19.36	10.42
111514_Z1_AP5	17293.19	2027.86	7205.07	1121.12	147.42	870.74	113.58	584.52	105.51	249.92	27.77	137.32	15.83	9.39
111514_Z1_AP6	14566.13	1840.15	6913.96	1168.42	157.03	910.31	119.87	625.66	111.16	262.69	28.14	137.11	16.25	12.32
111514_Z1_AP7	20088.24	2336.75	8208.29	1296.96	168.39	951.30	116.50	593.07	103.86	237.29	23.07	95.70	9.62	5.18
111514_Z1_AP8	14487.94	1932.54	7373.07	1199.69	166.35	879.79	111.30	542.63	89.52	197.71	19.81	95.99	10.66	6.70
111514_Z1_AP9	19006.58	2513.75	9560.69	1695.82	244.62	1333.54	191.46	1057.39	194.51	478.30	57.43	314.12	37.49	13.17
111514_Z2_AP1_core	14641.13	1786.38	6583.92	1068.08	136.86	824.52	116.68	636.65	111.96	252.59	31.34	165.05	19.34	8.68
111514_Z2_AP1_rim	14190.60	1765.60	6337.24	1056.20	146.61	814.68	114.43	603.97	105.38	267.46	29.28	166.98	19.82	9.00
111514_Z2_AP2_core	15243.58	1900.25	7147.27	1179.87	162.76	907.95	125.54	670.62	123.89	305.23	34.88	183.06	21.45	9.36
111514_Z2_AP3	15412.19	1904.58	7281.16	1280.62	192.55	1035.88	142.26	788.61	142.87	358.44	40.54	215.60	24.35	9.35
111514_Z2_AP4	16075.66	2062.35	8132.42	1509.11	230.55	1181.34	174.25	957.97	176.98	441.11	51.11	281.15	32.49	12.28
111514_Z2_AP5	18930.52	2475.11	9622.89	1697.82	247.03	1359.85	191.52	1054.83	192.26	476.16	56.10	303.03	34.58	14.17
111514_Z2_AP6	13838.43	1692.29	6482.77	1097.71	153.29	859.95	120.73	642.43	115.52	285.68	32.38	174.61	20.78	10.20
111514_Z2_AP7	13026.07	1648.14	6234.72	1055.54	153.79	832.81	113.32	613.50	111.83	276.45	30.87	173.97	20.01	10.08

Apatite LA-ICP-MS analysis Part 2c

Sample	Pb207	Pb208	Th	U	Pb	TREE	(Ce/Yb)N	Eu*
	(ppm)	(ppm)	(ppm)	(ppm)	(ppm)	(wt.%)		
111512_Z2_AP3	4.69	5.34	28.63	14.10	5.65	1.93	26.7	0.30
111512_Z2_AP4	5.27	5.60	39.17	13.55	5.96	2.07	26.2	0.32
111512_Z3_AP1_core	4.10	5.02	35.05	13.33	5.31	1.76	22.3	0.26
111512_Z3_AP1_rim	4.25	5.24	39.98	13.00	5.43	1.76	21.8	0.27
111512_Z3_AP2_core	4.86	5.63	41.38	13.05	5.78	1.80	21.3	0.28
111512_Z3_AP2_rim	3.91	4.53	26.13	20.67	5.11	1.76	23.1	0.28
111512_Z3_AP3	3.77	4.65	36.13	17.00	4.92	1.83	21.1	0.28
111512_Z3_AP4_core	4.08	4.61	41.70	13.68	4.95	1.73	20.0	0.29
111512_Z3_AP4_rim	3.44	4.23	30.28	21.34	4.86	1.79	21.0	0.28
111514_Z1_AP1	14.49	27.06	600.14	35.67	22.74	5.28	15.5	0.48
111514_Z1_AP10	11.97	14.26	128.45	11.76	13.92	6.06	28.3	0.46
111514_Z1_AP2	11.20	17.89	269.98	18.17	15.98	6.50	29.5	0.45
111514_Z1_AP4	8.30	10.38	61.17	4.28	9.96	4.15	35.1	0.45
111514_Z1_AP5	7.90	9.52	73.47	5.63	9.13	4.13	29.6	0.44
111514_Z1_AP6	10.75	12.04	56.84	2.79	11.82	3.56	58.5	0.45
111514_Z1_AP7	3.59	7.12	133.58	5.91	5.86	4.62	42.1	0.45
111514_Z1_AP8	4.70	7.51	111.73	8.81	6.69	3.41	16.9	0.48
111514_Z1_AP9	10.13	14.36	185.69	13.36	13.13	4.89	28.3	0.48
111514_Z2_AP1_core	6.76	7.85	53.27	7.02	7.81	3.54	24.7	0.43
111514_Z2_AP1_rim	6.75	8.69	80.41	10.08	8.34	3.43	23.7	0.47
111514_Z2_AP2_core	7.07	9.25	123.15	15.46	8.79	3.75	23.2	0.47
111514_Z2_AP3	6.81	10.96	174.85	14.79	9.64	3.90	19.9	0.49
111514_Z2_AP4	7.51	12.89	248.32	27.49	11.54	4.27	15.9	0.51
111514_Z2_AP5	7.96	14.70	328.57	35.21	13.07	4.95	17.4	0.48
111514_Z2_AP6	7.32	9.02	78.94	12.57	8.92	3.45	22.1	0.47
111514_Z2_AP7	6.96	8.55	73.81	11.04	8.57	3.29	20.9	0.49

Apatite LA-ICP-MS analysis Part 3a

Sample	P	Cl	Ca	Ca44	Ti	V	Mn	As	Sr	Y	Zr	Cd	Ba	La
	(ppm)	(ppm)	(ppm)	(ppm)	(ppm)	(ppm)	(ppm)	(ppm)	(ppm)	(ppm)	(ppm)	(ppm)	(ppm)	(ppm)
111517_Z1_AP1	160724	1926	400000	419351	8.80	16.63	1240.04	125.42	644.85	4830.13	8.85	1.85	0.94	12875.59
111517_Z1_AP2_core	154190	2171	400000	407314	7.78	18.33	1230.69	74.50	951.09	3469.43	1.45	1.59	2.73	4234.11
111517_Z1_AP2_rim	152255	1947	400000	407575	9.55	20.29	1248.48	85.95	954.23	3688.11	1.93	1.06	3.36	5334.82
111517_Z1_AP3	161608	2016	400000	422902	9.23	14.12	1090.61	104.40	717.78	2922.08	1.89	1.77	1.33	10039.11
111517_Z1_AP4_core	156056	2844	400000	412044	9.11	19.62	1423.84	84.33	548.23	6351.39	3.63	0.85	1.50	4843.57
111517_Z1_AP4_rim	159708	2479	400000	425177	9.99	20.89	1541.29	95.24	571.06	7308.92	5.12	0.99	1.53	4900.48
111517_Z1_AP5	154058	2052	400000	400407	8.74	1.31	1486.77	119.97	507.43	3793.64	0.26	0.87	1.12	2416.69
111517_Z2_AP1_core	155100	2099	400000	403624	9.11	14.35	930.25	92.78	695.42	5525.65	3.06	0.40	1.81	3120.57
111517_Z2_AP1_rim	151957	3311	400000	407109	7.62	16.00	1181.70	96.42	648.54	6238.18	7.50	0.36	1.72	4952.38
111517_Z2_AP2	156601	2708	400000	407903	8.86	17.55	1764.41	85.91	634.26	5514.36	3.20	0.80	1.38	4187.57
111517_Z2_AP3	156888	3081	400000	407540	8.24	17.45	1720.88	72.27	762.79	4876.94	5.05	0.63	1.47	6941.68
111517_Z2_AP4	156653	2168	400000	397511	7.47	11.25	1585.68	98.26	781.32	6726.58	2.72	0.42	1.32	5212.42
111517_Z2_AP5_core	162679	2138	400000	416702	9.81	13.88	1495.46	88.96	721.13	6365.77	2.81	0.67	1.22	3822.27
111517_Z2_AP5_rim	153611	1809	400000	411676	9.79	15.84	1533.44	79.99	755.94	6211.56	2.44	0.89	1.11	4461.85
111517_Z2_AP6	161645	1475	400000	394855	8.57	11.93	1368.29	85.81	714.02	5347.65	2.57	0.49	1.70	2919.69
111517_Z2_AP7	155843	2569	400000	399081	7.83	11.76	1439.03	94.37	769.86	7395.45	7.44	0.76	2.07	3643.91
111520_Z1_AP1_core	108792	39	400000	404335	4.99	14.54	949.15	23.27	282.30	702.99	7.45	0.03	0.39	3215.26
111520_Z1_AP1_rim	108785	429	400000	408825	4.22	4.39	1024.51	243.14	327.07	1234.51	0.24	0.07	0.76	4238.81
111520_Z1_AP2	106561	330	400000	406871	4.01	5.36	1043.61	186.95	224.79	832.59	0.49	0.08	0.57	5726.08
111520_Z1_AP3	110838	192	400000	417826	5.83	7.60	1115.14	191.97	228.48	967.22	1.15	0.00	0.42	6536.63
111520_Z2_AP1	110687	-316	400000	407161	3.89	5.08	1093.19	200.65	222.81	927.62	0.39	-0.04	0.38	5579.31
111520_Z3_AP1	125712	241	400000	411883	5.70	4.48	1104.65	228.32	237.37	885.76	0.29	0.05	0.49	4752.35
111520_Z4_AP1_core	121958	701	400000	415503	4.92	8.15	985.81	23.41	222.76	1491.13	9.98	0.03	0.48	3478.35
111520_Z4_AP1_middle	118794	577	400000	413999	6.48	7.65	962.94	21.61	220.77	1364.54	7.24	-0.03	0.82	3383.18
111520_Z4_AP1_rim	126339	730	400000	418280	4.59	6.22	963.92	52.54	224.49	1214.40	4.17	0.02	0.50	4893.52
111520_Z4_AP2	122799	389	400000	407171	6.18	5.27	768.87	15.17	212.72	619.15	1.02	0.02	0.58	6565.66



Apatite LA-ICP-MS analysis Part 3b

Sample	Ce	Pr	Nd	Sm	Eu	Gd	Tb	Dy	Ho	Er	Tm	Yb	Lu	Pb206
	(ppm)	(ppm)	(ppm)	(ppm)	(ppm)	(ppm)	(ppm)	(ppm)	(ppm)	(ppm)	(ppm)	(ppm)	(ppm)	(ppm)
111517_Z1_AP1	29749.94	3449.29	12238.16	1860.77	249.04	1383.60	189.04	1018.12	182.24	447.31	50.37	259.42	29.48	13.74
111517_Z1_AP2_core	12413.38	1686.15	6684.33	1137.51	155.35	875.45	121.66	678.99	125.27	319.12	39.39	215.26	25.63	12.48
111517_Z1_AP2_rim	14720.62	1907.16	7422.85	1230.89	167.33	934.67	134.09	740.31	133.38	345.41	42.30	237.57	28.07	12.97
111517_Z1_AP3	21186.78	2576.51	9243.08	1286.22	159.66	945.80	120.27	606.34	110.46	268.54	29.68	160.99	18.10	14.73
111517_Z1_AP4_core	15080.81	2106.44	8324.42	1563.64	229.00	1291.90	192.26	1092.49	216.01	586.39	75.58	409.41	46.55	13.11
111517_Z1_AP4_rim	16531.89	2303.90	9485.33	1812.61	258.10	1507.24	231.36	1362.68	256.35	694.56	88.48	490.40	53.33	16.12
111517_Z1_AP5	8098.94	1215.09	4926.67	982.28	138.56	796.76	118.47	686.26	131.00	328.63	41.09	216.49	24.36	6.07
111517_Z2_AP1_core	11337.36	1702.03	7248.18	1446.31	210.38	1171.06	180.62	1031.91	195.08	519.68	67.68	424.66	49.42	15.76
111517_Z2_AP1_rim	15595.94	2251.58	9170.81	1725.60	240.18	1348.17	199.13	1144.87	222.27	597.37	81.48	507.17	58.64	22.57
111517_Z2_AP2	13833.77	1991.20	8251.20	1479.26	213.35	1193.73	179.38	1017.14	192.02	491.51	66.90	403.90	46.45	18.94
111517_Z2_AP3	17491.19	2119.69	8160.70	1299.14	189.42	1037.01	155.46	894.38	173.16	461.31	61.04	373.76	42.25	8.36
111517_Z2_AP4	15568.32	2186.88	8683.64	1594.66	227.51	1294.62	207.94	1159.74	234.28	639.70	85.90	549.99	61.52	19.35
111517_Z2_AP5_core	12926.26	1912.70	8067.27	1526.77	219.70	1269.68	202.71	1160.03	227.03	628.60	81.55	519.64	57.90	14.86
111517_Z2_AP5_rim	13843.42	1879.82	7863.05	1443.11	209.80	1231.27	185.58	1110.81	216.25	605.08	81.02	509.55	58.26	16.76
111517_Z2_AP6	11702.21	1811.62	7656.34	1481.38	219.23	1182.26	184.66	949.52	183.98	478.92	61.76	353.30	41.12	15.25
111517_Z2_AP7	14014.27	2167.73	9091.36	1829.46	279.31	1597.19	248.63	1431.20	280.37	753.26	100.18	622.48	71.49	22.01
111520_Z1_AP1_core	4183.64	338.21	1030.40	157.13	26.41	135.44	18.71	104.97	20.52	56.89	7.77	49.35	8.12	3.67
111520_Z1_AP1_rim	5922.73	503.84	1572.19	253.85	44.19	216.60	30.47	169.83	34.61	93.60	12.35	85.32	13.27	13.92
111520_Z1_AP2	6555.75	493.04	1493.72	203.66	34.47	169.46	22.95	131.28	27.47	75.46	9.91	62.80	10.41	7.31
111520_Z1_AP3	7778.46	588.32	1747.57	233.73	41.70	195.76	27.36	156.53	31.42	87.42	11.71	75.99	12.45	8.62
111520_Z2_AP1	6785.02	547.84	1691.42	226.85	35.76	198.13	26.47	147.15	30.38	85.62	10.86	69.40	11.30	8.35
111520_Z3_AP1	6204.95	506.54	1576.78	212.96	30.06	181.99	24.06	139.67	28.66	80.93	10.27	69.30	11.11	5.82
111520_Z4_AP1_core	5936.41	639.54	2610.95	477.56	36.90	443.28	60.19	312.58	56.57	144.53	15.82	84.72	10.19	3.73
111520_Z4_AP1_middle	5483.69	551.27	2206.06	419.85	32.27	376.11	51.05	277.92	52.93	130.45	14.67	77.40	9.67	3.24
111520_Z4_AP1_rim	6793.31	630.25	2226.29	369.38	42.60	345.51	45.05	235.28	46.54	117.96	13.21	80.11	11.37	4.11
111520_Z4_AP2	8119.96	557.14	1553.07	176.42	44.78	146.52	18.85	100.77	20.30	59.86	8.22	59.08	10.43	5.48

Apatite LA-ICP-MS analysis Part 3c

Sample	Pb207	Pb208	Th	U	Pb	TREE	(Ce/Yb)N	Eu*
	(ppm)	(ppm)	(ppm)	(ppm)	(ppm)	(wt.%)		
111517_Z1_AP1	4.27	11.95	362.12	58.70	10.71	6.88	32.0	0.46
111517_Z1_AP2_core	8.32	10.43	96.75	20.80	10.49	3.22	16.1	0.46
111517_Z1_AP2_rim	8.31	11.54	140.88	27.67	11.17	3.71	17.3	0.46
111517_Z1_AP3	10.68	12.79	103.89	19.82	12.72	4.97	36.7	0.43
111517_Z1_AP4_core	6.93	11.80	256.64	41.56	11.04	4.24	10.3	0.48
111517_Z1_AP4_rim	7.09	13.88	310.94	58.85	12.93	4.73	9.4	0.46
111517_Z1_AP5	5.20	5.52	8.54	2.21	5.64	2.39	10.4	0.46
111517_Z2_AP1_core	4.84	9.73	268.81	70.14	10.13	3.42	7.4	0.48
111517_Z2_AP1_rim	6.36	15.31	444.49	113.10	15.13	4.43	8.6	0.47
111517_Z2_AP2	6.08	10.61	220.63	81.53	11.66	3.91	9.5	0.47
111517_Z2_AP3	6.18	6.96	45.53	12.04	7.10	4.43	13.0	0.48
111517_Z2_AP4	8.09	14.94	345.67	73.86	14.50	4.44	7.9	0.47
111517_Z2_AP5_core	6.16	11.72	284.12	58.41	11.25	3.90	6.9	0.47
111517_Z2_AP5_rim	8.26	13.01	260.44	58.43	12.86	3.99	7.6	0.47
111517_Z2_AP6	3.26	5.39	134.74	76.39	7.36	3.46	9.2	0.49
111517_Z2_AP7	5.34	9.55	238.04	116.79	11.71	4.35	6.3	0.48
111520_Z1_AP1_core	1.76	2.41	37.22	9.62	2.55	1.01	23.6	0.54
111520_Z1_AP1_rim	8.44	10.02	57.78	23.20	10.44	1.44	19.3	0.56
111520_Z1_AP2	1.45	3.29	103.45	37.21	3.83	1.58	29.1	0.55
111520_Z1_AP3	1.75	4.97	163.98	44.10	5.08	1.85	28.5	0.58
111520_Z2_AP1	1.49	3.23	93.10	41.73	3.99	1.64	27.2	0.50
111520_Z3_AP1	1.43	2.66	64.43	26.47	3.13	1.47	25.0	0.45
111520_Z4_AP1_core	1.07	2.68	75.84	15.60	2.55	1.58	19.5	0.24
111520_Z4_AP1_middle	1.13	2.44	65.48	13.46	2.32	1.44	19.7	0.24
111520_Z4_AP1_rim	1.24	2.81	80.11	16.97	2.74	1.71	23.6	0.35
111520_Z4_AP2	1.92	5.80	167.51	19.69	4.81	1.81	38.3	0.82

Apatite LA-ICP-MS analysis Part 4a

Sample	P	Cl	Ca	Ca44	Ti	V	Mn	As	Sr	Y	Zr	Cd	Ba	La
	(ppm)	(ppm)	(ppm)	(ppm)	(ppm)	(ppm)	(ppm)	(ppm)	(ppm)	(ppm)	(ppm)	(ppm)	(ppm)	(ppm)
111524_Z1_AP2	94401	3775	400000	407683	4.62	81.59	2870.57	30.38	275.23	1907.12	1.20	-0.07	0.10	2271.78
111524_Z1_AP3	89754	3622	400000	396106	10.74	60.86	2817.27	28.07	275.14	1865.23	2.19	0.00	0.25	2661.84
111524_Z1_AP4	96488	3575	400000	418780	6.58	54.44	2979.82	25.68	254.64	2480.40	0.78	-0.01	0.04	1680.85
111524_Z1_AP5	90988	3763	400000	413199	12.20	16.04	2846.67	29.48	260.43	2284.59	35.98	0.07	0.15	2796.30
111524_Z1_AP6	90211	3490	400000	412751	6.82	29.75	2884.84	27.22	253.10	2396.15	4.48	0.02	0.05	2132.07
111524_Z1_AP7	88191	4238	400000	399872	18.32	21.29	2822.56	27.12	252.48	2152.62	29.61	-0.05	0.13	2443.53
111524_Z1_AP8_core	92013	3428	400000	411593	6.18	28.88	2979.16	25.02	255.89	2034.20	1.80	0.02	0.17	2152.06
111524_Z1_AP8_rim	95782	2568	400000	417953	6.36	128.32	3439.04	29.08	245.46	2026.71	1.80	-0.03	0.07	1205.04
111524_Z2_AP1_core	92385	4055	400000	410945	9.21	30.56	2356.44	29.75	348.56	2636.90	20.00	0.07	0.14	2618.94
111524_Z2_AP1_rim	92798	3234	400000	415842	5.28	257.67	2365.88	53.93	327.21	2367.76	40.07	-0.01	0.17	1729.74
111524_Z2_AP2_core	96754	3686	400000	424594	9.40	32.77	2300.81	24.81	347.81	2141.21	6.01	0.05	0.08	1964.02
111524_Z2_AP2_rim	95477	3665	400000	412582	5.26	33.83	2315.69	24.09	337.12	2087.06	2.43	-0.06	0.09	1869.97
111524_Z3_1	93318	3970	400000	414271	5.97	25.03	2719.31	25.63	235.43	1324.36	8.28	0.03	0.06	1907.48
111524_Z3_2	94299	4340	400000	413204	9.08	15.03	2661.52	26.36	243.28	1551.86	31.93	-0.09	0.14	2798.84
111524_Z3_3	103108	3626	400000	416389	6.56	24.82	2647.32	24.20	238.85	1323.28	2.32	0.05	0.10	1833.42
195759_Z1_AP1	130354	1959	400000	408416	8.14	15.52	1530.02	18.97	2047.03	1081.36	29.29	0.28	3.34	2310.36
195759_Z1_AP2	127957	1477	400000	405882	4.82	12.38	1665.91	18.81	2092.26	1044.56	37.47	0.27	2.12	2311.45
195759_Z1_AP3	136398	2000	400000	417698	7.64	15.84	1760.35	24.50	2450.39	1297.78	34.03	0.30	4.20	2781.63
195759_Z1_AP4	132409	1719	400000	415704	8.55	19.11	1860.79	22.90	2379.52	1220.44	35.63	0.18	3.57	2647.26
195759_Z1_AP5_core	134706	1687	400000	423714	14.30	16.23	1570.42	21.31	2153.14	1166.34	31.90	0.20	4.82	2526.45
195759_Z1_AP5_rim	127334	1858	400000	408410	7.50	17.38	1697.93	18.89	2148.90	1017.87	29.75	0.26	3.94	2410.16
195759_Z2_AP2	120726	1406	400000	416853	8.02	19.43	911.67	19.13	2070.61	1160.51	28.35	0.08	1.90	2418.48
195759_Z2_AP3_core	120477	1755	400000	410931	8.61	16.90	963.99	17.40	2167.01	1078.69	25.46	0.18	4.40	2370.19
195759_Z2_AP3_core	125005	1474	400000	414721	7.26	19.12	893.15	20.92	2261.87	1173.77	27.02	0.14	4.68	2523.50
195759_Z2_AP4	124198	1702	400000	420890	6.40	22.75	1052.43	20.84	2205.67	1149.75	28.48	0.16	4.35	2573.12
195759_Z2_AP5	119419	1775	400000	411102	7.23	18.19	1117.56	19.83	2247.87	1189.65	30.20	0.27	2.12	2511.72

Apatite LA-ICP-MS analysis Part 4b

Sample	Ce	Pr	Nd	Sm	Eu	Gd	Tb	Dy	Ho	Er	Tm	Yb	Lu	Pb206
	(ppm)	(ppm)	(ppm)	(ppm)	(ppm)	(ppm)	(ppm)	(ppm)	(ppm)	(ppm)	(ppm)	(ppm)	(ppm)	(ppm)
111524_Z1_AP2	6223.71	866.49	3216.03	574.78	123.79	429.46	61.57	353.26	68.43	192.67	27.78	184.96	25.34	0.69
111524_Z1_AP3	6636.77	896.47	3257.36	562.41	120.30	416.56	60.04	345.63	67.47	184.10	26.78	181.21	24.49	6.84
111524_Z1_AP4	5120.32	805.75	3191.50	647.62	132.41	526.73	77.79	459.27	89.10	248.83	34.10	224.37	28.98	1.40
111524_Z1_AP5	7062.06	990.10	3721.10	649.69	127.74	518.78	75.76	425.31	83.19	234.89	31.44	205.07	26.60	1.45
111524_Z1_AP6	5948.61	886.86	3504.93	640.55	131.38	495.04	73.88	433.01	85.47	236.90	32.43	210.73	28.28	0.66
111524_Z1_AP7	6208.47	888.73	3495.10	628.31	121.00	481.09	69.74	405.92	79.32	218.30	30.07	197.35	26.72	1.14
111524_Z1_AP8_core	5798.93	861.67	3244.35	579.95	119.30	449.63	65.06	359.89	70.32	198.58	27.59	179.82	23.86	4.99
111524_Z1_AP8_rim	4012.62	623.31	2627.12	530.35	115.15	424.90	62.56	359.48	68.07	188.02	24.73	157.94	20.60	2.06
111524_Z2_AP1_core	6782.33	972.95	3594.10	618.79	223.34	488.84	73.16	441.40	89.60	255.50	35.41	217.95	28.19	1.32
111524_Z2_AP1_rim	5552.75	851.35	3169.09	565.77	220.54	464.74	66.08	393.44	78.25	214.63	27.92	163.05	19.66	0.73
111524_Z2_AP2_core	5676.07	855.44	3153.43	534.20	204.50	419.65	62.33	364.31	70.66	200.86	25.50	153.69	18.76	0.64
111524_Z2_AP2_rim	5542.67	818.41	3007.55	519.88	197.32	422.52	60.94	351.01	69.23	190.61	24.72	142.85	17.59	0.76
111524_Z3_1	6032.24	877.19	3269.31	537.60	105.38	395.22	50.48	261.11	46.62	113.63	13.16	73.74	9.05	0.80
111524_Z3_2	6537.42	975.10	3575.22	546.87	105.67	402.55	54.26	291.63	56.18	145.30	18.19	105.57	14.53	0.80
111524_Z3_3	6173.67	871.95	3218.29	528.24	103.01	387.32	49.32	248.50	44.15	108.08	12.08	65.75	7.87	0.76
195759_Z1_AP1	5311.02	628.86	2405.70	415.84	85.62	337.02	43.44	228.66	40.16	102.95	11.94	65.92	8.67	2.29
195759_Z1_AP2	5221.78	623.23	2389.49	408.85	82.71	329.75	43.65	227.66	42.11	100.96	11.94	63.88	8.60	2.38
195759_Z1_AP3	5403.50	660.65	2423.46	410.60	91.24	379.38	49.59	284.98	52.06	121.84	13.61	77.29	10.34	2.58
195759_Z1_AP4	5539.36	631.59	2461.96	416.22	90.12	356.61	53.05	276.23	47.36	113.85	13.89	74.37	10.30	2.45
195759_Z1_AP5_core	5798.31	671.56	2514.96	433.19	86.29	357.08	49.63	266.14	47.28	109.74	12.43	69.60	9.49	2.37
195759_Z1_AP5_rim	5124.42	612.50	2294.97	394.51	80.56	337.42	45.89	242.71	40.39	93.07	11.69	60.75	8.46	2.12
195759_Z2_AP2	5572.77	649.34	2439.09	421.30	86.12	335.76	45.19	232.63	43.00	108.38	12.54	69.11	8.71	1.94
195759_Z2_AP3_core	5114.69	609.83	2171.81	360.50	78.56	311.73	41.81	238.13	41.84	102.43	11.76	62.28	8.54	2.06
195759_Z2_AP3_core	5645.27	638.24	2418.15	405.57	86.69	350.35	45.24	248.70	45.10	110.23	12.69	69.24	9.10	2.32
195759_Z2_AP4	5629.82	626.08	2376.34	410.96	83.64	333.06	46.36	248.75	42.92	108.62	12.23	69.48	9.35	2.49
195759_Z2_AP5	5634.33	645.29	2368.88	400.32	87.36	343.96	48.52	247.97	44.33	109.17	13.40	72.43	9.51	2.19

Apatite LA-ICP-MS analysis Part 4c

Sample	Pb207	Pb208	Th	U	Pb	TREE	(Ce/Yb)N	Eu*
	(ppm)	(ppm)	(ppm)	(ppm)	(ppm)	(wt.%)		
111524_Z1_AP2	0.57	2.00	58.72	0.28	1.36	1.65	9.4	0.74
111524_Z1_AP3	6.49	8.29	70.19	0.39	7.55	1.73	10.2	0.74
111524_Z1_AP4	1.16	2.32	50.54	0.12	1.83	1.57	6.4	0.67
111524_Z1_AP5	0.65	3.04	106.73	4.12	2.12	1.92	9.6	0.65
111524_Z1_AP6	0.74	2.50	90.33	0.33	1.66	1.72	7.9	0.69
111524_Z1_AP7	0.77	2.75	90.08	2.15	1.92	1.74	8.8	0.65
111524_Z1_AP8_core	4.52	5.65	46.59	0.16	5.23	1.62	9.0	0.69
111524_Z1_AP8_rim	1.88	2.32	16.73	0.09	2.14	1.24	7.1	0.72
111524_Z2_AP1_core	0.67	3.82	144.80	3.97	2.50	1.91	8.7	1.20
111524_Z2_AP1_rim	0.61	2.58	97.95	0.60	1.70	1.59	9.5	1.27
111524_Z2_AP2_core	0.63	2.42	85.85	0.54	1.58	1.58	10.3	1.28
111524_Z2_AP2_rim	0.56	2.20	74.96	0.49	1.48	1.53	10.8	1.25
111524_Z3_1	0.62	1.23	31.93	0.35	0.98	1.50	22.8	0.68
111524_Z3_2	0.55	1.52	43.69	1.70	1.15	1.72	17.3	0.67
111524_Z3_3	0.62	1.20	24.12	0.11	0.96	1.50	26.2	0.67
195759_Z1_AP1	1.16	1.85	31.85	7.28	1.78	1.31	22.5	0.68
195759_Z1_AP2	1.05	1.80	31.42	7.06	1.72	1.29	22.8	0.67
195759_Z1_AP3	1.38	1.91	33.48	7.14	1.98	1.41	19.5	0.68
195759_Z1_AP4	1.25	1.95	34.37	7.37	1.92	1.40	20.8	0.69
195759_Z1_AP5_core	1.16	2.10	34.60	7.73	1.94	1.41	23.2	0.65
195759_Z1_AP5_rim	1.12	1.87	30.10	6.42	1.77	1.28	23.5	0.65
195759_Z2_AP2	0.97	1.64	32.78	7.08	1.58	1.36	22.5	0.68
195759_Z2_AP3_core	1.17	1.58	24.73	5.77	1.61	1.26	22.9	0.69
195759_Z2_AP3_core	1.06	1.77	30.58	6.47	1.78	1.38	22.7	0.68
195759_Z2_AP4	1.28	1.82	31.82	6.88	1.91	1.37	22.6	0.67
195759_Z2_AP5	0.87	1.66	30.89	6.80	1.62	1.37	21.7	0.70

Apatite LA-ICP-MS analysis Part 5a

Sample	P	Cl	Ca	Ca44	Ti	V	Mn	As	Sr	Y	Zr	Cd	Ba	La
	(ppm)	(ppm)	(ppm)	(ppm)	(ppm)	(ppm)	(ppm)	(ppm)	(ppm)	(ppm)	(ppm)	(ppm)	(ppm)	(ppm)
195759_Z2_AP6	116506	1941	400000	402254	8.21	18.54	1105.56	22.05	2235.02	1318.02	30.01	0.14	3.11	2748.09
195760-Z1-Ap10	133529	1666	400000	401602	8.29	12.38	817.56	32.87	1863.28	1819.47	28.31	0.29	0.85	4415.64
195760-Z1-Ap11	139044	1795	400000	404441	11.41	14.99	499.89	26.62	1823.85	1435.22	13.46	0.14	6.14	3591.83
195760-Z1-Ap1-core	102080	1927	400000	395876	6.99	13.21	640.31	35.23	1848.07	1933.01	27.71	0.28	2.96	4446.63
195760-Z1-Ap1-rim	100251	1549	400000	390717	7.35	17.33	612.28	32.61	1757.58	1786.43	19.78	0.32	2.56	4094.29
195760-Z1-Ap2	98747	1897	400000	399317	7.97	14.28	625.72	31.25	1826.52	1724.31	21.78	0.30	4.95	4007.24
195760-Z1-Ap3	97774	1857	400000	399125	8.38	19.48	477.13	28.85	1779.68	1531.72	14.71	0.22	5.57	3745.03
195760-Z1-Ap4-core	96726	1617	400000	393970	11.45	15.70	650.13	33.59	1775.57	1686.47	19.94	0.19	7.02	4975.71
195760-Z1-Ap4-rim	98526	1787	400000	406632	8.20	15.56	660.74	29.05	1859.92	1560.67	16.41	0.22	5.17	3766.43
195760-Z1-Ap5	98301	1600	400000	406649	10.86	14.01	719.99	31.75	1836.40	1762.88	25.79	0.25	9.09	4067.26
195760-Z1-Ap6-core	105586	1885	400000	394026	9.89	15.69	648.59	30.87	1833.71	1720.59	19.40	0.19	4.10	3954.96
195760-Z1-Ap6-rim	118903	1677	400000	401261	9.12	16.29	630.60	32.01	1854.21	1779.29	19.19	0.35	3.22	4200.02
195760-Z1-Ap7	117820	2040	400000	396046	6.58	13.91	723.71	30.55	1845.44	1691.89	21.49	0.21	2.56	4088.67
195760-Z1-Ap8	125990	1860	400000	405096	7.91	17.17	712.51	40.15	1876.84	2272.21	42.99	0.28	3.04	5191.83
195760-Z1-Ap9	130902	1811	400000	405504	7.49	10.13	672.88	30.44	1834.02	1671.61	17.95	0.21	6.37	3999.15
195761_Ap1	181116	1780	400000	403301	9.91	17.78	694.74	28.44	817.83	1483.56	23.68	0.46	3.33	3613.92
195761_Ap10	133739	1908	400000	409265	8.85	23.57	766.44	31.32	760.27	1771.19	35.23	0.11	2.24	3617.73
195761_Ap2_core	168893	1940	400000	408815	13.64	29.38	883.17	27.72	1291.51	1559.53	15.32	0.13	1.98	3414.57
195761_Ap2_rim	157719	1485	400000	416196	20.82	22.60	888.01	28.12	1235.98	1457.16	19.74	0.32	8.48	3913.23
195761_Ap3	154402	2028	400000	406140	8.12	43.79	756.63	24.04	1269.47	1340.30	17.40	0.17	0.18	3334.88
195761_Ap4	148764	2140	400000	411847	6.30	20.96	688.79	28.38	1291.16	1627.47	12.13	0.23	4.29	3679.70
195761_Ap5_core	164805	2080	400000	408678	13.05	22.56	797.08	30.25	1386.12	1853.65	18.81	0.25	10.25	3850.78
195761_Ap5_rim	132030	2072	400000	398682	10.31	19.93	732.43	27.27	1314.47	1611.08	12.45	0.27	4.50	3304.94
195761_Ap6	129356	1763	400000	400358	7.20	19.48	601.07	26.19	1292.90	1354.64	10.42	0.29	5.66	3121.55
195761_Ap7	127124	1682	400000	397795	9.71	32.10	845.17	27.71	1321.92	1461.05	20.15	0.18	12.13	3485.05
195761_Ap9	123142	1899	400000	408125	8.22	17.15	714.13	27.23	1212.40	1479.23	13.21	0.33	6.64	3384.64
195764_Z1_AP1	142520	979	400000	407356	8.96	12.17	770.09	50.26	239.68	2114.39	3.22	1.01	0.62	7392.32

Apatite LA-ICP-MS analysis Part 5b

Sample	Ce	Pr	Nd	Sm	Eu	Gd	Tb	Dy	Ho	Er	Tm	Yb	Lu	Pb206
	(ppm)	(ppm)	(ppm)	(ppm)	(ppm)	(ppm)	(ppm)	(ppm)	(ppm)	(ppm)	(ppm)	(ppm)	(ppm)	(ppm)
195759_Z2_AP6	5838.29	661.69	2498.97	423.88	91.67	372.73	51.20	266.83	46.38	118.15	14.59	76.73	9.59	2.36
195760-Z1-Ap10	9520.25	1151.08	4330.24	686.02	112.83	542.31	70.53	366.84	67.44	170.93	20.42	118.45	15.52	3.56
195760-Z1-Ap11	7664.48	935.06	3508.49	550.53	93.20	438.52	56.73	297.12	54.59	134.20	16.05	89.79	11.51	2.47
195760-Z1-Ap1-core	9631.30	1174.25	4501.71	719.30	116.68	571.17	73.26	396.12	72.90	182.45	21.90	128.78	16.28	3.26
195760-Z1-Ap1-rim	9059.84	1108.92	4194.00	668.01	108.92	531.18	68.76	374.62	68.26	170.82	20.06	118.70	15.74	2.95
195760-Z1-Ap2	8593.48	1041.93	3963.02	640.44	104.74	496.18	64.92	353.65	64.72	163.01	19.38	113.24	14.68	2.80
195760-Z1-Ap3	8134.20	989.78	3723.58	581.18	98.36	467.53	60.65	321.23	57.81	143.48	16.99	96.08	12.34	2.59
195760-Z1-Ap4-core	10591.10	1169.48	4607.94	638.59	106.06	502.10	66.67	337.43	60.57	159.18	18.68	110.20	14.21	2.56
195760-Z1-Ap4-rim	8011.40	987.81	3704.17	592.52	98.60	471.41	61.38	318.45	59.40	147.49	17.22	102.93	12.94	2.92
195760-Z1-Ap5	8666.77	1067.36	4154.61	651.70	107.18	511.47	66.78	353.23	65.48	166.53	19.41	114.29	15.07	3.04
195760-Z1-Ap6-core	9120.70	1084.77	3931.81	627.76	104.29	505.31	67.96	347.76	63.84	158.74	18.60	109.40	14.15	3.04
195760-Z1-Ap6-rim	9434.22	1119.79	4196.72	665.04	112.86	536.66	69.80	374.71	68.07	169.93	20.12	118.38	15.58	3.02
195760-Z1-Ap7	8901.51	1085.98	4098.37	638.56	104.56	509.10	67.36	356.72	65.12	164.60	19.40	110.94	14.68	2.66
195760-Z1-Ap8	11642.56	1414.73	5248.73	830.93	141.74	669.74	88.71	474.41	86.91	218.48	26.15	151.42	19.42	3.75
195760-Z1-Ap9	8781.57	1064.88	3969.21	618.30	106.50	510.21	65.05	351.11	63.05	159.37	18.67	109.13	14.38	3.18
195761_Ap1	7967.39	873.36	3243.34	512.16	66.70	453.30	61.07	320.73	62.07	145.23	17.38	105.03	13.00	1.95
195761_Ap10	8252.14	936.86	3645.42	600.14	69.33	512.61	69.83	359.42	67.58	168.74	20.21	113.93	14.79	2.29
195761_Ap2_core	7854.36	880.17	3143.19	536.26	94.17	474.44	63.50	302.53	52.96	145.92	17.00	93.23	11.83	2.46
195761_Ap2_rim	8010.72	915.11	3312.20	538.99	95.92	438.09	63.92	321.36	56.36	151.27	19.00	99.81	13.98	2.82
195761_Ap3	7117.79	841.76	2947.27	489.21	82.84	415.90	52.57	283.62	50.05	129.81	16.02	84.25	11.26	5.91
195761_Ap4	7850.32	916.92	3431.41	556.74	99.33	459.27	65.03	359.84	62.58	157.39	18.18	103.69	13.72	2.57
195761_Ap5_core	8440.63	947.19	3264.67	527.64	98.78	457.58	60.41	347.38	68.03	161.46	19.50	117.09	14.95	2.50
195761_Ap5_rim	7613.31	885.66	3256.11	525.29	94.34	468.15	62.70	326.31	59.99	151.33	18.10	104.39	14.34	2.13
195761_Ap6	6682.48	805.02	2873.86	464.70	81.61	399.40	53.31	281.99	53.60	130.07	15.17	89.41	10.89	2.24
195761_Ap7	7136.72	810.42	3081.93	505.62	89.78	426.40	58.12	316.70	56.84	141.69	16.41	91.82	12.03	2.70
195761_Ap9	7360.26	844.44	3201.91	503.52	92.61	434.24	60.54	320.83	57.40	144.18	17.40	94.88	12.33	2.80
195764_Z1_AP1	14910.17	1720.56	5898.93	828.26	114.96	645.93	84.45	409.66	70.59	171.95	19.51	100.65	12.76	6.84

Apatite LA-ICP-MS analysis Part 5c

Sample	Pb207	Pb208	Th	U	Pb	TREE	(Ce/Yb)N	Eu*
	(ppm)	(ppm)	(ppm)	(ppm)	(ppm)	(wt.%)		
195759_Z2_AP6	1.00	1.71	34.42	7.35	1.73	1.45	21.2	0.68
195760-Z1-Ap10	1.85	3.04	53.13	9.92	2.93	2.34	21.3	0.55
195760-Z1-Ap11	1.64	2.13	27.49	5.48	2.11	1.89	20.8	0.56
195760-Z1-Ap1-core	1.83	2.84	52.83	9.35	2.74	2.40	21.1	0.54
195760-Z1-Ap1-rim	1.76	2.64	45.44	8.29	2.52	2.24	23.6	0.54
195760-Z1-Ap2	1.58	2.57	39.97	7.48	2.43	2.14	26.8	0.55
195760-Z1-Ap3	1.56	2.22	33.11	6.56	2.17	2.00	21.7	0.56
195760-Z1-Ap4-core	1.62	2.42	48.55	7.63	2.28	2.50	21.1	0.55
195760-Z1-Ap4-rim	1.72	2.44	32.57	6.29	2.41	1.99	23.2	0.55
195760-Z1-Ap5	1.62	2.78	40.60	7.65	2.61	2.18	22.2	0.55
195760-Z1-Ap6-core	1.58	2.63	41.08	7.55	2.51	2.18	22.4	0.55
195760-Z1-Ap6-rim	1.84	2.61	44.68	8.20	2.58	2.29	21.4	0.56
195760-Z1-Ap7	1.60	2.37	40.30	7.76	2.29	2.19	22.4	0.54
195760-Z1-Ap8	1.82	3.33	81.15	14.09	3.12	2.85	22.4	0.56
195760-Z1-Ap9	1.82	2.65	38.78	7.40	2.60	2.15	23.8	0.56
195761_Ap1	1.08	1.54	28.97	5.84	1.65	1.89	21.1	0.41
195761_Ap10	0.97	1.95	47.56	8.54	1.82	2.02	23.5	0.37
195761_Ap2_core	1.35	1.89	25.03	5.83	2.00	1.86	22.4	0.55
195761_Ap2_rim	1.41	2.19	28.10	6.35	2.31	1.94	23.5	0.58
195761_Ap3	4.59	5.18	22.40	5.81	5.45	1.72	21.1	0.54
195761_Ap4	1.45	1.88	29.32	6.65	1.99	1.94	20.1	0.58
195761_Ap5_core	1.47	2.07	28.34	6.14	2.14	2.02	20.3	0.59
195761_Ap5_rim	1.18	1.62	24.84	5.95	1.68	1.85	20.8	0.56
195761_Ap6	1.56	1.69	20.29	4.85	1.88	1.64	21.7	0.56
195761_Ap7	1.78	2.30	24.06	5.54	2.29	1.77	21.6	0.57
195761_Ap9	1.54	2.05	25.37	5.77	2.18	1.80	20.2	0.59
195764_Z1_AP1	5.56	7.16	54.07	1.69	6.65	3.45	41.3	0.46



Apatite LA-ICP-MS analysis Part 6a

Sample	P	Cl	Ca	Ca44	Ti	V	Mn	As	Sr	Y	Zr	Cd	Ba	La
	(ppm)	(ppm)	(ppm)	(ppm)	(ppm)	(ppm)	(ppm)	(ppm)	(ppm)	(ppm)	(ppm)	(ppm)	(ppm)	(ppm)
195764_Z1_AP2	145425	1085	400000	388120	8.35	12.55	790.57	53.29	233.21	2583.75	8.48	0.69	0.83	8323.26
195764_Z1_AP3	149416	766	400000	412488	8.81	15.78	725.66	37.98	247.01	1573.96	1.31	0.57	0.63	5783.54
195764_Z1_AP4	149027	893	400000	395247	7.32	11.92	772.73	64.18	234.50	3844.60	6.90	0.57	2.41	5668.21
195764_Z1_AP5	148054	399	400000	388245	7.91	11.26	684.38	60.96	220.05	3547.49	2.97	0.41	0.48	5728.03
195764_Z1_AP6_core	156692	1462	400000	432086	7.00	12.63	2042.25	61.65	475.54	5536.41	2.63	0.60	2.20	5976.91
195764_Z1_AP6_rim	163310	814	400000	406777	7.72	13.81	2112.60	75.39	459.20	5444.85	3.55	0.68	2.20	7109.23
195764_Z2_AP1_core	159133	498	400000	402271	7.26	13.78	1026.92	59.33	338.15	6120.34	4.69	0.72	1.35	5486.30
195764_Z2_AP1_rim	161353	840	400000	414116	11.53	13.08	1132.03	57.30	334.62	5871.45	3.64	0.42	1.70	6005.71
195764_Z2_AP2	158317	701	400000	410785	5.66	12.22	832.13	60.05	295.50	3253.52	5.59	0.58	1.73	8852.74
195764_Z2_AP3	156895	885	400000	416559	5.59	13.51	837.89	65.70	291.36	4160.62	5.44	0.58	0.80	7161.52
195764_Z2_AP4	159934	1012	400000	403794	8.81	13.33	705.10	44.72	211.12	3316.95	5.04	0.42	0.99	6361.56
195764_Z2_AP5	155021	1261	400000	408333	7.90	14.80	776.96	60.04	220.55	3313.14	10.09	0.59	0.59	9008.00
195764_Z2_AP6_core	149032	1742	400000	403725	7.29	12.39	748.54	48.88	234.80	2662.53	8.17	0.51	0.61	6572.32
195764_Z2_AP6_rim	138632	1415	400000	405100	8.05	11.27	787.46	56.82	219.64	3255.06	13.92	0.72	0.69	7052.85

Apatite LA-ICP-MS analysis Part 6b

Sample	Ce	Pr	Nd	Sm	Eu	Gd	Tb	Dy	Ho	Er	Tm	Yb	Lu	Pb206
	(ppm)	(ppm)	(ppm)	(ppm)	(ppm)	(ppm)	(ppm)	(ppm)	(ppm)	(ppm)	(ppm)	(ppm)	(ppm)	(ppm)
195764_Z1_AP2	17348.09	1920.20	6810.61	969.02	131.07	756.10	104.73	532.96	93.57	220.01	25.49	139.39	17.26	9.20
195764_Z1_AP3	11536.47	1309.96	4442.99	637.98	88.73	506.99	65.00	317.44	54.05	127.84	14.39	75.34	9.23	5.99
195764_Z1_AP4	14856.48	1884.76	7228.48	1198.40	179.75	1020.78	143.89	800.49	140.00	353.87	41.35	226.16	25.67	8.36
195764_Z1_AP5	13743.64	1742.89	6503.64	1107.25	163.34	926.21	132.76	674.91	123.12	325.24	37.78	200.26	23.42	7.04
195764_Z1_AP6_core	14619.40	1787.56	6906.55	1268.99	180.79	1182.31	179.84	1021.04	193.33	489.91	58.81	322.55	39.64	22.18
195764_Z1_AP6_rim	17140.45	2088.60	7692.74	1319.00	202.62	1263.52	188.41	1031.54	196.97	511.98	62.30	345.09	41.08	21.78
195764_Z2_AP1_core	13180.36	1678.78	6363.27	1233.15	189.33	1174.19	182.35	1012.44	196.63	537.80	74.23	469.91	66.55	16.60
195764_Z2_AP1_rim	13175.82	1658.80	6339.81	1209.03	192.40	1130.52	186.07	1041.31	204.35	562.32	72.32	424.78	55.03	15.30
195764_Z2_AP2	18200.73	1988.50	7489.59	1166.01	159.85	925.02	124.77	678.53	120.72	288.22	33.22	171.60	20.43	10.89
195764_Z2_AP3	17137.98	2073.84	7739.63	1294.08	195.45	1106.42	153.51	799.09	147.19	336.49	35.98	168.27	18.40	10.47
195764_Z2_AP4	13358.61	1607.42	5749.72	955.12	150.39	806.30	121.85	643.13	114.83	280.04	32.09	165.59	21.19	7.67
195764_Z2_AP5	18918.27	2079.47	7103.67	1061.19	170.61	898.16	128.33	682.17	122.59	289.58	34.64	187.49	22.35	7.09
195764_Z2_AP6_core	14284.81	1628.25	5848.02	900.02	136.59	747.95	103.29	548.81	96.05	232.32	27.45	144.29	17.71	10.11
195764_Z2_AP6_rim	15407.40	1883.97	6607.18	1059.98	172.54	897.95	125.45	649.43	112.39	280.14	33.57	179.50	21.88	11.70

Apatite LA-ICP-MS analysis Part 6c

Sample	Pb207	Pb208	Th	U	Pb	TREE	(Ce/Yb)N	Eu*
	(ppm)	(ppm)	(ppm)	(ppm)	(ppm)	(wt.%)		
195764_Z1_AP2	6.35	8.69	111.41	15.21	8.31	4.00	34.7	0.45
195764_Z1_AP3	5.16	6.22	23.62	0.77	5.89	2.65	42.7	0.46
195764_Z1_AP4	7.12	10.04	103.11	3.52	8.96	3.76	18.3	0.48
195764_Z1_AP5	6.41	8.98	95.39	2.63	7.80	3.50	19.1	0.48
195764_Z1_AP6_core	18.63	20.89	99.85	16.58	20.61	3.98	12.6	0.44
195764_Z1_AP6_rim	17.29	20.90	92.14	17.61	20.14	4.46	13.8	0.46
195764_Z2_AP1_core	12.95	17.19	162.85	19.22	15.88	3.80	7.8	0.47
195764_Z2_AP1_rim	12.68	15.50	95.00	13.76	14.62	3.81	8.6	0.49
195764_Z2_AP2	8.02	9.61	76.18	11.46	9.48	4.35	29.6	0.46
195764_Z2_AP3	8.54	9.99	95.86	10.34	9.84	4.25	28.4	0.48
195764_Z2_AP4	5.97	7.72	77.97	9.86	7.34	3.37	22.5	0.51
195764_Z2_AP5	5.10	6.67	71.43	9.29	6.30	4.40	28.1	0.52
195764_Z2_AP6_core	6.42	8.99	92.91	16.32	8.53	3.40	27.6	0.49
195764_Z2_AP6_rim	6.75	10.53	165.23	26.10	9.82	3.77	23.9	0.52

